7760

II

ANL-7760

Part II

Argonne National Laboratory

RADIOLOGICAL PHYSICS DIVISION ANNUAL REPORT

Center for Human Radiobiology

July 1969—June 1970

The facilities of Argonne National Laboratory are owned by the United States Government. Under the terms of a contract (W-31-109-Eng-38) between the U. S. Atomic Energy Commission, Argonne Universities Association and The University of Chicago, the University employs the staff and operates the Laboratory in accordance with policies and programs formulated, approved and reviewed by the Association.

MEMBERS OF ARGONNE UNIVERSITIES ASSOCIATION

The University of Arizona
Carnegie-Mellon University
Case Western Reserve University
The University of Chicago
University of Cincinnati
Illinois Institute of Technology
University of Illinois
Indiana University
Iowa State University
The University of Iowa
Kansas State University
The University of Kansas
Loyola University
Marquette University
Michigan State University
The University of Michigan
University of Minnesota
University of Missouri
Northwestern University
University of Notre Dame
The Ohio State University
Ohio University
The Pennsylvania State University
Purdue University
Saint Louis University
Southern Illinois University
The University of Texas at Austin
Washington University
Wayne State University
The University of Wisconsin

NOTICE

This report was prepared as an account of work sponsored by the United States Government. Neither the United States nor the United States Atomic Energy Commission, nor any of their employees, nor any of their contractors, subcontractors, or their employees, makes any warranty, express or implied, or assumes any legal liability or responsibility for the accuracy, completeness or usefulness of any information, apparatus, product or process disclosed, or represents that its use would not infringe privately-owned rights.

Printed in the United States of America
Available from
National Technical Information Service
U.S. Department of Commerce
Springfield, Virginia 22151
Price: Printed Copy $3.00; Microfiche $0.65

ANL-7760
Part II
Biology and
Medicine

ARGONNE NATIONAL LABORATORY
9700 South Cass Avenue
Argonne, Illinois 60439

RADIOLOGICAL PHYSICS DIVISION ANNUAL REPORT

Center for Human Radiobiology

July 1969 through June 1970

R. E. Rowland, Division Director
P. F. Gustafson, Associate Division Director

Preceding Report: ANL-7615, July 1968-June 1969

FOREWORD

The Center for Human Radiobiology has been formed in the Radiological Physics Division of the Argonne National Laboratory. This center has been assigned the responsibility for the continuation of the investigations of the biological effects of radium in man, with the general understanding that in the future the responsibility may be broadened to include the study of human subjects contaminated with internal emitters other than radium.

One of the primary purposes underlying the foundation of the center is the need to obtain information from human subjects exposed to various internally deposited radionuclides and to apply this information to radiation protection guides. In this regard, the United Nations Scientific Committee on the Effects of Atomic Radiation reported in 1964, "...that investigations aimed at recording significant quantitative relationships between doses and observed incidence of any specific malignancy in man should be strongly encouraged and supported." Very probably, radiation protection guides for humans can best be obtained from the study of the biological effects of radiation on man. Although studies on laboratory animals can provide the basic framework, the experience obtained from man is extremely valuable and must be considered most carefully. However, these studies are difficult and time consuming, for human exposures are usually accidental, unexpected, difficult to evaluate and the consequences of these exposures may not be visible for many years. The numbers of people exposed are relatively small, and in order to obtain meaningful results, the largest available segment of the exposed populations should be rigorously studied until death.

These considerations have given rise to the concept that a single organization be formed with the primary responsibility of fulfilling our moral obligation to derive the greatest amount of information from those known cases of internal contamination from radionuclides. Such an organization should have a long lifetime with the necessary staff and equipment to provide the multiplicity of investigations required to extract the greatest

possible information from the available cases. This then is the basic concept on which the center was founded.

It is of interest to record here the history leading to the formation of the Center for Human Radiobiology. It was during the symposium on the Delayed Effects of Bone Seeking Radionuclides, held at Sun Valley, Idaho, September 1967, that Professor Robley D. Evans proposed the creation of a National Center for Human Radiobiology. This proposal was later discussed early in 1968 at a meeting of the AEC Advisory Committee for Biology and Medicine. Subsequently, a subcommittee of the ACBM was appointed and charged with the responsibility to advise the AEC on Professor Evans' proposal. The report of this subcommittee recommending the formation of the center at the Argonne National Laboratory was reviewed and subsequently approved by the ACBM on May 11, 1968.

The first assignment given the center was the responsibility for the continuation and extension of the radium studies which had been carried out previously at MIT under the direction of Professor Evans. This has resulted in the transfer of some personnel, medical records, and equipment from MIT to ANL which was completed by August 1970. As of 1 September of this year a satellite laboratory, funded by a subcontract from the Argonne National Laboratory, remains at MIT.

TABLE OF CONTENTS

Center for Human Radiobiology

A. F. Stehney, Section Head

Some Dose-Response Relationships for Tumor Incidence in Radium Patients 1
R. E. ROWLAND, PATRICIA M. FAILLA, A. T. KEANE, and A. F. STEHNEY

A Way to Put Error Bars on Points of Zero Incidence on Dose-Response Curves 18
J. H. MARSHALL

Skeletal Concentrations and Metabolic Parameters of ^{226}Ra in Radium-Burdened People 22
R. B. HOLTZMAN

^{210}Pb and ^{210}Po Metabolism in Radium-Dial Painters 35
R. B. HOLTZMAN

Measurements of Americium-241 in Two Subjects 36
JOHN RUNDO, A. T. KEANE, and H. A. MAY

Construction of New Shielded Rooms 45
JOHN RUNDO

Thorium and Uranium in Blood, Urine, and Cigarettes 47
H. F. LUCAS, JR. and FRANCIS MARKUN

Boat Sampling Methods for Analysis of Lead and Tellurium in Biological Materials 53
F. H. ILCEWICZ and R. B. HOLTZMAN

Quantitative Characterization of Bone. A Computer Analysis of Microradiographs 63
ELIZABETH LLOYD and DONALD HODGES

A Comprehensive Model of Alkaline Earth Metabolism in Bone: Preliminary Report 95
J. H. MARSHALL

^{45}Ca, ^{133}Ba, and ^{226}Ra in 6- to 10-Year-Old Beagle Dogs: a 100-Day Study 110
S. K. WOOD, J. E. FARNHAM, and J. H. MARSHALL

Estimates of the Radiation-Induced Leukemic Risk in Man 133
L. D. MARINELLI

Regularization Unfolding of Low γ-Ray Activity Measurements. II. Evaluation of Time-of-Flight Scanning in One Dimension 154
I. K. ABU-SHUMAYS, P. E. HESS, and L. D. MARINELLI

A Special Regularization-Unfolding Technique for the Numerical Solution of Two-Dimensional Fredholm Equations of the First Kind 176
I. K. ABU-SHUMAYS and L. D. MARINELLI

A Comparison of Recovery from α- and γ-Ray Induced Mitotic Delay in Fertilized Sea Urchin Eggs 202
PATRICIA M. FAILLA

Application of Cellulose Nitrate Films for Alpha Autoradiography of Bone. II. Resolution and Sensitivity of Cell Nitrate Films 208
D. J. SIMMONS and K. T. FITZGERALD

Chondroclastic Resorption in the Long Bones of Newts Treated with Parathyroid Extract 217
D. J. SIMMONS, D. J. MC WHINNIE, and H. T. CUMMINS

Development and Healing of Rickets in Rats. III. Studies with ^{3}H-Uridine 225
D. J. SIMMONS and A. S. KUNIN

Mineral Metabolism in the Skeletons of Teleosts--a Review 240
D. J. SIMMONS

Electron Microscope Measurements of Alkaline Earth Transport 242
ELIZABETH LLOYD

Publications 253

SOME DOSE-RESPONSE RELATIONSHIPS FOR TUMOR INCIDENCE IN RADIUM PATIENTS

R. E. Rowland, Patricia M. Failla, A. T. Keane, and A. F. Stehney

A population of 777 radium cases for whom the total dose received has been calculated was obtained by combining the MIT and the ANL-ACRH studies. Within this population a total of 71 malignancies were considered to be radiation induced: 51 sarcomas and 20 carcinomas. Dose-response functions of the form Incidence = KDe^{-D/D_0} and $I = KD^2e^{-D/D_0}$ are examined and found to provide reasonable fits to the data over most of the dose range.

The object of this review is to consider dose-response relationships that could be used to describe data on the radium cases that have been studied in this country during the past 40 years. The end points used are those malignancies which have been assumed to be radiation induced, i.e., the bone sarcomas and some carcinomas, primarily of the paranasal sinuses and the mastoid air cells.

Such an analysis is now possible, for we have, for the first time, dose calculations for all of the radium cases. The raw data, including the dose calculations for all of the cases studied at the Massachusetts Institute of Technology (MIT) by Professor R. D. Evans and his colleagues, have been transferred to the Center for Human Radiobiology here in the Radiological Physics Division of the Argonne National Laboratory. To these MIT cases we have added the data from the cases studied by Miller, Hasterlik, and Finkel.[1] This has been possible, even though no dose calculations were included in their detailed report, through the efforts of one of us (ATK) and Mary Margaret Shanahan of the MIT group, who have calculated the doses for all of the cases listed in the above-mentioned report.

Our concern is with the low-dose cases, and we have tried to find formulations compatible with the large number of these cases in which malignancies have not (as yet) developed. R. D. Evans and his colleagues[2]

have postulated a threshold concept to fit their data, and there is no doubt that it does fit well. On the other hand, we have examined continuous functions to see how well they might fit the data. It should be understood that we have attempted to fit response functions to the observed data, not to specify safety criteria which seek a linear relationship such that the observed incidence at any dose is less than that predicted.

We have so far identified 777 cases from the two series for which detectable levels of radium were found. In this group a total of 71 malignancies have been identified which are considered to be radiation induced: 51 sarcomas and 20 carcinomas. We have included all of the cases for which we have data, rather than attempt to select a group which could be considered epidemiologically suitable. We thus include cases found as a consequence of their symptoms, with the full realization that this may have a tendency to enhance the observed incidence of malignancies.

It is of interest, and quite important to bear in mind, that approximately 580 of these 777 cases are still living. The age distribution of the living cases is shown in Figure 1. The age at death of the remainder is shown in Figure 2. Since such a large fraction of the population is still living, it is entirely possible that the tumor incidence may change in future years. This fact emphasizes the importance of a continuous long-term

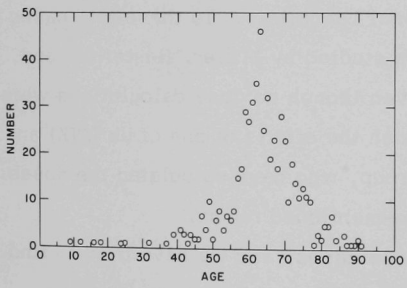

FIG. 1.--The age distribution of the living members of the population under study in 1969.

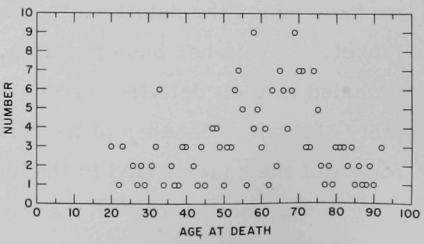

FIG. 2.--The distribution of the dead members of the population as of 1969 according to age at death.

follow-up of this population.

It is also of interest to note that there exists a remarkably consistent distribution of malignancies within the two independent studies. The malignancies and total number of cases considered in the report are shown in Table 1 and identified as to source.

TABLE 1. Distribution of Malignancies within Two Independent Studies

Location Studied	Cases	Sarcomas	Carcinomas
MIT	474	33	10
ANL-ACRH	316	20	11
Total[a]	777	51	20

[a] There are some cases that have been studied and reported on by both groups so that the total number of cases and malignancies is less than the sums from the independent studies.

The unit of dose employed for this analysis is the total number of rads accumulated by the skeleton from acquisition of radioactive material to death, or to diagnosis of a malignancy, or if neither of these events had occurred, to January 1, 1969. The validity and/or shortcomings of using the average skeletal dose calculated from a uniform distribution of radioactivity in the skeleton will be discussed later. The calculation requires evaluation of the expression

$$D = \int_0^T R(t)\,dt,$$

where R(t) is the average skeletal dose rate at any time, and D is the dose accumulated in time T. The calculation includes the contribution of ^{228}Ra and daughters as well as ^{226}Ra and daughters. This is identical to the "cumulative rads" as employed by Evans.[3]

We have considered dose-response functions of the following forms:

(1) Incidence = K D

(2) Incidence $= K_1 D e^{-D/D_1}$

(3) Incidence $= K_2 D^2 e^{-D/D_2}$.

As will be shown, the linear expression [Eq. (1)] does not fit all the data, and as is often the case, can only be employed in the low-dose region where no malignancies have been observed. We will make an attempt to define an upper limit (i.e., the linear equation with the largest slope that is not contradicted by the data) that could be used in this region. We have included an exponential term in Eqs. (2) and (3) for, as will be shown below, tumor incidence drops in the highest dose levels, where life expectancy spans were relatively short.

For our analysis we listed all of the cases in order of decreasing dose and then separated the cases into dose ranges. The results are shown in Table 2.

TABLE 2. Analysis of Cases in Order of Decreasing Dose

Dose Range, Rads	Median Dose, Rads	No. of Cases	All Assumed Radiogenic Tumors	Incidence, %
$2\text{-}5 \times 10^4$	2.32×10^4	16	4	25.0
$1\text{-}2 \times 10^4$	1.44×10^4	25	16	64.0
$5\text{-}10 \times 10^3$	6.90×10^3	42	20	47.6
$2\text{-}5 \times 10^3$	4.13×10^3	72	22	30.6
$1\text{-}2 \times 10^3$	1.36×10^3	42	9	21.4
$5\text{-}10 \times 10^2$	7.40×10^2	42	0	0
$2\text{-}5 \times 10^2$	2.82×10^2	79	0	0
$1\text{-}2 \times 10^2$	1.38×10^2	83	0	0
$5\text{-}10 \times 10$	6.50×10^1	88	0	0
$2\text{-}5 \times 10$	3.12×10^1	139	0	0
$1\text{-}2 \times 10$	1.49×10^1	73	0	0
1-10	5.20	74	0	0
0.2-1	0.45	6	0	0
Total		781	71	

In this tabulation it will be noted that we appear to have four cases more than the 777 we selected for analysis. This occurs because four cases have developed two independent tumors, in each case a carcinoma and a sarcoma. In some instances these tumors appeared many years apart. We calculated the doses to the time of tumor appearance and have listed each tumor separately. For example, Case 01-179 had an osteogenic sarcoma 19 years after radium injections and subsequently developed a carcinoma 42 years after the radium injections. Both tumors are considered to be a consequence of the radium burden. The doses for these two tumors are of the order of 3700 rads and 6100 rads, respectively. Therefore, this case appears twice, once in a range of 5000 to 10,000 rads (with a carcinoma) and once in the range of 2000 to 5000 rads (with a sarcoma).

The data are plotted on linear coordinates in Figure 3 as total tumor incidence vs. the median dose in rads. Along the top of this graph the extent of each dose range is indicated by the length of the solid bar. In the fraction appearing under the bar, the number of tumors is given as the numerator and the number of cases in the range as the denominator. It will be noted that this graph with linear coordinates has forced us to put about three-quarters of our cases in the lowest range, with zero tumor incidence.

A far better graphical representation of these low-dose cases occurs when we use semilogarithmic coordinates as in Figure 4.

On these graphs it will be noted that error bars have been placed on the tumor incidence points, including the points with zero incidence. Where there are tumors, the error bar is obtained from $\pm[\text{ number of tumors}]^{1/2}/[\text{number of cases}]$. In those ranges where no tumors have appeared, the error bar extends upward to indicate the value of the incidence had there been one tumor in that range. The reason for this choice is as follows: We ask, "At what incidence would an error bar extend exactly down to zero incidence?" It can easily be seen that, had there been one tumor in a given range, the error bar would extend down exactly to zero since $[1 - \sqrt{1}]/[\text{number of cases}] = 0$. Therefore, we have drawn our error bar up to this

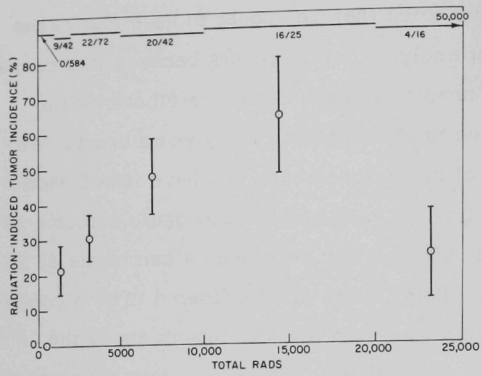

FIG. 3.--Percent tumor incidence as a function of the median value of total skeletal rads from Table 2 plotted on linear coordinates. The zero tumor incidence cases have all been combined in one dose range in this presentation. See text for discussion of dose ranges, error bars, etc.

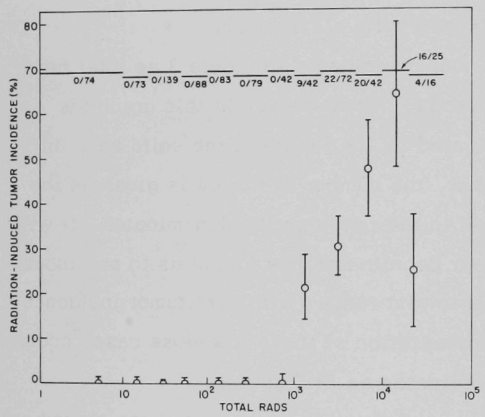

FIG. 4.--Semilogarithmic presentation of the data in Table 2. Percent total tumor incidence on a linear scale is plotted against the median value of total skeletal rads on a logarithmic scale. See text for further explanation.

incidence level for each of the ranges in which no tumors have been observed. [A more rigorous method of drawing error bars when zero incidence is observed is given by J. H. Marshall elsewhere in this publication.]

By means of a least squares fit[4] we have determined the constants for equations of the form

$$(2)\quad I = K_1 D e^{-D/D_1}$$

and

$$(3)\quad I = K_2 D^2 e^{-D/D_2},$$

where I is the fractional incidence and D is the total dose in rads delivered to the skeleton from exposure to diagnosis of a tumor.

The actual values of the parameters in these two equations are

(2) $I = 1.15 \times 10^{-4} D\, e^{-D/1.25 \times 10^4}$

(3) $I = 5.24 \times 10^{-8} D^2\, e^{-D/4.85 \times 10^3}$.

How well do these equations fit the data? As can be seen from Figure 5, in the region above 1000 rads where tumors have been observed, both equations appear adequate. However, below 1000 rads the linear equation predicts many more tumors than have been observed.

We can ask the question, "What would be the probability of observing no tumors if the hypothesis under consideration were true?" The binomial distribution provides us with the mechanism to answer this question, and we tabulate in Table 3 probabilities of seeing zero tumors, using each of our two equations for the seven dose ranges between 1 and 1000 rads.

It is evident that Eq. (2), the linear-exponential form, predicts significantly more tumors in these dose ranges, and therefore that this is a highly unlikely fit to the actual tumor incidence data in this region. In fact, when we combine the probabilities for these listed ranges, we find the overall probability of seeing no tumors when a total of 8.49 is predicted is of the order of 0.0002.

Equation (3), the dose-squared exponential form, is seen to fit this region of zero incidence far better, with a total probability of the order of 0.23 for seeing zero

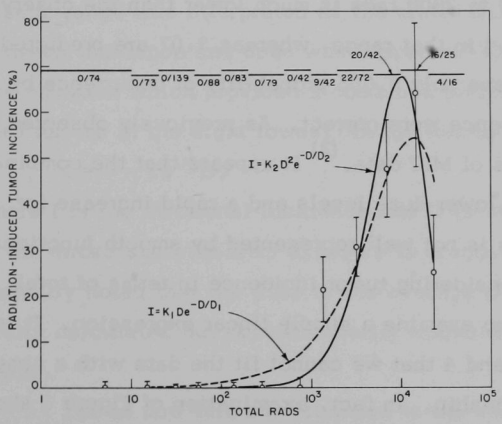

FIG. 5.--Least square fits of the functions $K_1 D e^{-D/D_1}$ and $K_2 D^2 e^{-D/D_2}$ superimposed on Figure 4.

TABLE 3. Probabilities of Seeing Zero Tumors, Calculated with Two Different Equations

Range, rads	Tumors Observed	Eq. (2) $I = K_1 D e^{-D/D_1}$		Eq. (3) $I = K_2 D^2 e^{-D/D_2}$	
		Tumors Predicted	Probability P_0	Tumors Predicted	Probability P_0
$5\text{-}10 \times 10^2$	0/42	3.37	0.030	1.03	0.351
$2\text{-}5 \times 10^2$	0/79	2.50	0.079	0.31	0.733
$1\text{-}2 \times 10^2$	0/83	1.30	0.269	0.08	0.923
$5\text{-}10 \times 10^1$	0/88	0.65	0.519	0.02	0.981
$2\text{-}5 \times 10^1$	0/139	0.50	0.608	0.01	0.993
$1\text{-}2 \times 10^1$	0/73	0.13	0.882	0	1.0
1-10	0/74	0.04	0.957	0	1.0
	Total	8.49		1.45	

tumors when 1.45 are predicted. On the other hand, the incidence predicted for the dose range of 1000 to 2000 rads is much lower than the observed value; 9 tumors were observed in that range, whereas 3.07 are predicted. Nine or more tumors would have only 0.005 probability of occurrence by chance if the predicted incidence were correct. As previously observed by Evans et al. in their analysis of MIT data,[2] it appears that the combination of zero incidence in the lower dose levels and a rapid increase for doses in excess of 1000 rads is not well represented by smooth functions.

While we are still considering tumor incidence in terms of total malignancies, it is in order to examine a simple linear expression. It is evident from both Figures 3 and 4 that we cannot fit the data with a simple linear incidence-dose relationship. In fact, examination of Figure 3 shows that we could put a different line through each of the five data points and the origin. If we did this, the maximum slope would be obtained by using the incidence in the lowest dose range in which tumors have been seen,

whereas the minimum slope would result from using the incidence in the highest dose range. It would perhaps be most logical to find the straight line that would predict the same total number of tumors for this population as we have observed, over the range of doses involved.

We have chosen, however, to determine an acceptable linear expression for the range in which no tumors have been observed. Table 2 indicates that no tumors were observed in the lowest eight dosage classes containing 584 cases. The best fit would be given by a prediction of zero incidence in this range. However, it is quite possible that a linear incidence of tumor induction is valid over this dose range, but that the limited population is too small to demonstrate its effect. We would, therefore, like to extract from these data a reasonable upper limit to the slope of a line with a zero intercept at zero dose.

Our approach was to find a slope with an acceptable probability of being too small. This was done by testing linear equations by the procedure previously employed in obtaining the probability data of Table 3. The product of the binomial probabilities of observing zero tumors in each dosage range was interpreted as the probability that the true relationship between incidence and dose was expressed by the equation being tested. The equation which provided a combined probability of 0.10 for observing zero tumors in the eight lowest dosage ranges was

$$I = 3 \times 10^{-5} D,$$

where I is the fractional incidence and D is total number of rads delivered to the entire skeleton from exposure to diagnosis of a tumor. It should be carefully noted that the dose is the average skeletal dose--a quantity easily calculated but not necessarily relevant. We will discuss this point below.

Let us now turn our attention to the two tumor types--the sarcomas and the carcinomas--for it may be that we should consider dose-response functions for the two types separately. Figure 6 (linear coordinates) and Figure 7 (semilog coordinates) show the incidence of the sarcomas and the

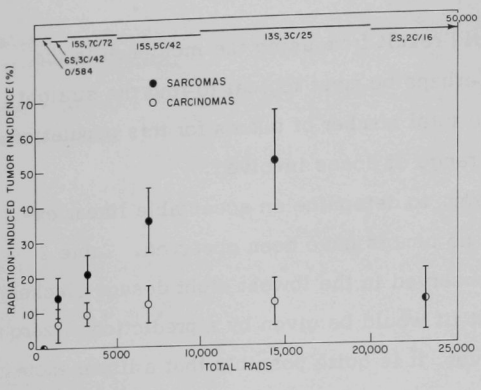

FIG. 6.--The percent incidence of sarcomas and carcinomas plotted separately against the median value of the total skeletal dose in rads in linear coordinates.

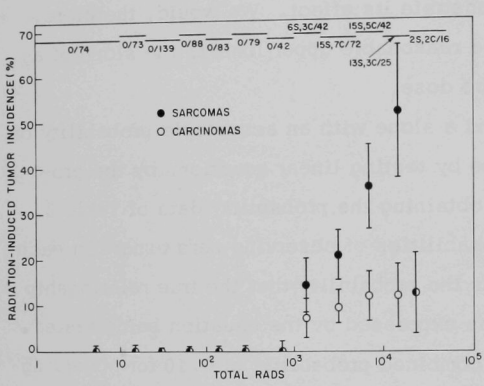

FIG. 7.--The percent incidence of sarcomas and carcinomas plotted separately on a linear scale against the median of the total skeletal dose in rads on a logarithmic scale.

carcinomas separately, using the same format as previously employed. Turning first to a simple linear hypothesis, we see immediately that, again, these data are not well represented by this kind of function. Indeed, the best we can do is define a linear slope for the region where no tumors are observed. This is, of course, for each tumor type, the same slope that we determined above for the sum of the two tumor types, for we are working with the same total population and the same incidence--zero.

The sarcoma data by themselves can be fitted with equations of the form previously used. The parameters for the least-squares fits are

(2) $I = 8.12 \times 10^{-5} D e^{-D/1.28 \times 10^4}$

(3) $I = 3.90 \times 10^{-8} D^2 e^{-D/4.85 \times 10^3}$

Again, due to the wide discrepancy between the predictions of the linear dose-exponential equation and the zero incidence levels immediately below 1000 rads, the dose squared exponential expression provides a better fit. The incidence predicted for the dose range of 1000 to 2000 rads is more compatible with the observed incidence (probability of 0.03) than was the case for the total tumor data. This expression is shown fitted to the sarcoma data in Figure 8.

The carcinoma incidence appears best fit by a threshold hypothesis, with zero incidence below 1000 rads and a fairly constant incidence above this level. However, quite an acceptable fit was obtained with the linear dose-exponential equation; the parameters are

(2) $I = 3.1 \times 10^{-5} D e^{-D/1.24 \times 10^4}$.

The fit of this expression to the carcinoma data is shown in Figure 8.

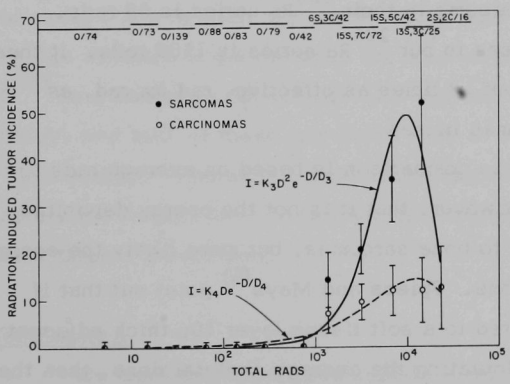

FIG. 8.--A least squares fit of the function $K_3D^2e^{-D/D3}$ superimposed on the sarcoma data of Figure 7 and a least squares fit of the function $K_4De^{-D/D4}$ superimposed on the carcinoma data of Figure 7.

Discussion

We are concerned with the interpretations that may be placed upon calculated doses, particularly in relation to the evaluation of the risk associated with low doses of various types of radiation. For example, we have come to the conclusion that, in the low dose range, a linear tumor incidence equation of the form

$$I = 3 \times 10^{-5} D,$$

where I is the fractional incidence and D is the total skeletal dose in rads, is a reasonable upper limit, considering the absence of observed tumors in the 584 radium patients. This expression may be rewritten as a tumor incidence of 0.3% per hundred rads.

This expression has been derived on the basis of there being only a 10% probability that a linear tumor incidence for these data could be this large. Nevertheless, since it has been proposed that the leukemia risk for man lies in the range 0.2 to 0.5% per hundred rads mean dose to the bone marrow,[5] one might be tempted to speculate that the similarity in magnitude of these risks was an indication of a fundamental consistency between dose and malignancy.

We doubt that this is true. For example, the data presented here are valid for ^{226}Ra and ^{228}Ra, but cannot even be extrapolated to cover the effects of ^{224}Ra in man. This is demonstrated by the recent study of Spiess and Mays[6] on the toxicity of ^{224}Ra. They point out that the lowest dose known to produce a sarcoma in their ^{224}Ra series is 90 rads, while the lowest comparable dose in our ^{226}Ra series is 1160 rads. It thus would appear that ^{224}Ra is about 13 times as effective, rad for rad, as ^{226}Ra in producing bone sarcomas in man.

This is the case when the comparison is based on average rads to the skeleton. It is obvious, however, that it is not the energy deposited in bone mineral that gives rise to bone sarcomas, but more likely the energy deposited in certain cells in bone. Spiess and Mays[6] point out that if one calculates the dose delivered to a soft tissue layer 10μ thick adjacent to bone surfaces instead of calculating the average skeletal dose, then the lowest ^{224}Ra sarcoma dose would be increased to 810 rads, while the lowest ^{226}Ra sarcoma dose would be reduced to 760 rads. Thus the 13-fold difference in dose disappears, and the ^{224}Ra and ^{226}Ra doses required to produce a sarcoma become almost identical.

The point we wish to emphasize is that the data we have presented

for ^{226}Ra and ^{228}Ra, based as they are on average skeletal dose, cannot be readily used to describe the toxicity of any other form of radiation. This is not to imply that results following exposure to one form of radiation cannot be used to estimate risks from a different type of radiation. Indeed, it is our expectation that they can, as is demonstrated by the agreement of ^{224}Ra and ^{226}Ra results when the relevant dosimetric basis is used. However, a thorough understanding of micro- and macrodosimetry appears to be required, as well as an understanding of the effects of the type of radiation involved, the dose rate, and the repair processes.

We use the average skeletal dose in our evaluation of the dose-response characteristics of radium in man with full knowledge of its shortcomings. The magnitude is relatively easy to calculate, and we feel relatively secure in comparing the doses received by various individuals in these terms. We are aware that it does not represent the actual dose received by the cells at risk, but then we really do not know where the cells at risk reside, nor how to determine the dose they receive in each of our cases. We caution those who would tend to generalize, that when average skeletal doses are used for bone-seeking radionuclides, a "rad" of ^{226}Ra α energy is not biologically equivalent to a "rad" of ^{224}Ra α energy, and both of these may differ from a "rad" of ^{239}Pu α energy or ^{90}Sr β energy. Meaningful dose comparisons can only be made when the appropriate targets have been identified and the energy distributions within these targets determined.

Conclusions

We have examined dose-response relationships which may be used to describe the total tumor invidence vs. total skeletal dose for a large group of radium patients, and conclude that a dose-squared exponential expression of the form

$$I = KD^2 e^{-D/D_0}$$

is contradicted only by the tumor incidence observed in one of our 13 dose

ranges. Such an expression can also be used to describe the incidence of bone sarcomas for this group of cases. The radiation-induced carcinomas, however, seem to be better fitted by an expression of the form

$$I = KDe^{-D/D_0},$$

but the fact that these malignancies appear later than the sarcomas, and that as yet they are relatively few in number, may caution us not to place too much significance on this result.

A total risk of malginancies of the order of 0.3% per hundred rads can be considered as an upper limit for the dose range below 1000 rads where no malignancies have been observed.

It should be kept in mind that if the natural incidence of sarcoma is of the order of 10^{-5} per man per year, then, based on a 40-year observation period, we would predict $40 \times 800 \times 10^{-5}$ naturally occurring sarcomas in our series, i.e., 0.3. Since we can only observe sarcomas as integers, it is reasonable to calculate the probabilities of having zero, one, or two natural sarcomas. These probabilities are, respectively, 73%, 23%, and 3.7%. Since we have no means at present for differentiating between a natural and a radiation-induced sarcoma, we will have to consider every sarcoma found, regardless of the dose level, as possibly being radiation induced.

This paper, originally prepared for oral presentation at the IVth International Congress of Radiation Research, Evian, France, has drawn on the work of many individuals. We have depended heavily on Mary Margaret Shanahan for interpretation of the MIT data and dose calculations, and on Dr. Harvey Schultz for retrieval of information from our files. The least squares fits were obtained with the help of Dr. John Rundo.

Appendix

The preceding paper has examined dose-response curves which are based on a sample of 777 radium cases in which a total of 71 malignancies were considered to be radium induced. For completeness, we tabulate here the cases with malignancies which we have included.

We request that these lists be considered preliminary and subject to change. With the extremely short time that the Center for Human Radiobiology has been in existence, there has been little or no time for verification on our part of the cases listed in Table 4.

TABLE 4. Malignancies in the ANL-ACRH Series

Case Number	Reference	Tumors Considered to be Radiation Induced	
		Sarcomas	Carcinomas
03-105	7		x
03-110	1	x	x
03-126	7		x
03-141	7		x
03-214	7		x
03-232	7		x
03-235	7		x
03-402	7	x	x
03-407	7		x
03-417	7		x
*03-648	7	x	x
03-118	7	x	
03-201	7	x	
03-209	7	x	
03-210	7	x	
03-212	7	x	
03-213	7	x	
03-215	7	x	
03-216	7	x	
03-227	7	x	
03-234	7	x	
03-401	7	x	
03-429	8	x	
03-455	1	x	
03-584	7	x	
03-619	7	x	
*03-649	7	x	
03-671	7	x	
Total		20	11

*These cases also appear in the MIT series.

TABLE 5. Malignancies in the MIT Series

Case No.	Tumors considered radiation induced		Case No.	Tumors considered radiation induced	
	Sarcomas	Carcinomas		Sarcomas	Carcinomas
01-006		x	01-024	x	
01-008		x	01-025	x	
*01-013	x	x	01-026	x	
01-014		x	01-031	x	
01-022		x	01-032	x	
01-145		x	01-033	x	
01-149		x	01-046	x	
01-171		x	01-059	x	
01-179	x	x	01-073	x	
01-573		x	01-079	x	
00-003	x		01-099	x	
00-004	x		01-105	x	
00-005	x		01-112	x	
00-006	x		01-172	x	
00-007	x		01-239	x	
00-027	x		01-268	x	
00-028	x		01-389	x	
01-007	x		01-439	x	
01-009	x		01-520	x	
01-011	x		05-215	x	
*01-023	x		Total	33	10

*These cases also appear in the ANL-ACRH Series.

A few comments regarding the selection of these cases is in order. First, since it is clearly stated in Reference 8 that Case 03-685 is not to be considered as having a malignant lesion, we have not included it. However, we have included a case the principal investigators of the ANL-ACRH studies did not include in their lists of malignancies. This is Case 03-110, which was suspected of having both a sarcoma of the left first metacarpal and a possible mastoid carcinoma.[1] We have included both of these suspected malignancies, for we would rather err on the conservative side (i.e., attributing a malignancy to radiation) than to leave out malignancies which might well be considered by some to be due to radiation.

To our knowledge, no published list of MIT malignancies exists, although all have been published in the MIT Annual Progress Reports. We have, therefore, compiled the data in Table 5 from the records in our possession. Errors of omission or commission which may be present in this compilation are not to be attributed to the MIT investigators; they are clearly the responsibility of the new Center for Human Radiobiology.

References

1. Miller, C. E., R. J. Hasterlik, and A. J. Finkel. The Argonne Radium Studies; Summary of Fundamental Data, ANL-7531 (January 1969).
2. Evans, R. D., A. T. Keane, R. J. Kolenkow, W. R. Neal, and M. M. Shanahan. Radiogenic tumors in the radium and mesothorium cases studied at MIT. Delayed Effects of Bone-Seeking Radionuclides, Ed. C. W. Mays, W. S. S. Jee, and R. D. Lloyd. University of Utah Press, Salt Lake City, 1969, pp. 157-194.
3. Evans, R. D. Dose variables and their calculations. Annual Progress Report, Radioactivity Center, Massachusetts Institute of Technology Report MIT-952-3 (May 1966), pp. 94-141.
4. Salmon, L. Unpublished computer program, Atomic Energy Research Establishment, Harwell, England.
5. Pochin, E. E. The development of the quantitative basis for radiation protection. Brit. J. Radiol. 43, 155-160 (1970).
6. Spiess, H. and C. W. Mays. Bone cancers induced by ^{224}Ra(ThX) in children and adults. Health Phys., in press.
7. Finkel, A. J., C. E. Miller, and R. J. Hasterlik. Radium-induced malignant tumors in man. Delayed Effects of Bone-Seeking Radionuclides, Ed. C. W. Mays, W. S. S. Jee, and R. D. Lloyd. University of Utah Press, Salt Lake City, 1969, pp. 195-225.
8. Finkel, A. J., C. E. Miller, and R. J. Hasterlik. Radiobiological parameters in human cancers attributable to long-term radium deposition. Radiation-Induced Cancer. Proc. Symp., Athens, April 28-May 2, 1969. Int. Atomic Energy Agency, Vienna, 1969, pp. 183-202.

A WAY TO PUT ERROR BARS ON POINTS OF ZERO INCIDENCE ON DOSE-RESPONSE CURVES

J. H. Marshall

If one considers the curve of tumor incidence as a function of dose, it is shown that in those groups in which zero tumors are observed in z cases, the standard error is $z/(z + 1)$ tumor.

A recurring problem arises in presenting data on the dose response of cancer incidence due to radiation. In general one observes a certain number of tumors in each of several high dose groups, a diminishing number of tumors as the dose is decreased, and zero tumors in a number of low dose groups. It is easy to assign standard errors to the points with greater-than-zero observed tumor incidence, but what does one do with the very important groups that received some radiation but developed no tumors? Certainly the observation of no tumors in a large group of cases is more significant than the observation of zero tumors in a small group. How can this significance be indicated on the graph? How can we assign a standard error to an observation of zero tumors?

Ordinarily one may use the definition of standard error in the Poisson distribution--the square root of the number of events observed--to obtain an estimate of the true standard error. But when the number of observed events is zero this approximation no longer works.

One way to handle the problem is to assume a function for the description of the dose-response curve--threshold, square, or linear response, for example--obtain the best fit to the data with this function, and then calculate the deviations of the observed points from this function, comparing them with a standard error calculated from the assumed function together with the number of cases in the group. While this method works well for comparing a single hypothesis with the data mathematically, it does not work when one wishes to graph the points in order to compare them with more than one theory. One cannot put an error on a zero point on such

a graph together with several hypothetical dose-response curves because a particular hypothesis was used to calculate the error on such a zero point. We would like to estimate the standard error on all experimental points in the light of observations, not theory. Unless we do this, we are mixing up theory and experiment. Error bars should belong to the experimental points to which they are attached and should not depend on which theoretical curve is being considered.

Of course, another way to handle the problem is to give up and plot error bars only for non-zero points. But this fails to present on the graph the very significant information carried by observations of zero incidence in large groups of cases with doses only a little smaller than those for groups with non-zero incidence.

There is a third, and I believe better, way to indicate graphically the accuracy of zero incidence observations. Suppose one has a group of 100 cases and that one has observed no tumors. The observed incidence is, of course, zero. How large might the true incidence be in view of the fact that zero tumors were observed? If the true incidence were 1%, then one tumor should have been observed. What is the probability of seeing no tumors when one is expected? That is given by the Binomial Distribution (Reference 1, p. 747),

$$P_x = z!\, p^x (1 - p)^{z-x} / (x!\,(z - x)!),$$

where x is the number of events observed

p is the probability of observing an event in one trial

z is the number of trials

P_x is the probability of observing x events.

Now if $x = 0$, then simply $P_0 = (1 - p)^z$, so that the probability of observing zero when $p = 1\%$ and $z = 100$ cases is $(0.99)^{100}$ or 0.366.

The square of the standard deviation for this Binomial Distribution is given by (Reference 1, p. 759)

$$\sigma^2 = pz(1 - p),$$

where σ is the standard deviation.

Now what is the value of p such that an observation of zero events is exactly one standard deviation less than pz? In other words, what p is the solution of the equation

$$pz - \sigma = 0 \quad ?$$

Substituting for σ

$$pz - \sqrt{pz(1 - p)} = 0$$

$$pz = \sqrt{pz(1 - p)} \ .$$

Square both sides:

$$(pz)^2 = pz(1 - p) \ .$$

Divide through by pz (remember that it is x and not p that is zero):

$$pz = 1 - p$$

$$pz + p = 1$$

$$p(z + 1) = 1$$

$$p = 1/(z + 1).$$

This is the probability of occurrence which would just permit us to observe zero events within one standard error given our number of cases z. This value of p is then one standard error away from our observed point of zero incidence. So we can plot a standard error bar on the zero point which extends upwards to the incidence $p = 1/(z + 1)$.

Suppose that zero tumors were observed in 1,000,000 cases. The p-value would be 0.000000999999 and the standard deviation of our zero point is almost exactly 1 tumor.

Suppose that zero tumors were observed in 100 cases. Our p-value would be 0.0099. The standard deviation of our zero point is again almost exactly 1 tumor.

If zero tumors were observed in five cases, then p would be 0.1667 and one standard deviation would be 0.8333 tumor. It is only when the number of cases z is not large that the Binomial Distribution indicates a standard error significantly different from one tumor when zero is observed.

This appears to be a rigorous solution to our problem. We have an

expression for the standard error of an observation of zero incidence $[1/(z + 1)]$ which does not depend upon the assumption of a particular dose-response curve but derives solely from experiment.

References

1. Evans, R. D. The Atomic Nucleus. McGraw-Hill, New York, 1955.

SKELETAL CONCENTRATIONS AND METABOLIC PARAMETERS OF ^{210}Pb AND ^{226}Ra IN RADIUM-BURDENED PEOPLE*

R. B. Holtzman

The concentrations of ^{226}Ra and its decay product, ^{210}Pb, were determined in 44 bone samples taken from 13 persons who had acquired the radium either as dial painters or under medical treatment. The whole-body burdens, carried 4 to 36 years, ranged from 0.4 to 10 μCi ^{226}Ra. The ^{210}Pb was derived almost entirely from the radium in bone, an assumption supported by measurements on radium-injected dogs with short-term exposures of 7 to 500 days. Despite great differences from sample to sample, such as differing body burdens, exposure times and methods of acquisition, differing bone types (femur, rib, vertebra, etc.), and large differences in ^{226}Ra concentration (10^2 to 10^4 pCi/g ash), the ratios of ^{210}Pb specific activities to those of ^{226}Ra were fairly uniform, with an average of 0.34 ± 0.03 (S.E.). This uniformity and the large variations in radium concentrations within an individual (factors of 10 or more) indicate either that the ^{226}Ra and ^{210}Pb were metabolized similarly, or that little ^{210}Pb was translocated from the site of formation. That some translocation may occur is shown by the high ratios of 1.6 to 30 in some samples. The low values of ^{226}Ra in these specimens relative to those in other samples from the same subject may indicate that little radium was taken up initially.

The effective half-life of the ^{210}Pb, based on the ^{210}Pb-to-^{226}Ra ratio of 0.34, appears to be about half that of the radium in an exponential retention model. The dose from the $^{210}Pb(^{210}Po)$ series appears to be about 10% of that of the ^{226}Ra series over the period of 10 to 40 years after acquisition.

Introduction

Studies of the skeletal distributions of ^{226}Ra and of its long-lived daughter, the 21.4-year ^{210}Pb, in people with large body burdens of ^{226}Ra can provide valuable information on the metabolism of both ^{210}Pb and stable Pb in man. The quantitative relations between the ^{210}Pb and the ^{226}Ra concentrations and determination of the whole-body content of the ^{226}Ra through whole-body counting of these people make possible the determination of the whole-body content of the ^{210}Pb. This latter quantity, which is

*Data in this paper were presented at the Second International Congress of the International Radiation Protection Association, Brighton, England, May 3-8, 1970 and abstracted in Health Phys. 19, 152 (1970).

not otherwise measurable in vivo, is necessary for the assessment of the metabolic parameters of ^{210}Pb and for the accurate evaluation of the radiation exposure of these people. In addition, these studies allow the confirmation of some of the metabolic parameters of ^{226}Ra and of its rare gas daughter, ^{222}Rn, such as retention and emanation rates.

Preliminary results on some of the data in this paper were reported earlier.[1] The ratio of the specific activity of ^{210}Pb to that of ^{226}Ra was about 0.3 at 30 years after acquisition. The residence time of ^{210}Pb appeared to be quite long; the exponent of the power function retention

$$R = AT^{-b}, \tag{1}$$

where R is the fractional retention, A is the retention at 1 day, and T is the burden time, was about 0.1. This value indicates a much slower release of Pb than of ^{226}Ra.[2,3]

Subsequently, Petrow reported ^{226}Ra and ^{210}Pb measurements on 89 bone sites from two radium dial painters with 48- and 49-year burden times.[4] The ratios of specific activities of ^{210}Pb to ^{226}Ra ranged from about 0.17 to 0.48, and corrected for storage time between death and measurement, the mean ratio weighted by sample size was 0.27 ± 0.01 (S.E.). The biological half-lives of both ^{226}Ra and ^{210}Pb were estimated to be identical at 15 to 20 years. The ratios of specific activities of ^{210}Pb to those of ^{226}Ra were fairly constant. In the long bones the ratios showed a small negative correlation with the ^{226}Ra concentrations.

Experimental

Presented in this paper are measurements of the specific activities of ^{226}Ra and ^{210}Pb in surgical and autopsy bone specimens taken from a group of 13 subjects characterized in Table 1 by the identification numbers and data from Miller et al.[5] They included 4 men and 9 women of whom 5 had been dial painters, 7 were patients injected with ^{226}Ra, and one had taken radium water for medicinal purposes. They had carried their burdens from 4 to 36 years, and their residual burdens ranged from 0.45 to 10.5 μCi,

TABLE 1. Data on Subjects

Subject Number[a]	Terminal Body Burden, μCi ^{226}Ra	Time Ra Carried, yr	Sex	Source of Radium[b]
03-140	0.5	4.08	M	I.V.
03-455	1.2	12	F	D.P.
03-118	3.09	24	F	I.V.
03-109	0.63	26	F	I.V.
03-117	1.54	26	M	I.V.
03-210	1.35	29	M	I.V.
03-402	1.2	31	F	D.P.
03-671	3.82	32	F	D.P.
03-215	4.00	33	M	I.V.
03-648	7.61	33	F	D.P.
03-551	1.33	35	F	D.P.
03-208	10.5	36	F	Ra H_2O
03-216	0.45	36	F	I.V.

(a) Case number of Miller et al.[5]

(b) Source of Radium: I.V. = Intravenous injection
D.P. = Dial painter
Ra H_2O = Drank radium water.

as measured by C. E. Miller.[5] Except for the specimen from Subject 03-455, which was preserved in formalin, the samples from each patient were preserved in ethanol and stored in a single glass bottle.

The ^{210}Pb was determined by wet-ashing the 0.2- to 2-g samples in nitric and perchloric acids and plating the ^{210}Po daughter onto a silver disk, and the α radiation was then α-counted.[6] The ^{226}Ra in the dissolved specimens was determined by the radon emanation method of Lucas.[7]

The errors originating in counting statistics were about 5% of the counting rate at the 90% confidence level and since they are much less than the variation between samples, will not be reported.

Corrections for the growth of ^{210}Pb from the ^{226}Ra during the period the specimens were stored, which ranged from 1.7 to 28 years, were calculated from

$$R_0 = \frac{R_m - f[(1 - \exp(-\lambda t)]}{\exp(-\lambda t)} , \qquad (2)$$

where R_0 is the $^{210}Pb/^{226}Ra$ ratio at the time of death or surgery, R_m is this ratio measured at time t (the storage time), f is the fraction of ^{222}Rn retained in the specimen during storage, and λ is the radioactive decay constant of ^{210}Pb; f was estimated as that value which when used to calculate the R_0's gave a minimum correlation between R_0 and the storage time (the correlation coefficient, $r \rightarrow 0$).

Only data from the subjects with burden times between 24 and 36 years were used in the calculations, so that R_0 would be approximately independent of burden time. In addition, only those data with ratios below 0.9 were included, since those specimens with greater ratios appeared to be in a different class, one which exhibited very low concentrations of both nuclides relative to those in other specimens from the same person.

Results and Discussion

The results of measurements on the particular specimens are shown in Table 2. In the last column are given the $^{210}Pb/^{226}Ra$ terminal ratios corrected for the growth and decay of ^{210}Pb during storage.

The terminal ratios (R_0) for each sample were calculated from Equation (2), based on f = 0.75. The mean ratio was 0.34 ± 0.03 (S.E.). The value of f is not critical in that a 30% variation in this number produces about a 15% variation in the mean ratio. In order to produce a statistically significant change ($P < 0.05$) it is necessary to vary f from 0.55 to 0.95.

The means of these ratios as a function of burden time for each subject are shown in Figure 1. The standard errors are also given and for reference the points represented by a single measurement are given standard errors which are twice the average of the calculated ones for the other points, 0.16, and represented by the dashed error bars. Also shown are the

TABLE 2. Specific Activities and Ratios in Individual Samples.

Subject[a]	Specimen Description	Sample Size, g ash	Storage Time, yr	Specific Activities, pCi/g ash ^{226}Ra	Specific Activities, pCi/g ash ^{210}Pb	$^{210}Pb/^{226}Ra$ Measured at $\tau = 0$	$^{210}Pb/^{226}Ra$ (f = 0.75) ± S.E.[b]
03-140	Femur shaft	0.367	24.55	234	114	0.488	0.169
	Femur shaft	0.296	24.55	77	47	0.611	0.442
	Femur shaft	0.219	24.55	167	67	0.401	-0.024
	Femur shaft	0.217	24.55	204	82	0.401	-0.024
							0.141 ± 0.11
03-455	Radius shaft	0.028	27.05	715	534	0.746	0.740
03-118	Femur shaft	0.056	7.10	675	220	0.326	.216
03-109	Femur shaft	0.390	2.18	811	214	0.264	0.228
03-117	Vertebra	0.0650	5.89	47	40	0.85	0.872
	Vertebra	0.179	8.07	187	53	0.291	0.228
	Femur shaft	0.065	5.89	661	238	0.360	0.278
							0.43 ± 0.22
03-210	Tibia shaft	0.626	1.74	105	39	0.375	0.353
	Tibia shaft	0.640	1.74	96	40	0.421	0.409
							0.38 ± 0.05
03-402	Femur shaft, cort.	0.052	9.12	855	343	0.401	0.281
	Femur joint, cort.	0.031	9.03	453	201	0.443	0.339
	Femur shaft, trab.	0.011	9.02	926	405	0.437	0.375
	Femur joint, cort.	0.0015	9.08	2353	1278	0.543	0.440
	Femur tumor	0.0013	9.04	0.51	2.25	4.4	9
							0.358 ± 0.033
03-671	Tibia shaft	0.064	8.98	891	362	0.406	0.290
03-215	Radius shaft	0.0175	4.93	411	144	0.350	0.281
	Radius, trab.	0.0057	4.93	262	108	0.412	0.353
	Humerus joint	0.0593	4.97	4480	1442	0.323	0.249
							0.294 ± 0.031
03-648	Vertebra A	0.0609	6.37	521	421	0.808	0.821
	Vertebra A1	0.116	8.66	362	236	0.652	0.620
	Rib	0.0609	6.38	3650	1475	0.404	0.324
	Femur shaft	0.0529	6.38	972	415	0.426	0.352
	Joint	0.0289	6.39	3330	969	0.291	0.185
	Femur joint, cort.	0.0018	6.39	107	169	1.58	2.0
	Femur joint, trab.	0.129	6.66	932	2360	2.53	3.0
							0.460 ± 0.114
03-551	Mastoid chips	0.0581	3.43	367	109	0.297	0.244
03-208	Humerus joint, trab.	0.290	8.74	1622	535	0.330	0.193
	Humerus joint, trab.	0.203	8.74	714	236	0.331	0.194
	Rib	0.0028	9.66	6000	3830	0.639	0.598
	Rib	0.0121	9.03	1110	686	0.618	0.573
	Rib	0.0469	12.23	4550	2050	0.451	0.305
	Sternum	0.0609	10.03	5620	2080	0.370	0.224
	Vertebra	0.0614	9.67	8130	3010	0.371	0.232
	Calvarium	0.0640	9.82	3.95	33.3	8.43	12
	Calvarium	0.0143	12.27	2.21	33.2	30	48
	Humerus joint	0.0593	9.68	10830	3950	0.365	0.223
	Femur shaft cort.	0.0640	10.04	0.91	12.1	13.3	20
	Femur shaft trab.	0.0204	9.97	12.6	161	12.8	19
							0.318 ± 0.060
03-216	Femur shaft (mid)	0.204	2.08	14.9	48	0.321	0.291
	Femur shaft (mid)	0.254	2.08	122	40	0.328	0.299
	Femur shaft (mid)	0.197	2.08	88	30	0.344	0.316
							0.302 ± 0.007

(a) Case number of Miller et al.[5]
(b) Ratios greater than 1.0 were not included in the averages. See text.

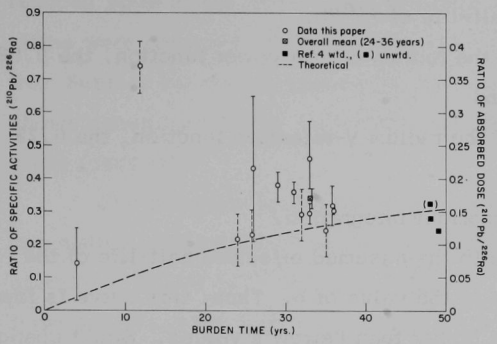

FIG. 1.--The mean terminal ratios of the activities of ^{210}Pb to ^{226}Ra and dose ratios for each subject as a function of burden time. The fractional retention of the ^{222}Rn during storage was estimated to be 0.75. Also shown are the theoretical curve and data from Reference 4, both weighted and unweighted (Subject 5278 in parentheses) by sample size (see text).

mean values for Petrow's 2 subjects at 48 and 49 years (the standard errors on these points are about the size of the symbols), corrected for storage time and weighted by sample size. In addition, the unweighted mean of his Subject 5278 is also shown in parentheses for comparison with the data of this paper. The unweighted and weighted means of the other subject were essentially identical.

The dashed line is a theoretical one representative of the change in ratio with time calculated from the γ-ray retention curve of Norris et al.,[2]

$$R_\gamma = 0.021t^{-0.28}, \tag{3}$$

their radium retention equation

$$R_{Ra} = 0.54t^{-0.52}, \tag{4}$$

and an exponential loss of ^{210}Pb with an effective half-life of 15 years.[8,9] The ratio of the specific activities of ^{210}Pb to that of ^{226}Ra, R_0, which is essentially the build-up of ^{210}Pb derived by Evans et al.,[10] is

$$R_0 = \frac{\lambda A_\gamma e^{-\lambda eT}}{0.54\, T^{-0.52}} \int_1^T e^{\lambda et} t^{-b} dt, \tag{5}$$

where T is the burden time,

λ is the physical half-life of ^{210}Pb,

λ_e is the effective half-life of ^{210}Pb,

A_γ is the constant of the radium gamma power function, the 0.021 in Equation (3), and

b is the exponent of the radium γ-retention function, the 0.28 in Equation (3).

The values are obtained by numerical integration.

R_0 is fairly insensitive to the assumed effective half-life of the ^{210}Pb, but it is very sensitive to the value of b. Thus, this curve is lower than the data of this paper and higher than Petrow's values. Slight changes in the empirical constants of the equations could change the location of the curve to fit either these data or Petrow's better.

One cause of apparent differences between samples could be that the ratios in cortical are different from those in highly trabeculated bone. Thus, the mean ratio in the cortical bone specimens is 0.311 ± 0.016 (S.E.), compared to 0.382 ± 0.057 (S.E.) of the more trabeculated specimens. However, because of the large range of values in the latter set (0.19-0.85) Student's t test showed no significant difference ($P > 0.10$). It should also be noted that the higher values of the ratios (> 0.45) were in the group of highly trabeculated bone.

The weighted averages taken from Petrow's data[4] were lower for cortical, 0.273 ± 0.042, than for highly trabeculated bone, 0.328 ± 0.069, and the difference is probably significant ($P < 0.05$). However, taking his first subject alone, the unweighted ratios 0.267 ± 0.036 for cortical and 0.343 ± 0.021 for trabecular bone, were significantly different (32 samples, $P < 0.001$), but for the second subject the respective ratios were much closer, 0.314 ± 0.054 and 0.353 ± 0.67. The difference was barely significant (57 samples, $P \approx 0.05$).

In addition to biological variation, the wide variations in the ratios reported here could be caused by the small sample sizes, 0.001 to 0.64 g ash, which could exaggerate the nonuniform distribution of ^{226}Ra as seen in autoradiographs. Larger, more representative samples might have

reduced some of the large variations.[11] Nevertheless, fairly uniform ratios were obtained for most of the specimens, and, although the sampling from Subject 03-216, in particular, previously presented by Lucas et al.[11] shows nonuniform ^{226}Ra and ^{210}Pb concentrations, the ratios were essentially identical.

One possible source of error in the estimates of ^{210}Pb metabolic parameters, especially if the loss rate of this nuclide is slow, is the possibility of uptake of ^{210}Pb along with the ^{226}Ra at the time of injection or ingestion since the injection solution may have been quite old at this time. However, such uptake appears to be small as shown by data based on the injections of 2 dogs with ^{226}Ra by Rowland and Marshall of this laboratory as shown in Table 3.[12,13] The ^{226}Ra solutions for these experiments were obtained about 1 month and 1-1/4 years prior to injection for the first and second dogs, respectively. On the first dog, 28 days after the last of 8 weekly injections, the ratio corrected for 50% radon retention* during storage was about 0.4% in the amputated left humerus; 353 days later on the other humerus it was only about 6%. For the second dog, with a single injection and sacrifice 7 days later, the ratio was less than 0.1%. Thus, it appears that little ^{210}Pb was likely to have been injected in the I.V. cases.

TABLE 3. ^{226}Ra-Injected Dogs.

Dog	Conditions	Time after Last Injection, Days	Storage Time, Days	Specific Activities, pCi/g ash ^{226}Ra	Specific Activities, pCi/g ash ^{210}Pb	$^{210}Pb/^{226}Ra$ Measured	$^{210}Pb/^{226}Ra$ Corrected (f = 0.50)
1	8 I.V. injections in 7 weeks	28	1332	797,000	47,400	0.059	0.004
		353	979	30,500	3,180	0.096	0.059
2	One I.V. injection	7	229	8,390	60	0.0072	-0.004

*A value of 50% retention was used in order to reduce the number of negative ratios.

Consistencies and variability of the data can be seen in Table 2 in Subject 03-208. Although the ^{226}Ra in the humerus joint and vertebra ranged from 714 to 10,800 pCi/g ash, the $^{210}Pb/^{226}Ra$ ratios were essentially identical. In the rib sample these ratios varied from 0.30 to 0.60, but 2 of the 3 values are similar and about 0.6. The ^{226}Ra concentrations are all within a factor of 6 of the mean skeletal concentration of about 4000 pCi/g ash. On the other hand, in calvarium and femur in this subject the concentrations are much lower and ratios much higher.

A bone of particular interest is the mastoid since this is a site of soft tissue tumors in the dial painters. A possible cause could be the deposition of ^{210}Pb from ^{222}Rn on the mastoid surfaces. However, in this one sample from Subject 03-551 (Table 2) the ^{226}Ra concentration is slightly lower than the 500 pCi/g expected for a uniform distribution, and there is no excess accumulation of ^{210}Pb, the ratio actually being a little lower than average.

The large variation in specific activities and the fairly uniform ratios of these activities in most specimens indicate that unless the ^{226}Ra and ^{210}Pb are metabolized nearly identically, only a small fraction of these nuclides is redistributed in the skeleton. However, some of the specimens have anomalously high ratios of 1.6 to 30 (measured) and these are associated with concentrations of ^{226}Ra and ^{210}Pb low relative to those in other specimens from the same subject. This effect could be caused by a high rate of removal of nuclide, especially ^{226}Ra, from these sites. However, the high ratio in newer tissue (tumor, Subject 03-402) indicates that this could also be caused either by a low initial deposition of Ra or resorption of both nuclides, and subsequent preferential deposition of the ^{210}Pb. These high ratios and low concentrations are also consistent with the inverse correlation of ratio with ^{226}Ra concentration in long bone shown by Petrow.[4]

In the case of calvarium (skull bone) there may have been little original deposition of ^{226}Ra with subsequent slow accumulation. This bone

is unusual, not only in its origin, but it apparently behaves differently as shown by some measurements on bone from people only environmentally exposed as shown in Table 4.[6] In two subjects, 1 and 2, the ^{226}Ra is much higher in the skull than in the other bones, while in Subjects 1 and 3 the ^{210}Pb values are much greater.

TABLE 4. Distribution of ^{226}Ra and ^{210}Pb in Bone of Unexposed People[a]

Subject	Age	Sex	Bone	^{226}Ra, pCi/g ash	^{210}Pb, pCi/g ash
1	68	M	Tibia	0.012	0.269
				0.019	0.247
			Mandible	0.012	0.093
			Skull	0.070	0.201
				0.070	0.419
			Joint	0.016	0.152
2	43	F	Tibia	0.025	0.090
			Mandible	0.028	0.049
			Skull	0.051	0.092
				0.100	0.146
			Joint	0.025	0.083
3	52	F	Tibia	0.026	0.078
				0.030	0.132
			Mandible	0.030	0.077
			Skull	0.032	0.366
				0.037	1.33
			Joint	0.027	0.071

[a] Taken from Reference 6, Table 4.

Finally, these results allow some estimates of the metabolic and dosimetric parameters. As noted in Figure 1 the more reliable data points (storage time less than 10 years) range in time from 24 to 36 years. Petrow's data extend the time to 49 years. Although there is some increase in ratio between 24 and 36 years, overall there appears to be little change. The theoretical curve based on a power function retention of ^{226}Ra and an

exponential loss of ^{210}Pb fits moderately well, i.e., it is only a slowly increasing function after 20 years. These values are not consistent with an exponential loss of both ^{226}Ra and ^{210}Pb with equal biological half-lives of these two nuclides.[4] For this condition the ratio is about 0.27 at 49 years, as found by Petrow, but at shorter times it is lower (at 30 years it is only 0.20). However, the biological half-lives derived from excretion data[8] indicate biological half-lives of 57 and 35 years for ^{210}Pb and ^{226}Ra, respectively. Thus, with an in vivo radon retention of 0.31,[5] the $^{210}Pb/^{226}Ra$ ratios are 0.19, 0.22, and 0.29 at burden times of 24, 30, and 50 years, respectively. The model using the power function radium gamma-ray retention model as shown in Figure 1 gives a better fit to the data over the 24- to 49-year region.

The absorbed skeletal dose due to the ^{210}Pb and its decay product, ^{210}Po, was estimated by Petrow to be about 5 to 6% that of the other members of the radium series.[4] However, the additional data of this paper indicate the dose to be somewhat higher, especially after about 10 years of burden time; this dose ratio could be 10% or more, as seen in Figure 1 (right-hand scale, in which it is assumed that the dose from the ^{210}Pb is 50% that from the ^{226}Ra and its daughters with 30% ^{222}Rn retention).[1] Although the dose depends on the retention model assumed in calculating the $^{210}Pb/^{226}Ra$ ratio, this factor does not appear to vary drastically from model to model.

If it is assumed that the dose-producing nuclide, ^{210}Po, with its 5.3-MeV alpha particle, is in radioactive equilibrium with the ^{210}Pb and that the Rn retention is 30%, then the dose rate from the ^{210}Pb per unit of activity is half that of the ^{226}Ra and its daughters. Thus, the dose rate from the ^{210}Pb-^{210}Po pair as shown in Figure 1 is about 12 to 15% that of the parent ^{226}Ra after about 24 years and 8 to 10% averaged over a long period of time after 10 years. For a single injection case the ^{210}Pb may be relatively small, only a few percent of the cumulative dose because of the initial high ^{226}Ra dose. However, for long-term intake, such as for

dial painters exposed for a year or more, the fractional dose of the ^{210}Pb may approach 10% or more that of the ^{226}Ra when averaged over 30 years or more.

Summary

In summary, these results show that many factors are highly variable. The ^{226}Ra concentrations may vary by more than a factor of 10 in a given individual, terminal body burdens may vary by factors of 20, and many different varieties of bone are involved. Nevertheless, the ratio of the specific activity of ^{210}Pb to that of ^{226}Ra is relatively constant at 0.34 ± 0.03. This factor is particularly useful in that it allows assessment of the whole-body content of ^{210}Pb from the ^{226}Ra whole-body measurements in high radium people which, because ^{210}Pb and its daughters emit no high energy γ rays, is not otherwise possible.

The constancy of the ratio indicates that there is little translocation of ^{210}Pb from its site of origin. However, some translocation does occur, as shown by some higher values of this ratio. Other results of very low ^{226}Ra concentrations and ratios greater than 10 indicate also that either initially little ^{226}Ra was taken up, or that the original bone was resorbed and rebuilt with preferential redeposition of the ^{210}Pb.

The $^{210}Pb/^{226}Ra$ ratio appears to be somewhat higher in more trabeculated bone than in cortex.

None of the models proposed appears to fit the data well. The single exponential models, with or without equal biological half-lives of ^{210}Pb and ^{226}Ra, fit the long-term results but are too low for the shorter-term ones. The model using the radium gamma-ray retention power function fits the 24- to 36-year data.

The absorbed dose from the ^{210}Pb averaged over long times is about 6% that of the ^{226}Ra and its daughters, but depending on the mode of acquisition, it may be 10% or more.

I thank Dr. R. J. Hasterlik for human bone specimens,

Dr. R. E. Rowland for both human and dog bone specimens, and Dr. C. E. Miller for use of his data on the ^{226}Ra whole-body content of these subjects.

References

1. Holtzman, R. B. RaD (^{210}Pb) in the Human Skeleton: Estimates of the Exponent of the Retention Function, the Skeletal Content, and Dose Rate in High-Radium People. Radiology 80, 122-123 (1963).
2. Norris, W. P., T. W. Speckman, and P. F. Gustafson. Studies of the Metabolism of Radium in Man. Am. J. Roentgenol. 73, 785-802 (1955).
3. Miller, C. E. and A. J. Finkel. Radium Retention in Man after Multiple Injections: The Power Function Re-evaluated. Am. J. Roentgenol. 103, 871-880 (1968).
4. Petrow, H. G. The Metabolic and Dosimetric Significance of ^{210}Pb and ^{226}Ra Ratios in the Bone of Radium Dial Painters. Proc. First Int. Congr. of Radiation Protection, Rome, September 5-10, 1966. (Pergamon Press, Oxford, 1968), Part I, pp. 727-741.
5. Miller, C. E., R. H. Hasterlik, and A. J. Finkel. The Argonne Radium Studies, Summary of Fundamental Data. Argonne National Laboratory and Argonne Cancer Research Hospital Report ANL-7531 (1969).
6. Holtzman, R. B. Measurement of the Natural Contents of RaD (^{210}Pb) and RaF(^{210}Po) in Human Bone--Estimates of Whole-Body Burdens. Health Phys. 9, 385-400 (1963).
7. Lucas, H. F., Jr. Correlation of the Natural Radioactivity of the Human Body to that of its Environment: Uptake and Retention of ^{226}Ra from Food and Water. Argonne National Laboratory Radiological Physics Division Semiannual Report, July-December 1960, ANL-6297, pp. 55-66.
8. Holtzman, R. B. and H. F. Lucas, Jr. Excretion of ^{210}Pb and ^{226}Ra by Radium Dial Painters, Health Phys. 13, 940 (1967).
9. Holtzman, R. B. ^{210}Pb and ^{210}Po Metabolism in Radium Dial Painters. Paper presented at a meeting, "The Biology and Ecology of Polonium and Radiolead," The Institute of Cancer Research, Belmont, Sutton, Surrey, England, April 30 and May 1, 1970.
10. Evans, R.D. et al. Radium and Mesothorium Poisoning and Dosimetry and Instrumentation Techniques in Applied Radioactivity. MIT Annual Progress Report, 1964. MIT-952-1, pp. 54-58.
11. Lucas, H. F., Jr., R. E. Rowland, C. E. Miller, R. B. Holtzman, R. J. Hasterlik, and A. J. Finkel. An Unusual Case of Radium Toxicity. Am. J. of Roentgenol. 90, 1042-1051 (1963).
12. Rowland, R. E. Microscopic Metabolism of ^{226}Ra in Canine Bone and Its Bearing on the Radiation Dosimetry of Internally Deposited Alkaline Earths. Radiat. Res. 15, 126-137 (1961).
13. Rowland, R. E. Personal communication.

^{210}Pb AND ^{210}Po METABOLISM IN RADIUM-DIAL PAINTERS*

R. B. Holtzman

The excretion rates and blood levels of ^{210}Pb and ^{210}Po were measured in 14 dial painters 35 to 40 years after their exposure to ^{226}Ra. The residual body burdens of the ^{226}Ra, ranging from 0.028 to 2.4 μCi, and of the associated daughters were sufficient to produce levels of ^{210}Pb and ^{210}Po in the blood and excreta much greater than those in unexposed persons.

The ratios of the urinary-to-fecal excretion rates were 1.7 and 0.12 for ^{210}Pb and ^{210}Po, respectively. Thus, urinary excretion was 63% for lead, but only 10% for polonium. The coefficients of excretion (fraction of body burden excreted per day) were 32×10^{-6} and 270×10^{-6} per day (1.2 and 9.8% per year) for the ^{210}Pb and ^{210}Po, respectively. These data, when fitted to a single exponential excretion model, led to biological half-lives of about 57 years for lead and 7 years for polonium. The blood clearance rates were 0.088 liters/day for ^{210}Pb and 1.2 liters/day for ^{210}Po. This rate for lead is low compared to the 10 liters/day for strontium and 100 liters/day for radium. However, if the concentration of lead in serum only is used, then the clearance rate is 1.6 liters/day which is similar to that of the polonium, but still less than that of strontium and radium.

These results make possible more accurate estimates of body burdens of humans exposed to high levels of lead and ^{210}Pb. Their application to evaluating the hazards of lead is presented.

---

* This is the abstract of a paper presented at the meeting on the Biology and Ecology of Polonium and Radiolead at The Institute of Cancer Research, Belmont, Surrey, U.K., April 30 and May 1, 1970.

MEASUREMENTS OF AMERICIUM-241 IN TWO SUBJECTS

John Rundo, A. T. Keane, and H. A. May

The "best" estimates of the americium-241 contents of the scientist and his 10-year-old son are 60 nCi and 40 nCi, respectively. The calibration methods are described in some detail.

For a period of 3 months in 1964 a scientist, H, worked in the detached garage of his home with a source of americium-241 of supposed strength about 10 mCi. The americium was reported by the supplier to be safe and not to release activity on smearing. The scientist's 4- year old son, R, followed the proceedings attentively.

In February, 1970, alpha-particle contamination at the scientist's new place of employment was identified as americium-241, and its origin was eventually traced to contaminated furniture and fittings in his new home. Body radioactivity measurements at a nearby research institute demonstrated the presence of americium-241 in all members of the household, but at levels of concern only in the scientist and his son (now aged 10). At the request of the local Department of Health we agreed to make confirmatory measurements of the levels in these two subjects.

Methods

Measurements were made in an iron room in the basement of Building 203, using the 6-inch diameter by 8-inch thick "log" crystal [1,2] and a new 11.5-inch diameter by 0.5-inch thick crystal with a thin window. Because of fluctuations in the radon concentration in the air in the room there was some instability of the counter backgrounds, and it was necessary to correct for this in some of the measurements.

The log crystal was used in tilting chair geometry to establish the general level of contamination in both subjects, and also in the multiposition method of Miller[1,2] with the subjects both supine and prone. The large-area thin crystal was similarly used in the multiposition technique,

but with the subjects supine only.

Calibration

The available sources of americium-241 had been prepared from a solution which had been standardised by absolute alpha counting. The detector (log crystal or thin crystal) was placed over the first position of the Presdwood phantom (Figure 1 of Reference 1), and the response was determined with a calibrated source placed in turn in each of the seven sections. This procedure was repeated with the crystal over each of the other six positions, to produce a 7 x 7 response matrix for the seven measurements made of the scientist's radioactivity. For his 10-year-old son, a much smaller phantom was prepared, and a 5 x 5 response matrix was obtained for the five measurements made of the boy's radioactivity.

Measurements were also made on two control subjects of similar builds to determine the response at 60 keV of the two detectors in the different geometries to the subjects' potassium-40 and caesium-137 contents. In Table 1 are set out the physical characteristics of the contaminated and control subjects, together with the counting-rates obtained in the energy

TABLE 1. Physical Characteristics of Contaminated and Control Subjects

	Height, cm	Weight, kg	Age, years	Counts/min,[a] 80-160 keV
Subject H	170	89	57	114.2
Control J.D.	169	88	50	112.4
Subject R	144	35	10	42.2
Control D.R.	144	39.5	10	44.0

[a] Measured with log crystal in chair geometry

band 80 to 160 keV (i.e., above the region of the photopeak at 60 keV from americium-241 but still in the energy region which is sensitive to the effects of body size). It can be seen that the control subjects are well matched

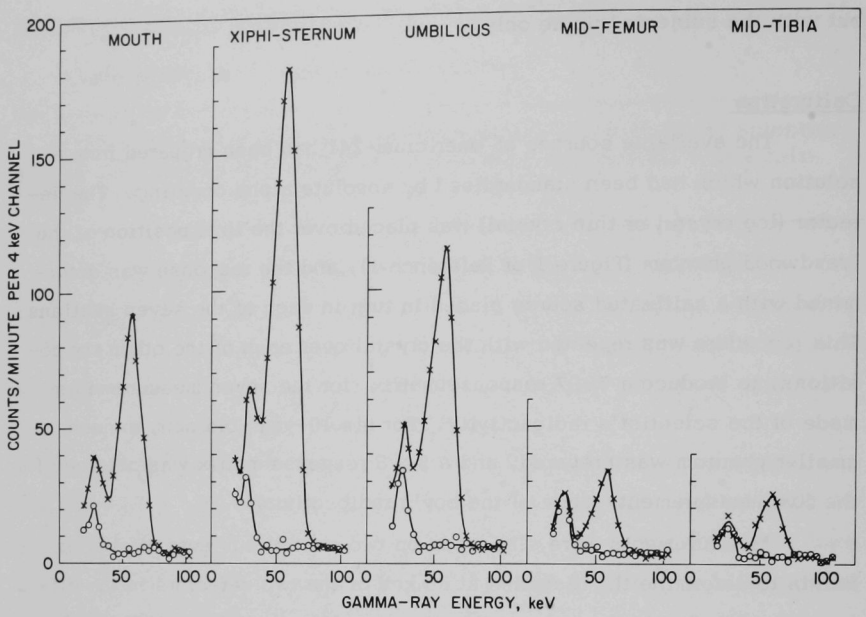

FIG. 1.--Gamma-ray spectra (20 to 100 keV) taken with the 11.5" x 0.5" crystal at five points above the supine subjects. The crystal was 30 cm above the bed and it was placed in turn over the indicated parts of the body. X, contaminated subject R; O, control subject D.R.

with the contaminated subjects in almost all respects. In Figure 1 are shown the gamma-ray spectra (20 to 100 keV) taken with the large thin crystal at five positions over the supine boys (contaminated and control subjects). The presence of americium-241 in the former is unequivocal.

The control subjects were also used to obtain calibration factors by determining the geometric mean of the counts observed with a calibrated source of americium-241 on the posterior and anterior surfaces of the subjects, at 7 or 5 points directly beneath the center of the respective detectors.

The counting-rates obtained in this way corresponded to the diagonals of the response matrices, and there were substantial differences between those obtained from the phantom and those from the control subjects. In Table 2 the sets of values are compared, for the 11.5-inch x 0.5-inch crystal. Differences are not unexpected, for in theory the geometric mean of counting rates on the posterior and anterior aspects of a phantom is not equal to the counting rate from a source at the center. Theoretical considerations show that for exponential absorption the former should exceed the latter by about 4% to 33% for a phantom thickness in the range 10 to 20 cm. However, the absorption of americium-241 gamma rays in Presdwood, determined with the large-area thin crystal, was not exponential because of the effects of forward scatter. Use of the experimental attenuation curve showed that the geometric mean of the two counting rates from a source on the surfaces should always be less than the counting rate from the source at the center, by an amount not greater than 11%. Thus the differences shown in Table 2 are not entirely due to the assumption that the geometric mean counting rate equals the counting rate with the source at the center. It seems likely, but has not been proved, that the principal cause of the differences is the

TABLE 2. Comparison of Response (counts/min/nCi) of Large-Area Thin Crystal to Americium-241 in Phantom with Geometric Means of Response to Sources on Posterior and Anterior Surfaces of the Control Subjects

	Counter Position Number						
	1	2	3	4	5	6	7
Large phantom	35.4	49.8	36.5	44.7	45.1	48.6	45.9
Control subject J.D.	27.7	31.4	27.5	25.0	34.2	30.3	26.2
Ratio	1.28	1.59	1.33	1.79	1.32	1.61	1.76
Small phantom	49.6	46.6	46.9	49.9	49.1		
Control subject D.R.	37.6	31.7	30.5	41.1	36.6		
Ratio	1.32	1.47	1.54	1.21	1.34		

inadequacy of the phantom (dimensions, shape, and composition). Thus, there is some uncertainty as to the more reliable sets of calibration data. Similar considerations apply to the data obtained with the log crystal.

A very approximate value for the body content of each subject was calculated from the measurements in chair geometry, using the potassium-40 as an internal standard. It was even possible to derive a result without a calibration for potassium; the necessary quantities are set out in Table 3.

TABLE 3. Data for the Calculation of Americium-241 Body Content from Potassium-40 Photopeak as Internal Standard

Subject	Wt, kg	Assumed K Concentration, g/kg body weight	Assumed Average Absorption Thickness, cm	^{40}K Counting Rate, counts/min
H	89	1.6	6	92.3
R	35	2.0	3	54.9

Specific γ-ray activity of potassium, 93 pCi/g; absorption coefficient in tissue at 1.46 MeV, 0.055 cm^{-1}; absorption coefficient in tissue at 0.06 MeV, 0.2 cm^{-1}; transmission of crystal can (0.05-cm steel) at 0.06 MeV, 0.644; photo-efficiency of log crystal at 1.46 MeV, 0.54; photo-efficiency of log crystal at 0.06 MeV (corrected for escape peak), 0.75; abundance of 0.06-MeV γ-ray in americium-241 decay scheme, 0.36.

For subject H the calculation for the counting efficiency for americium-241 is as follows

$$92.3 \times \frac{1000}{89 \times 1.6 \times 93} \times \frac{e^{-6 \times 0.2}}{e^{-6 \times 0.055}} \times \frac{0.75}{0.54} \times 0.644 \times 0.36 .$$

$$= 0.94 \text{ counts/min/nCi.}$$

Similarly, for subject R the counting efficiency for americium-241 was 1.8 counts/min/nCi. These calibration factors are probably not reliable to much better than a factor of about two.

Results

The simultaneous equations were solved by a matrix inversion method with the aid of a fast digital computer.

In Table 4 are set out the americium-241 contents of the two subjects computed from the multiposition γ-ray measurements with the two detectors. Two points are immediately apparent. First, despite considerable differences in the contents of the same regions as determined by the two detectors, the total contents are in respectable agreement (10%). The difference in the apparent distributions can be attributed to differences in detector positioning.

TABLE 4. Solutions of Matrix Equations

Position Number	Americium-241 Content, nCi			
	Subject H		Subject R	
	Log Crystal	Thin Crystal	Log Crystal	Thin Crystal
1	18.4 ± 1.5	4.2 ± 0.3	12.2 ± 1.0	3.2 ± 0.2
2	8.6 ± 2.3	17.3 ± 0.3	13.5 ± 1.6	17.4 ± 0.3
3	9.1 ± 2.5	8.6 ± 0.4	-8.3 ± 1.8	7.4 ± 0.3
4	1.4 ± 2.6	2.2 ± 0.3	1.8 ± 1.7	-1.8 ± 0.2
5	4.9 ± 2.7	2.6 ± 0.3	2.0 ± 1.3	2.4 ± 0.2
6	1.2 ± 2.8	4.0 ± 0.3		
7	2.2 ± 2.1	2.7 ± 0.2		
Total	45.8	41.6	26.2	28.6

Second, in the case of subject R, for the results from both detectors there is one position where the exact solution to the equation is negative. This is a consequence of the inadequacy of the phantom. The calibration matrices were such that the computed activity at position 2 (log crystal) or 3 (thin crystal) would contribute a higher counting rate than was observed at position 3 (log crystal) or 4 (thin crystal).

Thus we can put less faith in the values for the contents of the various regions than in the totals. However, the differences between the values along the diagonals of the calibration matrices and the geometric means of the response on posterior and anterior surfaces of the control subjects suggest that the values in Table 4 are probably all too low. If we multiply the results in Table 4 by the ratios of these responses we may obtain more reliable results and these values are shown in columns 2 and 4 of Table 5.

TABLE 5. Americium-241 Contents

	Log Crystal		Thin Crystal	
Position Number	Corrected Matrix, nCi	Empirical Method, nCi	Corrected Matrix, nCi	Empirical Method, nCi
Subject H				
1	21.2	10.8	5.4	10.8
2	18.1	29.2	27.5	22.3
3	12.0	9.3	11.4	13.0
4	2.5	8.0	4.0	6.0
5	7.7	5.1	3.5	4.0
6	1.8	4.8	6.4	5.5
7	2.8	4.3	4.7	5.4
Total	66.1	71.5	62.9	67.0
Subject R				
1	29.3	22.7	4.2	9.4
2	20.4	12.6	25.7	17.4
3	-4.9	5.3	11.4	10.8
4	2.9	2.7	-2.2	1.9
5	1.7	2.7	3.2	2.0
Total	49.4	46.0	42.3	41.5

Columns 3 and 5 of Table 5 contain results obtained by an alternative method. First, a value for the americium-241 content at each position was calculated from the observed net counting rate and the appropriate geometric mean response to the calibrated source. The values so obtained were all

overestimates because they ignored the contributions to the counting rates from activity in adjacent positions. Empirical (and approximate) corrections for this were derived from the phantom response matrix, by dividing the estimate at position i by the ratio

$$\frac{\sum_{j=1}^{j=n} C_{i,j}}{C_{i,i}},$$

where $\sum_{j=1}^{j=n} C_{i,j}$ is the sum of the responses of the counter in position i to the source in all n positions, $C_{i,i}$ is the response of the counter in position i to the source in position i, and n is 7 or 5. This correction factor would be exact only if there were equal activity in all n positions. However, since the response of the counter in position i to a source in position i ± 2 was not more than 5% of the response in position i, the error introduced by this empirical correction was not great. The total contents by this method were in quite good agreement with those from the matrix method after correction.

The best estimates we can make of the contents of H and R are 60 nCi and 40 nCi, respectively; the precision of the calibration does not warrant more than one significant figure. It is difficult to assess confidence limits on the estimated contents. Reliance solely on the phantom calibration matrix would give values about 25% lower; the uncertainty introduced by the assumption that the geometric mean rate is the same as that from a source in the center of the subject would raise the values by less than 10%. On the other hand, although the actual distribution within the body is not known, it is clear that the "effective" position of the americium-241 is not close to the center of any part of the body except perhaps the thighs and parts of the arm.

What does emerge from this analysis is that apparently about

three-quarters of the total content is in the upper half of the body in both subjects. If the distribution of the americium-241 is uniform throughout the skeleton (a major assumption of doubtful validity), this suggests that as much as half the total content could be in soft tissue, presumably liver and/or lung.

A single measurement was made with the thin crystal positioned over the liver of subject H. (An outline of the liver was cut out of a sheet of lead 3 mm thick which was used to shield the thorax and upper abdomen.) The americium-241 peak at 60 keV was clearly seen in the resulting spectrum; thus there was some evidence for activity in the liver.

The values for the total body contents from the measurements in chair geometry were 132 nCi and 193 nCi for subjects H and R, respectively. These are twice the values obtained from the detailed analysis described above, but in view of the imprecision of the calibration factors, there is no real inconsistency. An additional discrepancy arises because of the effect of distribution in the body; activity in liver or lung would be counted in the chair geometry with a higher efficiency than would activity in the whole skeleton.

There were several unsatisfactory features of the method adopted to derive the "best" estimates, in particular the empirical correction factors. Much work remains to be done to improve the method of calibration.

References

1. Miller, C. E. Multiple-crystal-position Technique for Whole Body Measurements. Argonne National Laboratory Health Division Gamma-Ray Spectroscopy Group Semiannual Report, January through June 1964. ANL-6839, pp. 12-17.
2. Miller, C. E. A New Technique for Determining the Distribution of Radium and Thorium in Living Persons. Assessment of Radioactivity in Man. Int. Atomic Energy Agency, Vienna, 1964, Vol. 1, pp. 67-77.

CONSTRUCTION OF NEW SHIELDED ROOMS

John Rundo

Three similar rooms for measurement of body radioactivity are under construction in the underground vault.

Three shielded rooms for measurements of body radioactivity are under construction in the underground vault. The internal dimensions of each room will be 8'6" long x 6'9" wide x 7'6" high (2.59 x 2.06 x 2.28 meters); adjacent rooms share a dividing wall. The shielding material is

FIG. 1.--Photograph taken in mid-June 1970 looking diagonally across the underground vault from the southwest corner, showing the stage reached in the construction of the three shielded rooms.

principally steel plates 1/4 inch thick, but one long wall is built from 4-inch thick lead bricks covered with 2 inches of steel. All other walls, the floors, and roofs are 8-inch thick steel. Figure 1 shows how far advanced construction was in mid-June 1970. At the extreme right the 2-foot wide door opening for room No. 3 can be partially seen; about 3 inches of the front wall of this room are in place. The middle room has one 1/4-inch layer of the front wall.

The method of construction adopted for these rooms is entirely different from that adopted in previous rooms erected here. The concept of "portability" has been abandoned, and all plates are welded in place. Selection of welding rods and attention to slag removal from the welds should minimize the contribution to the counter backgrounds from naturally radioactive materials in the welding rod flux. The steel being used for the rooms was originally that used for Iron Rooms I and II in this Division, together with that from the Biological and Medical Research Division's Iron Room. There should, therefore, be no problems of contamination in the steel itself.

THORIUM AND URANIUM IN BLOOD, URINE, AND CIGARETTES

H. F. Lucas, Jr. and Francis Markun

The analytic method previously developed for thorium in bone was modified to remove interference from sodium and bromine. The thorium in the red cell fraction of blood was 0.17 ppb, which was at least 4 times that for plasma. The uranium content was less than 0.4 ppb in both blood and urine. Thorium in urine ranged from 0.2 to 5 ppb but was detectable in only one half of the samples. Both the thorium and uranium content were 0.15 μg/cigarette or 3 μg/pack.

The concentration of thorium in human bone has been found to increase with age and exposure to thorium-containing dusts.[1] It was suspected that some of the scatter in these data resulted from the thorium contained in cigarette smoke.[1] While insoluble forms of thorium are retained by the lung with little or no resorption, soluble forms are resorbed rather rapidly.[2]

The uptake of thorium by the rat skeleton from intratracheal exposure is 4 to 8% of the administered dose.[2] Assuming that 50% of the thorium in cigarette smoke is retained by the lung and that 4 to 8% goes to the skeleton, then 0.03 to 0.06 μg/day would eventually double the concentration in the bone. Exposure to this level of thorium would be expected to increase the level in blood and urine of smokers relative to nonsmokers.

The neutron activation analysis system previously developed for bone had not been evaluated for use on blood, urine or cigarette ash.[3] It was the purpose of this preliminary study to evaluate the suitability of the method for these materials. Additional trace elements could be determined with only a slight additional effort, and measurements on these have been included.

Experimental Procedure

The blood samples were obtained from a blood bank and are presumed to be normal. They were lyophilized and then ashed with ionized oxygen at

100 W power to minimize heating.* The ash was placed in small polyethylene vials, several of which were irradiated with selected standards for 7 hr in the Juggernaut reactor at a flux of 2×10^{12} n cm^{-2} sec^{-1}. Three to four days after the end of the irradiation, the samples were dissolved with 9M HCl and a few drops of 30% hydrogen peroxide, and heated in a water bath. The samples appeared to be completely dissolved after about 30 min, but heating was continued for about 2 hr. The amount of each trace element in the sample was then determined using a slight modification of the radiochemical group separation, gamma-ray spectrometry technique previously described.[3]

The large amount of sodium in the blood and urine was removed by adding a 3/8" x 1" column of hydrated antimony pentoxide (HAP) ahead of the anion resin column.[4] Both urine and cigarettes contained very large amounts of bromine, which interfered with the analysis. This was removed by gassing with chlorine while heating.

The urine samples were obtained from employees and university students. All were believed to be exposed only to normal environmental dusts and vapors. Seven of the individuals smoked about one pack of cigarettes per day, while the remaining five had never smoked. The urine was collected directly into freeze-dry bottles, which had been cleaned by soaking in 6 N HNO_3, and was frozen with dry ice within 5 to 10 min of collection. The freeze-dry material was ashed with ionized oxygen and processed in the same way as the blood, except only about one day elapsed between end of irradiation and analysis.

The cigarettes were king size without filters (Chesterfield) purchased locally. Duplicates of five samples (2 cigarettes each) from a single pack were analyzed. They were ashed with ionized oxygen and irradiated in the same way as the blood and urine. These samples did not dissolve readily

---

*Tracerlab LTA-600, with large sample assembly.

or completely in 9M HCl or 7M HNO_3. The insoluble residue was collected on glass wool and treated separately, and the soluble fraction was treated in the same way as the blood and urine.

Results

Blood

The concentrations of Th, Co, Cd, Zn, Sb, Cr, and U in blood plasma and cells are summarized in Table 1. The ^{232}Th content of the cells averaged 0.17 ppb and was at least 4 times greater than that in the plasma. The Co, Cd, Zn, Sb, and Cr concentrations are very similar to values obtained for normal blood.[5] The uranium concentration of about 0.1 ppb is at the lower end of the range of 0.12 to 2.0 ppb recently reported by Hamilton.[6]

Urine

The concentrations of U and Th in urine are summarized in Table 2. Some difficulty was encountered due to the large amounts of bromine in some of the early samples so that except for sample 7A the high values reported (i.e., 1C, 4B, and 9A) are suspect until confirmed by repeated analysis.

Cigarettes

The Th, U, La, Co, Cd, Sb, Zn, and Cr contents of cigarettes are summarized in Table 3. The Cd content is equal to that reported earlier.[7]

It was estimated that the inhalation of 0.03 to 0.06 μg Th/day would eventually double the concentration in the bone. This is only 1 or

TABLE 1. Trace Elements in Blood

		Concentration in 10^{-9} g/g Wet Weight Estimated from Counting Statistics, ppb ± S.E.						
Blood Fraction	Sample Number	Th	Co	Cd	Zn	Sb	Cr	U
Plasma	13	< 0.04	1.03 ± 0.05	1.70 ± 0.35	742 ± 12	ND[a]	ND	< 0.04
Plasma	14	< 0.04	1.38 ± 0.08	3.58 ± 1.23	811 ± 10	3.25 ± 0.47	14.7 ± 1.3	< 0.13
Cells	16	0.21 ± 0.04	1.48 ± 0.07	ND	8636 ± 79	6.26 ± 0.21	ND	< 0.07
Cells	17	0.13 ± 0.04	2.56 ± 0.12	ND	7955 ± 92	3.83 ± 0.10	ND	0.26 ± 0.04

[a] ND = Not detected.

TABLE 2. Uranium and Thorium in Human Urine

Sample	Cigarettes Used[a]	Fresh Weight, g	U, ppb	Th, ppb
1A	Y	1.93	≤ 0.07	0.5 ± 0.2
B		4.32	≤ 0.03	≤ 0.7
C		2.72	≤ 0.4	2.7 ± 0.2
D		3.20	≤ 0.1	≤ 0.6
2A	Y	3.56	≤ 0.06	≤ 0.8
B		4.16	≤ 0.02	≤ 0.5
C		3.45	≤ 0.04	≤ 0.3
D		3.26	≤ 0.04	0.5 ± 0.2
3A	Y	3.92	≤ 0.02	0.7 ± 0.2
B		3.96	≤ 0.01	0.2 ± 0.1
4A	Y	2.48	≤ 0.04	≤ 0.5
B		1.54	≤ 0.06	2.1 ± 0.3
5A	Y	6.38	≤ 0.02	≤ 0.3
B		6.32	≤ 0.02	≤ 0.3
6A	Y	3.74	≤ 0.02	0.2 ± 0.1
B		3.79	≤ 0.03	0.2 ± 0.1
7A	Y	7.25	≤ 0.40	5.3 ± 0.2
8A	N	2.40	≤ 0.03	≤ 0.4
B		2.50	≤ 0.02	≤ 0.2
9A	N	5.06	≤ 0.03	3.3 ± 0.2
B		3.27	≤ 0.03	0.3 ± 0.1
10A	N	1.78	≤ 0.06	≤ 0.7
B		2.32	≤ 0.05	≤ 0.7
11A	N	3.23	≤ 0.09	0.5 ± 0.2
12A	N	3.57	≤ 0.10	≤ 1.0

[a] Y = Yes; N = No.

TABLE 3. Trace Elements in Cigarettes[a]

Exp. No.	Ash, g	Th, μg	U, μg	La, μg	Co, μg	Cd, μg	Sb, μg	Zn, μg	Cr, μg
04	0.31552	0.079±0.002	0.053±0.001	1.30±0.03	0.518±0.003	1.03±0.01	0.015±0.001	53.5±0.2	---
11	0.30912	0.127±0.002	0.063±0.001	1.51±0.03	0.555±0.006	1.99±0.03	0.090±0.002	51.7±0.9	---
12	0.30912	0.237±0.009	0.115±0.007	1.16±0.05	0.370±0.005	0.98±0.08	0.041±0.003	33.5±0.5	2.56±0.33
24	0.28309	0.152±0.007	0.132±0.008	1.04±0.05	0.503±0.006	0.96±0.05	0.084±0.003	47.9±0.9	5.15±0.29
25	0.28309	0.234±0.010	0.186±0.016	1.89±0.06	0.557±0.052	1.64±0.11	0.055±0.002	38.3±0.3	2.14±0.15
33	0.29681	0.119±0.019	0.191±0.020	1.88±0.04	0.539±0.005	1.47±0.02	0.103±0.002	47.2±0.4	4.90±0.68
34	0.29681	0.160±0.009	0.185±0.008	1.95±0.04	0.556±0.005	1.67±0.03	0.088±0.002	47.8±0.4	5.39±0.48
35	0.28252	0.166±0.011	0.160±0.011	1.75±0.04	0.505±0.005	1.36±0.02	0.074±0.002	42.1±0.4	5.19±0.49
36	0.28252	0.138±0.012	0.186±0.012	1.88±0.05	0.514±0.005	1.47±0.04	0.077±0.005	42.5±0.5	5.53±0.55
Mean + σ_M		0.16 ±0.02	0.14 ±0.02	1.60±0.02	0.51 ±0.02	1.40±0.12	0.07 ±0.01	45 ±2	4.41±0.54
Mean + σ_M[b]		0.17 ±0.02	0.17 ±0.01	1.65±0.14	0.51 ±0.02	1.37±0.10	0.08 ±0.01	43 ±2	4.41±0.54

[a] Values reported are per cigarette.
[b] Experiments 04 and 11 excluded.

2% of the Th in a single pack of cigarettes and may be a significant source of exposure to thorium. However, it is yet to be shown that Th is in the smoke or excreted by the smoker.

This study has shown that the analytic method previously developed for bone may be applied to blood and urine with little modification. The concentrations of U and Th were less than expected so that further work will require an increase in the integrated neutron flux.

References

1. Lucas, H. F., Jr., D. N. Edgington, and F. Markun. Natural thorium in human bone. Health Phys., in press; also Argonne National Laboratory Radiological Physics Division Annual Report, July 1968-June 1969, ANL-7615, pp. 57-58.
2. Kendysh, I. N. Distribution and Elimination of ^{232}Th. Distribution and Biological Effects of Radioactive Isotopes, Ed. Y. I. Moskalev. AEC-tr-6944 (Rev.), (1966).
3. Edgington, D. N. and H. F. Lucas, Jr. A System for the Neutron Activation Analysis of Trace Elements in Samples of Biological and Environmental Interest. J. Radioanal. Chem. 5, 233-250 (1970).
4. Girardi, F., R. Pietra, and E. Sabbioni. Radiochemical Separation by Retention on Ionic Precipitates--Adsorption Tests on 17 Materials. European Atomic Energy Community, EURATOM, Publ. EUR-4287-e (1969).
5. Comar, D. Clinical Application of Activation Analysis. Advances in Activation Analysis, Ed. J. M. A. Lenihan and S. J. Thompson. Academic Press, New York, 1969, pp. 163-206.

6. Hamilton, E. I. Uranium Content of Normal Blood. Nature 227, 501-502 (1970.
7. Nandi, M., D. Slone, H. Jick, S. Shapiro, and G. P. Lewis. Cadmium Content of Cigarettes. Lancet 2, 1329-1330 (1969).

BOAT SAMPLING METHODS FOR ANALYSIS OF LEAD AND TELLURIUM IN BIOLOGICAL MATERIALS

F. H. Ilcewicz and R. B. Holtzman

Two procedures using the atomic absorption boat sampling method were studied: one the direct mounting of a sample, and the other a prior extraction of the sample with APDC. Modifications in the method improved the sensitivity, and a detection limit of 0.0004 μg Pb and a precision of about 6% was attained. Extraction of the sample with APDC extended this method to the analysis of tellurium in raw urine with a detection limit of about 0.003 μg Te/ml urine, and to the analysis of lead in heavily salted solutions.

Introduction

Prior to the introduction of atomic absorption spectrophotometry, the most sensitive and precise analysis of lead was by the colorimetric dithizone method. The procedure is cumbersome and time consuming, and the many steps provide numerous chances for contamination from reagents and reaction vessels.

Atomic absorption techniques provide high analytical sensitivity and relative freedom from interference from other elements. For the analysis of some elements, such as zinc and cadmium, solutions may be aspirated directly without concentration or separation. However, for the determination of lead and tellurium in biological systems, the sensitivity of the instrument is limited and the normal concentrations are so low that a concentrating step is necessary.

Two methods with improved sensitivity have been developed. An increased concentration and a reduction in interferences from other elements is obtained by the extraction of lead from urine with ammonium pyrrolidine dithiocarbamate (APDC) in methyl-n-amyl ketone.[1] The organic solvent is aspirated into the flame. This method, however, requires 50 ml of urine for each lead determination, but provides a possible analysis for close to thirty metals.[2] An even greater sensitivity was obtained by Kahn, et al.[3,4] who utilized the sampling boat (TM) made by Perkin

Elmer Corporation. In this technique the total sample was analyzed. The detection limit for lead was reduced to 0.001 μg/ml, a factor of thirty improvement over the nebulization method. However, the method of additions, which is slower than the routine calibration curve method generally used with nebulization, must be used. The detection limit of tellurium (0.01 μg/ml) was also improved by a factor of thirty over that of the conventional aspiration method. Although the sensitivity of the boat method was very good, the precision seemed to be lacking.

This paper describes modifications of the boat method designed to improve the precision, sensitivity, and speed of analysis, as well as studies of the precision and consequent applicability of this method to the measurement of lead and tellurium in various environmental and biological materials. Also studied were the effects on precision and reduction of interferences from the sample matrix by the combination of the extraction procedure with the boat method.

Experimental

The data were taken on a Perkin Elmer Model 303 spectrophotometer equipped with a three-slot (Boling) burner head, a Perkin Elmer sampling boat holder, with a Sargent recorder (Model SRL). The Perkin Elmer sampling boats were modified by removing the arms and reshaping the ends to fit the special quartz holders in the flame. A tent-shaped quartz chimney with a 10-mm wide base and a 6.5-cm length with its axis parallel to the beam was placed approximately 2 mm above the boat during the measurements.

For sample preparation, the boats were placed in a special holder, an aluminum block slotted to accommodate the boats and equipped with a carrying handle. This unit could be placed on a hot plate for drying the samples prior to evaporation.

Working standard solutions ranging from 0.01 to 2.0 ppm were made

from a standard 1000-ppm lead solution.* The dilute standards were stored in polyethylene bottles and were found to be stable for at least six months. A 1000-ppm tellurium standard was prepared by dissolving 0.5000 g of Te metal in 20 ml HNO_3 and diluting to 500 ml with water. The ammonium pyrrolidine dithiocarbamate (APDC)† extractant was dissolved in water and filtered to give a 2% W/V solution. This solution was prepared daily.

The untreated samples consisted of rainwater and raw urine from humans suspected of having been exposed to abnormally large quantities of tellurium. The treated samples were wood drilled from a tree, urine, feces, and air filters which had been previously wet-ashed with nitric and perchloric acids.

Experimental Procedures

Samples were measured into the boats by means of automatic micropipettes of the proper volumes.‡ The precision of these pipettes was about 1% and accuracy was within 2%.

Direct Mount

At least two, but preferably three, identical aliquots of the sample were taken, and known quantities of Pb were added to all but one sample aliquot. Each of the series was then mounted and dried in a sampling boat on a boat drying holder on a hot plate. The volumes of the samples used varied from 0.0125 to 0.40 ml, depending on the concentration of lead present.

Extraction and Mount

Samples were aliquoted and appropriate additions of Pb or Te were made as in the direct method. The volume used in the determination of Te in raw urine was 5.0 ml, while 0.50 ml and 1.0 ml were used in the determination of Pb in wet-ashed fecal and urine samples, respectively.

---

*Fisher Scientific Co., certified atomic absorption standard.
†Eastman Kodak Chemicals.
‡Oxford Sampler Micro Pipetter, Fisher Scientific, or Microliter Pipette Eppendorf, Brinkmann Instruments.

Volumes were increased with water if necessary. The pH of the solution was adjusted to 2.2-2.8 for Pb or 6.2-6.8 for Te with 2M NaOH and 2M HCl. One-tenth ml of 2% APDC was added to raw urine for Te analysis and 0.01 ml to the wet-ashed samples. The samples were mixed for 1 min with 1.0 ml methyl isobutyl ketone (MIBK) and centrifuged for 1 min. Then 0.050 or 0.20 ml of the organic mixture was mounted for the Pb ot Te determination, respectively. Reagent blanks showed no detectable Pb or Te.

Measurements

For lead analysis the spectrophotometer wavelength was set at 283 mm and the slit at 4 (bandpass about 0.65 nm), and for tellurium the wavelength was 213 nm and the slit 3 (bandpass 0.2 nm). The flowmeters on the instrument were set at 6.0 and 6.5 for acetylene and air, respectively. The scale expansion for lead was either 1X or 3X, and for Te it was 1X. The noise suppression was 2 (time constant about 5 sec). (Note--the recorder was zeroed with the boat in the flame for Te determination because of flame absorption at this wavelength.) The sample boat was centered in the holder, the recorder was started (chart speed fast, 5 inches/min), and the boat was swiftly but gently pushed into the center of the flame. The boat was removed when a steady baseline was obtained after the initial peak. The chart was then stopped to reduce unnecessary accumulation of paper.

Results and Discussion

Several problems were encountered in these analyses. First, the sensitivity of the measurements varied from boat to boat by a factor of 2 or more, although in new boats this difference was often only a few percent. This problem was eliminated by making each set of measurements on a sample in a single boat.

A second problem was that the sensitivity was often found to be nonlinear (dependent on sample size), which is important since the method of additions implies a constant sensitivity (within limits) and a linear

extrapolation to zero absorbance. To check the linearity two or more additions were made to each sample. At least two factors had to be taken into account to insure linearity: the sample size must be below that needed to give 50% absorption (an inherent nonlinearity in atomic absorption), and the recorder response time had to be fast enough to follow the signal. With the mechanical 1-sec full-scale response time of the recorder, the sensitivity of the measurements dropped rapidly at 40% full scale of the recorder, even on the expanded 3X scale. This effect could have been reduced by using a faster recorder, or in our case, by using a noise suppression of 5 (5-sec time constant).

The sensitivity of the method was enhanced by the quartz chimney, as shown by measurements of lead in a wet-ashed tree sample. The absorbance increased from 0.025 without the chimney to 0.067 with it, an improvement of more than a factor of 2.5 in sensitivity. Since the background levels were not increased, the detection limits should be improved accordingly to about 0.0004 μg Pb.

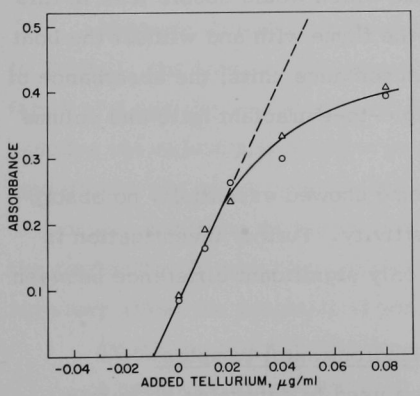

FIG. 1.--Determination of tellurium in urine.

Extraction of Te from Urine

2500 ml of urine were obtained from a subject suspected of being exposed to abnormally high levels of tellurium. This sample was acidified with 100 ml concentrated HNO_3 several days before analysis. Two series of 5-ml samples were run by the extraction method in different boats with 0, 0.05, 0.10, 0.20 and 0.40 μg Te added. The absorption readings of the peaks and the troughs were converted to absorbance and the net difference

plotted against ppm (μg/ml) Te in urine in Figure 1. Extrapolation of the curve to the baseline gave the concentration of Te in the urine. Because of the bending of the curve beyond 0.02 ppm added Te, the extrapolated value of 0.01 ppm Te in the urine should be considered a maximum value, but still probably within 20% of the true value.

Two additional samples of approximately 25 ml each, both from another individual exposed to tellurium, were aliquoted, extracted, and run in the same manner. The samples without added Te gave no detectable peak. Therefore, the concentrations in them were considerably less than 0.01 ppm Te in urine.

Despite the absorption from the flame in this region of the spectrum, the detection limit of the procedure is greater than 0.01 ppm in raw urine[3] probably 0.003 ppm. There is a possibility of improving this either by increasing the volume of urine extracted or by mounting more of the extractant, but the volumes used here appeared to be the practical limit. The sample-to-extractant ratio of 5 to 1 provided a fair amount of precipitate in the organic phase, and at times it was difficult to withdraw the extractant for mounting without including a portion of the precipitate. Another possibility, however, would be to go to a flame which would absorb less in this region. The difference in absorption of the flame with and without the boat present was approximately 13% or 0.06 absorbance units; the absorbance of 0.01 μg (ppm in urine, with present sample-to-extractant ratio and volume of mount) is approximately 0.12.

Initial tests of a hydrogen-air flame showed essentially no absorption, but there was a slight loss in sensitivity. Further investigation is needed to determine whether this is the only significant difference between the use of the two flames.

Direct Determination of Lead in Environmental Samples

The direct method of mounting was used to determine Pb in rain, tree, and air filter samples. The analysis of the rain samples was done by the method of additions, with lead being added to untreated samples. The

tree and air filter samples had been previously wet-ashed. The 17 wood samples from various parts of an oak tree and the 21 air filter samples from Puerto Rico were run in duplicate. For the wood a 0.10-ml aliquot of each sample was mounted. For the air filter a 0.025-ml aliquot of each sample was mixed with an equal volume of lead standard, and 0.025 ml of this volume was mounted. The precision of these analyses on rainwater was estimated from 7 identical aliquots taken from one sample, so that the standard deviation of the mean also represents the precision of the analytical procedure.

The precision of the analysis of the wood, air filter, and rain samples was estimated from the sample

$$S = \sqrt{\frac{\Sigma d^2}{2n}},$$

where d is the difference between the duplicate measurements in each set, and n is the number of duplicate sets.[5] A further measure of precision in cases where there is a variation with sample size is obtained from the mean fractional deviation (the mean value of the ratios of the difference of the duplicates to their respective means).

Although Pb values range from about 0.001 to 0.03 μg Pb/mount, as in Table 1, the standard deviations of the 3 types of samples are within a factor of 4 and the coefficients of variation as based on the means of the samples are essentially equal at about 6%. However, the mean fractional deviation of the wood is twice that of the air filters, a difference which is probably statistically significant ($P < 0.05$). This difference between the coefficient of variation and fractional deviation indicates that sample size may affect the precision of these measurements.

Extraction of Lead from Biological Samples

A series of wet-ashed urine samples was run by both the direct and extraction methods using 0.025 and 1.0 ml aliquots, respectively. The results in mg Pb excreted per day from the direct method, as shown in

TABLE 1. Statistical Data for Rain, Wood, and Air Filter Samples

Sample, Type and Number	Sample Size in Boat, ml	Mean, μg/mount	Standard Deviation, μg/mount	Coefficient of Variation, %	Mean Fractional Deviation, %	Range, μg/mount
Rain A[a] (7)	0.40	0.018	0.0012	6.8	(6.8)	
Wood (17)	0.10	0.0061	0.00035	6	9.6	0.0010-0.0130
Air filters (21	0.025	0.0131	0.00069	5.2	4.8	0.0011-0.0276

[a] Rain A is a set of 7 replicate measurements from one sample

Table 2, were consistently higher than those from the extraction. The higher values of the direct method are believed to be due mainly to the high salt concentrations and the difficulties entailed in mounting and drying of this type of sample. Part of the effect may be due to mass absorption, that is, the salts evaporated into the flame may have sufficient mass to absorb in the Pb resonance region , an effect not compensated for by the method of additions. Precision of the extraction method was estimated from one fecal sample analyzed 4 times, with the results shown in Table 2. The mean of (0.0418 ± 0.0035) μg Pb/mount has a coefficient of variation of 8.3%, which is not significantly different from those of the samples in Table 1.

Conclusion

The variety of samples which has been run to date indicates that with the direct and extraction methods of analysis most biological samples can be analyzed for lead and possibly tellurium using the sampling boat. The precision might be improved by establishing a more routine approach to the method of analysis based on sample type. Lead, like tellurium, can probably be determined by extraction from raw urine, since this is the procedure for analysis. Samples similar to the rains may be done directly without prior treatment, and samples with low salt content, as in the case of the air filters, may be mounted directly without further treatment. However, those with high salt concnetrations, as urine and feces, should first

TABLE 2. Determination of Lead in Urine and Feces by Direct and Extraction Methods

Sample	Extracted mg Pb/day	Extracted µg Pb/ml	Direct, mg Pb/day
Urine			
MB01U01	0.079		0.15
			0.12
MB01U02	0.095		0.12
			0.10
MB01U03	0.064		0.13
			0.12
MB01U04	0.057		0.13
			0.15
MB01U05	0.066		--
MB02U08	0.049		0.16
	0.051		0.22
			0.26
			0.15
			0.11
MB02U12	0.045		0.08
	0.048		0.12
			0.10
			0.08
Feces			
MB07F06	0.39	0.932	
	0.35	0.834	
	0.34	0.804	
	0.32	0.772	
Mean		0.836	
S.D.		±0.069	

be extracted. This facilitates the mounting and drying of the samples, which seems to be the most variable part of the procedure.

These results show that for lead and tellurium, the boat sampling technique can give a precision of 5 to 10%, a very satisfactory reproducibility in many cases, such as the measurement in biological materials. The very high sensitivity is extremely desirable when only small quantities

of materials are available, and it reduces the processing necessary in other cases. The application of extraction to the boat sampling technique opens the possibility of making measurements on samples of high salt content, which would not otherwise be possible.

References

1. Willis, J. B. Determination of Lead and Other Heavy Metals in Urine by Atomic Absorption Spectroscopy. Anal. Chem. 34, 614 (1962).
2. Malissa, H. and E. Schoffman. Über die Verwendung von substituierten Dithiocarbamaten in der Mikroanalyse. III. Mikrochim. Acta 1955, 187 (1955).
3. Kahn, H. L., G. E. Peterson, and J. E. Schallis. Atomic Absorption Microsampling with the "Sampling Boat" Technique. Atomic Absorption Newsletter 7, 35 (1968).
4. Kahn, H. L. and J. S. Sebestyen. The Determination of Lead in Blood and Urine by Atomic Absorption Spectrophotometry with the Sampling Boat System. Atomic Absorption Newsletter 9, 33 (1970).
5. Youden, W. J. Statistical Methods for Chemists. John Wiley and Sons, New York, 1951, p. 16.

QUANTITATIVE CHARACTERIZATION OF BONE. A COMPUTER ANALYSIS OF MICRORADIOGRAPHS

Elizabeth Lloyd and Donald Hodges*

A series of morphological measurements has been made by means of an automatic scanning device which characterizes bone mineral. The results obtained from a large number of measurements of various skeletal sites in man, dog, and mouse bones are reported. The application of these measurements to a number of problems in skeletal metabolism is cited.

Previous reports on bone mineral measurements have been confined to a few samples of bone. In order to characterize bone mineral from a whole skeleton an automatic system of analysis is essential. In addition to the facility for examining a very large number of samples in a very short time (less than a minute per sample) it also becomes possible with an automatic computer system to measure simultaneously a very large number of parameters for the same sample.

Such an automatic scanning device under the control of a computer (CHLOE) for scanning microradiographs of bone sections has already been described.[1] Our previous publications have dealt only with bone surface/volume ratios for a very small number of bones. The present report, therefore, is intended to provide a comprehensive survey of all of the parameters measured for a much larger number of bones. These parameters include bone volume, trabecular thickness, and sizes of marrow cavities. In addition, a comparison is made between values for the human skeleton and those for dogs and mice. This becomes particularly important when we try to extrapolate from the relative biological efficiency for different bone-seeking isotopes in animals to that which we would expect in man.

The amount of marrow irradiated from a radioisotope deposited in bone will depend on the size of the marrow cavities as well as the pattern

*Applied Mathematics Division, ANL.

of deposition and the range of the radiation. In particular it is important to know whether the isotope deposits throughout the whole volume of bone (such as ^{226}Ra) or on bone surfaces (such as ^{239}Pu or ^{241}Am). The relative biological effectiveness will only be the same in man and dog if the bone surface/volume ratio and the percentage of marrow irradiated are the same in both species, if we consider the marrow to be the target tissue for irradiation damage.

Another factor which is of paramount importance in comparing the toxicity of different isotopes in different species is the relative rate of bone turnover in the two species; it would be interesting to know if this is related to surface/volume ratios. In addition to the problem of relative toxicity of radioelements, measurements of bone mineral are important for the diagnosis of bone diseases. In studying small biopsy samples of bone it is important to know the variation in structure in different bones in the same normal individual as well as the type of variations to be expected due to small differences in positioning of the exact sampling location.

For the purpose of our study we obtained all the bones of a human skeleton of an Asian male in his mid-forties. The total skeletal dry, fat-free weight was 3.6 kg. The relative weights of the individual bones are given in Table 1. For comparison values are also given in the table for the average values of 10 adult male skeletons described by Trotter and Peterson.[2] As we can see from the table the relative values for the weight of different bones of the skeleton are very similar to the normal average values. From these data, together with the fact that no abnormalities were observable, it was concluded that the skeleton was representative of a normal male adult.

Experimental Methods

Individual bones from the adult skeleton were cut into convenient sizes, usually about 5 cm in length, for embedding in methyl methacrylate. Sections 100 μ thick, and less than 1 inch square, were cut from these

TABLE 1. Relative Weights of Individual Bones Taken from the Whole Skeleton

Bone	Weight, % of Whole Skeletal Weight: Trotter and Peterson[2] (Av. 10 adult Skeletons)	Lloyd (1 Skeleton)
Skull	17.1	18.9
Femora, tibia, fibulae	32.0	31.0
Humeri, radius, ulna	11.9	10.0
Vertebrae	10.5	13.2
Ribs	6.3	6.3
Other Bones (including hands, feet, and innominate bones)	22.2	20.6
Total	100	100
Total skeletal weight, kg	3.86	3.59

pieces. The sections were x-rayed using a Machlett x-ray tube with a tungsten filament, operated at 5 keV and 20 mA. The section was mounted in close contact with a high contrast film (Eastman Kodak, fine grain, positive). This was loaded into a 35-mm camera attached to the exit port of the x-ray tube. A typical exposure for a 100-μ thick section was 4 min. The film was developed in a high contrast developer (dextrol, 1:1 dilution) for 1-1/2 min.

The 35-mm film used here had several advantages over more conventional spectroscopic plates. First, scanning of the film to determine the perimeter and area was greatly facilitated by obtaining maximum contrast between the bone (white areas) and those areas where bone was absent (black areas). Second, 35-mm film made possible the automatic scanning of a large number of pictures on a roll of film; the computer program provided for film advance under the control of an on-line typewriter.

Scanner

The automatic scanner (CHLOE) was designed for the study of spark

chamber photographs. A detailed description of its design and operation is given elsewhere;[3,4] for the sake of completeness, a very brief summary of the operation is included here.

A spot of light (about 25 μ in diameter) generated by a cathode ray tube is focused into the film, and the transmitted light is detected by a photomultiplier. The light spot moves in discrete steps in the x direction, then returns to make successive scans. The separation of these scans can be varied by factors of 2 down to 7 μ. All parameters of the scan, including the rectangular boundaries of area scanned, are under the control of the on-line typewriter. The scanner system records the coordinates of the point at which the light spot detects a change from black to white or from white to black. A pair of such points marks the beginning and end of a line segment parallel to the x axis. The equipment can be programmed so that the line segments lie over either white areas on a black background or black areas on a white background.

Area

The area of bone is measured by taking the sum of the length of all line segments lying over the white area of a microradiograph and multiplying by the vertical separation between scans. Figure 1 shows the line segments over a small portion of trabecular bone. The line segment length in each linear scan is obtained by subtracting the x coordinates of the beginning and end of each line segment when scanning in the x direction. These are summed for all of the line scans--up to 2^{12} (4096) per inch. The scanning area is calibrated by using a 2-mm grid on 35-mm film and counting the number of scanning lines in each of the x and y directions corresponding to a known grid size.

Perimeter

The perimeter of bone, P, was determined by a computer calculation of the distance between the end points where successive line scans intersect the bone. This does not involve the assumption of random shapes as is implicit in the formula of Hennig[5] based on the number of line

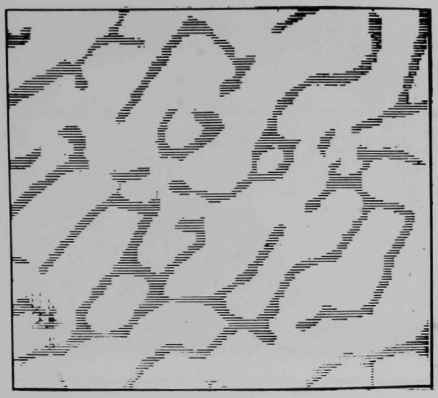

FIG. 1.--Computer printout of line segments over a small portion of trabecular bone.

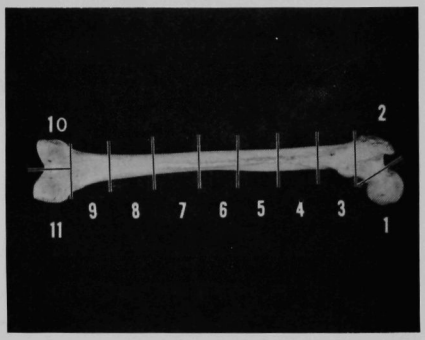

FIG. 2.--Human femur showing the eleven segments into which the bone was cut for sampling.

segments.

Surface/Volume Ratios

When cortical bone is measured, the ratio for surface/volume is identical to the two-dimensional ratio of perimeter/area because the bone surfaces in a cross section are not randomly oriented but lie predominantly parallel to the long axis of the bone. For trabecular bone, however, the orientation is more random and the difference between the two-dimensional and the three-dimensional ratio requires a correction factor of $4/\pi$. This factor and the reason for its use is discussed fully in the Appendix. This means that the values reported in our earlier paper for perimeter/area have to be increased by a factor of 1.273 to give the correct values for the surface/volume ratios for trabecular bone, although the surface/volume values for cortical bone are the same as those reported for perimeter/area. Table 2 shows a typical typewriter printout from the computer for an automatic scan of a bone section (rib).

Results

Femur: Cortex

The femur was segmented as shown in Figure 2. Figure 3 shows

TABLE 2. Typewriter Printout from the Computer of the Values Obtained from the Automatic Scan of a Microradiograph of the Rib[a]

```
H CS*10 75 x 12 Y 12 I 913WOB    RR6G22 PIC 164
NL 6679
LL/8  31629
P 015.729 CM
A 0.14233 CM.CM
TA 1.79712 CM.CM
FA 0.07920
ALS 284 MICRONS
P/A  110.513  CM/CM.CM
```

[a] The first line refers to the conditions of measurement and the picture designation.

NL = number of line segments.
LL = length of line segments.
P = Perimeter.
A = area.
TA = total area scanned.
FA = fractional area over bone.
ALS = average line segment length.
P/A = perimeter divided by area.

TABLE 3. Perimeter, Area, and Surface/Volume Ratios of Cortical Bone from the Midshaft of the Femur

Section Number	Perimeter, cm	Area, cm^2	Surface/Volume, cm^2/cm^3
RF 1	7.6	0.23	34
RF 2	9.6	0.32	31
RF 3	8.2	0.30	27
RF 4	4.0	0.13	30
		Mean	30

Haversian canals and resorption cavities seen in the microradiograph of cortical bone taken from segment 4 (Figure 2). Figure 4A is an enlargement of the "boxed" area of bone indicated in Figure 3, and Figure 4B is a computer printout of the line segments generated over the holes seen in the microradiograph. The separate line segments are not visible because the line spacings are only 7 μ apart. Table 3 gives values for the perimeter, area of bone studied, and surface/volume ratios for four different areas in

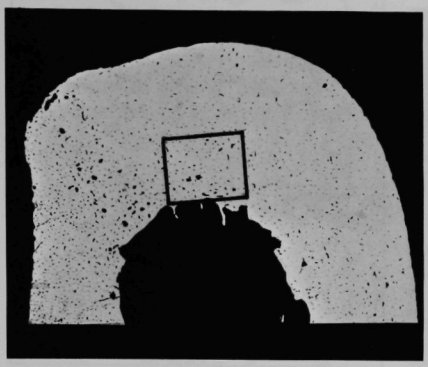

FIG. 3.--Microradiograph of a cross section of bone taken from the mid-cortex of the femur.

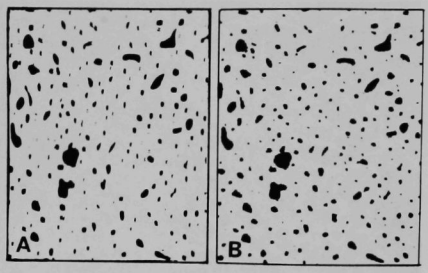

FIG. 4.--(A) Microradiograph of the portion of bone indicated in Figure 3 shown at a higher magnification. (B) Corresponding printout to the microradiograph.

the cortex. As already mentioned, the surface/volume ratio is numerically equal to perimeter/area for cortical bone. These measurements do not include the periosteal and endosteal surfaces. Separate measurements indicate that these surfaces add about 10% to the values listed.

Femur: Head

Figure 5A shows the microradiograph and 5B the computer printout of the square indicated in Figure 5A of a section taken from segment 1 of Figure 2. Table 4 gives values obtained for eight sites taken from this bone segment. As previously mentioned, and discussed later, the surface/volume ratio is obtained by multiplying the perimeter/area by 1.273.

Vertebra

Figure 6 shows a thin section taken from a thoracic vertebra. The "boxed in" area indicates the region over which the measurements were made. Values are given in Table 5 for the perimeter, area and surface/volume ratios for the "boxed in" portions of bone taken from eight different sections. In Table 6 the effect of including the whole bone is given for the same sections. When the cortex of the bone is included, the surface/volume ratios are reduced by about 5% from the values obtained for pure trabecular bone. Average values for the length of the line segments over bone

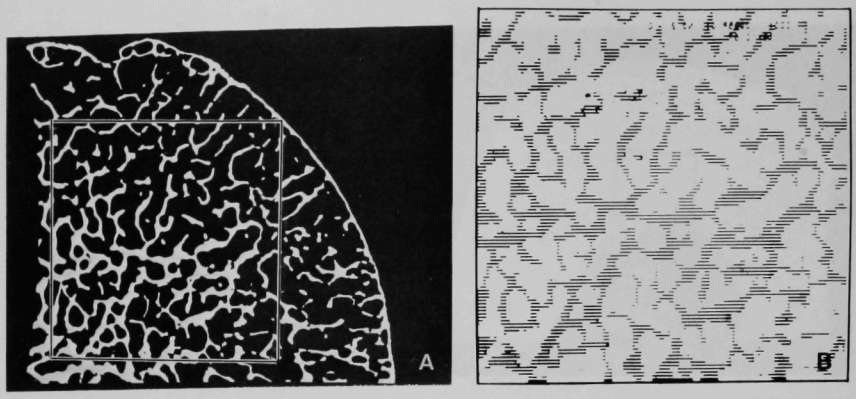

FIG. 5.--(A) Microradiograph of a portion of bone taken from the head of the femur. (B) Computer printout of the portion of the bone indicated in the micrograph.

are given in Table 7, both for the horizontal and vertical directions of each scan. These values refer to pure trabecular bone. As expected, the line segments are about 25% less in the horizontal direction than in the vertical scans, the average values for the line segments in the horizontal direction being about 300 μ. However, the variations in average line segment lengths for the eight sections was about a factor of two (200 to 400 μ).

Table 8 gives the corresponding values made over the marrow cavities. Again as expected the horizontal scans show average line segment lengths about 25% less than those found in the vertical scans. These values (~ 800 μ) are about two to three times the values obtained for the segment lengths over the bone, which fits well with a fractional volume of bone in any section being about 25% of the total volume. Exact measurements of fractional bone volume were made for the third lumbar vertebra. These are given in Table 9 and show variations between 20% and 36% for serial sagittal sections. Values for perimeter, area, and surface/volume ratios for the third lumbar vertebra are also given in Table 10. The surface/volume ratios appear to be of the same order as those found for the thoracic vertebra, although they are about 15% higher than those for the

TABLE 4. Perimeter, Area, and Surface/Volume Ratios of Trabecular Bone from Head of Femur (Segment 1).

Section Number	Perimeter, cm	Area, cm^2	Perimeter/Area cm/cm^2	Surface/Volume cm^2/cm^3
Ba 5	48	0.65	74	94
Ba 7	47	0.58	81	103
Ba 10	28	0.34	81	103
Ba 13	11	0.15	70	89
Bb 4	51	0.70	73	93
Bb 7	44	0.63	70	89
Bb 9	37	0.46	79	100
Bb 12	23	0.30	77	98
		Mean	76	96

TABLE 5. Perimeter, Area, and Surface/Volume Ratios in Sagittal Sections of Trabecular Portion of Bone from Human Thoracic Vertebra (Number 7).

Section Number	Perimeter, cm	Area, cm^2	Perimeter/Area cm/cm^2	Surface/Volume cm^2/cm^3
TV 7-A120	46.5	0.57	82	104
A121	40.6	0.32	127	162
A122	45.7	0.52	88	112
A123	45.8	0.48	95	120
A124	45.7	0.43	106	135
A125	45.2	0.55	82	104
A126	42.7	0.51	84	107
A127	46.8	0.71	66	84
		Mean	91	116

head of the femur (Table 4). Average values for the line segment length over bone are given in Table 11. The average value for the horizontal measurements is 300 μ. This is the same as that found for the thoracic vertebra.

Rib

The sixth rib was first cut into seven segments along its length, each segment being about 4.5 cm long. Measurements of 40 different cross

TABLE 6. Effect of Region Scanned on Values of Perimeter, Area, and Surface/Volume Ratios of Sagittal Sections of Thoracic Vertebra (Number 7).

Section Number	Whole Portion				Trabecular Portion			
	Perimeter, cm	Area, cm^2	Perimeter/Area, cm/cm^2	Surface/Volume, cm^2/cm^3	Perimeter, cm	Area, cm^2	Perimeter/Area, cm/cm^2	Surface/Volume, cm^2/cm^3
TV 7-A120	124	1.60	77	99	46.5	0.57	82	104
A121	126	1.02	123	156	40.6	0.32	126	160
A122	126	1.58	80	102	45.7	0.52	88	112
A123	130	1.48	88	112	45.8	0.48	94	120
A124	129	1.43	91	116	45.7	0.43	105	134
A125	125	1.57	79	101	45.2	0.55	82	105
A126	111	1.52	73	93	42.7	0.51	84	107
A127	105	1.52	69	88	46.8	0.71	66	84
			Mean 85	108			91	116

TABLE 7. Average Length of Line Segments (in Microns) over Bone in Human Thoracic Vertebra

Section Number	Vertical Scan	Horizontal Scan
A 120	451	302
A 121	302	197
A 122	407	289
A 123	369	269
A 124	328	247
A 125	399	322
A 126	411	310
A 127	531	384
Mean	400	296

TABLE 8. Average Length of Line Segments (in Microns) over Bone in Human Thoracic Vertebra (Number 7).

Section Number	Vertical Scan	Horizontal Scan
A 120	915	627
A 121	1223	843
A 122	938	677
A 123	965	695
A 124	960	743
A 125	875	699
A 126	983	763
A 127	784	579
Mean	955	703

TABLE 9. Percentage Volume of Bone Mineral in Trabecular Bone Tissue of the Human Third Lumbar Vertebra

Section Number	% Bone Volume
131	25.2
132	27.9
133	27.2
134	24.5
135	36.0
136	27.9
137	24.5
138	19.7
139	24.5
140	29.9
Mean	26.7

TABLE 10. Perimeter, Area, and Surface/Volume Ratios of Bone Mineral in the Human Third Lumbar Vertebra

Section Number	Perimeter, cm	Area, cm^2	Perimeter/Area, cm/cm^2	Surface/Volume, cm^2/cm^3
131	36.9	0.37	97	124
132	39.1	0.41	93	119
133	39.2	0.40	98	125
134	37.9	0.36	104	133
135	42.8	0.53	79	99
136	37.9	0.41	91	116
137	34.9	0.36	96	122
138	33.7	0.29	113	143
139	32.9	0.36	90	115
140	35.9	0.44	82	105
		Mean	94	120

TABLE 11. Average Line Segment Length (in Microns) over Bone and Marrow in the Human Third Lumbar Vertebra

	Bone		Marrow	
Section Number	Vertical Scan	Horizontal Scan	Vertical Scan	Horizontal Scan
131	365	286	1027	756
132	374	299	925	697
133	358	287	925	702
134	345	265	1040	742
135	432	360	748	581
136	383	308	958	735
137	336	315	1034	864
138	325	240	1213	859
139	371	327	1087	882
140	480	317	1100	702
Mean	377	300	1006	752

TABLE 12. Perimeter, Area, and Surface/Volume Ratios in Cross Sections of Bone Taken from Different Positions along the Length of a Human Rib.

	Section Number	Bone Area, cm^2	Bone Perimeter, cm	Perimeter/Area cm/cm^2	Surface/Volume cm^2/cm^3
Sternal end	8	0.16	28	176	195
	9	0.18	29.3	163	184
	10	0.13	25.1	193	218
	11	0.14	24.9	178	201
	13	0.11	19.4	176	199
	15	0.13			
	17	0.10	16.5	165	186
	19	0.13	15.2	117	132
	20	0.10	14.8	148	167
	21	0.12	15.2	127	144
	22	0.13	14.0	108	122
	25	0.13	17.3	135	153
	26	0.14	14.9	106	120
	28	0.14	15.1	107	121
	30	0.16	12.8	80	91
	31	0.16	13.1		
	34	0.16	14.7	92.0	104
	35	0.17	14.5	85.0	96
	38	0.16	15.1	94.4	107
	39	0.16	14.7	92.1	104
	42	0.18	14.8	82	93
	43	0.18	13.3	73	83
	45	0.22	17.1	77	88
	46	0.21	16.7	79	90
	49	0.20	16.4	82	93
	50	0.20	16.8	84	95
	52	0.23	20.0	87	98
	53	0.21	19.7	94	106
	55	0.24	19.8	82.5	93
	56	0.24	19.6	81.5	92
	60	0.36	15.5	43	48
	61	0.36	14.8	41	46
	63	0.34	12.9	38	43
	64	0.33	12.9	39	44
	66	0.27	14.8	55	62
	68	0.27	18.1	67	76
Vertebral end	72	0.25	21.0	84	95

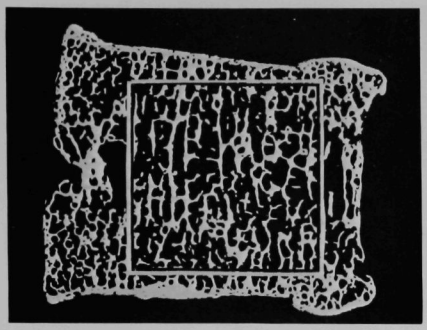

FIG. 6.--Microradiograph of the seventh thoracic vertebra.

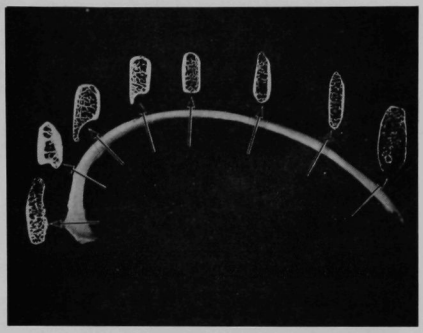

FIG. 7.--Picture of the sixth rib showing the appearance of microradiographs made from thin sections of bone from different locations.

sections were made.

Figure 7 demonstrates the appearance of microradiographs of the cross sections of bone taken at the junction of each of the seven segments. It is interesting to note that close to the costal cartilage junction the cortex is very thin, and this encloses a large number of very fine trabeculations. About 5 cm from the vertebral end the cortex is very much thicker and the trabeculations are fewer and coarser. Values for the cross-sectional area together with the surface length or perimeter of each of the bone sections studied is given in Table 12. Values of perimeter/area and surface/volume ratios are also listed. The correction factor applied to convert from perimeter/area to surface/volume was 1.13 instead of 1.27 used for pure trabecular bone, on the basis that about 1.2 of the bone was cortical.

The sections were numbered starting with number 1 taken from the sternal end of the rib and ranged up to number 72 taken from the vertebral end. The bone area changes from 0.10 cm^2 to 0.36 cm^2 while the perimeter changes from 12.9 cm to 29 cm. The bone area is greatest about 5 cm from the vertebral end where the cortex is thickest. The perimeter is small at this point, giving a value of 43 cm/cm^2 for perimeter/area (P/A) compared

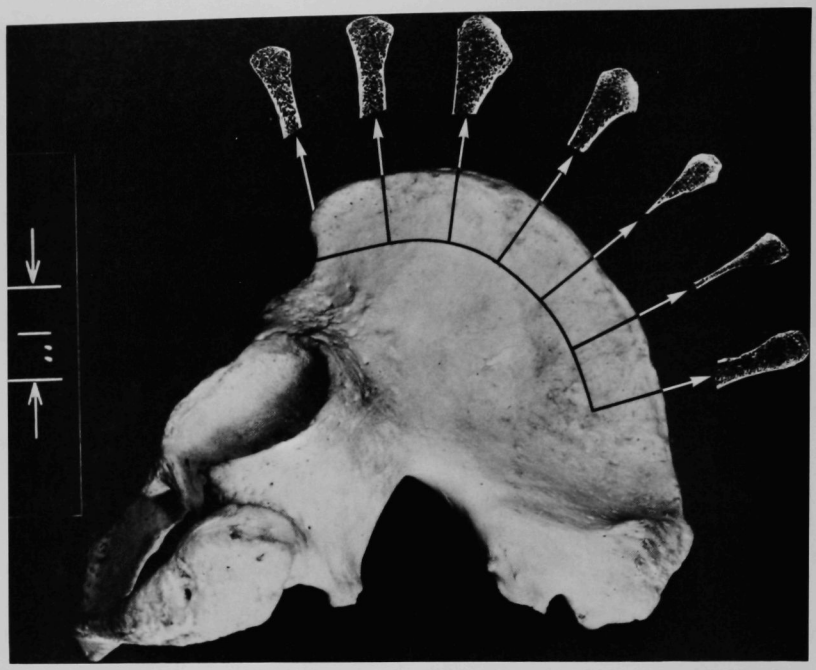

FIG. 8.--Picture of the iliac crest showing the appearance of microradiographs made from thin sections of bone from different locations.

with a value about 5 times greater obtained for a section taken close to the sternal end. The mean marrow space taken from a section about the middle of the rib measured 1200 μ, and the width of the trabeculae at this site averaged about 100 μ.

Iliac Crest

Figure 8 illustrates the cuts which were made to study the iliac crest. Examples of microradiographs taken from sections along its length are also shown. Table 13 gives values for pure trabecular bone together with values obtained for the whole bone section. Values for the whole bone are about 30% lower than those for the central portion of pure trabecular bone. The percentage volume of bone is very similar to that obtained for the third

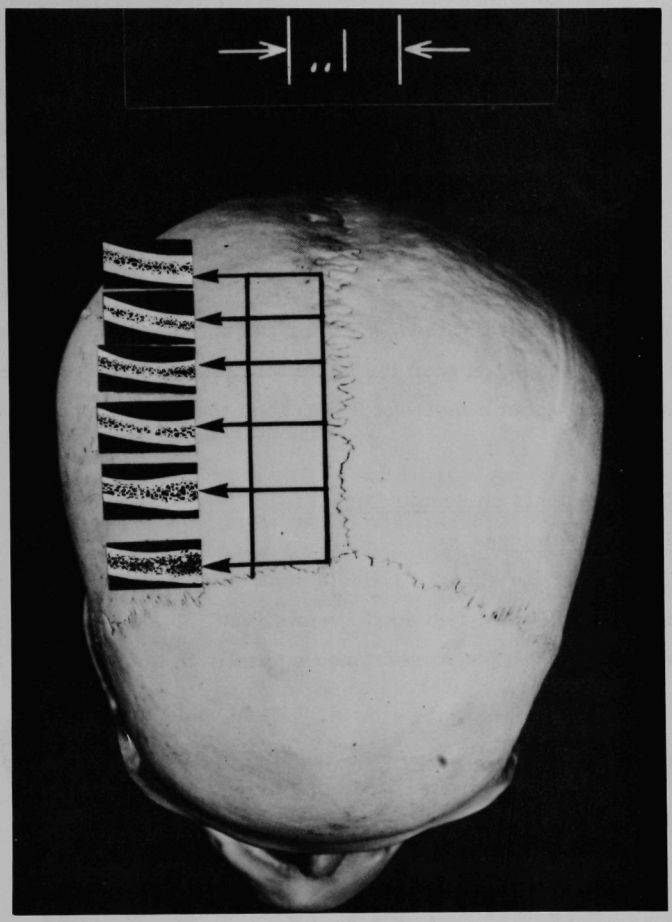

FIG. 9.--Picture of the human cranium showing the appearance of microradiographs made from thin sections of bone from different sites.

lumbar vertebra, being about 25%. The mean value for the trabecular thickness was 150 μ, and the average segment length of the marrow spaces was about 800 μ in a section taken about 2 cm from the anterior superior iliac spine. These values are very similar to those obtained for the thoracic

vertebra, except that the trabeculae are somewhat thinner.

Cranium

Sections of the cranium were studied at 2-cm intervals starting at the bregma and moving posteriorly parallel to the coronal suture as shown in Figure 9. Typical microradiographs taken at different sites are also illustrated. Table 14 gives values for the perimeter and area together with values for the surface/volume ratios. The correction factor of 1.13 was used to convert from perimeter/area to surface/volume. The average value for surface/volume ratio of the 9 sections measured was 41 cm^2/cm^3. This value is somewhat greater than the value for cortical bone from the midshaft of the femur, but about a factor of 3 less than the trabecular bone of the iliac crest.

Measurements on Beagle Dogs

Lumbar Vertebrae

The lumbar vertebrae of 3 beagle dogs (kindly given us by Dr. Webster Jee, University of Utah), two aged 2 years (MAC 56 and MAC 58) and one aged 3 years (MAC 71), were sectioned sagitally in the same way as the

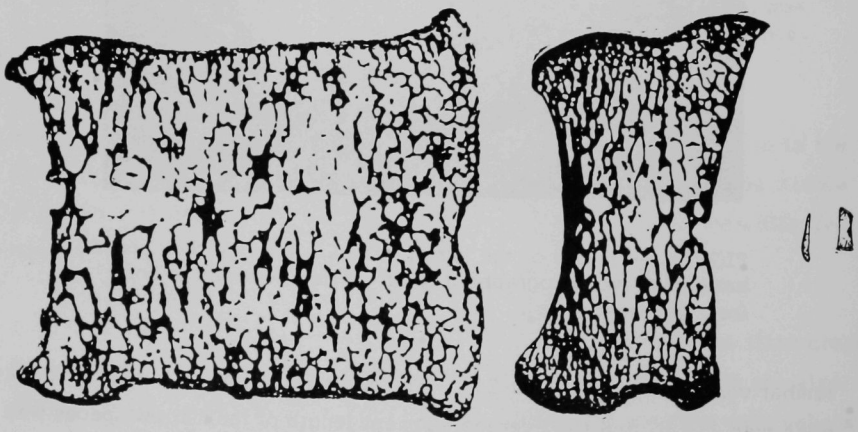

FIG. 10--Comparison of microradiographs of thin sections of bone from the vertebrae of the human, dog, and mouse skeleton.

TABLE 13. Perimeter, Area, Perimeter/Area, and Surface/Volume Ratios for Iliac Crest

Section Number	Perimeter, cm	Area, cm^2	Perimeter/Area, cm/cm^2	Pure Trabecular Surface/Volume, cm^2/cm^3	% Volume	Whole Section Surface/Volume cm^2/cm^3
3	24.1	0.183	131	167	27.8	121
6	36.0	0.244	148	188	24.6	113
8	26.1	0.204	128	162	27.5	98
11	37.6	0.258	146	186	22.9	113
16	22.0	0.202	109	139	30.4	115
17	14.4	0.088	163	207	18.8	135
23	21.0	0.125	169	215	22.5	136
25	10.2	0.057	180	229	23.3	120
30	11.2	0.076	148	188	32.3	113
32	11.3	0.069	164	209	26.8	115
37	14.0	0.063	223	284	20.7	146
38	31.8	0.162	197	251	18.6	155
			Mean	183	24.6	123

human lumbar vertebrae. Figure 10 shows sagittal sections from the vertebrae of man, dogs, and mouse at the same magnification. Values for the surface/volume ratios for two sections from each dog are given in Table 15. The percentage volume of bone for the whole bone section and for a "boxed in" portion of trabecular bone, excluding the cortex, are also given. The values for the surface/volume ratios (about 200 cm^2/cm^3) are 50 to 100% higher than the values obtained for the human; values of the percentage bone volume within the cortex (about 40%) are also greater by about the same amount. Correspondingly values for the average line segment lengths over the marrow spaces (300 μ) are much less than in the human vertebrae (about 800 μ). In the dog average values for line segment lengths over bone and over the marrow spaces are of the same order (Table 16), unlike the situation in humans where the segment lengths over the marrow spaces are in general two or three times the segment lengths over the bone.

Measurements on Mice

Lumbar Vertebrae

So far the measurements on mice (see Figure 10) have been confined to a very few sections; however, even for these few sections it is obvious that the surface/volume ratios are even larger than for the dog. Average values range between 250 and 350 cm^2/cm^3. The trabecular thickness is

TABLE 14. Perimeter, Area, and Surface/Volume Ratios of Bone from the Cranium of a Human Adult

Section Number	Perimeter, cm	Area, cm^2	Perimeter/Area cm/cm^2	Surface/Volume cm^2/cm^3
B 111	36.3	1.04	34	38
B 112	29.5	0.88	33	37
B 113	25.7	0.91	28	32
B 114	34.1	0.97	35	40
B 115	35.6	0.93	38	43
B 116	35.0	0.93	37	42
B 117	33.2	0.92	36	41
B 123	43.0	1.07	40	45
B 124	49.9	1.04	47	53
			Mean	41

TABLE 15. Surface/Volume Ratios and Percentage Bone Volume in the Lumbar Vertebrae of 3 Dogs

Dog No.	Section	Whole Bone Section Surface/Volume, cm^2/cm^3	Whole Bone Section % Bone Volume	Trabecular Bone Excluding Cortex Surface/Volume cm^2/cm^3	Trabecular Bone Excluding Cortex % Bone Volume
56	A	125	52	181	43
56	B	124	55	180	43
58	A	152	38	248	30
58	B	180	36	268	25
71	A	174	58	245	35
71	B	120	54	228	32
	Mean	146	49	225	35

TABLE 16. Line Segment Lengths over Bone and Marrow Spaces in the Lumbar Vertebrae of 3 Dogs

Dog No.	Section	Bone Average Line Segment Length, μ Horizontal	Bone Average Line Segment Length, μ Vertical	Marrow Average Line Segment Length, μ Horizontal	Marrow Average Line Segment Length, μ Vertical
56	A	320 (212)[a]	420 (300)	240	330
	B	325 (218)	430 (311)	240	330
58	A	270 (162)	350 (218)	320	440
	B	220 (139)	320 (226)	380	610
71	A	230 (165)	310 (220)	250	340
	B	330 (171)	460 (254)	310	450
	Mean	282 (177)	382 (255)	290	417

[a] Figures in brackets refer to the bone excluding the cortex.

TABLE 17. Comparison of Different Parameters Measured in Different Trabecular Bones of the Same Individual

Parameter	Iliac Crest	Thoracic Vertebra	Lumbar Vertebra	Head of Femur
% Bone Volume	25	29	27	30
Surface/Volume Ratio of Bone Mineral, cm^2/cm^3	180	120	120	100
Line Segment[a] Length over Bone, μ	220 (H) 290 (V)	300 (H) 400 (V)	300 (H) 380 (V)	300 390
Mean	255	350	340	345
Line Segment Length over Marrow Cavities, μ	650 (H) 880 (V)	700 (H) 950 (V)	750 (H) 1010 (V)	700 950
Mean	765	825	880	820

[a] H refers to horizontal scan; V refers to vertical scan.

much smaller, in the region of 80 μ, for an adult mouse (5 months old).

Femur

Provisional measurements on the femur cortex of mouse suggest that the surface/volume ratio is about 30 to 40 cm^2/cm^3. This value appears to be about the same as in the dog and in man.

Discussion

The measurements reported here have been made to characterize bone. The results of these measurements have immediate application in the calculation of:

1. Quantitative structural differences between bones of the same skeleton.
2. Bone turnover rates.
3. Radiation doses from bone-seeking isotopes.
4. The fraction of the total bone surface in cortical and in trabecular bone.
5. The relative biological effectiveness of surface and volume bone seekers in animals and in man.
6. Exchangeable bone calcium.

There is no doubt that many other applications of these measured parameters will be made, perhaps in areas we have not foreseen. For this reason we have tabulated our data in full for others to use in their own calculations.

Quantitative Structural Differences between Bones

In the human skeleton cortical bone taken from different sites appears to show very little difference in structure. More work, however, needs to be done to provide a realistic range of values to cover the extent of the variation found between different cortical bones. It is an interesting finding that in both dog and mouse bone the values obtained for the surface/volume ratio of cortical bone are of the same order as those found in human cortical bone (30 cm^2/cm^3).

For trabecular bone, as far as is known, there are no published data

on the quantitative structural differences of different cancellous bones taken from the same skeleton. Table 17 was, therefore, compiled to show typical values for four different trabecular bone sites.

Perhaps the most significant feature in this comparison is the similarity rather than the differences in the average values for each parameter for different trabecular bones, even though as seen in the preceding tables there is a wide variation between samples taken from the same bone. The percentage volume of the bone within the cortex of the iliac crest, lumbar and thoracic vertebrae, and the head of the femur are all of the same order, between 25 and 30%. The surface/volume ratios fall within the range of a factor of two (100-180). The average trabecular line segment widths also fall within a factor of two (220-330 μ for all the horizontal scans and 290-400 μ for the vertical scans).

Although no published data are available on comparisons between different cancellous bones in the same individual, there are quite a lot of published data on the physical characteristics of the lumber vertebrae. Some of these studies have involved sampling of a large number of vertebrae

TABLE 18. Summary of Published Data on Normal Human Lumbar Vertebrae

Source	% Bone Volume[a]	Sample Thickness	Perimeter/Area, cm/cm^2	Surface Area/ Volume Bone Mineral, cm^2/cm^3	Surface Area/ Volume Bone Tissue, cm^2/cm^3
Dyson et al.[9]	13.5 (1)	Surface only	165	207	28
Dunhill et al.[6]	25 (30)	?	-	-	-
Amstutz and Sissons[10]	25 (avg. 4 areas in 1 vert.)	27 μ	-	147	33
Atkinson[7]	69 (calc.) (28)	2.5 mm	-	-	-
Bromley et al.[8]	15 (7)	8 μ	100	127	19
Lloyd (present study)	27 (1)	100 μ	94	120	32

[a] Number of cases in parentheses.

from different postmortem samples to determine changes with age, sex, and disease.[6,7,8] Table 18 summarizes the values obtained by other workers together with the values obtained in the present study. For purposes of comparison with our studies only those normal cases in the age group 20 to 50 were selected. The number of vertebrae studied and the thickness of the sections used are given in the table.

From the table we see that values for the percentage bone volume reported by all the authors for normal human lumbar vertebrae lie between 13.5 and 33% apart from one value of 69% calculated from the porosity values given by Atkinson.[7] This high value may be the result of the method of measurement, which involved using radiographs of very thick sections (2.5 mm thick). It would appear that projection of the thickness of the section would lead to an overestimate of values for bone volume. In our work we were unable to demonstrate any difference in our bone volume measurements between sections which were 30 μ and 100 μ thick. The preparation of much thinner sections, it was felt, carried the risk of cracking or total loss of some spicules of bone. Our value of 25% for bone volume, therefore, appears to lie within the normal range of values reported by other authors.

Values reported for surface/volume ratios of bone mineral in the vertebrae are also given in Table 18. Our value is in good agreement with the value given by Amstutz and Sissons[10] and that reported by Bromley et al.[8] but is almost a factor of two lower than the value of Dyson et al.[9] Values for the surface area of bone per unit of bone tissue volume are also given in the table. These values are obtained by multiplying the surface area/unit volume of bone mineral by the fraction of bone volume. Our value of 32 cm^2/cm^3 is within the range of the values reported by others (19-33 cm^2/cm^3). Measurements on the iliac crest have also been made on a large number of cases by Wakamatsu and Sissons,[11] who report an average value for the percentage of bone volume of 23%, which is in good agreement with our value of 25%. However, no values are available in their

publication for line segment lengths over bone and marrow; instead they have defined another parameter, "trabecular bone thickness," which will always be smaller than our measurements of bone segment lengths.

Other bone sites for which values should be available soon include radius, ulna, phalanx, temporal bone, clavicle, sternum, and os calcis.

Relation of Bone Mineral (Surface/Volume) Ratios to Bone Turnover

If we know the percentage of bone surface which is involved in bone formation, then knowing the surface/volume ratio of bone mineral together with the linear apposition rate, we can calculate the percentage bone turnover.

In the midshaft of the adult femur, Jowsey et al.[12] found that 3% of the bone surface was involved in bone formation. If we assume a linear growth rate of 1 μ (10^{-4} cm) per day[13] together with our surface/volume ratio of 30 cm^2/cm^3, then the fractional volume, F, of cortical bone formed per day will be

$$F = \frac{3}{100} \times 30 \frac{cm^2}{cm^3} \times \frac{10^{-4} cm}{day}$$

$$= 9 \times 10^{-5}/day,$$

i.e., 0.009%/day or 3.3%/year.

This value is in good agreement with measurements reported by Frost[14] using tetracycline labeling. It is also in close agreement with values reported by Rowland,[15] which were derived from long-term radium studies. An average value of 7.4% for the percentage of bone-forming surface in the iliac crest has also been reported.[12] Using this value together with our surface/volume ratio of 180 cm^2/cm^3 and 1 μ/day linear apposition rate (a value found by Lee[13] to be the same as in cortical bone), we can calculate the fraction, F, of trabecular bone formed per day.

$$F = \frac{7.4}{100} \times \frac{180\ cm^2}{cm^3} \times \frac{10^{-4} cm}{day} = 1.33 \times 10^{-3}/day,$$

i.e., 0.133%/day or 48.6%/year.

No reliable results for trabecular bone turnover from tetracycline labeling have been reported; however, the relative rates of trabecular and cortical turnover can be inferred from radioactive tracer experiments. In a ^{45}Ca tracer experiment in rabbits we found the rate of bone turnover in the trabecular bone (vertebrae)[16] to be about a factor of 4 higher than in cortical bone.

Values obtained for the concentration of ^{226}Ra in different human bones from the MIT series[17] and plotted as a function of time after intake[18] also suggest about the same difference in relative turnover rates between trabecular and cortical bone. Hence, one might expect values of about 12 to 15%/year for trabecular bone turnover compared to the value of about 50% calculated here from the percentage bone surface involved in bone formation. This divergence could result from an accumulation of errors, all tending to make the calculated value too high. Such a set of circumstances would arise if 1) the linear growth rate of 1 μ/day were too high, 2) the surface taking part in bone formation were overestimated, 3) the rate of turnover in the iliac crest is greater than the rate of turnover in the vertebrae. Measurements for the surface/volume ratio of the iliac crest reported here (180 cm^2/cm^3) appear to be in excellent agreement with those found by Sissons et al.[19] (183 cm^2/cm^3 for cases aged 20 to 50). Hence, it is unlikely that the error in the calculation is due to an error in the surface/volume ratio.

Calculation of Radiation Doses from Bone-Seeking Isotopes

In radiation protection work the important tissues for the consideration of radiation damage from bone-seeking isotopes are thought to be the red bone marrow found in trabecular cavities and the osteoprogenitor cells which lie close to bone surfaces. Previous calculations have been made of the doses from trabecular bone containing $^{90}Sr + {}^{90}Y$ by approximating different bone shapes and sizes to spheres and slabs.[20] More recently, however, Spiers[21] has evolved a much more rigorous method for calculating the radiation dose for β emitters by assuming that β particles travel in

straight lines. By calculating the energy losses of the ionizing particles as they cross the linear path lengths through bone and marrow, the dose to the bone surface cells and the marrow can be obtained. The lengths of line segments over bone and marrow given here should be directly applicable to these calculations and allow better estimates to be made of doses to a large number of different sites for all the important radionuclides which deposit in bone.

Estimation of Total Bone Surface in Cortical and Trabecular Bone

If we assume that the weight of the average wet fat-free skeleton is 4.5 kg and the density of the wet bone mineral is 2 g/cm^3, we can calculate the amount of bone surface in cortical bone and in trabecular bone on the basis that 80% of the skeleton is cortical and 20% trabecular.

The surface area of cortical bone

$$= \frac{80}{100} \times \frac{30\ \text{cm}^2}{\text{cm}^3} \times \frac{4500\ \text{g}}{2\ \text{g/cm}^3} = 54{,}000\ \text{cm}^2$$

or 5.4 square meters.

Correspondingly, the surface area of trabecular bone is

$$\frac{20}{100} \times \frac{130\ \text{cm}^2}{\text{cm}^3} \times \frac{4500\ \text{g}}{2\ \text{g/cm}^3} = 5.8 \text{ square meters.}$$

This leads to a value of 11.2 square meters for the total bone surface, about half in trabecular bone and the other half in cortical bone. An average value for surface/volume ratio for the whole skeleton combining the figures for cortical and trabecular bone is

$$\frac{80}{100} \times \frac{30\ \text{cm}^2}{\text{cm}^3} + \frac{20}{100} \times \frac{130\ \text{cm}^2}{\text{cm}^3} = 50\ \text{cm}^2/\text{cm}^3 .$$

This figure allows for a calculation of total bone surfaces to be made if the skeletal fat free weight can be estimated from body weight.

Extrapolation of the Relative Biological Effectiveness of Surface and Volume Bone Seekers in Animals to that Expected in Man

Our best estimations of maximum permissible doses of bone-seeking isotopes are based on a comparison with radium toxicity in man. For this reason, many experiments have been designed to relate the toxicity of different radioisotopes in experimental animals to radium. If, however, we compare the relative toxicity of a surface seeker such as ^{239}Pu to the volume seeker ^{226}Ra in the beagle in the absence of other modifying factors, one would only expect the relationship to be the same if the surface/volume ratio in the two species were the same.

The total skeletal surface/volume ratio for the beagle dog calculated in the same way as shown above, using 40 cm^2/cm^3 for cortical bone and 225 cm^2/cm^3 for trabecular bone (Table 15)

$$= \frac{80}{100} \times \frac{40\ cm^2}{cm^3} \times \frac{20}{100} \times \frac{225\ cm^2}{cm^3}$$

$$= 77\ cm^2/cm^3 .$$

This value is about 50% higher than the value calculated for man. However, it must be regarded as preliminary, awaiting more extensive sampling on the beagles. It does, however, suggest that the ratio for the relative toxicity $^{239}Pu/^{226}Ra$ in the dog is lower than that which we would expect in man. In turn, the relative effectiveness of the two isotopes compared in mice would be expected to be even less. However, it is recognized that the percentage of bone surface taking part in bone formation and the extent to which this surface becomes buried may turn out to be of much greater importance in the comparison of the relative toxicity of these elements in dog and man. It is certainly apparent that we cannot take the relative toxicity in one species and apply this directly to man without consideration of all these factors together.

Exchangeable Bone Calcium

Rowland[22] has used quantitative autoradiography to determine the

amount of calcium which is rapidly exchangeable on bone surfaces when ^{45}Ca is injected into dogs and rabbits. He estimated that bone surfaces would be required to exchange an amount of calcium equivalent to that contained within 2000 Å of the bone surface to account for the rapid deposition of ^{45}Ca on these surfaces. If the thickness of this layer is the same in man as in dogs and rabbits, the total amount of bone calcium involved in this short-term exchange compartment in man can be calculated using the surface/volume ratio.[23] Assuming our value of 50 cm^2/cm^3, this is 0.1% of bone calcium:

$$2000 \times 10^8 cm \times 50 \frac{cm^2}{cm^3} \times 100 = 10^{-1} \%.$$

This value is one-fifth of the value obtained from kinetic studies for the total short-term exchangeable calcium in man. The rest of the short-term exchangeable calcium is probably contained in soft tissues and body fluids. The importance of this short-term exchange compartment in the measurements and models of skeletal metabolism is discussed fully by Marshall.[23]

Summary

An automatic scanning device has made possible for the first time the quantitation of a large number of parameters which characterize a large number of bone sites in the skeleton. To date we have made measurements of bones from man, dog, and mouse. The parameters measured include bone volume, surface/volume ratios, linear path lengths over bone, and trabecular spaces.

The results of these measurements are shown to have applications in the assessment of quantitative structural differences between bones, bone turnover rates, calcium kinetic studies, radiation doses from bone-seeking isotopes, and the extrapolation of the relative biological effectiveness of surface and volume bone seekers in animals to that in man. The data have been tabulated in full so that they are available to others to make their own calculations.

Thanks are due to R. E. Rowland and J. H. Marshall who read the script and made useful suggestions. I am also grateful to Joseph Farnham, Joanne Sha, and Bernice Cobb for technical assistance.

Appendix

Different formulas have been used for the estimation of surface/volume ratios. The most common is that derived by Hennig,[5]

$$\text{Surface/Volume} = \frac{2n}{L} \quad .$$

In this formula it is assumed that a body of volume V is intersected by a total length, L, of straight lines arranged at random in space. The total number of intersections with the specimen is n. In practice, measurements are normally made of a section in a two-dimensional plane. For these measurements a single line of length ℓ is thrown at random over the two-dimensional specimen a large number of times and the average intercept of the length calculated from adding up the total lengths of the intercepts and dividing by the number of intersections. The formula for surface/volume then becomes

$$S/V = 2/\ell_m,$$

where ℓ_m is the mean linear intercept. This is an exact equation. However, in the system used here it has to be remembered that the length of the two-dimensional perimeter multiplied by the thickness of the section underestimates the surface area by the amount $\sin\theta$, where θ is the angle of the surface to the section plane. In the case of haversian canals where the surfaces of the canals are at right angles to the cutting plane, $\sin\theta = 1$; hence, no correction is necessary to extrapolate from the two-dimensional to the three-dimensional surface by using the section thickness. However, in the case of trabecular bone where the trabeculae are to a first approximation oriented randomly, the average value for all angles of $\sin\theta$ is $4/\pi = 1.273$. Measurement of the volume of bone, unlike the surface problem, is inde-

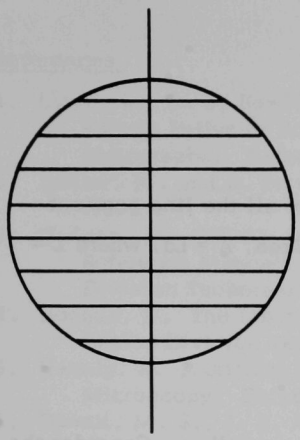

FIG. 11.--Circle showing Diameter and line segments.

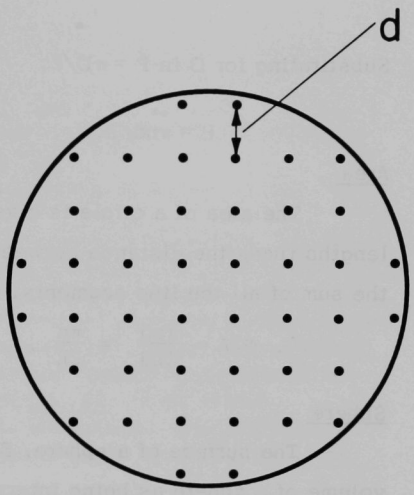

FIG. 12.--Cross section of a sphere indicating the corners of square rods seen in cross section.

pendent of the direction of sectioning and is always obtained by multiplying the area of the section by its thickness. Hence, for random shapes the three-dimensional parameter surface/volume is numerically equal to $4/\pi$ times perimeter/area. This relationship can be easily seen by comparing the perimeter/area of a circle with the surface/volume of a sphere.

Circle

Perimeter

For the circle, the perimeter $P = \pi D$, where D is the diameter (Fig. 11). The diameter $D = n_1 d$, where n_1 = the number of line segments crossing it and d = the distance between successive lines. Each line segment gives rise to 2 intersections with the surface; therefore, $n = 2n_1$, where n = the number of intersections.

$$D, \text{ therefore, } = \frac{nd}{2}.$$

Substituting for D in $P = \pi D/2$,

$$P = \pi nd/2.$$

Area

The area of a circle is given by the sum of all the line segment lengths times the distance between them, i.e., Area, $A = Ld$, where L = the sum of all the line segments.

$$\therefore \; P/A = \frac{\pi nd}{2Ld} = \frac{\pi n}{2L} .$$

Sphere

The surface of a sphere, $S = 4\pi r^2$, where r = radius. Consider the volume of a sphere as being intersected by a series of rods with square cross sections having a side d (Figure 12), then the number of square rods through a plane of the sphere will be

$$n = \frac{2\pi r^2}{d^2} \; ; \qquad \therefore \; r^2 = \frac{nd^2}{2\pi} .$$

Substituting for r^2 in the equation for the sphere surface

$$S = 4\pi r^2 \; ;$$

this becomes

$$S = \frac{4\pi nd^2}{2\pi} .$$

Volume

The volume of the sphere, $V = \Sigma \ell d^2$ where Σl is the sum of all the lengths of the square rods of side d.

$$\therefore \; \text{Surface/Volume} = \frac{4\pi nd^2}{2\pi \cdot \Sigma \ell d^2} \text{ or } \frac{2n}{L} ,$$

where $L = \Sigma \ell$.

Comparing this formula for S/V with P/A, we see that $S/V = 4/\pi$ times P/A.

References

1. Lloyd, E., R. E. Rowland, D. Hodges, and J. H. Marshll. Surface-to-Volume Ratios of Bone Determined by Computer Analysis of Microradiographs. Nature 218, 365-366 (1968).
2. Trotter, M. and R. Peterson. Library of Congress Document ADI-7153 (1962).
3. Hodges, D. CHLOE--An Automatic Film Scanning Equipment, Hardware Reference Manual. Argonne National Laboratory Applied Mathematics Division Technical Memo Number 61, 1963. Unpublished.
4. Hodges, D. The Liberator. Argonne National Laboratory Applied Mathematics Division Technical Memo Number 127, 1966. Unpublished.
5. Hennig, A. A critical Survey of Volume and Surface Measurement in Microscopy. Zeiss Werkzeitschrift No. 30, 78-87 (1958).
6. Dunnil, M. S., J. A. Anderson, and R. Whitehead. Quantitative Histological Studies on Age Changes in Bone. J. Path. Bact. 94, 275-285 (1967).
7. Atkinson, P. J. Variation in Trabecular Structure of Vertebrae with Age. Calc. Tiss. Res. 1, 24-32 (1967).
8. Bromley, R. G., N. L. Dockum, J. S. Arnold, and W. S. S. Jee. Quantitative Histological Study of Human Lumbar Vertebrae. J. Gerontol. 21, 537-543 (1966).
9. Dyson, E. D., C. K. Jackson, and W. J. Whitehouse. Scanning Electron Microscope Studies on Human Trabecular Bone. Nature 225, 957-959 (1970).
10. Amstutz, H. C. and H. A. Sissons. The Structure of the Vertebral Spongiosa. J. Bone Joint Surg. 51B, 540-550 (1969).
11. Wakamatsu, E. and H. A. Sissons. The Cancellous Bone of the Iliac Crest. Calc. Tiss. Res. 4, 147-161 (1969).
12. Jowsey, J., P. J. Kelly, B. L. Riggs, A. J. Bianco, Jr., D. A. Scholz, and J. Gershon-Cohen. Quantitative Microradiographic Studies of Normal and Osteoporotic Bone. J. Bone Joint Surg. 47A, 785 (1965).
13. Lee, W. R. Bone Formation in Paget's Disease: A Quantitative Microscopic Study Using Tetracycline Markers. J. Bone Joint Surg. 49B, 146-153 (1967).
14. Frost, H. M. Lamellar Ostoid Mineralized Per Day in Man. Henry Ford Hosp. Med. Bull. 8, 267 (1960).
15. Rowland, R. E. Resorption and Bone Physiology. Bone Biodynamics, Ed. H. Frost. Little, Brown & Co., Boston, 1964, pp. 335-351.
16. Kshirsager, S. G., E. Lloyd, and J. Vaughan. Discrimination between Strontium and Calcium in Bone and the Transfer from Blood to Bone in the Rabbit. Brit. J. Radiol. 39, 131-140 (1966).
17. Evans, R. D. Radium and Mesothorium Poisoning and Dosimetry and Instrumentation Techniques in Applied Radioactivity. MIT Ann. Progress Report MIT-952-2 (May 1965).

18. Lloyd, E. Nonuniformity in the Retention of the Alkaline Earths in Animals and Man. Argonne National Laboratory Radiological Physics Division Annual Report, July 1968 through June 1969. ANL-7615, pp. 49-53.

19. Sissons, H. A., K. J. Holley, and J. Heighway. Normal Bone Structure in Relation to Osteomalacia. L'Osteomalacie, Symp., Ed. D. J. Hioco. Masson et Cie, Paris, 1967, pp. 19-37.

20. Spiers, F. W. Dose to Bone from Strontium-90: Implications from the Setting of the Maximum Permissible Body Burden. Rad. Res. 28, 624 (1966).

2.1 Spiers. F. W. Dose to Trabecular Bone from Internal Beta Emitters. Proc. 1st Int. Congr. of Radiation Protection, Rome, 1966. Pergamon Press, New York, 1968, p. 165.

22. Rowland, R. E. Exchangeable Bone Calcium. Clin. Orthopaed. 49, 233-248 (1966).

23. Marshall, J. H. Measurements and Models of Skeletal Metabolism. Mineral Metabolism, Ed. C. Comar and F. Bronner. Academic Press, New York, 1969, pp. 2-122.

A COMPREHENSIVE MODEL OF ALKALINE EARTH METABOLISM: PRELIMINARY REPORT*+

J. H. Marshall

The power function model of whole-body retention is extended to provide a description of the microscopic processes of accretion, resorption, and diffusion in cortical and trabecular bone, bone surface exchange, and soft tissue retention in dog and adult man.

Terms and Concepts

Local Retention Function (Definition)

The model provides retention functions for the whole body, R, and for several parts of it, $R_{SUBSCRIPT}$. These retention functions represent the fraction of the activity which is injected into the blood and which is to be found in the given region at any time from injection (time zero) to infinite time. The unit of time used is the day (unless otherwise indicated). Therefore, $R(0) = 1$ and $R(\infty) = 0$ are the boundary conditions on whole-body retention, whereas $R_{SUBSCRIPT}(0) = 0$ and $R_{SUBSCRIPT}(\infty) = 0$ are the boundary conditions for any part of bone or soft tissue other than blood. Note that these retention functions refer to the biological retention and to not include radioactive decay.

Cortical and Trabecular Bone

It is useful to consider the skeleton as being composed of just two types of bone, one with a surface/volume ratio of about 30 cm^2/cm^3, which we will call cortical, and the other with a surface/volume ratio of about 120 cm^2/cm^3, which we will call trabecular. (See work described by Elizabeth Lloyd elsewhere in this report.) Different bones are then considered to contain different amounts of the two types of bone. We consider bone to be 20% trabecular and 80% cortical, either by mass or by calcium

*This is an abridged version of a report to ICRP by J. H. Marshall, Chairman of the ICRP Task Group on the Local Retention Functions of Bone Seekers.
+The parameters and parameter values of this new bone model are not yet final and should not be used for dose calculations.

content. (All bone is considered to have a density of 2 g/cm^3 and a calcium content of 0.25 g_{Ca}/g.)

Hotspots and the Diffuse Component

The activity in the volume of either cortical or trabecular bone is classified according to the mechanism of its uptake. Part of the uptake is due to accretion, the formation and mineralization of new bone; the rest is due to diffusion into existing bone. The former we will, for convenience, refer to as HOTSPOTS, and the latter as DIFFUSE. (These terms are here understood to be mechanistic rather than operational because one expects a distribution of both hotspot and diffuse intensities with no clear distinction between them at low levels of autoradiographic intensity without the use of tetracycline labeling.) Both the HOTSPOT COMPONENT and the DIFFUSE COMPONENT are considered part of BONE VOLUME activity. The bone surface activity described in the next paragraph is considered to be independent of and additional to both the hotspot and the diffuse components of bone volume.

Bone Surface Activity

Rowland has shown that the rapidly exchangeable calcium of bone is to be found on anatomical bone surfaces, the endosteal and periosteal surfaces of cortical bone, the surfaces of haversian and volkmann canals, and the surfaces of trabeculae, all of which we term BONE SURFACE.[1] Bone surface should not be confused with the surfaces of bone crystals, which, contrary to some current authors, take no part in the rapid exchange of calcium between blood and bone unless they are also at BONE SURFACE.

We consider that half of bone surface is in cortical bone, the other half in trabecular bone. This follows from the mass fraction multiplied by the surface/volume ratio: for cortical bone, 80% x 30 cm^2/cm^3, and for trabecular bone, 20% x 120 cm^2/cm^3.

We consider that the fraction of bone surface activity per unit area of bone is the same in cortical bone as in trabecular bone.

Diminution and Resorption

The removal of alkaline earths from bone is of two kinds, diminution and resorption.[2] Resorption describes the removal of activity together with the bone containing it. It is the classical process associated with osteoclasts. Diminution describes the removal of activity from bone volume without resorption of the bone itself. Diminution is primarily due to diffusion within the calcified matrix of bone but also includes any osteolysis which may occur. Resorption reduces locally the volume of bone. Diminution reduces the specific activity of radionuclides in existing bone. Diminution removes activity from bone that has been deposited both by accretion (HOTSPOTS) and by diffusion (DIFFUSE), though the former has been found to be somewhat less rapid than the latter. Similarly, resorption removes activity deposited both by accretion and by diffusion.

Age Invariance of the Retention Functions

The model assumes that for adult man and for adult dog each of the retention functions is independent of the age of the animal or man at the time of injection.

Recycling

Activity that is removed from soft tissue or from bone enters the blood stream again and has a chance of being redeposited rather than excreted. We consider that this removed activity mixes rapidly with the blood and so may be treated exactly like a new intravenous injection.

Whatever activity reenters the blood owing to the processes of removal contributes to the current value of the specific activity of the blood plasma, S. We derive the function for blood specific activity, S, by taking the negative derivative of the whole-body retention function, R, and dividing by the rate of excretory plasma clearance, ηk. This procedure[3] results in a realistic expression for plasma specific activity which has been verified many times by experiment. The uptake of activity in bone is then referred to this actual plasma specific activity S over all time, which automatically accounts for recycling.

Retention Functions Given by the Model

The following ten functions describe the retention vs. time of one unit of intravenously injected activity in different regions:

R	Whole body (includes bone, blood, and soft tissue)
R_{SOFT}	Soft tissue excluding blood
$R_{SURFACE}$	Bone surface excluding blood (half of bone surface being in cortical bone, the other half being in trabecular bone).
R_{CORT}	Cortical bone volume (all the activity in cortical bone other than blood and bone surface activity).
R_{TRAB}	Trabecular bone volume (all the activity in trabecular bone other than blood and bone surface activity)
$R_{CORTHOT}$	The part of R_{CORT} representing accretion [formation and mineralization of new bone (HOTSPOTS)].
$R_{CORTDIF}$	The part of R_{CORT} which represents diffusion of activity into nonforming bone (DIFFUSE).
$R_{TRABHOT}$	The part of R_{TRAB} representing accretion (HOTSPOTS).
$R_{TRABDIF}$	The part of R_{TRAB} representing diffusion (DIFFUSE).
R_{BLOOD}	The retention of activity in the blood is considered to be 3×10^{-4} cS, where C is the whole body calcium and S is the specific activity of the blood (plasma), fraction of injected activity per gram calcium.

Retention Functions in Detail

Bone Volume

The fractional retention of alkaline earth tracer in the volume of cortical bone, taken to be 80% by weight or by calcium content of bone as a whole, is

$$R_{CORT} = \beta\epsilon^{b} (t + \theta)^{-b} e^{-\lambda t} , \qquad (1)$$

where β is the fraction of bone volume activity picked up by cortical bone,

θ is a time-dependent factor which makes R_{CORT} rise in proportion to the time integral of serum specific activity until t becomes comparable to θ,

b is a positive decimal less than one (power function slope),

ϵ is the time at which the extrapolated whole-body retention is

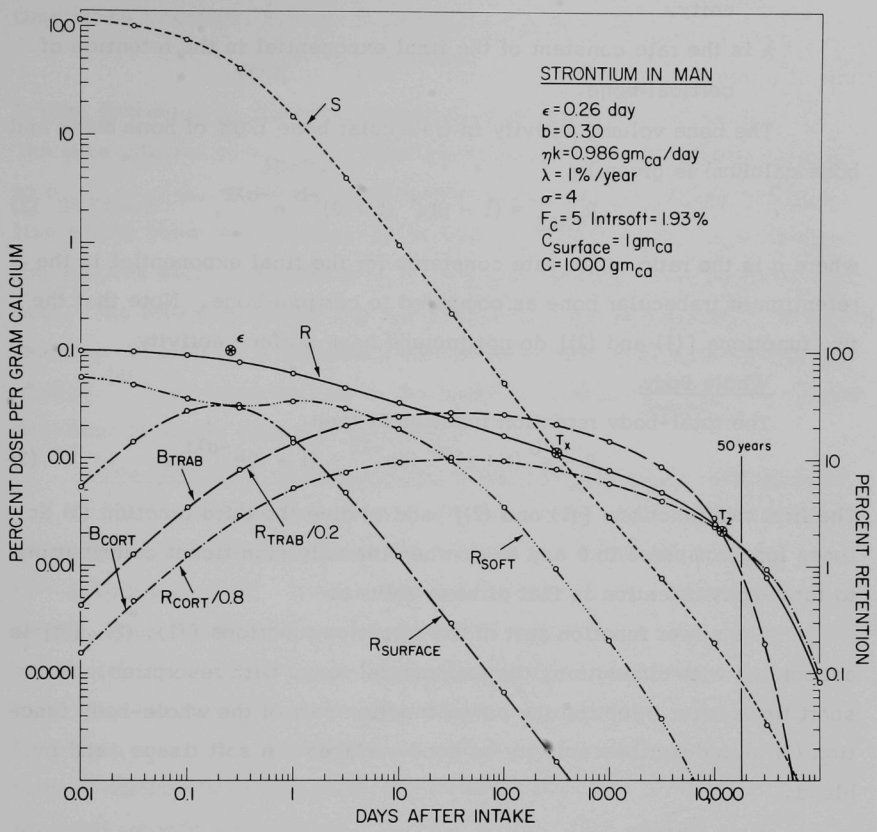

FIG. 1.--An example of the model for strontium in man. The curves for R_{SOFT} and $R_{SURFACE}$ are to be read only on the right-hand scale, the curves S, B_{TRAB} and B_{CORT} only on the left-hand scale. $B_{CORT} = R_{CORT}/0.8C$; $B_{TRAB} = R_{TRAB}/0.2C$. The R curve for whole-body retention may be read on both scales. (INTRSOFT is the fraction of body activity that one expects to be in soft tissue under continuous intake.)

unity,

λ is the rate constant of the final exponential in the retention of cortical bone.

The bone volume activity in trabecular bone (20% of bone mass and bone calcium) is given by

$$R_{TRAB} = (1 - \beta)\epsilon^{b} (t + \theta)^{-b} e^{-\sigma\lambda t}, \qquad (2)$$

where σ is the ratio of the rate constants for the final exponential in the retention of trabecular bone as compared to cortical bone. Note that the two functions [(1) and (2)] do <u>not</u> include bone surface activity.

<u>Whole Body</u>

The total-body retention function is then

$$R = \epsilon^{b} (t + \epsilon)^{-b} (\beta e^{-\lambda t} + (1 - \beta)e^{-\sigma\lambda t}). \qquad (3)$$

The first two functions [(1) and (2)] add to give the third function (3) at times long compared to θ and to ϵ, when the only significant contribution to total-body retention is that of bone volume.

The power function part of the retention functions [(1), (2), (3)] is associated with diminution, the exponential terms with resorption. At short times after injection the power function part of the whole-body function (3) also describes activity on bone surfaces, in soft tissue, and in blood.

<u>Bone Surface</u>

The retention of activity on bone surface is given by

$$R_{SURFACE} = b(b + 1)\, c_{SURFACE}\, t(t + SUR)^{-b-2} / \eta k (SUR)^{-b}, \qquad (4)$$

where $c_{SURFACE}$ is the calcium content of the exchangeable pool at bone surface, and

SUR is a time in days which determines the time at which $R_{SURFACE}$ reaches its maximum and starts decreasing.

Half of this surface is considered to be in trabecular bone, the other half in cortical bone.

This bone surface retention function rises in direct proportion to

time since injection, t, until it reaches a maximum at

$$T_{MAX} = (SUR)/(b + 1). \tag{5}$$

It then decreases in direct proportion to blood specific activity (t^{-b-1}). The time integral of $R_{SURFACE}$ from the time zero to time infinity is equal to $c_{SURFACE}/\eta k$, so that it predicts the surface uptake and loss of alkaline earths other than calcium on the basis of no discrimination between the alkaline earth and calcium in the transfer between blood and bone surface. The effect of urinary and fecal discrimination is accounted for by the factor η. If there is a preference for barium or radium in bone surface exchange,[4] it is accounted for in the model by letting $c_{SURFACE}$ for barium or radium be larger than that for calcium.

The Fraction β of Bone Volume Activity Picked up by Cortical Bone

The fraction of bone volume activity picked up by cortical bone is given by the factor β in function (1), and that by trabecular bone by $(1 - \beta)$ in function (2). If one considers the ratio σ as an independent parameter, then the factor β can be derived by considering the behavior of the two functions (1) and (2) under continuous radioisotope intake. Suppose a long-lived isotope of calcium were injected continuously for an indefinitely long time. We have no reason to expect that the final specific activity of cortical bone should be any different from that of trabecular bone, provided we wait long enough. In other words, there should be no discrimination for calcium between blood and bone volume in either cortical or trabecular bone. If there were a discrimination for any of the other alkaline earths, we would expect that it would be the same in cortical as in trabecular bone. The activity retained under continuous intake can be derived by taking the time integral of the corresponding (age-invariant) retention function. This retained activity is converted to specific activity by dividing by the corresponding mass fraction.

Therefore, we equate the time integrals of $R_{CORT}/0.8$ and $R_{TRAB}/0.2$ and solve for β. For simplicity these integrations are performed in two steps. First, the variable θ is replaced by the constant ϵ in both

(1) and (2). The solution for β is then

$$\beta = 4/(\sigma^{1-b} + 4) \qquad \text{(first approximation)}. \qquad (6)$$

In other words, if the final exponentials stand in the ratio σ, then the ratio of the early average specific activities of trabecular and cortical bone is approximately σ^{1-b}. This solution would be exact if the activity on bone surfaces and in soft tissue could be neglected.

The second step in solving for β is to reintroduce the variable θ into (1) and (2) and to perform the integrations again. Because the correct answer is very close to that given in (6) and because the integrations are now very difficult, the second integration is performed numerically using the form

$$\beta = 4/(\alpha\,\sigma^{1-b} + 4) \qquad \text{(second approximation)}, \qquad (7)$$

where α is a correction factor between 1.0 and 1.3. (One estimates α, works out the whole-body retention function, R, and the formula for θ, and then obtains a corrected value of α. Two or three successive approximations suffice for convergence to within 0.1%.)

The ratio of the average specific activity of trabecular bone to that of cortical bone is then $\alpha\sigma^{1-b}$ during the whole period before trabecular resorption becomes important and before $e^{-\sigma\lambda t}$ becomes significantly less than one.

The ratio σ is considered to be the ratio between the apposition-resorption rate of trabecular bone and that of cortical bone. We believe that the best value for σ is about 4. A factor of 4 is also the ratio of the surface/volume ratios of trabecular and cortical bone, so that a σ-value of 4 implies that in any given metabolic state the amount of apposition and resorption per unit time per unit area of bone surface is the same in cortical as in trabecular bone, a physiologically reasonable hypothesis.

Blood Specific Activity

The specific activity of the blood plasma, S, vs. time is derived from the whole-body retention function R by means of the excretion

postulate:

$$S = -(dR/dt)/\eta k\ , \tag{8}$$

where ηk is the rate of excretory plasma clearance in grams calcium per day, both urinary and fecal. (For an alkaline earth other than calcium ηk is the rate of excretory plasma clearance in liters/day times the calcium content of plasma, 0.1 grams calcium per liter, and η is the ratio of that clearance to that for calcium.)

The time integral of this plasma specific activity is then

$$\int_0^t S\ dt = (1 - R)/\eta k\ , \tag{9}$$

where R refers to the whole-body retention at time t.

Uptake of Activity in Bone Volume

Formulas (1) and (2) so far describe the retention of activity in cortical and trabecular bone only at times long compared to θ, because the form of θ has not yet been specified. We would like to find a form for θ that would make bone volume activity zero at the time of injection. We would then like bone volume activity to increase as it would because of a constant rate of transfer of calcium from blood to bone. This calcium transfer would carry with it a number of radioactive alkaline earth ions which depends directly upon the current specific activity of the blood plasma.

Take, for example, the formation and mineralization of new bone in cortical bone. Let the rate of new bone apposition in cortical bone be λ, in units of day^{-1} (fraction of the existing bone volume per day). Then the rate of increase of radioactivity in cortical bone due to this apposition rate is

$$dR_{CORTHOT}/dt = 0.8\ c\lambda\ S. \tag{10}$$

Since cortical bone contains 80% of body calcium, c, the rate of calcium transfer from blood to bone due to cortical apposition is $0.8\ c\lambda$, grams

calcium per day. Multiplying this rate by plasma specific activity, S, fraction of injected dose per gram calcium, yields the rate of increase of $R_{CORTHOT}$ in fraction of injected dose per day.

To find the amount of activity taken up in cortical bone due to apposition at any time t we integrate expression (10)

$$R_{CORTHOT} = 0.8\ c\lambda \int_0^t S\,dt \quad \text{(uptake only)}. \tag{11}$$

Substituting the expression for the time integral of S from (9) into expression (11) we obtain

$$R_{CORTHOT} = 0.8\ c\lambda\ (1 - R)/\eta k\ . \quad \text{(uptake only)}. \tag{12}$$

Note that we now have a realistic expression for the uptake of activity due to the formation of new bone, but we have not yet considered the effects of diminution and resorption upon this accreted activity as time progresses.

But before we do that, let us construct a description of the total uptake of activity in cortical bone volume. Owing to the diffuse component, this total uptake will be greater than that due to bone formation alone. Just how much greater we leave to experiment and introduce a new model parameter F_C. The total uptake of activity in cortical bone volume is then

$$R_{CORT} = F_C\,(0.8\ c\lambda\ (1 - R)/\eta k), \quad \text{(uptake only)}, \tag{13}$$

where F_C is the ratio of total uptake to appositional uptake of activity in cortical bone volume at any time after injection. F_C is assumed to be a constant.

Now we have two expressions for R_{CORT}, the one we have just derived (13), which should be an accurate description at times early enough to preclude diminution and resorption, and the expression given in (1), which has the correct relation to whole-body retention over times long compared to θ. We need a way to make a smooth transition from formula (13) to formula (1). This can be done by letting

$$\theta = \left[F_C \, 0.8 \, c\lambda \quad (1 - R)/\epsilon^b \, \beta \eta k \right]^{-1/b} \tag{14}$$

This expression, when substituted into formula (1) turns formula (1) into formula (13) at times short compared to θ, and makes a smooth transition back to formula (1) at times long compared to θ. The value of θ can then be adjusted to experimental data by proper choice of the parameter F_C. (This mathematical trick was invented only after the failure of innumerable other methods to provide retention functions in agreement with the available data on alkaline earths in man and dogs.)

We assume that all four bone volume components, $R_{CORTHOT}$, $R_{CORTDIF}$, $R_{TRABHOT}$, and $R_{TRABDIF}$ have the same time dependence as $R_{CORTHOT}$ at short times. In other words, before diminution and resorption have a chance to take effect, we assume that all four processes involve constant rates of calcium transfer from blood to bone and therefore involve uptakes of radioactivity which are different from each other but all of which are proportional to the time integral of plasma specific activity.

Let us assume that trabecular bone has an apposition rate (rate of bone formation) that is σ times the rate in cortical bone. This is the model parameter σ which was introduced in formula (2) and discussed earlier. Then the total uptake of activity in trabecular bone volume is proportional to R_{CORT} of (13) and equal to

$$R_{TRAB} = F_T \, (0.2 \, c\sigma\lambda \quad (1 - R)/\eta k) \quad \text{(uptake only)}, \tag{15}$$

where F_T is the ratio of total uptake to appositional uptake of activity in trabecular bone volume.

We then have two expressions for R_{TRAB} at times short compared to θ, the one we have just derived (15) and the one which results from the substitution of the formula for θ (14) into formula (2). Therefore, we equate these two expressions for R_{TRAB}, let t be negligible compared to θ, and solve for F_T. The result is

$$F_T = 4\, F_C\, (1 - \beta)/\beta\sigma. \tag{16}$$

F_T is, therefore, not an independent parameter of the model, but follows directly from the values for β, σ, and F_C

Complete Retention Functions for Bone Volume

We have now constructed complete retention functions for R_{CORT} [(1), (14)] and for R_{TRAB} [(2), (14)]. Let us now use these functions to derive complete retention functions for the four bone volume components, $R_{CORTHOT}$, $R_{CORTDIF}$, $R_{TRABHOT}$, and $R_{TRABDIF}$.

The first and third of these functions could be obtained simply by dividing R_{CORT} and R_{TRAB} by the constant factors F_C and F_T, respectively. Then, however, it would follow that the diminution of all four bone volume components would be exactly the same. Though there is some experimental evidence that this might not be an untenable assumption,[5] such an assumption would conflict with autoradiographic data for ^{45}Ca in rabbits[6] and for ^{226}Ra in man.[7] In the latter work, Rowland found that bone formation hotspots in multiply-injected radium patients observed 25 years after the radium injections showed a factor of 3 diminution from the specific activity which calculation shows they picked up by accretion. On the other hand, the diminution of the diffuse component in cortical bone was a factor of 10 as measured over this same period of time. (The ratio diffuse/uniform label in Mays' radium patients who died 141 days and 400 days after injection was equal to the same ratio in the Elgin patients 25 years after injection, so that the specific activity of the diffuse component in cortical bone in the absence of resorption was falling at the same rate as whole-body retention.)

Therefore, a new model parameter, D_C, was introduced in order to increase the diminution of the cortical diffuse component by a factor D_C at the expense of diminution in cortical hotspots. This was done by constructing the variable F_{SC} (a factor which shifts the diminution balance in cortical bone) so that

$$R_{CORTHOT} = (R_{CORT}/F_C)\,(F_{SC}), \tag{17}$$

where

$$F_{SC} = (t + 700 \text{ days})/(H_C t + 700 \text{ days}).$$

Function F_{SC} is equal to unity at times much less than 700 days, changing smoothly to the value $1/H_C$ at times much greater than 700 days.

If the diminution of cortical volume activity as a whole is to remain unchanged, then the relation between H_C and D_C must be

$$H_C = D_C/(D_C F_C - F_C + 1). \tag{18}$$

In trabecular bone one would expect a similar situation, greater diminution in the diffuse component than in hotspots. In fact, one would also expect that diminution of the trabecular diffuse component would be greater than diminution of the cortical diffuse component. The former probably has a larger coefficient of diffusion because the average age of the bone is less than that in the cortex. Therefore, one would expect greater uptake of activity per gram calcium and subsequently greater diminution of that activity. Let us introduce the variable F_{ST} (a factor which shifts the diminution balance in trabecular bone) so that

$$R_{TRABHOT} = (R_{TRAB}/F_T)(F_{ST}), \tag{19}$$

where

$$F_{ST} = (t + 700 \text{ days})/(H_T t + 700 \text{ days}).$$

Function F_{ST} is equal to unity at times much less than 700 days, changing smoothly to the value $1/H_T$ at times much greater than 700 days.

Experimental evidence on diffuse diminution in trabecular bone is entirely lacking, so there is no point in increasing the number of independent parameters in the model. Instead, let us set the enhancement factor for trabecular diffuse diminution, D_T, equal to the initial ratio of the specific activities of the diffuse components in trabecular as compared to cortical bone. In this way, if there is a greater uptake of diffuse activity in trabecular bone, then subsequently there will be a greater loss by diminution, so that the specific activities of the diffuse components in the absence of

resorption in trabecular and in cortical bone will at long times become equal. To do this we set

$$D_T = D_C(\text{DIFRATIO}), \tag{20}$$

where DIFRATIO is the initial ratio of the specific activities in the diffuse components of trabecular as compared to cortical bone (a constant).

The value of the constant, DIFRATIO, follows directly from parameters already defined:

$$\text{DIFRATIO} = (F_C \alpha \sigma^{1-b} - \sigma)/(F_C - 1).$$

If the diminution of trabecular bone volume activity as a whole is to remain unchanged, then it follows that the relation between H_T and D_T must be

$$H_T = D_T/(D_T F_T - F_T + 1), \tag{21}$$

which is analagous to the formula for cortical bone (18).

Finally, to complete the chain of reasoning concerning bone volume, let us derive the retention functions for diffuse activity, $R_{CORTDIF}$ and $R_{TRABDIF}$, from the obviously necessary relationships

$$R_{CORTDIF} = R_{CORT} - R_{CORTHOT} \tag{22}$$

and

$$R_{TRABDIF} = R_{TRAB} - R_{TRABHOT}. \tag{23}$$

We now have an internally consistent set of retention functions for the four components of bone volume, $R_{CORTHOT}$ (17), $R_{TRABHOT}$ (19), $R_{CORTDIF}$ (22), and $R_{TRABDIF}$ (23).

Soft Tissue

The fraction of the injected activity in soft tissue as a function of

time is then obtained as a difference between the whole-body retention functions and the retention functions for all other components:

$$R_{SOFT} = R - R_{CORT} - R_{TRAB} - R_{SURFACE} - R_{BLOOD}.$$

As the model is successively fitted to all available data for alkaline earths in man and dog, further changes in the parameters and parameter values will undoubtedly become necessary.

References

1. Rowland, R. E. Exchangeable Bone Calcium. Clin. Orthoped. 49, 233 (1966).
2. Marshall, J. H. Measurements and Models of Skeletal Metabolism. Mineral Metabolism, Ed. C. Comar and F. Bronner. Academic Press, New York, 1969, Vol. III, pp. 1-122.
3. Marshall, J. H. Theory of Alkaline Earth Metabolism. The Power Function Makes Possible a Simple but Comprehensive Model of Skeletal Systems. J. Theoret. Biol. 6, 386 (1964).
4. Ellsasser, J. C., J. E. Farnham, and J. H. Marshall. Comparative Kinetics and Autoradiography of ^{45}Ca and ^{133}Ba in Ten-Year-Old Beagle Dogs. J. Bone Joint Surg. 51-A, 1397 (1969).
5. Sears, K. A., W. S. S. Jee, and C. W. Mays. Radium Dosimetry. University of Utah, College of Medicine Radiobiology Division Report COO-226 (1962), p. 86.
6. Lloyd, E. Quantitative autoradiography of ^{45}Ca in bone. Calcified Tissues, Ed. L. J. Richelle and M. J. Dallemagne. University of Liege, Liege, 1965, pp. 381-390.
7. Rowland, R. E. and J. H. Marshall. Radium in Human Bone: The Dose in Microscopic Volumes of Bone. Radiat. Res. 11, 299 (1959).

^{45}Ca, ^{133}Ba, AND ^{226}Ra IN 6- TO 10-YEAR-OLD BEAGLE DOGS: A 100-DAY STUDY

S. K. Wood,* J. E. Farnham, and J. H. Marshall

An exhaustive study has been performed on fourteen 6- to 10-year-old beagle dogs from the Argonne stock line to follow their bone and alkaline earth metabolism. The isotopes ^{45}Ca, ^{133}Ba, and ^{226}Ra were used with tetracycline to mark growing bone, age matched pairs of dogs being injected with either ^{45}Ca or $^{133}Ba/^{226}Ra$ mixture.

Ellsasser, Farnham, and Marshall have reported observations on the short-term behavior of ^{45}Ca and ^{133}Ba in ten-year-old beagle dogs.[1,2] The study showed that for calcium the specific activity of the blood declined as a power function t^{-b} after the first day, where $b \simeq 1.7$. A similar decline but even steeper was shown for barium, $b \simeq 1.84$. The slope of these curves approached the slope of the blood specific activity curves for similar experiments in adult humans and also the "break" in the blood curve at time ϵ fitted with similar human data, giving further evidence of the similarity in kinetic behavior between these dogs and human subjects.[3,4]

A second observation made was that at short times (seven days) the autoradiographic appearance of ^{45}Ca and ^{133}Ba differed considerably. The difference could not be interpreted as due solely to a difference in the effect of the varying emissions from the isotopes on the autoradiographic emulsion. Barium appeared to be retained on bone surfaces, and only a small proportion of the isotope passed into bone volume.

Because of the similarity to human data and the different behavior of barium, which has been shown to be a good tracer for radium, it was decided to undertake a more extensive study of 6- to 10-year-old beagle dogs to gather as much information as possible about their bones and alkaline

* Visiting Scientist, Department of Orthopaedic Surgery, The Western Infirmary, University of Glasgow.

earth metabolism.

Apart from the injection of either ^{45}Ca or $^{133}Ba/^{226}Ra$ isotope into age-matched pairs of dogs, oxytetracycline injections were used to assess bone formation at the time of isotope injection and also to identify hotspots on the autoradiographs not associated with new bone formation. The long-term animals sacrificed at 100 days were given a demethylchlortetracycline label toward the end of the experiment so that any change in bone formation rate could be detected.

Blood, bone, and soft tissue were collected. Plasma specific activity was determined at times from 5 min to 100 days after injection. Bone and soft tissue samples were collected at sacrifice for radiochemical analysis and/or autoradiography. The times of sacrifice ranged from 12 min to 100 days after injection.

Measurement of soft tissue specific activity will result in a curve of uptake and release of the different isotopes from soft tissue and will also allow a determination of the isotope distribution within the whole body.

Autoradiographs from a variety of skeletal sites will allow a wide study of isotope behavior in bone, including the extent of activity not associated with newly forming bone, the amount of activity on surfaces, and the kinetics of isotope exchange on bone surfaces and also in bone volume. From the skeletons of the dogs sacrificed at 25 and 100 days (dissected free of soft tissue) selected bone samples were taken for autoradiography, and the remainder of the skeleton was ashed to obtain a radiochemical analysis of isotope retention. In the ^{45}Ca dogs this will give us values for retention at 25 and 100 days. From these, and values of retention at shorter times from other work, a composite retention curve can be assembled.

Whole-body counting was carried out on the $^{133}Ba/^{226}Ra$ dogs so that retention curves could be constructed. Retention of ^{45}Ca was not investigated except in the 25- and 100-day dogs owing to the problems of estimating fecal and urinary excretion in the large number of animals

involved.

Microradiography of the bone sections will allow a study of varying mineralization in hotspots and diffuse label both in cortical and trabecular bone, while the addition of tetracycline labeling improves the sophistication of the technique by identifying hotspots not associated with new bone formation. The double tetracycline labeling of the long-term animals will, we hope, demonstrate that bone formation rates have remained steady during the period of the experiment. It will be possible to measure any change in bone formation rate if this has occurred.

Much information has yet to be extracted from the experiment. When all the information has been accumulated, we expect to have a better understanding of alkaline earth metabolism in man, which will help in formulating radiation safety codes.

Materials and Methods

Fourteen old beagle dogs obtained from the Argonne National Laboratory stock line were used in this experiment. The ages of the animals ranged between 6 and 10 years. The dogs were housed in individual large metabolism cages for a few days prior to injection and continuously after injection until time of sacrifice. They were fed the standard dry pellet dog diet ad lib. during the experimental period.

Tetracycline (doses of 20 mg/kg body weight) used to label new bone growth sites was injected directly into the cephalic vein at the times before and after isotope injection (Table 1). The two 100-day dogs (Nos. SJ1 and SJ2) were given demethylchlortetracycline* additionally in the same dosage 85 and 95 days after the isotope injection. All the dogs were injected with oxytetracycline HCl.

---

*Declomycin powder (DMCT) from Lederle Laboratories. The dry powder dissolved with great difficulty in water, yielding a highly acid solution. In weak NaOH the powder dissolved easily without change in pH to yield a clear yellow solution. This solution could be brought to pH 8 without precipitation of DMCT, and the drug was injected in this form.

TABLE 1. Experimental Plan.

Dog. No.	ANL Stock No.	Age at Injection, yr	Weight at Injection, kg	Isotope Injected Day t_0, μCi	Days of Tetracycline Injection	Day of Sacrifice
				^{45}Ca		
SJ14	621	6.5	14.5	1500	$t_{-13}+t_3$	t_0 (12 min)
SJ6	505	7	15.0	1500	$t_{-12}+t_{-2}$	t_0 (1 hr
SJ7	512	7	15.5	1500	$t_{-13}+t_{-3}$	t_0 (5 hr)
SJ11	421	6	9.2	900	$t_{-13}+t_{-2}$	t_1
SJ12	33B	10	13.4	1350	$t_{-11}+t_2$	t_5
SJ10	453	6	15.4	1500	$t_{-5}+t_5$	t_{25}
SJ3	167	10	12.5	1200	$t_{-5}+t_5+t_{85}+t_{95}$	t_{100}
				$^{133}Ba/^{226}Ra$		
SJ13	483	8	15.4	235.7/1.57	$t_{-13}+t_{-3}$	t_0 (12 min)
SJ4	479	7	15.2	235.7/1.57	$t_{-12}+t_{-2}$	t_0 (1 hr)
SJ5	511	7	14.3	214.3/1.40	$t_{-9}+t_{-2}$	t_0 (5 hr)
SJ9	408	6	11.0	171.4/1.14	$t_{-14}+t_{-2}$	t_1
SJ8	170	11	16.5	257.1/1.70	$t_{-12}+t_{-2}$	t_5
SJ2	451	6	15.6	235.7/1.57	$t_{-5}+t_6$	t_{25}
SJ1	163	10	7.7	112.5/0.75	$t_{-5}+t_5+t_{85}+t_{95}$	t_{100}

The radioactive tracers used were ^{45}Ca (dose level of 100 μCi/kg body weight); ^{133}Ba (15 μCi/kg); and ^{226}Ra (0.1 μCi/kg). Seven dogs were injected with ^{45}Ca and each sacrificed by injection of an overdose of sodium pentobarbital at one of the following time periods from time of injection: 12 min, 1 hr, 5 hr, 1 day, 5 days, 25 days, and 100 days. The other 7 dogs, age matched with the ^{45}Ca dogs, were given a mixture of ^{133}Ba and ^{226}Ra and were sacrificed at the same time periods as the ^{45}Ca dogs.

All radioactive tracers were injected in the following manner: A smooth flowing intravenous infusion of normal saline solution was established in the cephalic vein of each animal just prior to the tracer injection. The radioactive tracer in 0.1 N HCl was then injected into the animal via a side "Y" tube in the infusion line. The injection syringe was back-washed with fresh saline 3 or 4 times to insure complete injection of the tracer. The saline infusion line was then removed and checked with a survey meter to make sure no activity was left behind in the tube or syringe. All inject-

ion data are listed in Table 1.

Venous blood samples for plasma clearance studies were taken at frequent intervals on the day of injection and periodically thereafter until the time of sacrifice. Each blood sample was collected in a heparinized syringe, transferred to a centrifuge tube, and spun to separate plasma and cell fractions. The plasma was then transferred to clean polyethylene vials. Appropriate aliquots were taken from these vials for the various quantitative measurements for stable calcium and radioactivity.

Plasma aliquots containing ^{45}Ca were dissolved in liquid scintillation vials, using 1 ml of hydroxide of hyamine 10x (Packard Instrument Co.), 10 ml of absolute alcohol, and 10 ml of scintillation solution. Quantitative determinations were made using a two-channel Packard Tri-carb liquid scintillation spectrometer system, Model 3002. Quenching was controlled by gain adjustments and observations of spectrum shifts through simultaneous two-channel counting with one narrow and one wide window opening. Known amounts of the injection solution were prepared in liquid scintillation vials as ^{45}Ca standards and counted periodically throughout the experiment. All ^{45}Ca data have been normalized to the date that the stock injection solution was prepared. Table 2 lists the calcium blood specific activities for all animals.

Plasma aliquots containing ^{133}Ba and ^{226}Ra activity were dissolved in clean plastic vials using 10 ml of 0.5 M EDTA solution. These sample vials were then counted, along with ^{133}Ba standard vials, on a 3" x 5" NaI(Tl) crystal, and the data were processed using the least-squares analysis.[5] (See Table 3.)

Stable calcium determinations on plasma samples, as well as on bone and soft tissue samples, were made on a Perkin-Elmer Model 303 atomic absorption spectrometer. The method of analysis used is described in the Perkin-Elmer handbook.[6]

Quantitative measurements of the ^{226}Ra in our sample were made using the Rn emanation technique.[7] The level of the ^{226}Ra activity in the

TABLE 2. Specific Activity of ^{45}Ca in Plasma.

		% Injected Dose/mg Ca x 10^{-3}						
		Dog No.						
Days	Hr	SJ3	SJ10	SJ12	SJ11	SJ7	SJ6	SJ14
0.0035	(0.08)	372.27	374.74	490.56	530.14	305.48	307.59	211.82
0.0069	(0.17)	295.01	345.66	415.57	487.81	303.66	241.49	174.76[a]
0.014	(0.33)		266.18	383.53	442.58	240.27	227.62	
0.017	(0.42)	268.93						
0.028	(0.67)	284.33	261.19	334.84	365.66	149.95	204.06	
0.042	(1)						194.29	
0.056	(1.33)	262.73		256.44	357.06	127.79		
0.069	(1.67)		232.26					
0.11	(2.67)	199.95	137.48	256.23	305.93	121.20		
0.21	(5)					91.29		
0.22	(5.33)	150.82	163.59	196.23	223.37			
0.40	(9.67)		125.57					
0.42	(10)				200.68			
0.44	(10.67)	112.64						
0.51	(12.25)			151.01				
1		75.83	100.49	142.12	202.56			
2		44.50	68.01	104.05				
5		12.34	17.21	53.35				
8		9.12	14.00					
15		4.45	1.32					
25		0.69	0.60					
50		0.23						
100		0.21						

[a] 0.0083 day = 0.2 hr.

samples was so low that we were able to ignore its gamma contribution in the spectra obtained when counting for ^{133}Ba determinations.

At sacrifice soft tissue samples were immediately dissected from each animal and placed in 70% alcohol. Six types of tissue were collected: skeletal muscle, heart muscle, liver, lung, fat, and cartilage. After fixation the tissues were air dried and then ashed at 600°C. The ash was weighed and dissolved in 2 N HCl in volumetric flasks. Radiochemical and stable calcium measurements were made using the same techniques as were used for the blood plasma analysis.

The entire skeleton from each 25-day and 100-day dog was obtained by sharp dissection at the time of sacrifice. On the following listed bone samples were obtained in the same manner from the other 10 dogs at sacrifice. The samples were the left femur, lumbar vertebrae 5 and 6, left rib 6, and a left metacarpal. All bone samples were stored in 70% alcohol until

TABLE 3. Specific Activity ^{133}Ba in Plasma.

		% Injected Dose/mg Ca x 10^{-3}						
		Dog No.						
Days	Hr	SJ1	SJ2	SJ8	SJ9	SJ5	SJ4	SJ13
0.0035	(0.08)			395.67	391.58	494.04	202.18	378.01
0.0069	(0.17)			330.53	283.08	373.86	279.22	335.77[a]
0.014	(0.33)		270.15	281.71	282.77	318.80	225.42	
0.022	(0.52)	277.93						
0.028	(0.67)	345.92	252.87	236.22	238.54	249.59	189.06	
0.042	(1)						168.09	
0.056	(1.33)	282.10	185.73	195.03	203.87	195.55		
0.11	(2.67)	210.91	116.36	143.90	162.06	118.89		
0.21	(5)					85.24		
0.22	(5.33)	129.09		100.39	118.22			
0.23	(5.42)		67.40					
0.32	(7.58)		61.71					
0.44	(10.67)	84.63		66.58	70.33			
1		32.77	15.76	34.20	46.62			
2		21.44	13.45	16.75				
5		6.89		5.07				
6			2.26					
8		2.85	1.86					
15		1.41	0.99					
25		0.50	0.22					
52		0.24						
100		0.38						

[a] 0.0083 day = 0.2 hr.

ready for radiochemical analysis or embedding in methyl methacrylate.

In the radiochemical analysis the right paired bones only were ashed and analyzed together with the right half of the skull and right half of the mandible. Representative vertebrae were retained and the remainder ashed. The analysis of the ^{133}Ba samples, when corrected for the absent bones, yielded a total skeletal burden in close agreement with the whole-body retention values. Ten days after the isotope injection into dog SJ1 and eight days after injection into dog SJ3, biopsies of a rib and a right lateral toe were removed from each animal. These bone samples were stored in 70% alcohol for later autoradiographic and tetracycline comparisons with comparable bone samples obtained much later at sacrifice of the animals.

Representative bone samples from all animals were prepared for autoradiographic, microradiographic, and tetracycline labeling studies in

the following manner: After alcohol fixation, the bones were defatted in a 50-50% solution of ether and methyl alcohol. They were then cut into pieces and identified as either proximal femur plus metaphysis, distal femur plus metaphysis, midshaft femur, distal end rib, proximal end rib, midshaft rib, lumbar vertebra longitudinal section, lumbar vertebra transverse section, or metacarpal. The marrow spaces were cleaned out with a fine jet of water prior to dehydration of the bone in a series of ethyl alcohols. The samples were transferred to acetone and then embedded in methyl methacrylate. For analysis several sections approximately 100 μ thick were cut from each embedded bone block. Autoradiographic exposures were made on Eastman Kodak Type A autoradiographic plates. Besides being exposed to a specific bone section in close contact, each Type A plate was exposed to a plaster of paris radiator.[8] Microdensitometric measurements on these autoradiographic plates were performed with a Leitz Ortholux microscope, a 30-μ aperture substage condenser, and a photovolt multiplier photometer, series 520A, equipped with a standard 21C photomultiplier tube. For direct comparison, all autoradiographic exposures made from bone sections containing ^{45}Ca were exposed for identical times. The same procedure was followed for the ^{133}Ba autoradiographic exposures.

Whole-body retention measurements were made on the 5-, 25-, and 100-day ^{133}Ba injected dogs, using the technique described by Farnham and Rowland.[9] The dogs were counted immediately after injection and then at 1, 5, 8, 15, 25, 53, and 100 days after injection or until the day of sacrifice. The retention data are listed in Table 3 as fractional retention and as percent injected dose per gram calcium. The fractional retention is calculated by dividing the observed counts on a specific day by the observed counts on the day of injection.

Results and Conclusions

Plasma Clearance Studies

In Figures 1 and 2 we have plotted the observed values of the plasma

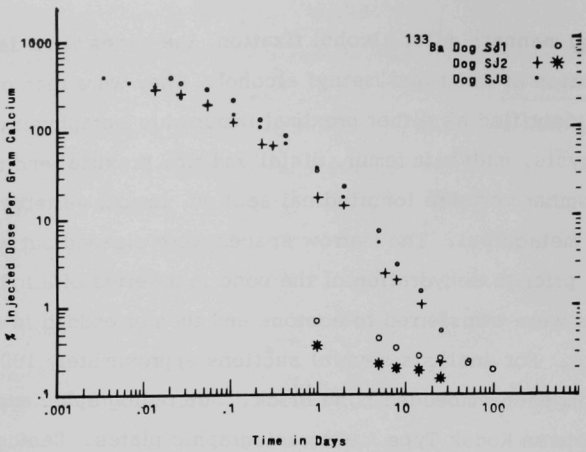

FIG. 1.--Plasma clearance and whole body-calcium curves for ^{133}Ba. Upper curves--plasma clearance. Lower curves--whole-body retention.

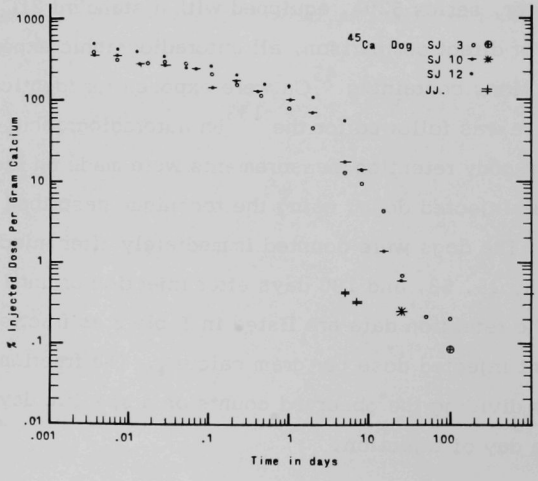

FIG. 2.--Plasma clearance and whole-body retention curves for ^{45}Ca. Upper curves--plasma clearance. Lower curve--composite whole-body retention.

specific activity for the 5-, 25-, and 100-day dogs. The data are expressed as percent injected dose per gram calcium. It should be noted that the data from these old animals indicate that the blood values start out at the same level and end up at the same level by 50 to 100 days after injection. However, at early times, up to about 3 days, the barium values are falling with a steeper slope than the calcium. At this point the calcium starts on a steeper slope than the barium, and reaches approximately the same value as barium at 100 days. The slope of these ^{133}Ba curves between 1 and 100 days is approximately 1.25. Farnham and Rowland show a slope of ≈ 1.27 for the dogs used in their experiment. The slope of the composite ^{45}Ca plasma specific activity curve for the 5-, 25-, and 100-day dogs used in this experiment was 1.63.

Soft Tissue Analysis

Much analysis is yet to be done on the soft tissue samples. Some preliminary values of percent injected dose per gram calcium for various soft tissues acquired at sacrifice of four of the dogs are listed in Table 4. If the sparse data thus far obtained are any indication of what the total experiment will show, we can see that soft tissue does not contain much of the barium tracer, whereas there is a considerable amount of the ^{45}Ca tracer in the soft tissues at short times after injection. Another important fact seen in these data is that the soft tissue activity is real and not due to blood contamination. This can be stated because all soft tissue samples taken from both the ^{45}Ca and the ^{133}Ba dogs were collected and handled in an identical manner. Liver and lung, which are highly vascular tissues and could be suspected to contain a large component of blood contamination, do show large ^{45}Ca content. However, it could be argued from the ^{133}Ba data on these two soft tissues that the ^{45}Ca contents are really a component of the tissue and not blood contamination.

Bone Analysis

The whole-body retention data for those ^{133}Ba animals measured by gamma counting are listed in Table 5. The data have been expressed both

TABLE 4. Retention of Isotopes in Soft Tissue

	% Injected Dose/g Calcium			
	^{45}Ca		^{133}Ba	
Tissue	1 hr	5 hr	1 hr	5 hr
Skeletal muscle	44.22	49.24	0.02	0.011
Heart muscle	81.2		0.06	0.007
Liver	227.8		0.046	0.01
Fat	21.34	3.21	0.003	0.0009
Lung	129.6	108.65	0.07	0.05
Cartilage	1.35			
Blood plasma	280.	119.	240.	100.

TABLE 5. Retention of Barium Tracer

Days after Injection	Fractional Retention				% Injected Dose/g Calcium			
	Dog No.				Dog No.			
	SJ1	SJ2	SJ8	SJ9	SJ1	SJ2	SJ8	SJ9
0	1	1	1	1				
1	0.596	0.480	0.799	0.944	0.651	0.349	0.484	0.858
5	0.373	0.291	0.414		0.407	0.212	0.251	
8	0.291	0.268			0.318	0.195		
15	0.251	0.255			0.274	0.186		
25	0.240	0.212			0.262	0.154		
53	0.192				0.210			
100	0.170				0.186			

as fractional retention and as percent of injected dose per gram calcium. The data are also plotted on the same graph as the plasma specific activity (Figure 1), allowing us to observe the relationship between the bone and blood. It should be noted that the terminal whole-body retention values of 17% and 21% derived from the gamma counting analysis are in close agreement with the values of 13.2% and 19.9% obtained from the radiochemical analysis of the entire skeleton (Table 6). Close inspection of Figure 1

TABLE 6. Skeletal Radiochemical Values.

Dog No.	Isotope	Day of Sacrifice	Total Skeletal Activity, μCi	Activity, % Injected Dose	Skeletal Ash Wt., g	Activity, % Injected Dose/g Ca	Activity, % Injected Dose/g Ca Normalized to 500 g Skeletal Wt.
SJ1	^{133}Ba	100	14.89	13.21	247.41	0.144	0.071
SJ2	^{133}Ba	25	46.83	19.87	355.54	0.151	0.107
SJ3	^{45}Ca	100	152.56	12.71	328.77	0.105	0.069
SJ10	^{45}Ca	25	462.47	30.83	409.75	0.203	0.171

shows that the "crossover" point (the intercept of the plasma specific activity curve with the whole-body retention curve) is between 50 and 60 days for the 25- and 100-day barium dogs. This crossover time falls just between 14- and 100-day values reported by Farnham and Rowland. These figures compare well with data on ^{226}Ra in 1- to 3-year-old dogs having a crossover at 40 days,[10] and with human ^{226}Ra data showing a 50- to 100-day crossover.[11] Our figures lie within the human range, but the times are longer for the old than the young dogs, thus strengthening the belief that these old animals make good models for human kinetics.

The measured retention and plasma clearance are expressed as power functions in Table 7. The coefficients of the retention and plasma functions are the measured values when t = 1 day. The slope of the curves was measured directly from Figure 1.

The skeletal retention of ^{45}Ca in the 25-day dog (SJ10) was found to be $R_{25} = 0.261$ percent of the injected dose per gram calcium, whereas in the 100-day dog (SJ3) $R_{100} = 0.084$. Ellsasser et al. reported values of $R_5 = 0.419$ and $R_7 = 0.326$ in one animal and $R_5 = 0.434$ and $R_7 = 0.334$ in another.[2] These points have been plotted in Figure 2 as a composite retention curve. Using this retention curve with the plasma specific activity curve shown in the same figure, we can observe a crossover point of approximately 100 days for calcium.

Radiochemical Results

The bones of the two 25-day and two 100-day animals previously indicated were ashed and analyzed radiochemically. The results from the

TABLE 7. Whole-Body Retention and Plasma Clearance of ^{133}Ba and ^{45}Ca

Dog No.	Measured Retention, Fraction of Injected Dose[a]	Measured Plasma Concentration, % Injected Dose/ml Plasma[a]
	^{133}Ba	
SJ1	$0.65 \times t^{-0.25}$	$3.28 \times 10^{-3} t^{-1.31}$
SJ2	$0.35 \times t^{-0.24}$	$1.58 \times 10^{-3} t^{-1.29}$
	^{45}Ca	
SJ3	$2.9 \times t^{-0.77}$	$2.00 \times 10^{-2} t^{-1.62}$
SJ10		$5.8 \times 10^{-2} t^{-2.14}$
JJ	$1.46 \times t^{-0.77}$	$1.21 \times 10^{-2} t^{-1.69}$

[a] t is in days.

above determinations are shown in Table 8. The stable calcium content of the ash was determined on several samples from each animal and found to be a constant of approximately 37%. This figure was used in calculating the activity per gram calcium shown for all samples. Radiochemical analysis for ^{226}Ra is incomplete at this time, but some preliminary figures are given in Table 9.

Bone Specific Activities

Further explanation of Table 8 is in order. Owing to the large size of the vertebrae in some of the animals, the samples for ashing had to be subdivided into smaller groups. In the case of the cervical vertebrae one group consisted of the atlas and axis. Group II refers to analysis of the lower cervical vertebrae. In the thoracic and lumbar vertebrae, division into I and II was carried out arbitrarily to equalize the sample sizes, that is, the upper vertebrae being in sample I and the lower in sample II. Sample III listed in the table for each type of vertebra is an average value of samples I and II, where present, and represents activity of all the vertebrae in the group. In one dog (SJ10) the patella was ashed separately, whereas in the

TABLE 8. Bone Specific Activity.

	% Injected Dose/g Ash			
	^{133}Ba		^{45}Ca	
Bone	Dog SJ1 100 days	Dog SJ2 25 days	Dog SJ3 100 days	Dog SJ10 25 days
Atlas and Axis	0.029		0.021	
Cervical Vertebra II	0.066		0.047	
Cervical Vertebra III	0.048	0.047	0.034	0.068
Thoracic Vertebra I	0.135	0.128	0.045	
Thoracic Vertebra II	0.093	0.125	0.055	
Thoracic Vertebra III	0.114	0.127	0.050	0.154
Lumbar Vertebra I	0.095		0.080	
Lumbar Vertebra II	0.099		0.038	
Lumbar Vertebra III	0.097	0.101	0.059	0.130
Sacrum and Caudal vertebra	0.105	0.091	0.074	0.101
Sternum	0.242	0.229	0.128	0.287
Proximal Rib	0.107	0.077	0.059	0.104
Shaft of Rib	0.105	0.083	0.050	0.114
Distal Rib	0.258	0.252	0.115	0.284
Scapula	0.077	0.064	0.032	0.084
Proximal Humerus	0.162	0.076	0.047	0.139
Shaft of Humerus	0.041	0.029	0.030	0.047
Distal Humerus	0.051	0.031	0.027	0.045
Proximal Ulna	0.038	0.029	0.030	0.035
Shaft of Ulna	0.025	0.022	0.026	0.038
Distal Ulna	0.043	0.041	0.026	0.061
Proximal Radius	0.048	0.033	0.038	0.046
Shaft of Radius	0.025	0.021	0.025	0.035
Distal Radius	0.059	0.064	0.030	0.060
Pelvis	0.083	0.063	0.037	0.091
Proximal Femur	0.079	0.064	0.038	0.097
Shaft of Femur	0.029	0.029	0.024	0.050
Distal Femur	0.109	0.063	0.043	0.094
Proximal Tibia	0.079	0.059	0.035	0.089
Shaft of Tibia	0.029	0.023	0.023	0.047
Distal Tibia	0.041	0.037	0.030	0.055
Fibula	0.037	0.054	0.021	0.043
Tarsus/Carpus	0.034	0.033	0.015	0.039
Patella				0.042
Metatarsus, Metacarpal, Phalanges	0.037	0.028	0.027	0.038
Skull	0.053	0.033	0.032	0.044
Mandible	0.038	0.025	0.026	0.039

TABLE 9. Radium Activity in Bone

		% Injected Dose μCi/g Ash	
Dog No.	Day of Sacrifice	Vertebra	Femur Midshaft
SJ1	100	0.027	0.035
SJ2	25	0.128	0.038

other cases it was included in the sample containing tarsus and carpus.

The results in Table 8 cannot be compared between animals as the ash weight of the individual bones is different. To allow a comparison, these figures have been adjusted to a theoretical skeletal ash weight of 500 g. This adjusted activity is shown in Table 10. (Note that this adjustment has been applied to the values in Table 8 although these values are not for the whole skeleton. This explains the differences in average activity between Table 6 and Table 10.)

When the normalized results in Table 10 are considered and also the normalized whole-body activities in Table 6, it is seen that at 100 days the figures for ^{45}Ca and ^{133}Ba are similar although there is a divergence in the values at 25 days, ^{133}Ba being lower by a factor ≈ 1.5. This observation bears out the plasma clearance curves which show a similar divergence. This difference may be related to the lack of diffuse activity as seen in the ^{133}Ba autoradiographs and discussed later in this report. Complete quantitative analysis of the autoradiographs is still in progress, and more data are required to confirm the above observation.

In Table 11 the ratio of the activity of the individual sites to the average activity of all the sites listed in Table 10 is shown. Included also are the same ratios for ^{133}Ba and ^{45}Ca from the JJ dogs analyzed at 7 days. These ratios appear consistent throughout, suggesting a similar distribution of isotope within each animal including the JJ dogs. Trabecular bone shows consistently throughout the skeletons a much higher ratio of activity than cortical bone. The vertebral ratios are uniform with the exception of the

TABLE 10. Normalized Activity per Gram Ash

Bone	% Injected Dose (500 g)			
	^{133}Ba		^{45}Ca	
	Dog SJ1 100 days	Dog SJ2 25 days	Dog SJ3 100 days	Dog SJ10 25 days
Atlas and Axis	0.014		0.014	
Cervical Vertebra II	0.032		0.031	
Cervical Vertebra III	0.023	0.033	0.022	0.056
Upper Thoracic Vertebra	0.066	0.091	0.030	
Lower Thoracic Vertebra	0.035	0.089	0.036	
All Thoracic Vertebrae	0.056	0.090	0.033	0.126
Upper Lumbar Vertebra	0.047		0.053	
Lower Lumbar Vertebra	0.049		0.025	
All Lumbar Vertebrae	0.048	0.072	0.039	0.107
Sacrum and Caudal Vertebrae	0.051	0.065	0.049	0.083
Sternum	0.119	0.163	0.084	0.235
Proximal Rib	0.052	0.055	0.039	0.085
Shaft of Rib	0.051	0.059	0.033	0.093
Distal Rib	0.126	0.179	0.076	0.233
Scapula	0.038	0.045	0.021	0.069
Proximal Humerus	0.079	0.054	0.031	0.114
Shaft of Humerus	0.020	0.021	01020	0.039
Distal Humerus	0.025	0.022	0.018	0.037
Proximal Ulna	0.019	0.021	0.020	0.029
Shaft of Ulna	0.012	0.017	0.017	0.031
Distal Ulna	0.021	0.029	0.017	0.050
Proximal Radius	0.024	0.023	0.025	0.038
Shaft of Radius	0.012	0.015	0.017	0.029
Distal Radius	0.029	0.045	0.020	0.049
Innominate Bone	0.041	0.045	01024	0.075
Proximal Femur	0.039	0.045	0.025	0.808
Shaft of Femur	0.014	0.021	0.016	0.041
Distal Femur	0.053	0.045	0.028	0.077
Proximal Tibia	0.039	0.042	0.023	0.073
Shaft of Tibia	0.014	0.016	0.015	0.039
Distal Tibia	0.020	0.026	0.020	0.045
Fibula	0.018	0.038	0.014	0.035
Tarsus/Carpus	0.017	0.023	0.010	0.032
Patella				0.034
Metatarsus, Metacarpal, Phalanges	0.018	0.020	0.018	0.031
Skull	0.026	0.023	0.021	0.036
Mandible	0.019	0.018	0.017	0.032
Average	0.039	0.048	0.027	0.069

TABLE 11. Ratio of Local/Average Skeletal Activity.

Dog No.	SJ1 100 Days	SJ2 25 Days	SJ3 100 Days	SJ10 25 Days	JJ Dogs 7 days ^{133}Ba	JJ Dogs 7 days ^{45}Ca
Atlas and Axis	0.36		0.52			
Cervical Vertebra II	0.82		1.15			
Cervical Vertebra III	0.59	0.69	0.81	0.81	0.805	0.845
Upper Thoracic Vertebra	1.69	1.90	1.11			
Lower Thoracic Vertebra	1.18	1.85	1.33			
All Thoracic Vertebrae	1.44	1.88	1.22	1.83	2.01	1.94
Upper Lumbar Vertebra	1.21		1.96			
Lower Lumbar Vertebra	1.26		0.93			
All Lumbar Vertebrae	1.23	1.50	1.44	1.55	1.69	1.69
Sacrum & Caudal Vertebra	1.31	1.35	1.81	1.20	1.67	1.56
Sternum	3.05	3.40	3.11	3.41	3.94	3.49
Proximal Rib	1.33	1.15	1.44	1.23		
Shaft of Rib	1.31	1.23	1.22	1.35	1.49	1.37
Distal Rib	3.23	3.73	2.81	3.38		
Scapula	0.97	0.94	0.78	1.00	0.93	0.88
Proximal Humerus	2.03	1.13	1.15	1.65		
Shaft of Humerus	0.51	0.44	0.74	0.57	1.09	1.115
Distal Humerus	0.64	0.46	0.67	0.54		
Proximal Ulna	0.49	0.44	0.74	0.42		
Shaft of Ulna	0.31	0.35	0.63	0.45	0.59	0.59
Distal Ulna	0.54	0.60	0.63	0.72		
Proximal Radius	0.62	0.48	0.93	0.55		
Shaft of Radius	0.31	0.31	0.63	0.42	0.53	0.55
Distal Radius	0.74	0.94	0.74	0.71		
Innominate Bone	1.05	0.94	0.89	1.09	1.20	1.19
Proximal Femur	1.00	0.94	0.93	1.16	1.385	1.16
Shaft of Femur	0.36	0.44	0.59	0.59	0.48	0.56
Distal Femur	1.36	0.94	1.04	1.12	1.425	1.34
Proximal Tibia	1.00	0.88	0.85	1.06		
Shaft of Tibia	0.36	0.33	0.56	0.57		
Distal Tibia	0.51	0.54	0.74	0.65	0.61	0.71
Fibula	0.46	0.79	0.52	0.51		
Tarsus/Carpus	0.44	0.48	0.37	0.46	0.610	0.49
Patella				0.49		
Metatarsus, Metacarpal Phalanges	0.46	0.42	0.67	0.45	0.685	0.49
Skull	0.67	0.48	0.78	0.52	0.66	0.72
Mandible	0.49	0.38	0.63	0.46	0.62	0.72

axis plus atlas sample. This sample is more like compact bone than trabecular bone. An unexpected finding is the very high ratios found in the sternum and in the distal parts of the ribs. In the 100-day animals the ratio is smaller than that at 25 days, and this ratio is smaller than that at 7 days (JJ dogs). This suggests that the sternum in all these dogs has a much higher turnover rate than the rest of the skeleton. The change in the ratio is greater with ^{133}Ba than with ^{45}Ca. A similar change, though less marked, is seen in the vertebrae of the dogs.

The specific activity of ^{45}Ca (Table 10) is consistently lower in all samples at 100 days compared with 25 days after injection. The decrease of ^{133}Ba activity between 25 and 100 days is not as great. This may be due to the retention of ^{133}Ba on bone surfaces, which is seen in the autoradiographs.

In Table 12 the activities of selected bones from the skeletons of the SJ dogs are compared with the activities of the same bones from previous experimental work.[9] To allow for a direct comparison the activities, expressed as percent injected dose per gram ash, have been normalized by a factor to bring the ash weight of the selected bones to 50 grams. The ^{133}Ba data extend to 3118 days after injection, although the last data are not really comparable to the present work as the animal injected was only 8 months old at the time of injection. The average activity values have been plotted, and if one ignores the last point from the 8 month old dog, it is possible to draw a straight line through the points on log-log paper. The line has a slope of $t^{-0.137}$. A similar plot for the ^{45}Ca points produces a slope of $t^{-0.382}$ although it would be equally possible to make this slope steeper or shallower. The ratio of the above slopes is very similar to the ratio of the retention slopes listed in Table 7, suggesting a constant difference in the handling of ^{45}Ca and ^{133}Ba.

Autoradiographic studies

As previously stated, a complete autoradiographic, microradiographic, and tetracycline comparative analysis has been started on bone

TABLE 12. Activities Normalized to 50-g Total Sample Ash Weight

Bone	% Injected Dose per Gram Ash								
	^{133}Ba						^{45}Ca		
Dog	156	A22D	SJ2	SJ1	576	A22B[a]	A22B[a]	SJ10	SJ3
Days from injection	7	7	25	100	1508	3113	7	25	100
Femur	0.052	0.110	0.067	0.051	0.042	0.064	0.105	0.114	0.040
Tibia	0.036	0.058	0.052	0.041	0.037	0.066	0.066	0.092	0.032
Humerus	0.055	0.104	0.059	0.066	0.036	0.066	0.091	0.112	0.040
Radius	0.032	0.047	0.071	0.036	0.036	0.082		0.067	0.035
							0.049		
Ulna	0.034	0.057	0.040	0.029	0.042	0.070		0.065	0.030
Lumbar vertebra	0.072	0.078	0.132	0.079	0.039	0.040	0.124	0.186	0.065
Average	0.034	0.079	0.069	0.050	0.037	0.065	0.088	0.108	0.040

[a] This animal was 8 months old at the time of injection of ^{133}Ba and ten years old at the time of the ^{45}Ca injection.

samples from all fourteen dogs used in this experiment. Most of the final microscopic measurements are still to be made. A few preliminary measurements on some autoradiographs are given in Table 13. These are raw data of densitometer measurements of maximum surface density, that is, the density on the autoradiograph in an area that corresponds to an intense surface uptake of the isotope. It should be further noted that the surface areas chosen were not related to tetracycline label and thus were not growing surfaces.

Qualitative studies of the autoradiographs together with fluorescence observation of the corresponding section show that not all areas of intense activity are associated with the tetracycline label. There is only slight diffuse activity of ^{133}Ba, and even at one hundred days a clear surface activity is distinguishable in the ^{133}Ba autoradiographs in contrast to ^{45}Ca autoradiographs. Comparison of autoradiographs from the 25- and 100-day dogs shows a fall in activity between these two times comparable to the fall in activity seen in the radiochemical data.

TABLE 13. Surface Density Measurements

Time after Injection	Autoradiographic Film Darkening[a] ^{133}Ba	^{45}Ca
12 min	1.12	
1 hr	1.70	
5 hr	2.19	0.77
1 day	1.82	1.30
5 days	1.12	1.00
25 days	0.98	0.27
100 days	0.80	0.00

[a] Darkening (D) is used in place of photographic density. $D = \log_{10} I0/I$, where I_0 and I are the incident and transmitted light intensities, respectively.

During the qualitative studies, tetracycline labeling in two animals from a dose of tetracycline given in 1960 was observed. This long-term retention of the tetracycline label is inconsistent with high bone turnover rates which have been proposed.

Kinetics

Table 14 lists the parameters used for the calculation of kinetic A-values. Kinetic A-values express the long-term rate of ion flow from blood to bone and are expressed in grams of calcium per day. The calculations were performed using the formula

$$A = \frac{R(\lambda_S - \lambda_R)}{S + \lambda_S I},$$

where R = fractional retention in the whole animal

S = the plasma specific activity (% injected dose/g Ca)

λ_S = the rate constant of the tangent to the S curve

λ_R = the rate constant of the tangent to the R curve

I = the time integral of S from the time of injection.

The time used for all calculations was 5 days.

Each of the parameters is derived from an experimental observation with certain exceptions. In Dogs SJ3 and SJ10, R_5 was calculated from the final retention determined by ashing. The value of R_5 in SJ12 was taken as the average of R_5 value of SJ3 and SJ10.

TABLE 14. Kinetic A-Values.

Dog No.	Isotope	R_5, %	S_5, % Dose/gCa	I_5, % Dose Days/gCa	λ_S, Day^{-1}	λ_R, Day^{-1}	A_5/c, %/day	Ba/Ca, A_5/c
SJ1	^{133}Ba	33	6.88	133	0.252	0.099	0.136	1.50
SJ3	^{45}Ca	48	12.34	230	0.204	0.063	0.094	
SJ2	^{133}Ba	29.5	3.20	68	0.204	0.116	0.116	1.45
SJ10	^{45}Ca	56	17.21	300	0.289	0.063	0.080	
SJ8	^{133}Ba	41.4	5.07	129.6	0.277	0.107	0.116	3.37
SJ12	^{45}Ca	52	53.35	475	0.217	0.063	0.038	

In the calculation of A_5/c the total skeletal calcium (c) of SJ8 and SJ12 was calculated from whole-body weight using the ratios of skeletal calcium/whole-body weight found experimentally in the other four dogs. This ratio (0.010) is much the same as found by Ellsasser et al. but lower than the ratio suggested by Van Dilla of 0.0135.[10]

A_5/c values in these dogs differ somewhat from those of the JJ dogs. Generally, ^{133}Ba values are lower and the ^{45}Ca values higher. Nevertheless, the ratios

$$\frac{^{133}Ba\ A_5/c}{^{45}Ca\ A_5/c}$$

are consistent with the Ellsasser values.

Summary

An exhaustive study has been performed on fourteen 6- to 10-year-old beagle dogs from the Argonne stock line to follow their bone and alkaline earth metabolism. The isotopes ^{45}Ca, ^{133}Ba, and ^{226}Ra were used with tetracycline to mark growing bone. Age-matched pairs of dogs were injected with either ^{45}Ca or $^{133}Ba/^{226}Ra$ mixture. All dogs received tetracycline markers. Blood was taken serially until sacrifice, which followed at from 12 min to 100 days after injection of isotope. Dogs injected with $^{133}Ba/^{226}Ra$ which were to survive longer than one day were also studied with whole-body counting techniques.

At sacrifice selected bones were studied autoradiographically, and in several animals total skeletal radiochemical studies were undertaken. In all animals samples of soft tissue also were taken for radiochemical analysis. Plasma clearance curves have been constructed for all animals and also whole-body retention curves for the ^{133}Ba dogs. Terminal ^{45}Ca retention is available in two dogs. Results to date show that the long-term retention of ^{133}Ba is higher than that of ^{45}Ca, and autoradiographically this appears to be due to persistence of surface activity. The plasma specific activity of ^{45}Ca after an initial delay falls more steeply than the ^{133}Ba curve although at 100 days the values were almost identical. Much of the ^{133}Ba activity is not associated with growth areas as identified by the tetracycline label, whereas areas of high ^{45}Ca activity are more commonly so associated.

In two animals a tetracycline dose given therapeutically in puppyhood was still widely present in the bones, demonstrating long-term survival of some parts of the matrix. Much further work has to be carried out before all the information available has been extracted from this equipment.

References

1. Ellsasser, J. C., J. E. Farnham, and J. H. Marshall. Comparative Kinetics and Autoradiography of ^{45}Ca and ^{133}Ba in Ten-Year-Old Beagle Dogs. Argonne National Laboratory Radiological Physics

Division Annual Report, July 1967 through June 1968. ANL-7489, pp. 25-30.

2. Ellsasser, J. C., J. E. Farnham, and J. H. Marshall. Comparative Kinetics and Autoradiography of ^{45}Ca and ^{133}Ba in Ten-Year-Old Beagle Dogs. J. Bone Joint Surg. 51A, 1397-1412 (1969).
3. Marshall, J. H. Theory of Alkaline Earth Metabolism. The Power Function Makes Possible a Simple but Comprehensive Model of Skeletal Systems. J. Theoret. Biol. 6, 386 (1964).
4. Marshall, J. H. Measurements and Models of Skeletal Metabolism. Mineral Metabolism, Ed. C. Comar and F. Bronner. Academic Press, New York, 1969, Vol. III, pp. 1-122.
5. Parr, R. M., and H. F. Lucas, Jr. A Rigorous Least Squares Analysis of Complex Gamma-Ray Spectra with Partial Compensation for Instrumental Stability. IEEE Trans. Nucl. Sci. NS-11 (3), 349-357 (1964).
6. Analytical Methods for Atomic Absorption Spectrophotometry. Perkin-Elmer, Norwalk, Conn., 1968.
7. Lucas, H. F., Jr. Correlation of the Natural Radioactivity of the Human Body to that of its Environment: Uptake and Retention of ^{226}Ra from Food and Water. Argonne National Laboratory Radiological Physics Division Semiannual Report July-December 1960. ANL-6297, pp. 55-66.
8. Dudley, R. A., and B. M. Dobyns. The Use of Autoradiographs in the Quantitative Determination of Radiation Dosage from ^{45}Ca in Bone. Science 109, 327 (1949).
9. Farnham, J. E. and R. E. Rowland. The Retention of ^{133}Ba in Beagles. Argonne National Laboratory Radiological Physics Division Annual Report July 1968 through June 1969, ANL-7615, pp. 32-38.
10. Van Dilla, M. A., B. J. Stover, R. L. Floyd, D. R. Atherton, and D. H. Taysum. Radium (^{226}Ra) and Radon (^{222}Em) Metabolism in Dogs. Radiation Res. 8, 417-437 (1958).
11. Maletskos, C. J., A. L. Keane, A. C. Telles, and R. D. Evans. The Metabolism of Intravenously Administered Radium and Thorium in Human Beings and the Relative Absorption from the Gastro-intestinal Tract of Radium and Thorium in Simulated Radium Dial Paints. MIT Annual Progress Report MIT 952-3 (May 1966), pp. 202-318.

ESTIMATES OF THE RADIATION-INDUCED LEUKEMIC RISK IN MAN*

L. D. Marinelli

The radiation-induced leukemic risk in man is calculated from data available in the literature up to mid-year 1970 on leukemogenesis induced by internal and external radiation. The calculations support a) the validity of the use of integral dose in estimates of risk in partial exposure and b) the lack of effect of dose fractionation. Both results apply to high dose rates. There is some evidence of lowered leukemogenic efficiency at low dose rates, in accord with experimental evidence in laboratory animals. The results, however, are not beyond the limits of statistical uncertainty.

Introduction

The accelerated growth of the atomic power industry has brought to focus the need of refining estimates of human risks resulting from exposure to ionizing radiation.

Although considerable knowledge has accumulated on the characteristics of radiation injury in laboratory animals, the problem of translating quantitative effects from animals to man remains unsolved. Without a detailed knowledge of the mechanisms operating in the species involved, this translation will always remain on somewhat questionable grounds. Even if one were willing to accept empirical extrapolation, there remains the task of extending comparisons among several species, choosing several end effects and choosing irradiation conditions comparable to those which are relevant to radiation protection. The requisite of low dose rates and low incidence of effect adds to logistic difficulties, as discussed and elaborated repeatedly in the past.[1,2] It seems obvious, therefore, that in order to obtain credible estimates of risk it is imperative to gather as many data as possible directly on man.

The sources of this information are not many: the Japanese survivors

*Invited paper presented at the XVI National Congress of the Associazione Italiana di Fisica Sanitaria e Protezione contro le Radiazioni, Florence, September 24-26, 1970.

rank among the most relevant, inasmuch as they were exposed in toto; in their case, the most troublesome problem is the assessment of the doses involved. This task is yet to be completed to this day.[3] Another group is concerned with past industrial exposure to internal emitters, namely with the contamination of radium dial painters, where dosimetric problems are tedious but solvable, but where the range of burden values is rather wide, considering the number of individuals at risk.[4,5]

The next group where dosimetry is wholly acceptable involves patients exposed to therapeutic and to diagnostic radiation including radiation from internal emitters, such as ThO_2. With certain precautions involving dose magnitudes and type of patients, these medical groups have yielded the largest number of suitable individuals. Lastly, there are large populations exposed to different amounts of background radiation; as we shall see later, the estimates from this group (which under ideal conditions should yield the most reliable results because the dose rate is close to those prescribed by maximum permissible levels) are subject to imponderable uncertainties introduced by quasi-epidemiological factors for which satisfactory corrections are difficult, if not impossible, to make.

At the present time the ICRP is proceeding most vigorously, yet carefully, in the estimate of risks; it assumes that the magnitude of the effect is linear with dose, irrespective of its fractionation, both temporal and spatial, and of the rate at which it is being delivered.

Calculations of Approximate Incidence of Risk

In the estimates that follow, the risk considered is restricted to the occurrence of all leukemias except the chronic lymphocytic type. For exposure times short compared to the time at risk, the risk is calculated by the following expression

$$\epsilon = \frac{n}{NDT} = \frac{\dot{n}}{N} \cdot \frac{1}{D} \quad ,$$

where ϵ is oncogenic risk per man-year per rad, n is the number of leukemia cases in excess of those expected observed during an average period of time T after irradiation, N is the total population exposed and D is the total mean dose to the marrow. Numerically ϵ is equal to the average rate of incidence per year, $\dot{n}$, per unit population, divided by the total mean dose.

If the exposure is constant at rate $\dot{D}$ and prolonged, one proceeds to consider the rate of increase in leukemias arising in a population N at time t; namely,

$$\frac{dn}{dt} = \epsilon N\dot{D}t \ .$$

After the irradiation time t and a period of risk T-t (T being the time between beginning of irradiation and time of observation), the total number of cases will be

$$n\Big]_0^T = \epsilon N\dot{D} \int_0^t (T-t)dt \ ;$$

following integration, the preceding equation can be written as

$$n = \epsilon N\dot{D}t(T-t/2)$$

from which one obtains

$$\epsilon = \frac{n}{ND} \frac{1}{(T - \frac{t}{2})} \ ,$$

where $D = \dot{D}t$ = total dose and $T - \frac{t}{2}$ is the average time at risk. For the case where t = T (irradiation time = maximum period of observation) this expression becomes:

$$\epsilon = 2\bar{\dot{n}}/ND \ .$$

This equation is applicable to the marrow dose due to thorotrast injections. These equations are similar to the one applicable to instantaneous irradiation if either the average accumulated dose $\dot{D}T/2$ is substituted for the total dose or the time at risk considered is the average for the population.

A formula for use in calculations of risk to a population exposed to

background radiation can be derived when the number of leukemias has been observed for an age range $T_2 - T_1$, where T_2 is the population life-span. One calculates the number of cases n_2 and n_1 corresponding to continual exposure for times T_2 and T_1 respectively as

$$n_2 = \epsilon N \dot{D} T_2^2/2 \qquad n_1 = \epsilon N \dot{D} T_1^2/2 ,$$

from which the total number of cases occurring between age T_2 and T_1 is simply

$$n_2 - n_1 = \epsilon N \dot{D}(T_2^2 - T_1^2)/2 .$$

From this expression the average rate of incidence in the age group can be calculated as follows:

$$2\bar{\dot{n}} \Big|_{T_1}^{T_2} = 2(n_2 - n_1)/(T_2 - T_1) = \epsilon N \dot{D}(T_2 + T_1)$$

or

$$\epsilon = \bar{\dot{n}}\,[N\dot{D}(T_2 + T_1)/2]^{-1} = \bar{\dot{n}}\,[N(D_1 + D_2)/2]^{-1} .$$

This expression tells that the oncogenic risk ϵ is equal to the average number of cases observed per unit time during the <u>period of observation</u> divided by the population times the total dose accumulated <u>up to the middle of the age span under consideration</u>.

It is well to note that the last formula is only approximate, even for the case of a linear dose-effect relationship, since it does not take into account the age composition of the population. More precisely, the assumption is made that the number of individuals within a given age interval is constant throughout the population and that there is a single life-span for all individuals.

Leukemogenesis from Partial Body Irradiation at High Doses

A category of patient which is extremely useful because it gives us an insight as to what areas epidemiological studies must avoid, has been covered by two surveys of therapeutically treated patients suffering from cancer of the cervix uteri.[6,7] Since both give comparable results (shown in Table 1), we shall discuss the one covering the largest number of patients, approximately 25,500, from several countries. The period of follow-up was short, only 2.1 yr, but it did cover post-treatment periods greater than 15 yr. The actual number of proved and suspected leukemia cases reported in irradiated patients was 6 (vs. 5.1 to 5.8 expected), and of these only two were of the granulocytic type. Of those remaining, two were definitely chronic lymphocytic and two were either probable or unspecified lymphocytic leukemia. Although the difference is not significant, we may calculate an order of magnitude of the effect by noting that two cases, vs. 1.6 expected, were noticed in the post-treatment period of 4 to 8 yr. This subgroup with 18,305 man-yr at risk yields the positive leukemogenic index of 2×10^{-8}/man-rad/yr, nearly two orders of magnitude below the well-known incidences of the spondylitics and the Japanese survivors. Even if the upper 1% confidence limit of the incidence excess is taken, i.e., 35×10^{-5} per 10^3 rads, the leukemogenic index of 0.35 would still be lower by a factor of 4.

The series of Dickson, much smaller but followed longer, where less than one case would be expected, yielded no cases of leukemia.

These results are in general accord with the experimental findings that cancer incidence per rad under high doses declines as the doses get to 1,000 rads and beyond. One must recall that in these examples the actual average dose delivered to about 1/3 of the marrow was definitely cytotoxic, being in the vicinity of 3,000 rads.

That the cytotoxic factor is the most likely to account for these medically negative results is suggested by the fact that in treatment of uterine bleeding, where practically the same anatomical region is treated,

TABLE 1. Radiation-Induced Leukemia: Adults

Population	N	T	D	$\bar{D}$	n	ϵ	Ref.
			High doses				
Hutchinson	NT = 18305		3000	1000	0.4	0.02	6
Dickson	858	> 15	3000	1000	0.0	0.0	7
			Medium doses				
Court-Brown, et al.	14554	7	250-3000	~400	52	1.3	8 (pp.6,7)
Japanese surv.	1.4×10^5	11	ICRP	#14	149	1.5	9
Doll and Smith	2068	13.6	400	136	4.7	1.2	10
Brinkley, et al.	277	16.0	400	136	0	0	11
Dickson	1817	15.2	140	66	3-5	1.6-2.7	7

N = population at risk T = years at risk D = local dose
$\bar{D}$ = average dose to the marrow n = excess cases of leukemia
ϵ = leukemic risk per 10^6-man-year-rads. Doses in rads

but with doses only 1/6 to 1/8 as high, the leukemogenic efficiency is much higher, as we shall see.

Medium Doses

The epidemiological group covering moderate radiation dose to substantial fractions of the hemopoietic system have yielded, at least in two instances, risk estimates which have attracted the attention of both the ICRP[8] and the UNSCEAR.[9]

The results from these two groups, namely the spondylitics and the Japanese survivors, have been analyzed repeatedly and will not be examined further except to point out that the risk estimates are fairly consistent, even though the pattern of temporal and spatial distribution of the dose is quite different in the two groups. Different also is the fact that the synergistic effect of medication might have been present in the first instance and not in the other. From the statistical point of view they offer the largest number of cases and yield--although not very precisely--some information on the dose-effect relationship. The latter is consistent with linearity.

Added to these data, the information resulting from three recent studies may be of great value; in Table 1 they follow the two studies just mentioned. They involve the follow-ups of women treated for uterine bleeding either by external x-ray radiation[10,11] or the use of internal radium therapy.[7]

The first two involve two surveys of 2,068 and 277 patients each followed for 13.6 and 16.0 yr, respectively. The average doses to portions of the marrow and the mean dose to the whole marrow have been explicitly stated by the authors of the first study, and there is very little reason to think that they differ very much in the other series.

The leukemogenic efficiencies in these two series are compatible since in the series of Brinkley et al. the expected number of cases is only 0.24, in accord with no cases observed. Combining both series with appropriate weights would bring ϵ down to a little over the figure of 1×10^{-6} man-yr^{-1}/rad, that is, not significantly different from the rest of the group. Of considerable interest is the series of 1,817 cases of Dickson treated for the same reason but at lower doses because intrauterine radium treatment was used exclusively. This limited the local marrow doses to less than 400 rads at any one point and the pelvic average to 140 rads, bringing down the average for the whole marrow to only 66 rads. There is no question that the uncertainty in these doses may be considerable and hence merits direct investigation. What is remarkable is the fact that the leukemogenic index of 1.6 to 2.7 of this series is not statistically different from the results obtained from the spondylitics and the Japanese survivors, where a much greater fraction of the marrow was irradiated.

Low Dose Rates

It would be of great usefulness to be able to derive a reliable figure for the cancerogenic risk index for man of radiation delivered at dose rates comparable to maximum permissible levels. The difficulties are great because of the large populations required to obtain statistically significant

results and of the requirement to control--or at least recognize and allow for--the many extraneous factors unrelated to radiation that can vitiate the results. An attempt to do so is shown in Table 2.

TABLE 2. Radiation-Induced Leukemia: Adults

Populations	N	T	D	$\bar{D}$	n	ϵ	Ref.
			Low dose rates				
Radiologists	3521	13.9	2000	600(?)	11.3	0.4	13
Single I^{131} dose	18379	6.5	20	20	1.0	0.5	15
			Special populations				
Repeated I^{131}	4021	10.5	20	20	4.6	5.5	15
I^{131} after surgery	3.311	7.8	21	21	6.0	11.0	15
P^{32} in Polycythemia	329	13.2	141	141	35	60.0	17
			Background radiation				
Three cities in Scotland	1.8×10^5	17	0.7	0.02	42	16	18

N = population T = years of follow-up D = local cose.
$\bar{D}$ = average dose to marrow n = excess cases of leukemia ϵ = leukemia risk per 10^6 man-year-rad
Doses in rads

The group consisting of practicing radiologists would be very useful, inasmuch as there has been found in the older fraction of the profession a net increase in leukemia which has practically disappeared as more stringent norms of protection have come into practice.[13] The most difficult parameter to assess is the average dose to the marrow, since no suitable instrumentation was available at the time to measure scattered radiation reaching the radiologist. Measurements with modern instruments on antiquated diagnostic apparatus have been made by Braestrup[14] who estimated a cumulative exposure of 2,000 surface roentgens for a professional lifetime of 40 yr. This would average to a lifetime dose of about 600 rads to the marrow, delivered at the order of about 0.1 rad/day. With these dosimetric assumptions the leukemogenic risk comes to the order of 0.40×10^{-6} man-yr^{-1} rad^{-1}. Unfortunately, very serious doubts can be cast on this figure

because the range of the average dose received by the individual radiologist could have varied easily by two or more orders of magnitude, and only those most exposed could have been the victims of the disease; the average obtained would be strictly valid only if a linear dose-effect relationship were to apply over such a wide range. The only useful hint that one may get from these figures is that the risk at low dose rates may be lower than that from the high-dose-rate exposures.

Of higher reliability is the survey on the incidence of leukemia following treatment of hyperthyroidism.[15] This study is of unusual interest because it concerns the effect of low doses on the marrow, namely averages of 20 rads[16] delivered at a mean rate of less than 3 rads/day. The maximum rate at any one time does not exceed 700 mrad/hr and hence is closer to rates of relevance in protection than the dose rates used therapeutically. In order to balance out a possible relationship between incidence of hyperthyroidism and incidence of leukemia, the comparison was made by studying patients treated surgically with those treated with I^{131}. The incidence observed was 14 cases for 119,000 man-yr for the I^{131} treated group and 10 cases for 114,000 man-yr for the surgically treated group. When age and time of follow-up adjustments were made, the resulting incidences were 11 ± 2.8 and 10 ± 3.01 cases for 100,000 man-yr. The actual difference in the rate, which comes to 1 ± 4.2, can be expressed as a risk of 0.5 cases for 10^6 man-yr rad. This is lower by a factor of 3 than the leukemogenic efficiency found in the irradiations delivered at therapeutic dose-rate levels, but it is not statistically significant since the upper 95% confidence limit exceeds the high dose rate figure of 1.5 cases/10^6 man-yr rad. We can only say at this moment that the result is in the same direction as the results which one repeatedly finds in radiation biology, namely, that at low dose rates the effect per unit dose diminishes because recovery from radiation intervenes. A confirmation of this result with better statistical significance would be invaluable for a better and more realistic estimation of radiation risks at maximum permissible levels.

This study has also revealed the statistically significant effect of pretreatment surgery on the effect of I^{131}. In a subsample of 26,000 man-yr the incidence of leukemia in the surgical-I^{131} group is over 2.5 times that of the other groups combined. When account is taken of the control incidence, the leukemogenic effect of radiation is shown to increase more than twenty-fold. A lesser but definite increase is shown also after repeated doses of I^{131}. These results are consistent with the hypothesis that the stress of partial thyroidectomy acts synergistically with the leukemogenic effect of radiation on the hemopoietic system.

A group of patients which appears to be also unusually sensitive to radiation leukemogenesis is the group of polycythemics treated with P^{32}.[17] The dose rate to the marrow is definitely lower than the rates used in x-ray therapy. The results of Modan et al. have been analyzed from their raw data. The average dose to the marrow of 141 rads is not as low as in some other surveys, but the number of leukemias in his follow-up is over 10% of the number of patients treated. The leukemogenic index is the highest recorded, 60×10^{-6} man-yr^{-1}rad^{-1}. The explanation for this result has been advanced by several clinicians: it is not the transmutation effect of P^{32} in cell nuclei that is suspected but the propensity of the polycythemic state to change spontaneously into the leukemic state with the passage of time. This becomes possible and evident with the increase in survival time afforded by P^{32} therapy.

We close this class of exposure with the results of Court-Brown, Doll, Spiers, Duffy, and McHugh[18] on the geographical variation in leukemia mortality in relation to background radiation and other factors. The leukemia rate, as calculated from vital statistics in certain cities of Scotland, was compared to the backgrounds existing therein, as assayed by comprehensive physical measurements. The difference of the radiation background rate, due mostly to the nature of the building materials prevailing in the different towns, amounted to an average maximum of about 20 mrads/yr. The mortality rates due to leukemia were different and in the right direction,

although not entirely consistent with the dose rates measured at the four cities. The difference is, however, statistically significant and yields a leukemogenic efficiency 10 times higher than the one obtained for the spondylitics and Japanese survivors.

This result illustrates what imponderable factors may be interjected when the effect of very low radiation doses are considered; in this case the difference observed is attributed to socio-economic factors, better case findings, effect of different use of medical x ray, etc.

The conclusions that one may reach examining the result obtained with surveys covering low dose rates is that it is virtually hopeless to depend on values of dose rates differing by only a fraction of the natural background radiation. According to Buck[19] a study of leukemic risk could barely be made with the population of the state of Kerala in India if the dose received there were of the order of 1 rad/yr, namely 50 times the maximum difference considered here. The main difficulty would be that of finding a suitable control population and a uniform case finding service in order to avoid the difficulties encountered in Scotland.

It is also obvious that populations susceptible to leukemia such as the polycythemics should be avoided and that, as in the cases of hyperthyroids, special endocrinological factors should be examined and corrected for when interpretation of results is in order.

Thus far the group most likely to succeed in yielding reliable results at low dose rate seems to be the thyrotoxicosis cases, provided that the present medical practice of using surgery will continue and allow the accumulation of a sufficient number of controls. The possibility of international cooperation has a lot to recommend it for enlarging the group under observation. The results of this group is in accord with current radiobiological experience, but it is obvious that it could be invaluable in estimating more accurately the safety factor which may be present at low dose rates.

Leukemia in Children and Infants

Three studies can be related to the risk of leukemia in children who were irradiated before the age of ten, and there is some interest in asking whether the risk of leukemogenesis could differ from that of the adult. Results are shown in Table 3.

TABLE 3. Radiation-Induced Leukemia in Children and Infants

Populations	N	T	D	$\bar{D}$	n	ϵ	$\bar{t}$	Ref.
Tinea Capitis pts.	2043	12	305-462	30	4	4 to 5	7.84	23
Thymic enlargement	2878	7	243	48	4	4	<0.5y	20
Japanese children	~ 2700	11	ICRP #14 (1969)			3.0	4.5y	24

N = population at risk T = years of follow-up D = average local dose
$\bar{D}$ = average dose to total marrow n = excess no. of leukemias
ϵ = leukemia risk per 10^6 man-year-rads; $\bar{t}$ = mean age at irradiation
Doses in rads.

Chronologically the work of Hempelman et al.[20] should be considered first, although it is perhaps less stringently defined from the dosimetric point of view. The leukemias followed therapeutic irradiation of a group of 2,878 infants of less than 6 months of age treated for the purpose of reducing thymic enlargement.

It should be kept in mind that the average dose to the marrow is only imperfectly known since the children were treated by different techniques. It is assumed that only 20% of the patient's marrow has been irradiated on the average, including most of the ribs and less than half of the spine. It should be also noted that in other series (Saenger[21] Conti and Patton[22]), where the field was smaller and the thymus was of normal size, comparable numbers of children were irradiated with comparable doses, but the appearance of leukemia was not more frequent than in unirradiated controls. It should also be noted that Hempelman et al. did not find an increase in leukemia after 7 yr past the irradiation.

Another series of an entirely different nature is presented by the work of Albert et al.[23] covering the leukemogenic sequelae of about 2,000 children whose scalps were irradiated with x rays for treatment of tinea capitis. In this case, the dosimetric information is on a much surer footing with regard to air dose and average dose to the exposed marrow. Some uncertainty exists as to whether the fraction of marrow exposed is about 10% of the total, as assumed in these calculations.

The elapsed time to diagnosis averages 9 yr, definitely longer than the accepted latent period following intra-uterine irradiation, but in fair accord with observations following irradiation of the adults. The absolute oncogenic risk is practically identical to that of the infants, although the average age at irradiation was 7.8 yr; this statement must be weighed by the considerable dosimetric uncertainty which faces the thymic patients.

The third series of individuals irradiated in childhood (less than 9 years old) is represented by Japanese survivors. The oncogenic risk, as calculated in the ICRP publication, p. 64,[24] on the basis of the latest data on the air dose at Hiroshima and Nagasaki results in the figure of 3×10^{-6} man-yr^{-1} rad^{-1}, but it should be noticed that no account has been taken of the probable effect of shielding. Once this is done, one more reliable figure will result which may decide definitely whether the leukemic risk, following partial irradiation of the body, can be calculated by considering the fraction of the marrow irradiated. As of now there is, from these three examples, a strong implication that integral dose averages can be made in estimating risk for homogeneous tissues, such as the marrow (Reference 24, p. 10). It will be recalled that the same conclusion was reached after examination of the results obtained from moderate irradiation of pelvic organs in women.

Irradiation in Utero

There exists a category of individuals that has gathered a considerable deal of attention from the radio-epidemiological point of view. This is the population irradiated in utero for diagnostic purposes. They are con-

sidered in Table 4.

TABLE 4. Leukemia: Irradiation in Utero

Population	N	T	$\overline{D}$	n	ϵ	Ref.
Japanese surv.	~ 500	20	~ 50	0	0	24
Mac Mahon	7.3×10^5	10	(2-5)	154*	10-4**	26

*Calculated by sampling of fraction of children irradiated

**Incidence of leukemia in irradiated children is usually expressed in terms of the incidence in non-irradiated children. Some samples: Mac Mahon 1.42; Graham, et al., 1.60; Stewart, et al. 1.60

The attention is well deserved since a) the total dose delivered is small and most probably of a mean value of 2 rads (1.5 to 3.0 rads),[25] and b) the radiation is delivered to the entire body and is fairly uniform. Fortunately, studies involving an adequately large number of individuals have been made in three instances, two in different sections of the United States[26, 27] and one in England.[28] These results on the relative risk of leukemia arising from in-utero radiation are eminently satisfactory from the statistical point of view. However, one must take into consideration the possible existence of extraneous factors modifying the relative incidence of leukemia in the child.

There are several characteristics in the results which deserve mention. One is the apparently high leukemogenic efficiency of diagnostic fetal radiation which appears to be from 3 to 6 times higher than in the adult. This is in sharp contrast to the apparently total lack of leukemia in the 500 Japanese survivors that were irradiated in utero at doses 25 to 30 times higher and have been followed for 20 yr. The calculated efficiency ϵ in these cases is zero, but there is a 5% chance that it could have been

as high as 6×10^{-6} man-yr^{-1} rad^{-1}. However, since some of the mothers might have been shielded and the effective dose could have been smaller, we can only conclude that the results of the Japanese survivors do not contradict the findings implicated by the results of diagnostic radiology. Of great interest is the analysis of Gibson et al.[29] who have been studying the effect of fetal diagnostic radiology in the children of a population of about 13 million people. In their quest of a possible combination of factors which might influence synergistically the incidence of fetal irradiation leukemogenesis they have limited their analysis to leukemia appearing at from one to four years of age, a period in which 50% of all leukemias appearing in the first decade of life take place.

Their results implicate the presence of the following leukemogenic cofactors associated with uterine radiation: 1) reproductive wastage (namely spontaneous miscarriages and stillbirths), 2) the presence of virus disease in the child plus preconception irradiation of the mother, and finally 3) the sum of these three cofactors.

The influence of the cofactors is shown in Table 5. The significance of these findings is not obvious, inasmuch as the radioleukemogenic risk

TABLE 5. Relative Leukemic Risk of Children Irradiated in Utero*

Factors and co-factors	Relative risk
No exposure	1.0
I.U. radiation only	1.06
I.U. radiation and reproductive wastage	7.71
I.U. pre-conception rad. and child virus	3.20
I.U. pre-conception rad. and virus and reprod. wast.	4.64
I.U. radiation (no other factors considered)	1.60

*From R. W. Gibson, et al., 1968[29]

due to reproductive wastage is sharply curtailed by the presence of child virus disease and preconception irradiation.

Fortunately, studies on cofactors and characteristics of latent periods is proceeding both in England and America, and there is a good chance that more light can be thrown on this subject, which apparently involves the most radiosensitive period of man.

Patients Injected with Thorotrast

Many of the patients injected for diagnostic purposes with Thorotrast--a colloidal suspension of ThO_2--do represent a specially important population for two reasons: a) many of their tissues are exposed to α radiation and b) the dose rate is low and protracted during their entire lifetimes.

TABLE 6. Leukemias: ThO_2 Cases (Internal α Emitter)

Country	N	$\dot{D}$	T	n	ϵ	Ref.
Denmark	758	7.7 - 12.9	22	7	4.8 - 2.9	30
Portugal	930	9.4 - 15.6	23	9	3.9 - 2.3	31
Sweden	436	5.8 - 9.7	22	1	1.6 - 1.0	32
Total	2124	8.1 - 13.4	22.7	17	3.85 - 2.3	

Risk = $\epsilon = 2n/N\dot{D} \times 10^6$ = incidence per million man-year-rad

$\dot{D}$ = rads y^{-1} (Parr and Kaul[12]) N = population at risk

T = years at risk n = no. of leukemic cases

The relevant data in Table 6 have been gathered from the published literature.[30-32] They show that in over 2,000 people the follow-up time averages 23 yr and the average dose rate to the marrow ranges between 8 and 13 rads/yr. The average latent period for leukemia in this group is about 17 yr, namely a period much longer than that corresponding to acute exposures. It must be noted that this figure is appropriate only to the follow-up

time of 23 yr because the leukemia appearance rate should increase with time, since the marrow is being irradiated continually at a nearly uniform rate. Hence, the specific risk, as calculated by the appropriate formula, namely 2.3 to 3.8 cases/yr/million man-rads, is probably a low provisional estimate.

It is of interest to calculate the RBE for α-radiation leukemogenesis in man from these numbers. We can attempt the calculation by comparison of the ε's between the Thorotrast group and two others. These are the medium dose (high dose rate) group and the low dose (low dose rate) group of the hyperthyroids treated with I^{131}. In Table 7 we see that the RBE's are from 2.6 to 1.5 for the first case and from 7.5 to 4.6 in the second case.

TABLE 7. Comparisons of RBE

Leukemia in man (α vs. x-ray radiation)

$$\frac{\text{Thorotrast: } \alpha \text{ (low dose rate)}}{\text{Spondyl.: x-ray (high dose rate)}} = \frac{3.85}{1.5} = 2.6 \text{ max; } \frac{2.3}{1.5} = 1.5 \text{ min.}$$

Myeloid leukemia in mice (neutrons vs. x-ray radiation) Ref. 34

$$\text{RBE} = \frac{\text{neutrons (low dose rate)}}{\text{x-ray (high dose rate)}} = 0.9; \text{ for thymic lymphoma RBE} = 1.2$$

$$\text{RBE} = \frac{\text{neutrons (low dose rate)}}{\text{x-ray (low dose rate)}} = 16; \text{ for thymic lymphoma RBE} = 3.3$$

For man

$$\text{RBE} = \frac{\text{Thorotrast } (\alpha\text{-low dose rate})}{I^{131} \text{ (low dose rate electrons)}} = \frac{3.85}{0.5} = 7.5 \text{ max; } \frac{2.3}{0.5} = 4.6 \text{ min.}$$

These figures can be compared with the latest RBE values given by Upton et al.[34] on murine myeloid leukemia and on thymic lymphoma following irradiation by neutrons and γ rays. As also shown in Table 7, these RBE's are 0.9 when neutrons are compared to x rays at high dose rate for the

production of leukemia and 1.2 for thymic lymphoma induction; if one considers that the RBE of α radiation used in man corresponds to a higher LET than the neutrons used in mice, these numbers cannot be deemed too discordant, and they may well fall in within experimental error.

The human data also parallel the murine data when the RBE is calculated for low dose rates of high LET radiation and low dose rates of γ and x radiation. The murine RBE in this case is 16 for myeloid leukemia and 3.3 for thymic lymphoma. These figures bridge very nicely the figures of 7.5 and 4.6 obtained in man and mentioned above. We also notice that the RBE values for cancerogenesis mentioned in the Report of the RBE Committee to the ICRP[35] are also comparable to the calculations presented here on man.

Conclusions

We may conclude that, by exercising a modicum of selective judgment based on radiobiological principles, computations of risk in man do carry in themselves a remarkable amount of consistency despite the various difficulties in dose and statistics. The most consistent figures rely, at this moment, on doses of less than 1000 rads delivered at dose rates of several to many rads per minute. At these rates the linear theory of risk seems to be supported, or at least not contradicted, down to very low doses, by the observations on irradiation in utero. However, the investigation of possible synergistic effects of various biological factors that are usually associated with diagnostic uterine exposures remains to be implemented.

Surprising in a way, but fairly well documented, seems to be the validity of the concept of spatial averaging of the dose, as evidenced by similarity of risk estimates per average rad to the entire marrow in cases involving partial irradiation of the marrow in adults, as in the treatment of spondylitics and metorrhagic women. In children, the same applies, as the studies of tineas capitis patients and the Japanese survivors clearly show.

The most important of the issues remains unsolved, however. It is the question of the magnitude of the effect at dose rates comparable to occupationsl exposures; we have seen that the populations most likely to yield tangible results are those subjected to I^{131} irradiation for the therapy of hyperthyroidism. We have seen also that results to date, although consistent with those obtained in animals, would profit very much from the study of many more cases.

Finally, it should be realized that the epidemiological studies of radiation effects should be extended to the recording of all malignancies; this task has been initiated but it has not been pursued as diligently as that of leukemia.

References

1. Brues, A. M. Somatic Effects. Low-Level Irradiation. Ed. A. M. Brues. Am. Assoc. Advan. Sci. Publ. No. 59, Washington, D. C., 1959, pp. 73-86.
2. Mole, R. H. Problems of low-level irradiation. Some Aspects of Internal Irradiation. Ed. T. M. Dougherty et al. Pergamon Press, New York, 1962, pp. 207-232.
3. Hashizume, T. et al. Estimation of the air dose from the atomic bombs in Hiroshima and Nagasaki. Health Phys. 13, 149-161 (1967).
4. Evans, R. D., A. T. Keane, R. J. Kolenkow, W. R. Neal, and M. M. Shanahan. Radiogenic tumors in radium and mesothorium cases studied at M.I.T. Delayed Effects of Bone-Seeking Radionuclides, Ed. C. W. Mays et al. University of Utah Press, 1969, pp. 157-194.
5. Finkel, A. J., C. E. Miller and R. J. Hasterlik. Radium-induced malignant tumors in man. Ibid., pp. 195-226.
6. Hutchinson, G. B. Leukemia in patients with cancer of the cervix uteri treated with radiation: A report covering the first five years of an international study. J. Nat. Cancer Inst. 40, 951-982 (1968).
7. Dickson, R. J. The late results of radium treatment of benign uterine haemorrhage. Brit. J. Radiol. 42, 582-594 (1967).
8. International Commission on Radiological Protection. Publ. No. 8, Pergamon Press, London, 1966.
9. UNSCEAR (1964) Report of the United Nations Scientific Committee of the Effects of Atomic Radiation. General Assembly Official Records, 19th Session, Supplement No. 14 (A/581A)-1964.

10. Doll, R. and P. G. Smith. The long-term effects of x-irradiation in patients treated for metropathia haemorragica. Brit. J. Radiol. 41, 362-368 (1968).
11. Brinkley, D. and J. L. Haylittle. The late effects of artificial menopause by x-radiation. Brit. J. Radiol. 42, 519-521 (1969).
12. Parr, R. M., H. F. Lucas, and M. L. Griem. Metabolism of ^{232}Th decay series radionuclides in man and other animals following intravascular administration of Thorotrast. Radiological Physics Division Report, July 1968-June 1969. ANL-7615. pp. 97-115.
13. Seltser, R. and P. E. Sartwell. The influence of occupational exposure to radiation on the mortality of American radiologists and other medical specialists. Am. J. Epidemiology 81, 2-22 (1965).
14. Braestrup, C. B. Past and present exposure to radiologists from the point of view of life expectancy. Am. J. Roentgenol. 78, 988-992 (1957).
15. Saenger, E. L., G. E. Thoma, and E. A. Tompkins. Incidence of leukemia following treatment of hyperthyroidism. J. Am. Med. Assoc. 205, 855-862 (1968).
16. Spiers, F. W. Radioisotopes in the human body; physical and biological aspects. Academic Press, New York, 1968, p. 115.
17. Modan, B. and A. M. Lilienfeld. Leukemogenic effect of ionizing-irradiation treatment in polcythemia. The Lancet, August 29, 1964, pp. 439-441.
18. Court-Brown, W. M., R. Doll, F. W. Spiers, B. J. Duffy and M. J. McHugh. Geographical variation in leukemia mortality in relation to background radiation and other factors. Brit. Med. J. 1, June 11, 1960, pp. 1753-1759.
19. Buck, C. Population size required for investigating threshold dose in radiation-induced leukemia. Science 129, 1357-1358 (1959).
20. Hempelman, L. H. Neoplasms in youthful populations following x-ray treatment in infancy. Environ. Res. 1, 338-358 (1967).
21. Saenger, E. L., F. N. Silverman, T. D. Sterling and M. E. Turner. Neoplasia following therapeutic irradiation for benign conditions in childhood. Radiology 74, 889-904 (1960).
22. Conti, E. A., G. D. Patton, J. E. Conti, and L. H. Hempelman. Present health of children given x-ray treatment to the anterior mediastinum in infancy. Radiology 74, 386-391 (1960).
23. Albert, E. R. and A. R. Omran. Follow-up study of patients treated by x-ray epilation for Tinea capitis. Arch. Environ. Health 17, 899-950 (1968).
24. International Commission on Radiological Protection, ICRP Publication No. 14. Pergamon Press, London, 1969.
25. Griem, M. L., P. Meyer and G. D. Dobben. Analysis of the morbidity and mortality of children irradiated early in life. Radiology 88, 347 (1967).

26. MacMahon, B. Prenatal x-ray exposure and childhood cancer. J. Nat. Cancer Inst. 28, 1173-1191 (1962).
27. Graham, S., M. L. Levin, A. M. Lilienfeld, L. Schuman, R. Gibson, J. E. Dowd, and L. Hempelman. Preconception, intrauterine, and postnatal irradiation as related to leukemia. Nat. Cancer Inst. Monograph No. 19, (1966), pp. 347-371.
28. Stewart, A., J. Webb, and D. Hewitt. A survey of childhood malignancies. Brit. Med. J. 1, 1495 (1958).
29. Gibson, R. W., I. D. J. Bross, S. Graham, A. M. Lilienfeld, L. M. Schuman, M. L. Levin, and J. E. Dorod. Leukemia in children exposed to multiple risk factors. New Eng. J. Med. 279, 906-909 (1968).
30. Faber, M. Epidemiological experience with thorotrast in Denmark. The dosimetry and toxicity of thorotrast. Int. Atomic Energy Agency Technical Report IAEA-106, Vienna, 1968, pp. 139-146.
31. da Silva Horta, J., J. D. Abbat, L. A. R. C. Cayolla da Motta, and M. L. Roriz. Malignancy and other late effects following administration of thorotrast. The Lancet, ii, 201 (1965).
32. Blomberg, R. L., E. Larsson, B. Lindell, and E. Lindren. Late effects of thorotrast in cerebral angiography. Acta Radiol. (Diagnosis) 1, 995-1006 (1963).
33. Spiess, H. ^{224}Ra-induced tumors in children and adults. Delayed Effects of Bone-Seeking Radionuclides, Ed. C. W. Mays, et al. University of Utah Press, Salt Lake City, 1969, pp. 227-248.
34. Upton, A. C., M. L. Randolph, and J. W. Conklin. Late effects of fast neutrons and gamma-rays in mice as influenced by the dose rate of irradiation: Induction of neoplasia. Rad. Res. 41, 467-491 (1970).
35. Report of the RBE Committee to the International Commission on Radiological Protection and on Radiological Units and Measurements. Health Phys. 9, 357-386 (1963).

REGULARIZATION UNFOLDING OF LOW γ-RAY ACTIVITY MEASUREMENTS. II. EVALUATION OF TIME-OF-FLIGHT SCANNING IN ONE DIMENSION

I. K. Abu-Shumays,* P. E. Hess, and L. D. Marinelli

The main aim of the work reported here is to investigate the potential usefulness of plastic scintillator rods as "time-of-flight gamma-ray cameras" for the mapping of the measured distribution "spectra" of low-level radioactivities in vivo. The relationship between the distribution of the activity and of the corresponding scintillations in the camera is described by a Fredholm equation of the first kind.

The spectra corresponding to three linear sources at a distance of (about) 10 cm from the rod are measured without collimation. The measurements are repeated in the presence of a 2-cm x 2-cm lead and also a 2-cm x 2 cm-tungsten brick collimator.** The resulting spectra are unfolded by a regularization (smoothing) technique. This work, therefore, demonstrates the applicability of the regularization technique to the solution of Fredholm equations of the first kind when the kernel of the equation (the response to a point source) has a wide FWHM (full width at half maximum) and is also asymmetric and dependent on the position on the rod, especially in the presence of collimation.

Introduction

The main emphasis of this paper is on extending some of the results established previously[1-7] to the measurement and the regularization unfolding of the time-of-flight gamma-ray density "spectrum"† of a linear radioactive source.

In Refs. 1-4, jointly with others, we describe the localization of scintillations in long fluorescent rods. The detector used here is a plastic scintillator (2" in diameter and 2' long) coupled to an RCA-8575 photomultiplier at each end (see Fig. 1A). Sufficiently accurate localization of scintillations in the rod results from timing the delay between pulses arising in

* Applied Mathematics Division.

** A 2-x2-cm collimator means a free rod segment 2 cm long followed by a 2-cm space covered by lead or tungsten brick.

† In the rest of the paper the words "spectrum of the source" will denote the density distribution of the activity in the radioactive source.

the photomultipliers.

In Ref. 5 we outlined the regularization unfolding (smoothing) method[1,6,7] for the numerical solution of the Fredholm equation of the first kind, relating measured "spectra" and corresponding radioactive source densities. A linear source of radioactivity was simulated by a suitably shaped filiform source (see below), and the corresponding density spectrum was measured by a 3" x 3" NaI crystal displaced parallel to the plane of the source. That work was devoted to studying the influence which various experimental parameters exert on the accuracy of the numerical method of solution and suggested how best to choose these parameters whenever a choice exists.

This project is devoted to the regularization unfolding of the delay spectra measured by the time-of-flight technique. The relevant steps in the numerical methods of solution are summarized.

This paper differs from the preliminary paper[5] inasmuch as (a) lead and tungsten collimators are used to improve the resolution of the spectra, and (b) the effect of smoothing the experimental data to minimize the noise inherent in them before proceeding to solve for the corresponding radioactive source density is analyzed. Thus, this paper is somewhat more than a straightforward generalization of our previous work.

Method of Solution--Brief Description

We shall restrict our treatment here to one dimension. The density function f(x) representing the activity per unit length of a linear source, and the corresponding measured spectrum g(x), are related by the following Fredholm equation of the first kind:

$$g(x) \simeq g(x) + \epsilon(x) = \int_a^b K(x,x')f(x')dx' \ . \qquad (1)$$

Here the interval [a,b] is the range of the spectrum (rather than the length of the source); the kernel K(x,x') is the response of the scintillation rod at

point x due to a point source located at x'; and the term $\epsilon(x)$ is the statistical and experimental error superimposed on the spectrum $g(x)$.

For numerical computation, the interval $[a,b]$ is divided into n parts $a = x_1 < x_2 < \ldots < x_n = b$. Equation (1) is then approximated by

$$g_j \simeq g_j + \epsilon_j = \sum_{i=1}^{n} K_{ji} w_i f_i , \tag{2}$$

where $g_j = g(x_j)$, $K_{ji} = K(x_j, x_i)$, etc., and w_i are weights that depend on the quadrature formula chosen. Since ϵ_j stands for the error in the spectrum g at an individual point x_j, two more meaningful measures of the error are the weighted averages

$$\overline{\epsilon} \equiv \sum_{j=1}^{n} p_j \, |\epsilon_j| = \sum_{j=1}^{n} p_j \left| \sum_{i=1}^{n} K_{ji} w_i f_i - g_j \right| \tag{3}$$

and

$$\overline{\epsilon^2} \equiv \sum_{j=1}^{n} p_j \, \epsilon_j^2 = \sum_{j=1}^{n} p_j \left(\sum_{i=1}^{n} K_{ji} w_i f_i - g_j \right)^2 , \tag{4}$$

where p_j are appropriate weight factors. If there is no a priori evidence that parts of the spectra are more accurate than others (as is the case for the results reported here), then one may set $p_j = 1/n$ for all j.

The regularization (smoothing) technique consists in finding the solution $f_i, i = 1,\ldots,n$, of Eq. (2) which minimizes the error $\overline{\epsilon^2}$ of Eq. (4) subject to suitable smoothness constraints. The smoothness constraints, introduced by D. L. Phillips in 1962,[6] are suitable formulation of the physical assumption that except possibly at isolated locations, the activity (the density function f(x)) does not vary abruptly between one point and adjacent points. Additional constraints, such as prior knowledge of the total amount of radioactivity C of the linear source, can also be introduced as we have indicated elsewhere,[1,5] but will not be used here. Introduc-

ing the notation $A = (a_{ji}) = (K_{ji}w_i)$, $\underline{f} = (f_i)$, and $\underline{g} = (g_i)$, the regularization technique leads to the solution (in matrix notation)

$$\underline{f} = [A^T A + \gamma^2 S^T S]^{-1} A^T \underline{g} , \tag{5}$$

where A^T (T = transpose) is the matrix transpose of A (the response kernel $K(x,x')$ with quadrature weights; S, S^T are smoothness matrices which for the computations reported below were such as to minimize the terms $(f_{i-1} - 2f_i + f_{i+1})^2$ (i.e., for almost all i, the density function f_i at the point x_i is expected to be reasonably close to the average of its values f_{i-1} and f_{i+1} at adjacent points), and γ^2, the weight factor multiplying $S^T S$, is an optional constant which controls the degree of smoothness of the solution $\underline{f}$. It is evident that, holding other parameters constant, each choice of γ leads to a different solution $\underline{f}$ and consequently leads to different degrees of errors given by $\overline{\epsilon}$ and $\overline{\epsilon^2}$ computed from $\underline{f} = (f_i)$ and Eqs. (3) and (4). Normally, in a given experiment, the expected values of the errors $\overline{\epsilon}$ and $\overline{\epsilon^2}$ can be estimated, and the γ to be chosen ought to be the one which gives an acceptable value of $\overline{\epsilon}$ and/or $\overline{\epsilon^2}$. The spectra we measured over a range [a,b] due to either point sources (to evaluate the kernel) or to extended sources have small fluctuations which could not be due to fluctuations in the density of the source, but rather are caused in part by statistical error. We expect these fluctuations to be negligible if we carry the individual measurements over an extended period of time. Instead, we conjecture that a properly smoothed version of the experimental data minimizes the so-called noise-to-signal ratio and results in an improved (or enhanced) representation of the spectra. In fact, it will be shown below that the difference between a given spectrum and a smoothed version of it supplies an excellent estimate of the order of magnitude of the expected errors $\overline{\epsilon}$ and $\overline{\epsilon^2}$.

We have experimented with smoothing the data in five known[8] ways and found the results comparable (books on numerical analysis list other methods of smoothing which we have not tried). We have used the following least-squares polynomial approximations, which are relevant to three points,

five points, and seven points, respectively.

$$y_i^{k+1} = \frac{1}{3}\,(y_i^k + y_i^k + y_{i+1}^k), \tag{6}$$

$$y_i^{k+1} = \frac{1}{35}\,(-3y_{i-2}^k = 12y_{i-1}^k + 17y_i^k + 12_{i+1}^k - 3y_{i+2}^k), \tag{7}$$

and

$$y_i^{k+1} = \frac{1}{231}\,(5y_{i-3}^k - 30y_{i-2}^k + 75y_{i-1}^k + 131y_i^k + 75y_{i+1}^k$$

$$-30y_{i+2}^k + 5y_{i+3}^k)\ . \tag{8}$$

These formulae are equivalent to replacing each tabulated value by the values taken on by least-squares polynomials of degrees one, three, and five, respectively, centered at the point i at which the entry is to be modified. We refer to Ref. 8 for the corresponding formulae relevant to the points i near the end of the range of values considered. The smoothing is repeated (the superscript k in Eqs. (6)-(8) denote the number of iterations) until most of the noise is eliminated without appreciably modifying the essential characteristic of the function.

We note that Eq. (6) averages each three consecutive points to correct the value at the central point. We have also tried to give more weight to the point i under consideration by using the formula

$$y_i^{k+1} = \frac{1}{4}\,(y_{i-1}^k + 2y_i^k + y_{i+1}^k)\ . \tag{9}$$

Finally, we have tried smoothing with our program to solve Fredholm equations of the first kind. Here we solve the matrix equation

$$f = I\,\underline{g} \qquad (I \equiv \text{ unit } n \times n \text{ matrix}), \tag{10a}$$

subject to the constraint that $\underline{f}$ be sufficiently smooth. The solution, Eq. (5),

here reduces to

$$\underline{f} = [I + \gamma^2 S^T S]^{-1} \underline{g}. \tag{10b}$$

Here again, γ controls the degree of smoothness of f; good results are usually achieved for γ close to one.

The Experiment, the Computations, and the Results

The γ-Ray Camera

The scintillator rod (our time-of-flight camera) together with parts of its attachments are shown in Figure 1A. The photomultipliers at each end are operated at approximately 2600 V. The output of the tubes is fed to discriminators and a time-to-pulse height converter and then to a RIDL 400-channel analyzer as described elsewhere.[1] The system is calibrated to correspond to 60 cm of the rod and to give 2 channels in the analyzer memory per centimeter, for a total of 120 channels. The response of the system is maintained by adjusting the discriminators to give the same count within 1% for a 5.0-μCi source placed at 10 cm and 50 cm from the end positions along the axis of the 60-cm rod. The data are read out of the analyzer on paper tape and then written on magnetic tape for processing on an IBM-360 Model 50/75 computer. To reduce background, the detector is shielded with 4 inches of lead as shown in Figure 1A, in addition to the shielding of the underground counting facility. For additional information on the time-of-flight γ-ray camera we refer to Refs. 1 and 4.

The Kernel

Figure 1A also shows a point source of 4.486-μCi activity 10.5 cm from the external surface of the rod sliding on a scale parallel to the axis of the rod and calibrated in centimeters for the useful distance of 60 cm. The response of the rod at point x due to the point source positioned at point x' is the response kernel K(x,x') of the Fredholm Eq. (1). Thus the kernel is measured experimentally for 120 positions of x (every 0.5 cm) for suitable selected positions x' of the collimated point source and about 140

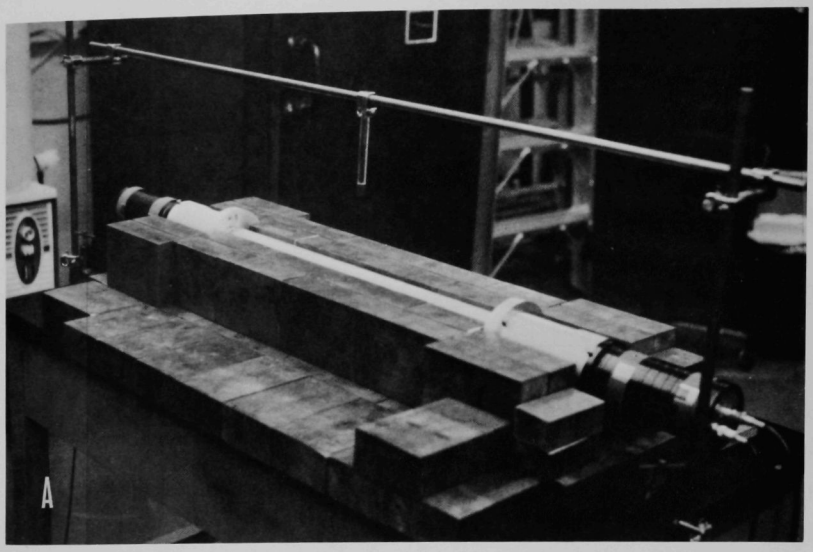

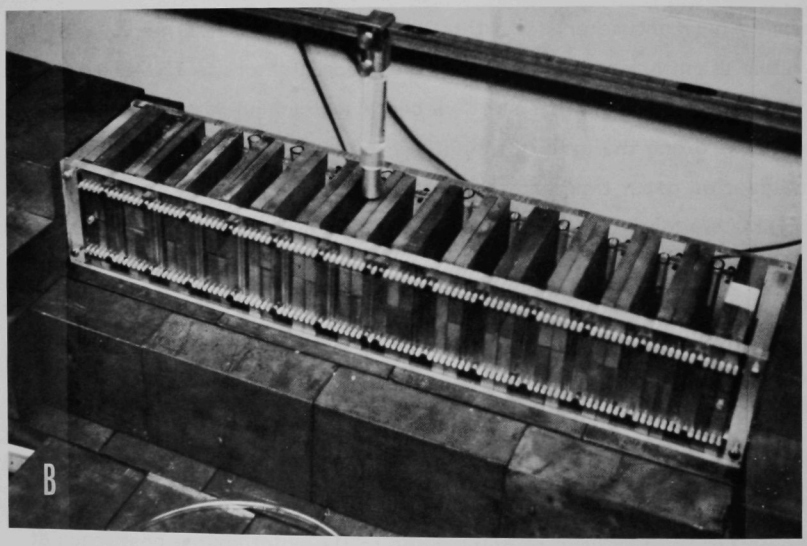

FIG. 1.--(A) Scintillator rod and point source of activity. (B) Same with tungsten collimator in place.

for the uncollimated one.

In our computations we considered only the 50-cm distance between the 5-cm position and the 55-cm position on the rod. For the case of no collimation, we placed the point source at every centimeter position and used interpolation to compute the kernel at other positions. In the presence of the 2-cm x 2-cm lead brick and the 2-cm x 2-cm tungsten brick collimators, the determination of the kernel was modified as follows: for the lead collimator the point source was placed at every centimeter position for the left half of the rod, and symmetry was used to compute the kernel at the remaining positions; for the tungsten collimator the point source was placed at every centimeter for the 50 cm of interest. Figure 1B shows the tungsten collimator.

In our previous work[1, 4] we restricted ourselves to simple kernels of the form $K(x,x') = K(|x-x'|)$. This restriction is here removed, as can be seen from Figure 2. Figures 2A, B, and C show the kernel for x' at the center of the rod, 10 cm, and 25 cm away from the center. Thus we note that the response of the rod varies from its center to its edge. Figures 2D, E, and F show the kernel for x' at the center between two bricks, at the edge of a brick, and at the center of a brick. We note the attenuation of both amplitude and FWHM relative to the case of no collimation. We also note that when the source is at the center of a brick, the kernel has two peaks, with a relatively small valley between them.* Figures 2G, H, and I correspond to Figures 2D, E, and F, but with the tungsten collimator instead of the lead. We note that since tungsten is a denser absorber than lead, the kernel is attenuated more and, contrary to Fig. 2F, Fig. 2I has one rather than two peaks.

---

*We remark here that when a 5-cm x 5-cm lead collimator was used, we were unable to resolve a distributed source without further modification of our procedure. This is because the thick brick suppresses the source behind it, and consequently, without appropriately weighing the various parts of the spectra, the program assigns for the activity behind a brick two attenuated sources in the spaces adjacent to the brick. We plan to analyze this situation further and report our conclusions elsewhere.

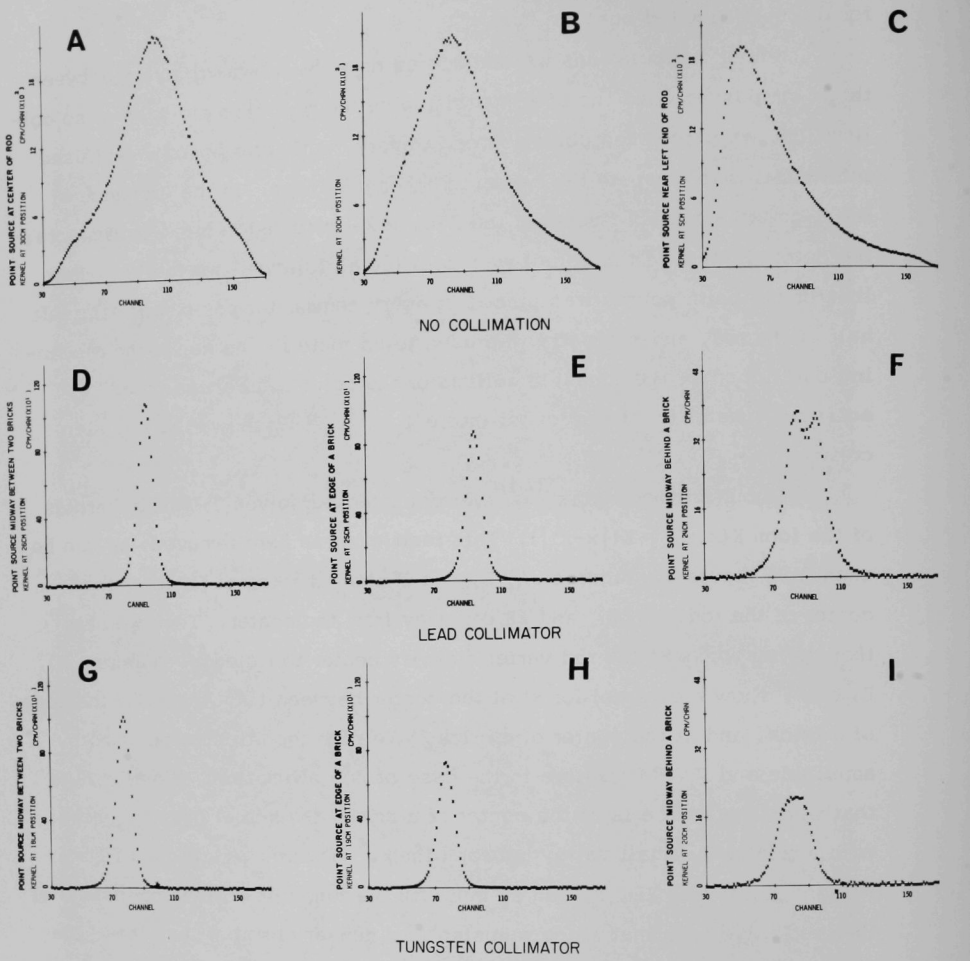

FIG. 2.--Response kernel for typical positions of the point source in the presence or absence of collimation.

The Distributed Sources and their Spectra

Three density functions F1 (symmetric), F2 (asymmetric), and F3 (combination of F1 and F2), to represent extended linear sources of activity, were constructed from radioactive ^{137}Cs microspheres (about 0.725 mm in diameter) filling nylon beads 5.5 mm in diameter, which were placed in plastic tubings 50 cm long. Details are given elsewhere.[9] The density functions are shown in Figure 3 (Figure 3A represents F1 and Figure 3B represents F2).

The total activities for the density functions F1, F2, and F3 were respectively 0.357, 0.261, and 0.618 μCi, or C1 = 0.080, C2 = 0.058, and C3 = 0.138 when normalized relative to the 4.49-μCi point source used to measure the response kernel.

The spectra corresponding to the three radioactive source densities given above were measured for the case with no collimation, for the 2-cm x 2-cm lead and the 2-cm x 2-cm tungsten collimators. The results are shown in Figure 4. We note two things in particular:

a) The fluctuations between adjacent points on the spectra (see Figures 4 and 5) are primarily due to statistical errors and represent so-called "noise" which can be minimized by smoothing the data. The fluctuations are indicative of the order of magnitude of the error in the spectra, as will be indicated below.

b) In the absence of collimation, the response kernel is so wide (see Figure 2) that the two peaks of the density function F3 are not resolved in G3 (Figure 4). However, for the lead, and especially for the tungsten collimator, the spectra resemble the density functions in shape though not in magnitude.

Smoothing and Error Estimates

We have experimented with smoothing the data as was indicated above. Figure 5 shows the results for G3 using Eqs. (6), (7), (9), and (10). Clearly, the results are not noticeably different. For convenience and in order to minimize the time for computation, we have implemented only

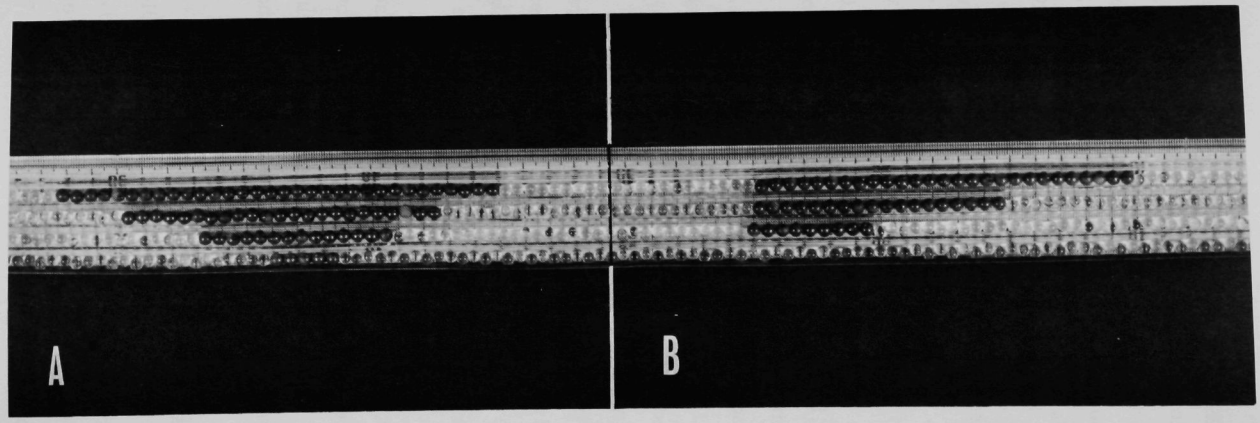

FIG. 3.--Density function F3: (A) symmetric, and (B) asymmetric sources of radioactivity combined.

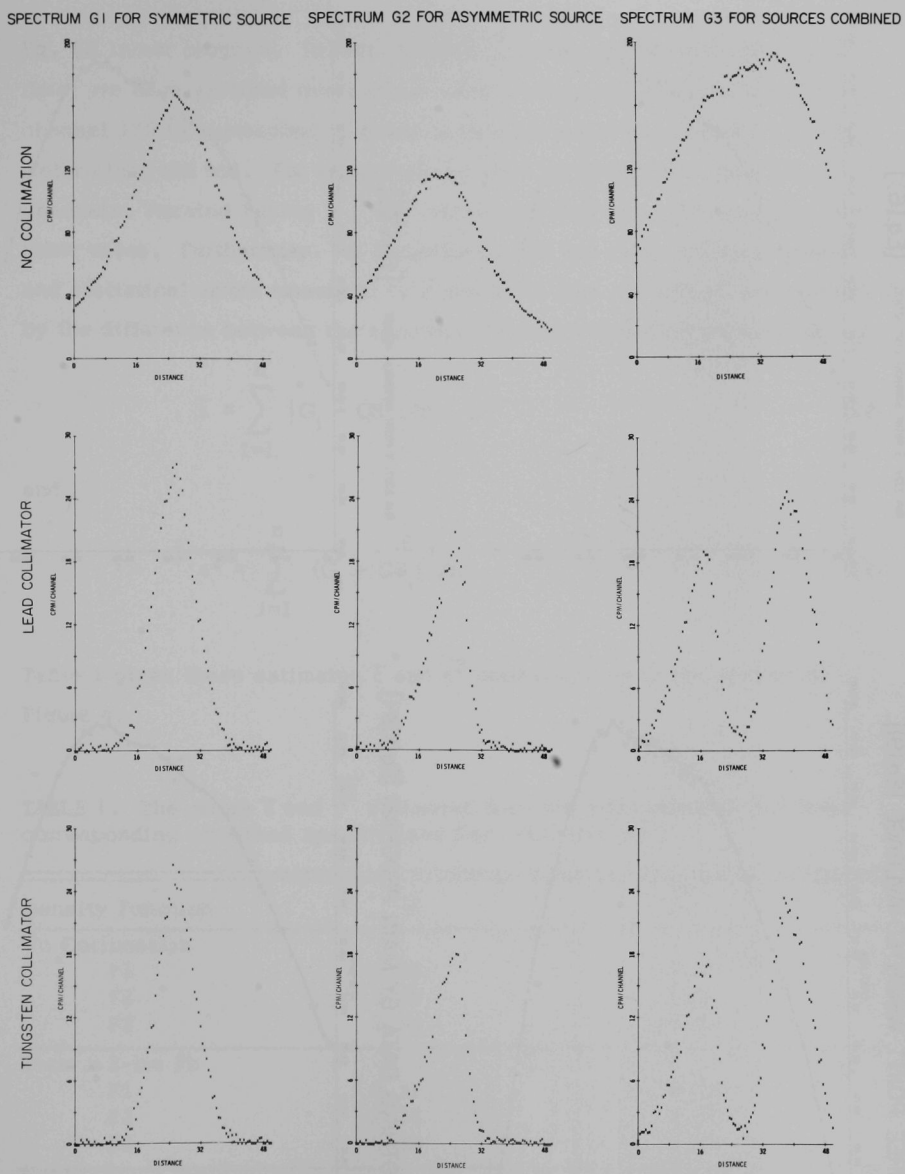

FIG. 4.--Measured spectra.

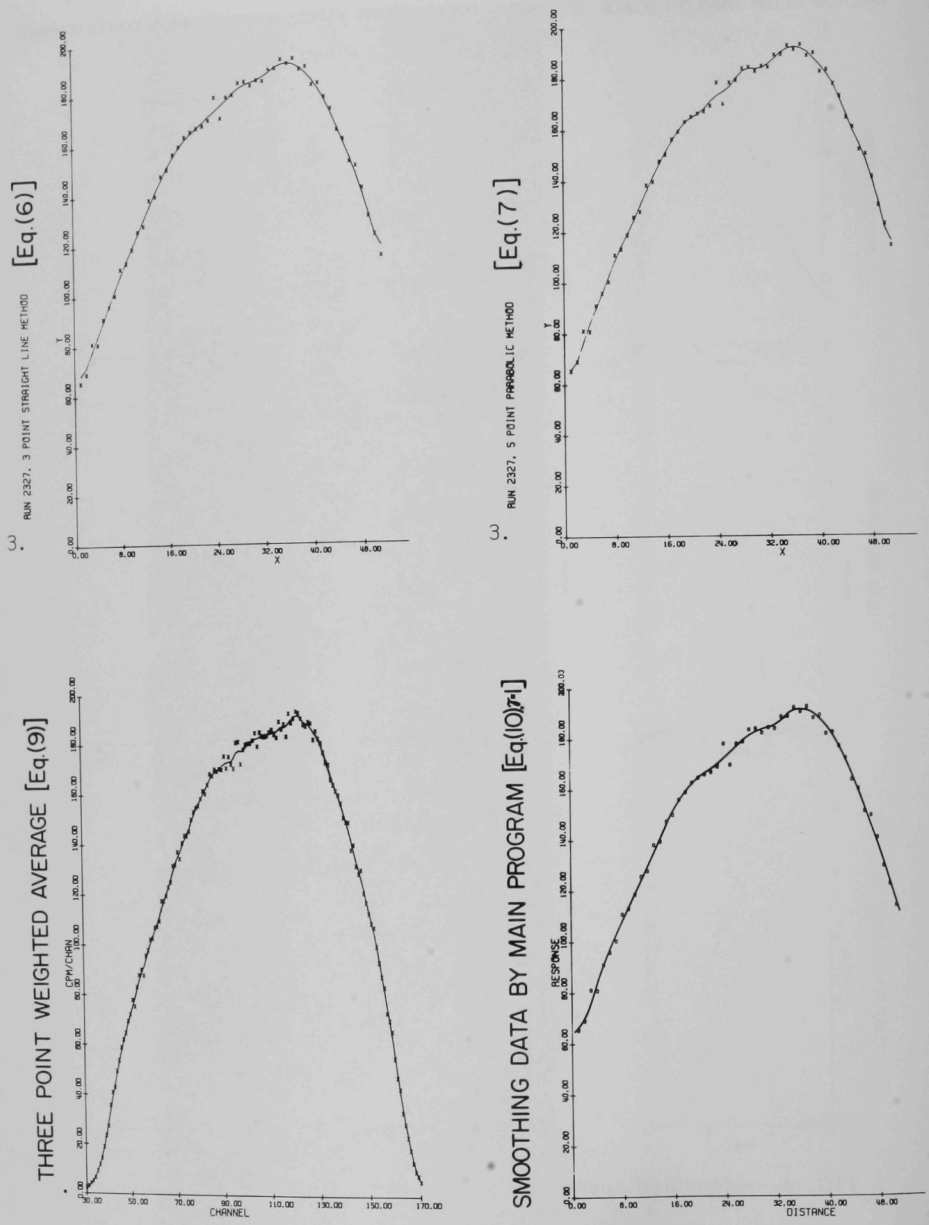

FIG. 5.--Smoothing the initial data in four different ways.

Eq. (9) in our program. In fact, to save on computer storage computation time, we have selected every other point of the spectra from channel 50 to channel 150 to correspond to every centimeter rather than every half centimeter along the rod. For smoothing we used the actual data from all the channels, iterated [using Eq. (9)] three or five times, and recorded every other value. Furthermore, we conjectured that the expected experimental and statistical errors measured by $\overline{\epsilon}$ and $\overline{\epsilon^2}$ of Eqs. (3) and (4) are estimated by the difference between the spectrum G and its smoothed version GS; thus

$$\overline{\epsilon} \simeq \sum_{i=1}^{n} |G_i - GS_i|/n \quad , \tag{11}$$

and

$$\overline{\epsilon^2} \simeq \sum_{i=1}^{n} (G_i - GS_i)^2/n \ . \tag{12}$$

Table 1 gives these estimates $\overline{\epsilon}$ and $\overline{\epsilon^2}$ corresponding to the spectra of Figure 4.

TABLE 1. The errors $\overline{\epsilon}$ and $\overline{\epsilon^2}$ estimated from the measurements and their corresponding smoothed spectra [see Eqs. (11) and (12)]

Density Function	$\overline{\epsilon}$	$\overline{\epsilon^2}$
No Collimation		
F1	0.96	1.4
F2	0.85	1.4
F3	1.59	4.0
2-cm x 2-cm Pb		
F1	0.31	0.18
F2	0.28	0.17
F3	0.35	0.17
2-cm x 2-cm W		
F1	0.32	0.23
F2	0.27	0.16
F3	0.45	0.35

Regularization Unfolding of the Measured and of the Smoothed Spectra

We have made desirable changes in our computer program based on the regularization (smoothing) unfolding technique for the numerical solution of Fredholm equations of the first kind. These include, in addition to smoothing the data before solving for the source density function, the computations of the errors in $\overline{\epsilon}$ and $\overline{\epsilon^2}$ corresponding to each value of γ in Eq. (5) and hence corresponding to each solution. Figures 6 to 10 give a graphical representation of a sample of our computed results, and Table 2 indicates the range of γ for which the computed solution is a reasonable representation for the actual density function measured. This table also gives for each value of γ the errors $\overline{\epsilon}$ and $\overline{\epsilon^2}$ in the computed solution together with the corresponding total activity denoted by C1, C2, or C3.

TABLE 2. Range γ of acceptable solutions for the density functions F1, F1S, F2, F2S, F3, F3S [(a)] together with the corresponding errors $\overline{\epsilon}$, $\overline{\epsilon^2}$, and the computed total activity.

	No Collimation				2-cm x 2-cm Lead				2-cm x 2-cm Tungsten			
	γ	$\overline{\epsilon}$	$\overline{\epsilon^2}$	C	γ	$\overline{\epsilon}$	$\overline{\epsilon^2}$	C	γ	$\overline{\epsilon}$	$\overline{\epsilon^2}$	C
F1	1000	1.03	1.78	0.083	2000	0.32	0.17	0.084	500	0.31	0.20	0.080
	2000	1.04	1.84	0.083	4000	0.33	0.21	0.084	1000	0.32	0.21	0.080
	5000	1.04	1.91	0.083	6000	0.34	0.24	0.084	2000	0.32	0.22	0.080
	10000	1.06	2.02	0.083					6000	0.38	0.32	0.080
F1S	1000	0.46	0.35	0.083	4000	0.17	0.05	0.083	500	0.08	0.01	0.081
	2000	0.48	0.39	0.083	6000	0.22	0.09	0.083	1000	0.09	0.01	0.081
	5000	0.51	0.48	0.083	8000	0.26	0.12	0.083	2000	0.11	0.02	0.081
	10000	0.57	0.62	0.083	10000	0.30	0.16	0.083	6000	0.22	0.09	0.081
F2	500	0.94	1.56	0.061	1000	0.30	0.16	0.055	500	0.29	0.17	0.052
	1000	0.96	1.65	0.061	2000	0.35	0.25	0.055	1000	0.29	0.18	0.052
	2000	0.98	1.70	0.061	4000	0.41	0.37	0.055	2000	0.31	0.21	0.052
	5000	1.00	1.74	0.061					6000	0.48	0.56	0.052
F2S	500	0.33	0.19	0.060	1000	0.13	0.03	0.054	1000	0.13	0.03	0.052
	1000	0.34	0.20	0.060	2000	0.17	0.07	0.054	3000	0.24	0.12	0.052
	2000	0.35	0.20	0.060	4000	0.24	0.13	0.054	3000	0.30	0.19	0.052
	5000	0.38	0.23	0.060	6000	0.28	0.20	0.055	5000	0.35	0.27	0.052
F3	1000	1.52	3.73	0.143	1000	0.36	0.21	0.133	500	0.45	0.34	0.133
	2000	1.53	3.76	0.144	2000	0.39	0.25	0.133	1000	0.46	0.34	0.133
	5000	1.55	3.80	0.144	4000	0.52	0.42	0.133	2000	0.49	0.38	0.133
F3S	1000	0.40	0.27	0.144	1000	0.19	0.06	0.132	500	0.09	0.02	0.134
	2000	0.43	0.30	0.144	3000	0.33	0.19	0.132	2000	0.20	0.07	0.134
	5000	0.46	0.35	0.144	4000	0.41	0.29	0.132	5000	0.38	0.25	0.134
					5000	0.47	0.38	0.132	10000	0.60	0.59	0.134

[(a)] S denotes smoothing the data before solving for the density function.

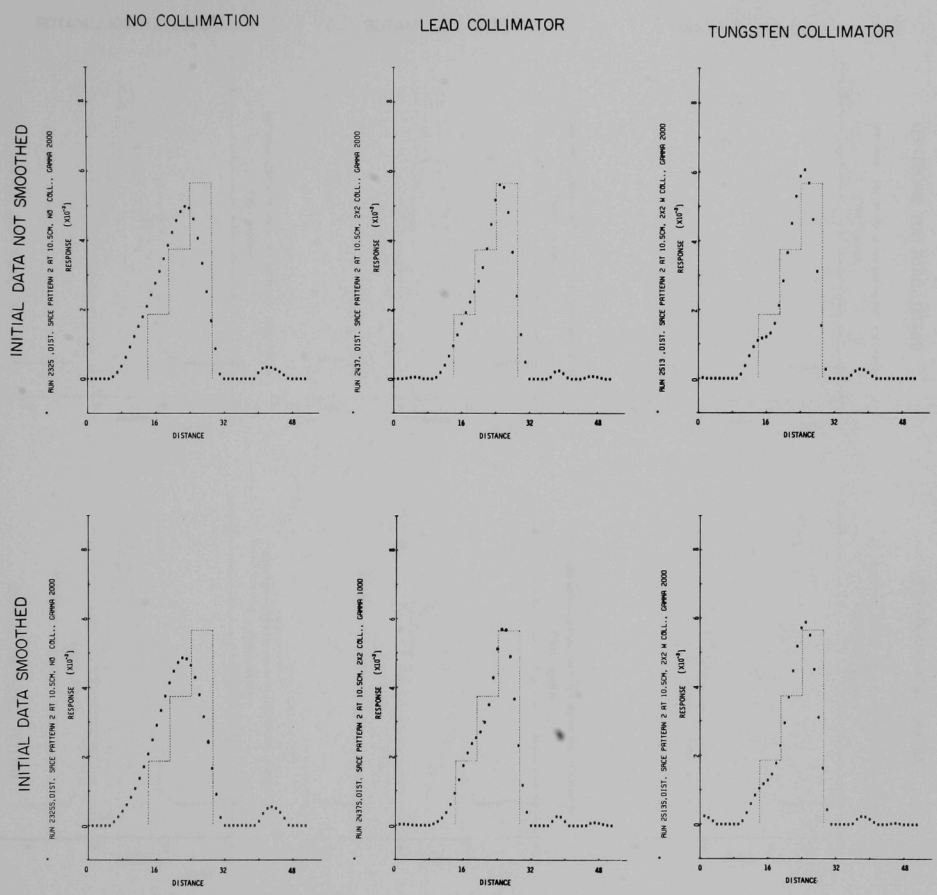

FIG. 6.--Typical results for the computed density function F1. The dotted line represents the actual radioactive source.

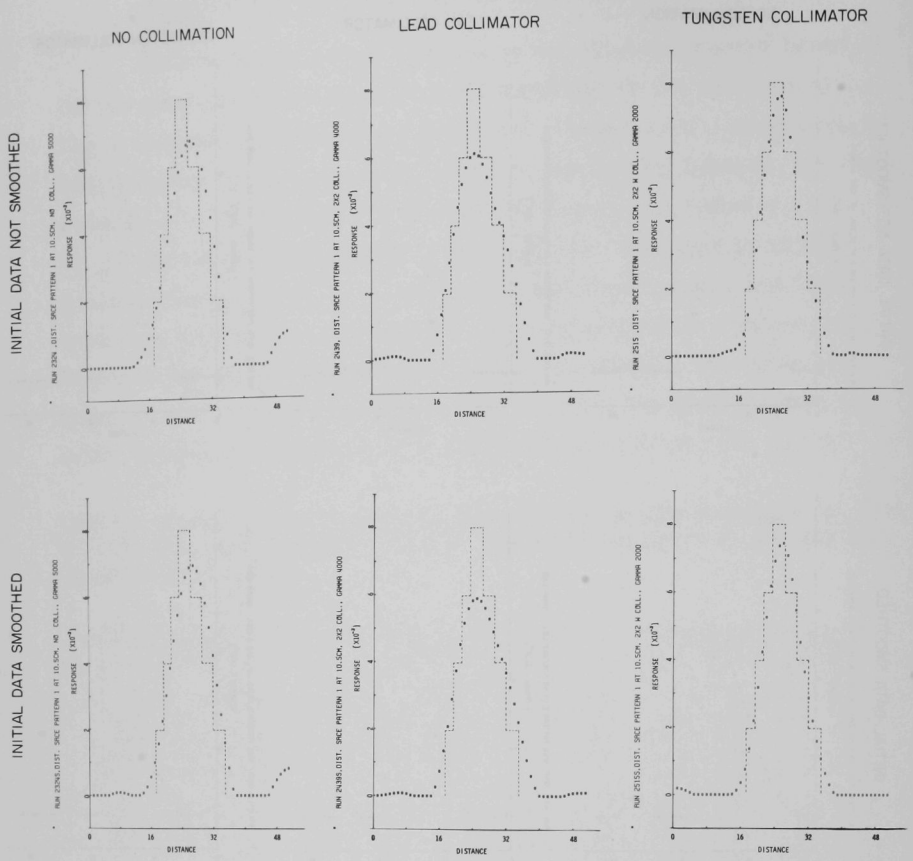

FIG. 7.--Typical results for the computed density function F2. The dotted line represents the actual radioactive source.

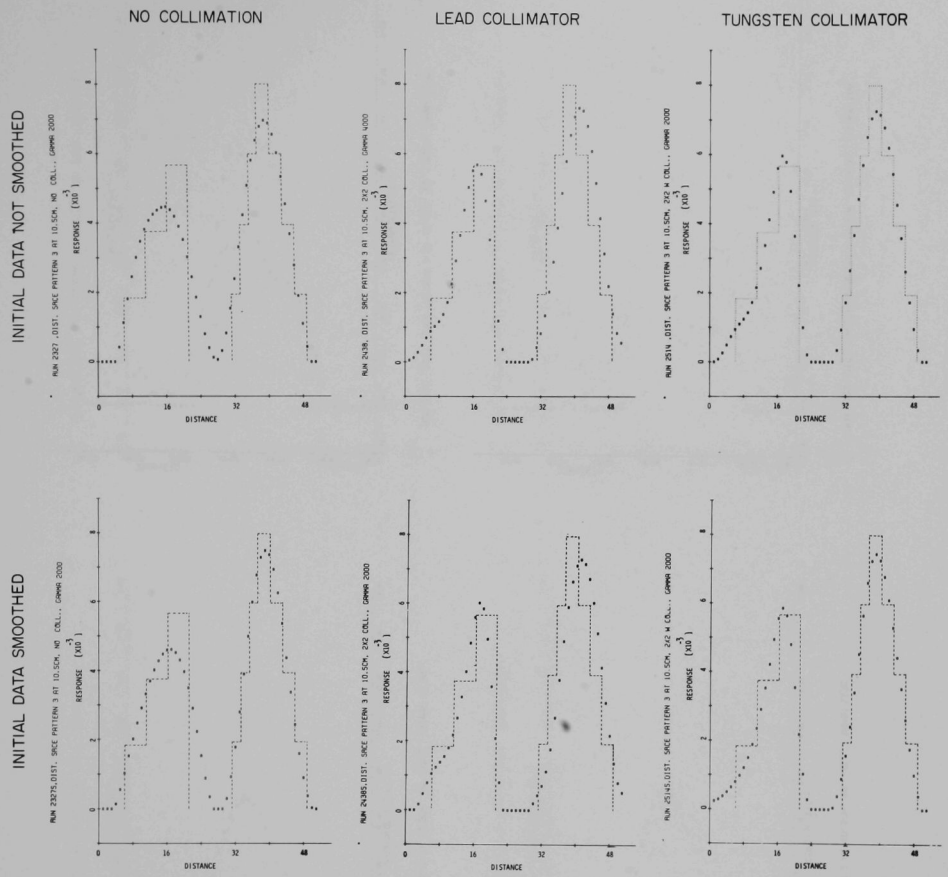

FIG. 8.--Typical results for the computed density function F3. The dotted line represents the actual radioactive source.

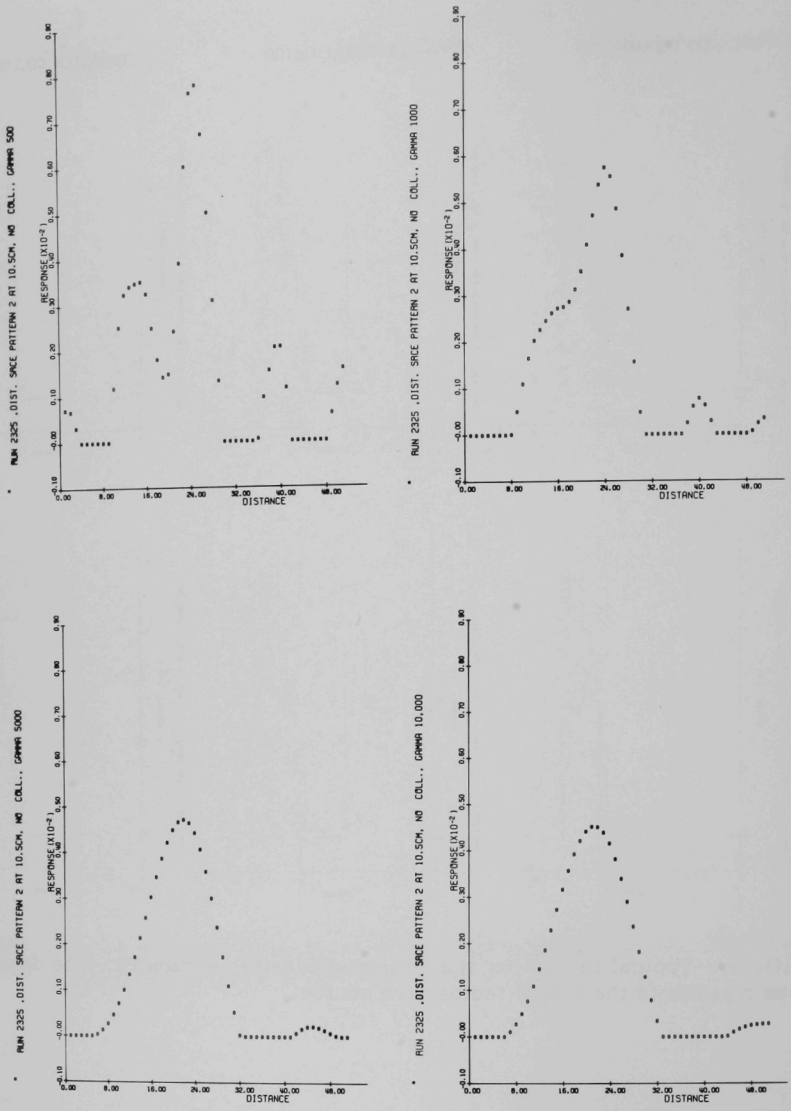

FIG. 9.--Range of computed density function for various values of γ. No collimation. Initial data not smoothed.

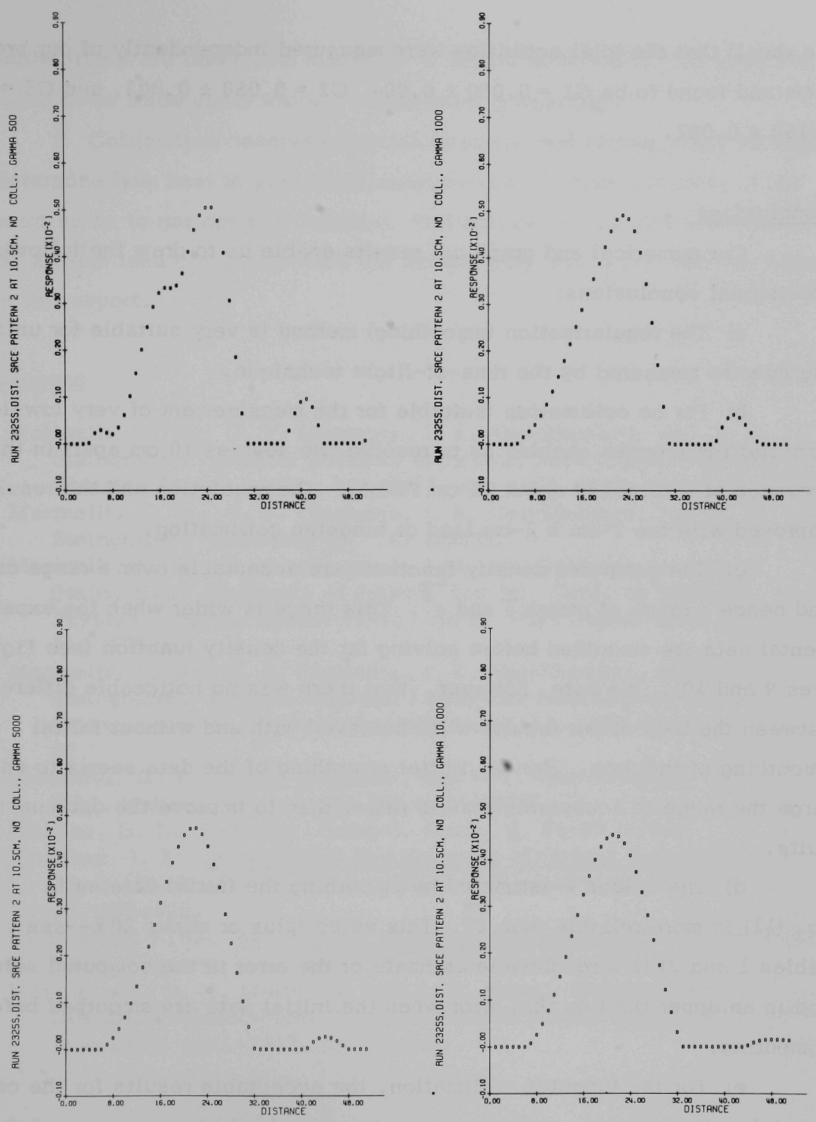

FIG. 10.--Range of computed density function for various values of γ. No collimation. Initial data smoothed.

We recall that the total activities were measured independently of our program and found to be C1 = 0.080 ± 0.004, C2 = 0.058 ± 0.003, and C3 = 0.138 ± 0.007.

Conclusions

Our numerical and graphical results enable us to draw the following provisional conclusions:

a) The regularization (smoothing) method is very suitable for unfolding spectra measured by the time-of-flight technique.

b) For no collimation (suitable for the measurement of very low-level activity) the program enabled us to resolve two sources 10 cm apart in the presence of a kernel of about 25 cm FWHM. The resolution and the results improved with the 2-cm x 2-cm lead or tungsten collimation.

c) The computed density functions are acceptable over a range of γ and hence a range of errors $\overline{\epsilon}$ and $\overline{\epsilon^2}$. This range is wider when the experimental data are smoothed before solving for the density function (see Figures 9 and 10). We note, however, that there was no noticeable difference between the best of our results when achieved with and without initial smoothing of the data. Hence, initial smoothing of the data seems to enlarge the range of acceptable results rather than to improve the optimum results.

d) The values $\overline{\epsilon}$ estimated by smoothing the initial data as in Eq. (11) is more reliable than $\overline{\epsilon^2}$. This value (plus or minus 20%--see Tables 1 and 2) is a reasonable estimate of the error in the computed solution and is an upper limit on this error when the initial data are smoothed before computing.

e) For the tungsten collimation, the acceptable results for the computed density functions varied over a range of γ (and hence a range of the errors $\overline{\epsilon}$ and $\overline{\epsilon^2}$) larger than that for the lead collimator. The optimum results for the computed density functions were also slightly better for the tungsten collimator than for the lead collimator. Our limited results, however, indicate that for the present, the use of tungsten is not justified if financial

considerations are taken into account. A deeper analysis of this question remains to be made under various collimation geometries,

f) Collimation deserves special attention and further study in order to determine how best to assign different weights to different parts of the spectra so as to get optimum results. Preliminary results obtained with a 5-cm x 5-cm lead collimator were not satisfactory and hence were excluded from this report.

References

1. Marinelli, L. D., G. F. Clemente, I. K. Abu-Shumays, and O. J. Steingraber. Argonne National Laboratory Radiological Physics Division Annual Report, July 1967-June 1968. ANL-7489, pp. 1-12.
2. Marinelli, L. D., G. F. Clemente, I. K. Abu-Shumays, and O. J. Steingraber. Radiology 92, 167 (1969).
3. Marinelli, L. D., G. F. Clemente, I. K. Abu-Shumays, and O. J. Steingraber. Abstracts of Papers, 2nd Int. Conf. on Medical Physics, Boston, August 11-15, 1969. Phys. Med. Biol. 5, 160 (1970).
4. Marinelli, L. D., G. F. Clemente, I. K. Abu-Shumays, and O. J. Steingraber. Argonne National Laboratory Radiological Physics Division Annual Report, July 1968-June 1969. ANL-7615, pp. 81-87.
5. Clemente, G. F., L. D. Marinelli, and I. K. Abu-Shumays. Int. J. Appl. Radiat. Isotopes 21, 307-318 (1970).
6. Phillips, D. L. J. Assoc. Comput. Mach. 9, 84-97 (1962).
7. Monahan, J. E. Scintillation Spectroscopy of Gamma Radiation, Ed. S. M. Shafroth. Gordon and Breach, New York (1968), pp. 371-428.
8. Hildebrand, F. G. Introduction to Numerical Analysis. McGraw-Hill Book Company, Inc., New York, 1956, Section 7.13.
9. May, H. A., L. D. Marinelli, and P. E. Hess. Argonne National Laboratory Radiological Physics Division Annual Report, July 1968-June 1969. ANL-7615, pp. 76-81.

A SPECIAL REGULARIZATION-UNFOLDING TECHNIQUE FOR THE NUMERICAL SOLUTION OF TWO-DIMENSIONAL FREDHOLM EQUATIONS OF THE FIRST KIND

I. K. Abu-Shumays and L. D. Marinelli

Density functions, such as the density of radioactivity in vivo, are related to the measured distribution "spectra" of their signals by Fredholm equations of the first kind. The experimental and statistical errors in a measurement may render the corresponding solution for the density function physically meaningless in the absence of additional constraints. This paper attempts the solution of two-dimensional Fredholm equations where the physical kernel can be approximated by a separable kernel. It introduces a smoothness constraint on the solution which results, essentially, in smoothness by convolution. Two numerical experiments are given.

Introduction

During the past two years the authors, jointly with others,[1,2] have studied the various available numerical methods for solving the Fredholm equation of the first kind:

$$\int_D K(\underline{x},\underline{x}')f(\underline{x}')d\underline{x}' = g(\underline{x}) \ , \ \underline{x} \in \mathcal{R} . \tag{1}$$

Our treatment then, was confined to the one-dimensional form of Eq. (1) with the kernel $K(x,x')$ fairly accurately known and the spectra $g(x)$ experimentally measured with modest accuracy. Equation (1) can be regarded as a linear operator, operating on a density function $f(\underline{x})$ in the domain D to produce a spectrum $g(\underline{x})$ in the range $\mathcal{R}$. It is well known[3] that this operator does <u>not have a bounded inverse</u> (we assume here that the kernel is nonsingular and that the operator has an inverse) and furthermore that an <u>infinitesimal change in g may cause a finite change in f</u>. Thus, the problem is mathematically "ill-posed."

In recent years it has become increasingly evident that reliable methods of solving Eq. (1) would serve many useful purposes, with

applications over a wide range of significant physical problems. We have already[1,2] adapted with considerable success the regularization (smoothing) techniques [initiated in 1962 by D. L. Phillips[3] and somewhat simplified by S. Twomey[4] in 1963 (see Marshall[4]] for the one-dimensional model for determining the unknown concentration of radioactivity per unit length of the human body.

Our initial investigations encourage us to generalize the regularization techniques to solve two-dimensional Fredholm equations of the first kind. It is evident that a two- or three-dimensional description of the concentration of small amounts of radioactivity in vivo would have many applications, ranging from localization of internal or external contamination in research and industrial personnel, to the distribution of radioactivated natural element contents (Na^{24}, Ca^{49}, etc.) in man occupationally exposed to tolerable doses of neutrons.

In principle, the smoothing technique of D. L. Phillips can be readily extended to two or more dimensions. Using an appropriate quadrature formula, the Fredholm equation of the first kind, Eq. (1), can, in a naive manner, be approximated by a linear system of equations with the unknowns $f_{i_1, i_2, \ldots i_n}$, where n is the dimensionality of the problem. For example, in two dimensions, if we select a 20 x 20 mesh we would obtain 400 equations in the 400 unknowns $f_{i,j}$. An elementary way to solve such a system would require inverting a 400 x 400 matrix. We understand that in order to invert a 350 x 350 matrix on the IBM 360 Model 75 with 250,000 word capacity, it is necessary to use external storage and such an operation may take over 20 minutes. If we note that a) some of the matrices we would expect to invert are almost singular, and b) to achieve an acceptable solution we would need a large number of other operations (which would certainly require external storage), we realize that such an approach would be impractical for two dimensions, not to mention higher dimensions.

In arriving at the method presented below, we were seeking both a simplified form and a reduction of the time required for computations.

These requirements lead us to assume that the kernel of the Fredholm equation is separable, a justifiable simplifying assumption in our case. Furthermore, we assume that the unknown density function f is piecewise smooth. We will proceed to explain the method and apply it to two mathematical models.

Method of Solution

The Fredholm equation under consideration here takes the form

$$\int_a^b dx' \int_c^d dy' \, K(x,x',y,y')f(x',y') = g(x,y) + \varepsilon(x,y), \tag{2}$$

where the density function $f(x',y')$ is the unknown density of radioactivity, $g(x,y)$ is the measured spectrum subject to both statistical and experimental error, and $\varepsilon(x,y)$ is the error. The actual value of the error $\varepsilon(x,y)$ is unknown, but the bounds on this error are known from knowledge of $g(x,y)$. As mentioned above, if one eliminates ε from Eq. (1), the result is a mathematically "ill-posed" problem. The measurement g is relatively insensitive to fictitious (positive-negative) density functions f' which satisfy the inequality

$$\int_a^b dz' \int_c^d dy' \, K(x,x',y,y')f'(x',y') \leq \varepsilon'(x,y),$$

where ε' is a distribution whose amplitude is of the order of the statistical or experimental error in the measurement of $g(x,y)$. In other words, small errors in $g(x,y)$ may be amplified to such an extent that the exact solution of the Fredholm equation (2) [deleting $\varepsilon(x,y)$] is physically meaningless. In addition, we note that the effect of an error in g on a calculated value of f depends on the smoothness of the kernel. Thus the success of solving Eq. (2) by any method depends to a large extent on the accuracy of the measured spectrum g and the shape of the kernel K.

For the present report, we make the further assumption that the

kernel $K(x,x',y,y')$ is separable, i.e.

$$K(x,x',y,y') = K^{(1)}(x,x')\, K^{(2)}(y',y) \quad . \tag{3}$$

We expect kernels for physical problems to depend upon the distance between the point at which a measurement is made and the point measured as follows:

$$K(x,x',y,y') = K([x-x']^2 + [y-y']^2) \quad . \tag{4}$$

For the one-dimensional distribution of radioactivity in vivo, which we have reported elsewhere,[1,2] our experimental results indicate that the kernel can often be approximated by a Gaussian. For two dimensions, such a kernel takes the form

$$K(x,x',y,y') = A\,\mathrm{Exp.}\,\{-[(x-x')^2 + (y-y')^2]/4\sigma^2\}\,, \tag{5}$$

and is indeed separable as in Eq. (3). Thus the assumption of separability of the kernel of Eq. (3) is a reasonable approximation for our problem of determining the distribution of radioactivity in vivo, and we expect this assumption to hold in several other physical situations.

The separability of the kernel given by Eq. (3) allows us to approximate the Fredholm equation (2) by a matrix equation. We assume that the domain of $f(x',y')$ (the region $[a,b] \times [c,d]$) and the range of $g(x,y)$ coincide and thus use (x',y') and $x,y)$ interchangeably. If in practice the range of $g(x,y)$ happens to be larger than the domain of $f(x,y)$ (for example, when measuring radioactivity in the human body, it is advantageous to take counts over a range including the body and extending beyond it, thus increasing the information content), then the domain is extended to coincide with the range, with the added restriction that the density function $f(x,y)$ should vanish beyond the original region. The interval $[a,b]$ is subdivided into m parts $a = x_1 < x_2 < \cdots < x_m = b$, and we associate with these divisions appropriate quadrature weights $v_1, v_2, \ldots, v_m$. Similarly, the interval $[c,d]$ is subdivided into n parts $c = y_1 < y_2 < \cdots < y_n = d$, and

we associate with these divisions appropriate quadrature weights $u_1, u_2, \ldots, u_n$. Using Eq. (3), Eq. (2) can now be approximated as follows:

$$g(x_k, y_\ell) + \varepsilon(x_k, y_\ell) = \int_a^b dx' \, K^{(1)}(x_k, x') \int_c^d f(x', y') K^{(2)}(y', y_\ell) dy'$$

$$\simeq \int_a^b dx' \, K^{(1)}(x_k, x') \sum_{j=1}^{n} f(x', y_j') u_j \, K^{(2)}(y_j', y_\ell)$$

$$\simeq \sum_{i=1}^{m} \sum_{j=1}^{n} K^{(1)}(x_k, x_i') v_i f(x_i', y_j') u_j \, K^{(2)}(y_j', y_\ell) \quad ,$$

$$(k = 1, 2, \cdots, m) \; , \; (\ell = 1, 2, \cdots . n) \quad . \tag{6}$$

Using the brief notation $g_{k\ell}$ for $g(x_k, y_\ell)$, etc., we replace the approximate Eq. (6) by

$$g_{k\ell} + \varepsilon_{k\ell} = \sum_{i=1}^{m} \sum_{j=1}^{n} K_{ki}^{(1)} v_i f_{ij} u_j K_{j\ell}^{(2)} \quad . \tag{7}$$

If the quadrature formula is sufficiently accurate, we expect f_{ij} of Eq. (7) to approximate $f(x_i', y_j')$ of Eq. (2). Assuming that $\varepsilon_{k\ell}$ is negligible compared to $g_{k\ell}$ and introducing the matrix notation $G = (g_{k\ell})$, $F = (f_{ij})$, $A = (K_{ki}^{(1)} v_i)$ and $B = (u_j K_{j\ell}^{(2)})$, Eq. (7) becomes

$$G = AFB \quad . \tag{8}$$

Equation (8) as such incorporates the statistical and experimental errors in evaluating the elements of G and the quadrature error in the integrations leading to the new kernels A and B. Thus, from the considerations given above we expect the exact solution $F = A^{-1}GB^{-1}$ of Eq. (8) to be meaningless, and hence we need additional constraints in order to get a physically meaningful solution. The regularization unfolding is based

on the physically meaningful assumption that (except possibly at a few irregular locations) the magnitude of the density function $f(x,y)$ cannot change abruptly a) between one point and its immediate neighbors on the grid $i = 1,\cdots,m$; $j = 1,\cdots,n$; and b) between adjacent grids. In other words, we require the surface $f(x,y)$ of the distribution to be sufficiently smooth. Thus we seek a solution of Eqs. (6), (7), and (8) which is piecewise smooth and such that the results of its integration over x alone and over y alone as in Eq. (6) are also piecewise smooth. Typical smoothness constraints are to minimize the sum of the squares of second differences, e.g., in one dimention[1,3] to require each three adjacent points (say f_{j-1}, f_j, f_{j+1}) to be on or very close to a straight line. A suitable formulation of the problem is then to find the solutions $f_{k\ell}$ which minimize the function

$$
\begin{aligned}
&H(f_{11}, f_{12}, \cdots, f_{mn}; \gamma_1, \gamma_2) \\
&= \sum_{k,\ell} P_{k\ell}\, \varepsilon_{k\ell}^2 + \gamma_2 \sum_{k,\ell} p_k [(AF)_{k,\ell-1} - 2(AF)_{k,\ell} + (AF)_{k,\ell+1}]^2 \\
&+ \gamma_1 \sum_{k,\ell} q_k [(FB)_{k-1,\ell} - 2(FB)_{k,\ell} + (FB)_{k+1,\ell}]^2 \\
&+ \gamma_1 \gamma_2 \sum_{k,\ell} [f_{k-1,\ell-1} - 2f_{k-1,\ell} + f_{k-1,\ell+1} - 2f_{k,\ell-1} \\
&\qquad + 4f_{k,\ell} - 2f_{k,\ell+1} \\
&+ f_{k+1,\ell-1} - 2f_{k+1,\ell} + f_{k+1,\ell+1}]^2 + \text{Boundary Terms} . \qquad (9)
\end{aligned}
$$

We note that the first term on the right-hand side of Eq. (9) is a measure of the error in solving Eq. (8). This term in detail [using Eq. (7)] is

$$e^2 = \sum_{k=1}^{m} \sum_{\ell=1}^{n} P_{k\ell} \left(g_{k\ell} - \sum_{i=1}^{m} \sum_{j=1}^{n} A_{ki} f_{ij} B_{j\ell}\right)^2 , \tag{10}$$

where $P_{k\ell} = p_k q_\ell$ are appropriate weight factors. If there is no a priori evidence that some of the $g_{k\ell}$'s are more accurate than others, then one may set $P_{k\ell} = p_k = q_\ell = 1$ for all k, ℓ. Minimizing this measure of the error e^2, yields the least squares solution*

$$F = [A^T A]^{-1} A^T G B^T [B B^T]^{-1} . \tag{11}$$

This solution is equivalent to the exact solution of Eq. (8), and is likewise expected to be meaningless whenever A and B are not well conditioned (that is, nearly singular) and/or G has appreciable error.

The coefficients γ_1 and γ_2 of the smoothing terms in Eq. (9) denote optional weights that control the degree of smoothing along the x and y directions, respectively. The second and third terms on the right-hand side of Eq. (9) have the effect of bringing the elements of each row or column close to the elements of the two neighboring rows or columns. The fourth term corrects for expected random fluctuations at each point of the solution of the density function by weighing each net of nine neighboring points as is indicated in Figure 1.

Finally, the last terms in Eq. (9) control the value of the density functions at the boundaries, as will be indicated below in connection with the smoothing matrices.

The algebra of minimizing H of (9) while holding γ_1 and γ_2 constant leads to the result

$$[A^T A + \gamma_1 S_1^T S_1] F [B B^T + \gamma_2 S_2 S_2^T] = A^T G B^T .$$

Hence, the desired solution for the density function f(x,y) is

---

*The superscript T denotes transpose.

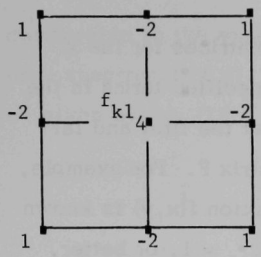

FIG. 1.--A net of nine points and their corresponding weights. These weights, appearing in the fourth term on the right-hand side of Eq. (9), have the effect of minimizing the fourth difference $\partial^4 f/\partial x^2 \partial y^2$ and reducing unnecessary fluctuations.

$$F = [A^T A + \gamma_1 S_1^T S_1]^{-1} A^T G B^T [BB^T + \gamma_2 S_2 S_2^T]^{-1} , \tag{12}$$

where S_1 and S_2 are the following square matrices:

$$S_1 = \begin{bmatrix} S^1_{11} & S^1_{12} & & & & & & & 0 \\ 1 & -2 & 1 & & & & & & \\ & 1 & -2 & 1 & & & & & \\ & & \cdot & \cdot & \cdot & & & & \\ & & & \cdot & \cdot & \cdot & & & \\ & & & & \cdot & \cdot & \cdot & & \\ & & & & & \cdot & \cdot & \cdot & \\ & & & & & & 1 & -2 & 1 \\ 0 & & & & & & & S^1_{m,m-1} & S^1_{mm} \end{bmatrix} \tag{13 a}$$

$$S_2 = \begin{bmatrix} S^2_{11} & 1 & & & & & 0 \\ S^2_{21} & -2 & 1 & & & & \\ & 1 & -2 & & & & \\ & & 1 & \cdot & & & \\ & & & \cdot & 1 & & \\ & & & & -2 & S^2_{n-1,n} & \\ 0 & & & & 1 & S^2_{nn} & \end{bmatrix} \tag{13 b}$$

The matrices S_1 and S_2 are defined as the smoothing matrices for the x variables and the y variables, respectively. The unspecified terms in the matrices S_1 and S_2 of Eq. (13) control the conditions at the first and last rows and the first and last columns of the solution matrix F. For example, if the first row of F is known to be zero [if the distribution f(x,y) is known to be zero at the edge x = a], one writes $S^1_{12} = 0$ and $S^1_{11} = 1$, or better, S^1_{11} = large number [the dominant term for f(x,y) in this case can be shown to be $f(a,y) = \text{constant}/S^1_{11}$]; if the first row is known to be almost the same as the second row [if for y fixed f(x,y) is known to approach a constant as x approaches the edge x = a] one puts $S^1_{11} = -S^1_{12} = 1$, and if no condition is to be given at the first row [at the end point x = a] one sets $S^1_{11} = S^1_{12} = 0$. The equivalent conditions hold for the last row and the first and last columns of F.

We have so far specified only one option of smoothing by the matrices given in Eq. (13). One may choose to smooth by minimizing the sum of the squares of the first or fourth differences or any suitable combination thereof, rather than the second.[4] In fact the choice of the smoothing matrices S_1 and S_2 is optional and may depend on the problem considered and the amount of initial information available. If a given row (column) of F, say the kth row (column) is known to vanish [for example when the range of g(x,y) exceeds the actual domain of f(x,y)] then, as in the treatment of boundary terms above, the element S^1_{kk} (S^2_{kk}) of the matrix S_1 (S_2) is set equal to a large number, while the rest of the elements in the row and column of S_1 (S_2) containing the element S^1_{kk} (S^2_{kk}) are set equal to zero.

As mentioned above, γ_1 and γ_2 are weights that control the degree of smoothness of the solution Eq. (12). Usually it suffices to compute the right-hand side of Eq. (12) for a few values of γ_1 and γ_2 in order to estimate the acceptable values of these weights γ_1 and γ_2. The acceptable values of γ_1 and γ_2 are those which would lead to a new (computed) spectrum g'(x,y) which deviates from g(x,y) by an amount

comparable to the expected statistical and experimental error in the measured spectrum $g(x,y)$. We have already specified one measure of the error, e^2 given by Eq. (10). Another useful measure of the error is

$$\bar{\varepsilon} \equiv \sum_{k=1}^{m} \sum_{\ell=1}^{n} \bar{P}_{k\ell} |\varepsilon_{k\ell}| / mn \tag{14}$$

where $|\varepsilon_{k\ell}|$ is the absolute value of the difference between the spectrum $g_{k\ell}$ at (x_k, y_ℓ) and its value computed on the basis of the solution Eq. (12); more precisely

$$\bar{\varepsilon} \equiv \sum_{k=1}^{m} \sum_{\ell=1}^{n} \bar{P}_{k\ell} \left| g_{k\ell} - \sum_{i=1}^{m} \sum_{j=1}^{n} A_{ki} f_{ij} B_{j\ell} \right| / mn \ . \tag{15}$$

The factors $\bar{P}_{k\ell}$ are appropriate weights which again may be set $\bar{P}_{k\ell} = 1$ if there is no a priori evidence that some of the $g_{k\ell}$'s are more accurate than others.

If necessary, the physical constraint that the density function F should be non-negative can be imposed by an addition of a one-step iteration to the solution Eq. (12). The details are similar to what we have reported in Ref. 1 for one dimension and will be omitted here. However, from our experience in one dimension, we have reason to believe that the correct choice of γ_1 and γ_2 will invariably lead to an essentially non-negative solution (i.e., $f \geq -\varepsilon$, $\varepsilon \to 0$) whenever such a solution is required by the physics of the problem.

Preliminary Applications

A computer program for the IBM 360 has been written by Mrs. Alice Meyer to solve Eqs. (9) and (12). (The program has a large number of options and for details we refer to Ref. 5.) Among the options are various ways to specify the kernel, the smoothing matrices, and the weights for quadrature and for different regions of the measured spectrum $g(x,y)$. The program allows numerical and graphical printouts.

In order to investigate the applicability of the method described above, we have elected to treat the two mathematical models presented below.

Example 1. Single Peak Distribution

In this and in the following example, simple surface distributions and separable kernels [as in Eq. (3)] are chosen. Here we select the elliptic paraboloid density function

$$z = f(x,y) = \alpha \{2 - (\frac{x}{x_0} - 1)^2 - (\frac{y}{y_0} - 1)^2\} . \tag{16}$$

This surface is symmetric with respect to the planes $x = x_0$ and $y = y_0$. It is concave downwards and limited to the region $z \leq 2\alpha$. Each plane z = constant ($z < 2\alpha$) perpendicular to the z-axis cuts the surface in an ellipse, and each plane x = constant or y = constant cuts the surface in a parabola. We confine our attention to the region above the x-y plane with a base restricted to the interval $x \in [0, 2x_0]$, $y \in [0, 2y_0]$. The general shape of the density function f(x,y) is given in Figure 2.

The kernel is selected to be the Gaussian

$$K(x,x',y,y') = a^2 e^{-\{(x-x')^2+(y-y')^2\}/4\sigma^2} . \tag{17}$$

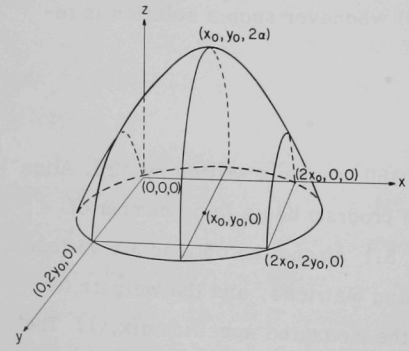

FIG. 2.--Density function f(x,y).

The spectrum $g(x,y)$ is then given by

$$g(x,y) = \int_0^{2x_0} dx' \int_0^{2y_0} dy'$$

$$a^2 e^{-\{(x-x')^2+(y-y')^2\}/4\sigma^2} \alpha\{2-(\frac{x'}{x_0} - 1)^2 - \frac{y'}{y_0} - 1)^2\}. \quad (18)$$

Carrying out the integration, we get

$$g(x,y) = \alpha a^2 [\sigma^2 \pi\{\Phi(\frac{2y_0-y}{2\sigma}) + \Phi(\frac{2x_0-x}{2\sigma})$$

$$+ \Phi(\frac{x}{2\sigma})\}\{2-(\frac{x}{x_0} - 1)^2 - (\frac{y}{y_0} - 1)^2 - \frac{2\sigma^2}{y^2} - \frac{2\sigma^2}{x_0^2}\}$$

$$+ \frac{2\sigma^3\sqrt{\pi}}{y_0^2} \{\Phi(\frac{2x_0-x}{2\sigma}) + \Phi(\frac{x}{2\sigma})\}\{y\, e^{-(2y_0-y)^2/4\sigma^2} + (2y_0-y)e^{-y^2/4\sigma^2}\}$$

$$+ \frac{2\sigma^3\sqrt{\pi}}{x_0^2} \{\Phi(\frac{2y_0-y}{2\sigma}) + \Phi(\frac{y}{2\sigma})\}\{x\, e^{-(2x_0-x)^2/4\sigma^2} + (2x_0-x)e^{x^2/4\sigma^2}] . \quad (19)$$

Where $\Phi(t)$ is the error function

$$\Phi(t) = \mathrm{erf}(t) = \frac{2}{\sqrt{\pi}} \int_0^t e^{-t^2} dt . \quad (20)$$

For the purpose of numerical computations we select $\alpha = 1$, $a = 10$, $x_0 = 5$ and $y_0 = 10$. We also select three values of σ, $\sigma = 0.5$, 1 and 2, and two mesh sizes* $M \times N = 11 \times 21$ and 21×41 for the region $[0,10] \times [0,20]$.

---

*M and N are used in the rest of the paper, instead of m and n, so as to be consistent with the computer program[5] and the figures and tables.

The process of solving a Fredholm equation of the first kind [Eq. (2)] by approximating it with a matrix equation [Eq. (8)] involves quadrature error which depends on the following variables: the kernel shape and size, the order of the matrices (the grid density or mesh size, M x N), and the particular density function studied. For the present example, we have computed the matrix G in two ways, a) from Eq. (19) for the analytical representation of the spectra, and b) directly from the matrix Eq. (8) with the matrix F for the density function, and the response matrices A and B computed on the basis of Eqs. (16) and (17), respectively. The results are summarized in Table 1. As we would expect, the response kernel is better represented, and hence the quadrature error becomes smaller, as the kernel becomes wider and/or grid lines become denser (i.e., as the order of the matrices F, G, and hence the order of A and B increases). Table 1 could have been simplified by scaling the kernel in such a way that the maximum value of g(x,y) (or the volume under the surface g(x,y) as a function of (x,y) is independent of kernel width. Our own choice, however, is more in line with anticipated experimental situations.

In the present example, we will eliminate the quadrature error by starting with the spectra G computed on the basis of the matrix Eq. (8) rather than the integral (Fredholm) Eq. (2). In other words, we assume that we are asked to solve a matrix equation of the form (8) rather than the integral Eq. (2). This choice allows us to concentrate on the effect of the ill conditioning of the matrices A and B on the solution for the density matrix. Depending on the shape of the response kernel K, the matrices A^TA and BB^T may have an eigenvalue very close to zero and hence may be almost singular (or singular due to machine limits on the accuracy of matrix computations). This situation makes the solution of the matrix Eq. (8) meaningless, if not impossible.

We have applied the regularization method described above to unfolding the spectra G of sizes M x N = 11 x 21 and 21 x 41. Tables 2 and 3 summarize the main results when G = AFB is used and also when an error

TABLE 1. Quadrature Error. Magnitude of error introduced by computing G = AFB by quadrature. The error is larger the narrower the kernel and is smaller the larger the order M x N of the matrices F and G.

σ and G / M x N	Narrow Kernel σ = 0.5 G = xx. = xxx.*	Medium Kernel σ = 1.0 G = xxx. - xxxx.	Wide Kernel σ = 2.0 G = xxxx.
11 x 21	.x - xx.	.0 - x.	.0x - .x
21 x 41	.00x - .x	.00x - .x	.000x - .0x

* Each x stands for a digit between 0 and 9 in the position it occupies relative to the decimal point indicated -- xx., xxx., give the order of magnitude of the value under consideration.

TABLE 2. Evaluation of the computed density matrix F for the single peak distribution relative to its exact value; summary of numerical results for M x N = 11 x 12. The ratings are: A+ = Exact; A = Very Good; B = Good; C = Fair; D = Large Error; and E = Unacceptable.

	Narrow Kernel σ = 0.5 G = xx. - xxx.*			Medium Kernel σ = 1.0 G = xxx. -xxx.			Wide Kernel σ = 2.0 G = xxxx.		
	$\gamma_1 = \gamma_2$	$\bar{\epsilon}$**	Computed F	$\gamma_1 = \gamma_2$	$\bar{\epsilon}$	Computed F	$\gamma_1 = \gamma_2$	$\bar{\epsilon}$	Computed F
G=AFB	0.0		A+	0.0		D	0.0	NO SOLUTION	
	10^{-4}	1.3×10^{-5}	A+	10^{-4}	5.5×10^{-4}	A	10^{-4}	5.6×10^{-3}	A
	10^{-2}	1.3×10^{-3}	A	10^{-2}	1.5×10^{-2}	B	10^{-3}	8.9×10^{-3}	B
							10^{-2}	2.4×10^{-2}	B
Comments	Problem correctly posed			A, B ill conditioned			A^TA and BB^T singular		
G Reduced to 4 S.F.	0.0		A	0.0		E	0.0	NO SOLUTION	
	10^{-4}	1.3×10^{-5}	A	0.01	2.4×10^{-2}	B	0.1	0.20	C
	10^{-2}	1.3×10^{-3}	B	0.1	7.3×10^{-2}	A	0.3	0.41	B
				0.5	0.23	B	0.5	0.51	C
G Reduced to 3 S.F.	0.0		B	0.0		E	0.0	NO SOLUTION	
	0.1	1.2×10^{-2}	B	0.1	0.21	C	0.1	0.27	C
	0.5	4.0×10^{-2}	A	0.5	0.29	B	0.5	0.54	B
	1.0	6.2×10^{-2}	B	1.0	0.35	C	0.7	0.60	C
G Reduced to 2 S.F.	0.0		C	0.0		E	0.0	NO SOLUTION	
	0.5	8.9×10^{-2}	C	5.0	2.1	C	1.0	2.6	C
	1.0	0.13	B	10.0	2.3	B	5.0	2.6	B
	5.0	0.28	C	20.0	2.5	C	10.0	2.6	C

* See footnote for Table 1.
** $\bar{\epsilon}$ stands for the average error in G corresponding to the computed F.

TABLE 3. Evaluation of the computed density matrix F for the single peak distribution relative to its exact value; summary of numerical results for M x N = 21 x 41.*

	Narrow Kernel $\sigma = 0.5$ G = xx. - xxx.			Medium Kernel $\sigma = 1.0$ G = xxx. - xxxx.			Wide Kernel $\sigma = 2.0$ G = xxxx.		
	$\gamma_1=\gamma_2$	$\bar{\varepsilon}$	Computed F	$\gamma_1=\gamma_2$	$\bar{\varepsilon}$	Computed F	$\gamma_1=\gamma_2$	$\bar{\varepsilon}$	Computed F
G=AFB	0.0		C	0.0	NO SOLUTION		0.0	NO SOLUTION	
	10^{-4}	7.6×10^{-5}	A+	10^{-4}	5.5×10^{-4}	A+	10^{-3}	3.4×10^{-3}	A
	10^{-2}	1.3×10^{-3}	A	10^{-2}	4.9×10^{-3}	A	10^{-2}	3.9×10^{-3}	B
Comments	A, B ill conditioned			A^TA and BB^T singular			A^TA and BB^T singular		
G Reduced to 4 S.F.	0.0		E	0.0	NO SOLUTION		0.0	NO SOLUTION	
	0.01	2.3×10^{-3}	A	0.1	2.4×10^{-2}	B	0.1	0.028	D
	0.1	6.9×10^{-3}	B	0.5	3.2×10^{-2}	A	0.5	0.084	C
				1.0	5.2×10^{-2}	B	1.0	0.15	B
G Reduced to 3 S.F.	0.0		E	0.0	NO SOLUTION		0.0	NO SOLUTION	
	0.1	2.1×10^{-2}	B	1.0	0.22	B	1.0	0.30	C
	1.0	3.0×10^{-2}	A	5.0	0.24	A	5.0	0.48	B
	10.0	6.9×10^{-2}	B	10.0	0.26	B	10.0	0.58	C
G Reduced to 2 S.F.	0.0		E	0.0	NO SOLUTION		0.0	NO SOLUTION	
	1.0	0.19	B	5.0	2.2	C	10.0	2.46	D
	5.0	0.20	A	10.0	2.3	C	50.0	2.51	C
	10.0	0.22	A	50.0	2.4	B	100.0	2.52	C
	50.0	0.30	B						

*See footnotes to Tables 1 and 2. See also Table 2 for rating the computed solution F.

is introduced in G by reducing its elements to 4 S.F. (significant figures), 3 S.F. and 2 S.F. The results for γ_1 and $\gamma_2 = 0$ represent the usual (unsmoothed) solutions; other values of γ_1 and γ_2 represent different degrees of smoothing. A sample of the graphical results is given in Figures 3-6. These figures show contours for the spectrum G and the corresponding exact density matrix and/or solution matrix F.

We observe that for the narrow response kernel ($\sigma = 0.5$) the matrices A^TA and BB^T are positive, definite and well conditioned (possess well-defined inverses). As the response kernel becomes wider, these matrices become more and more ill conditioned (their smallest eigenvalues become closer and closer to zero). In fact, for $\sigma = 2.0$ and M x N = 11 x 21 and for $\sigma = 1.0$, $\sigma = 2.0$ and M x N = 21 x 41, the computer program indicated

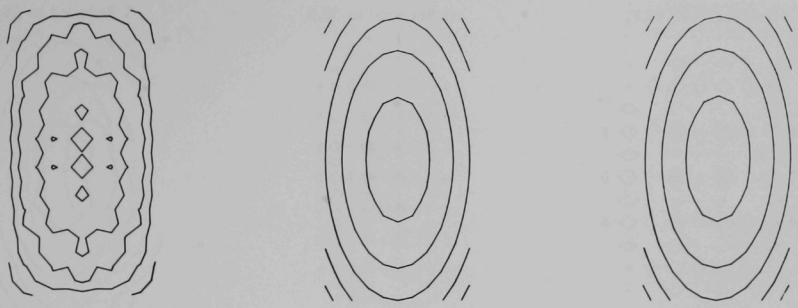

a) Spectrum G b) Exact Density F c) F for $\gamma \equiv \gamma_1 = \gamma_2 = 0$ (No Smoothing)

Fig. 3. Narrow Kernel: $\sigma = 0.5$, $M \times N = 11 \times 21$

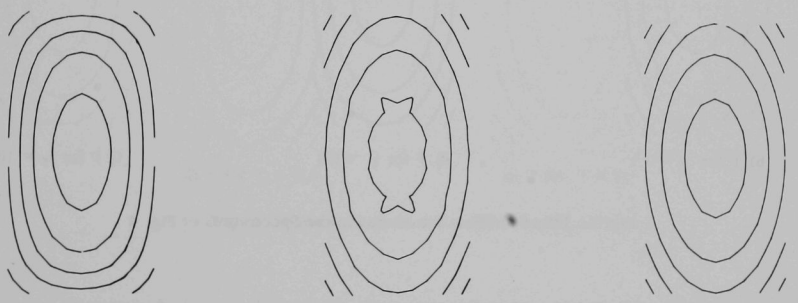

a) Spectrum G b) F for $\gamma = 0$ c) F for $\gamma = .0001$

Fig. 4. Average Kernel: $\sigma = 1.0$, $M \times N = 11 \times 21$

that these matrices are singular to within double precision (16 digit) accuracy. We were able to satisfy our curiousity, however, and get inverses for A^TA and BB^T by rescaling these matrices. The details will be omitted, but the corresponding solutions of the matrix equation $G = AFB$ were highly oscillatory and physically meaningless.

The above justifies the results given in Tables 2 and 3 and shown in Figures 3-6. For $\sigma = 0.5$, $M \times N = 11 \times 21$, although the shape of the

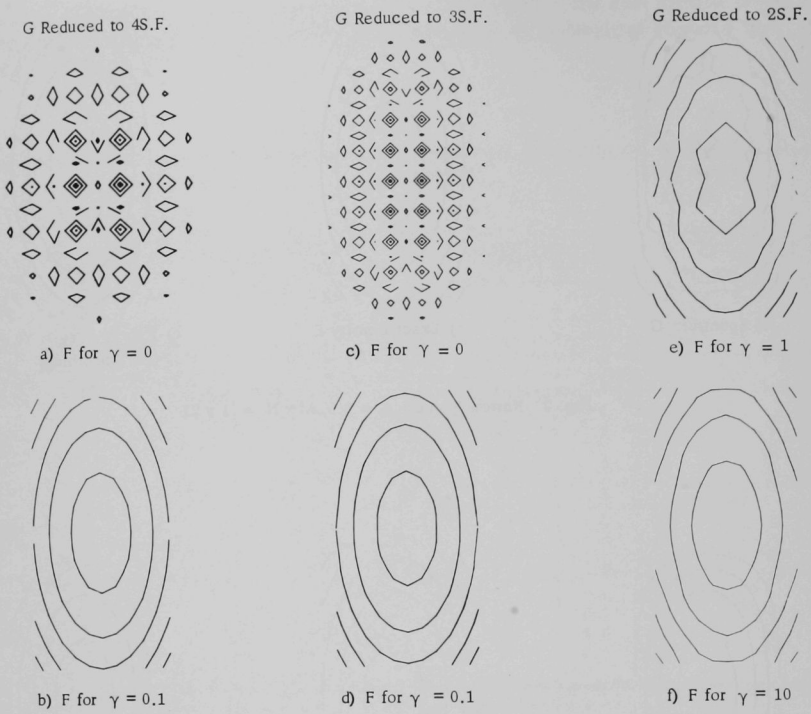

Fig. 5. Effect of Errors Introduced in the Spectrum G of Fig. 4

spectrum is distorted because of quadrature error in evaluating G by AF(exact)B [Eq. (8)] instead of Eq. (19); the solution given by Eq. (11) is stable as shown in Figure 3. In this case smoothing becomes necessary only if very large errors are introduced in the spectra. Smoothing is necessary for $\sigma = 1.0$ and $\sigma = 2.0$. We note that the values of $\gamma_1 = \gamma_2$ (for an explanation of how to choose γ_1 and γ_2 (for an explanation of how to choose γ_1 and γ_2, see the main text above and Example 2 below) and hence the degree of smoothness needed to yield an optimum solution for the density matrix F increases as the error in G increases and, in general, as the response matrices become more and more ill conditioned.

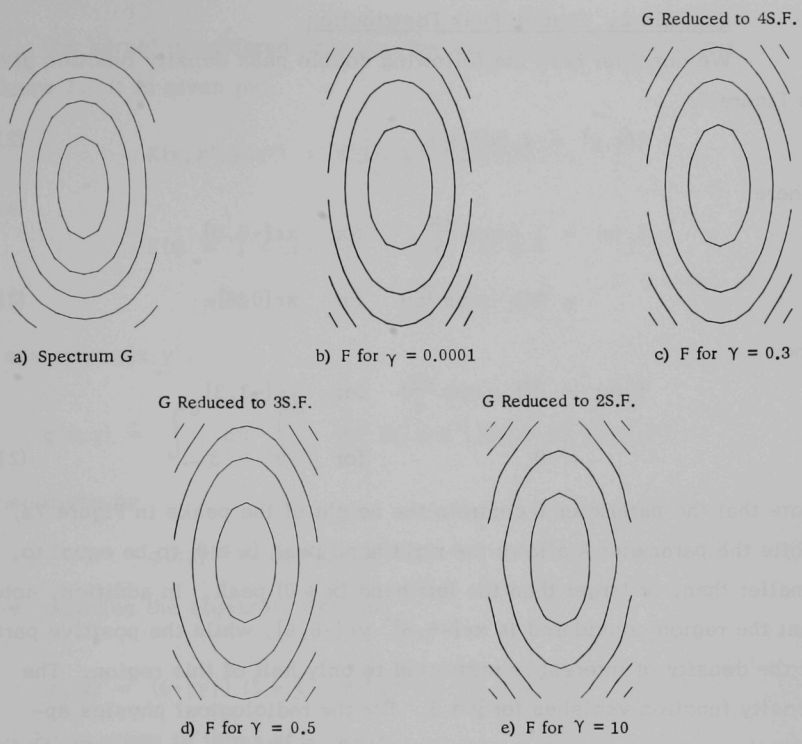

Fig. 6. Wide Kernel: $\sigma = 2.0$, M x N = 11 x 21

Figures 4 and 5 illustrate the situation for $\sigma = 1.0$. Figure 4 shows that the unsmoothed solution ($\gamma_1 = \gamma_2 = 0$) is only slightly distorted, and the distortion is removed by smoothing with $\gamma_1 = \gamma_2 = 0.0001$. Figure 5a shows that an error of less than 0.1% introduced by reducing G to 4 S.F. (retaining only the largest 4 significant figures for each value of G) leads to an unacceptable solution. The desirable solution of Figure 5b is achieved by smoothing with $\gamma_1 = \gamma_2 = 0.1$. The rest of Figure 5 illustrates the results when G is reduced to 3 S.F. and to 2 S.F. For $\sigma = 2.0$ the unsmoothed solution is unacceptable; Figure 6 shows the contours for G = AF(exact)B and for the smoothed solutions corresponding to this value of G and to G reduced to 4 S.F., 3 S.F., and 2 S.F.

Example 2. Double Peak Distribution

We consider here the following double peak density function given in Figure 7:

$$f(x,y) = f_1(x) f_2(y) \tag{21 a}$$

where

$$f_1(x) = 1 - \cos\frac{\pi x}{3} \quad \text{for} \quad x \varepsilon [-6,0]$$

$$= A(1 - \cos\frac{\pi x}{3}) \quad \text{for} \quad x \varepsilon [0,6] \tag{21 b}$$

and

$$f_2(y) = B(1 + \cos\frac{\pi y}{3}) \quad \text{for} \quad y \varepsilon [-3,3]$$

$$= 0 \quad \text{for} \quad |y| \geq 3 \ . \tag{21 c}$$

Note that the parameter B controls the height of the peaks in Figure 7a, while the parameter A allows the right hand peak ($x \geq 0$) to be equal to, smaller than, or larger than the left hand ($x \leq 0$) peak. In addition, note that the region considered is $x \varepsilon [-6,6]$, $y \varepsilon [-6,6]$, while the positive part of the density of interest is restricted to only half of this region. The density function vanishes for $y \geq 3$. For the radiological physics applications we have in mind, this example is analogous to extending the measurements of the radioactivity beyond the human body, or, to the case in which certain parts of the human body have no activity or a negligible amount.

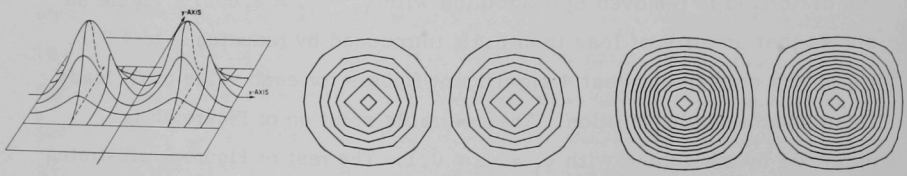

a) Actual Shape b) Contours for M x N = 13 x 13 c) Contours for M x N = 25 x 25

Fig. 7. Exact Density Function

The kernel considered here has the same shape as one of the peaks in Figure 7. It is given by

$$K(x,x',y,y') = K(|x-x'|)K(|y-y'|) \quad , \tag{22 a}$$

where

$$\begin{aligned} K(t) &= 1 + \cos\frac{\pi t}{3} && \text{for} \quad |t| \le 3 \\ &= 0 && \text{for} \quad |t| \ge 3 \quad . \end{aligned} \tag{22 b}$$

The spectrum $g(x,y)$,

$$g(x,y) = \int_{-6}^{6} dx' \int_{-6}^{6} dy' \, K(|x-x'|)K(|y-y'|)f(x',y')$$

is then given by

$$g(x,y) = Bg_1(x)g_2(y) \quad , \tag{23}$$

where, omitting the algebraic details,[3]

$$g_2(y) = (6-|y|)\,(1 + \tfrac{1}{2}\cos\frac{\pi|y|}{3}) + \frac{9}{2\pi}\sin\frac{\pi|y|}{3} \quad , \quad y\varepsilon[-6,6] \tag{24}$$

and $g_1(x)$ is given in terms of g_2 as

$$\begin{aligned} g_1 &= g_2(x+3) && \text{for } x\varepsilon[-6,-3] \\ &= g_2(x+3) + Ag_2(x-3) && \text{for } x\varepsilon[-3,3] \\ &= Ag_2(x-3) && \text{for } x\varepsilon[3,6] \quad . \end{aligned} \tag{25}$$

For the purpose of numerical computations we select $A = B = 1$ (the two peaks are of the same height for the results reported here). Furthermore, we compute the elements $G_{ij} = g(x_i, y_i)$ from the analytic expressions Eqs. (23) - (25) and thus, contrary to what was done in Example 1, we do not eliminate the quadrature error here. Table 4 summarizes the computational and graphical results corresponding to the grid density $M \times N = 13 \times 13$. For this case, the quadrature error is bounded by 0.4, and seems to dominate the errors artificially introduced by reducing g to 4 S.F., 3 S.F.,

TABLE 4. Evaluation of the computed density matrix F for the double peak distribution relative to its exact value; summary of numerical results for M x N = 13 x 13.*

	G : $G_{ij} \le$ xx.** $\varepsilon_{ij} \le$ .x			G reduced to 4 S.F.			G reduced to 3 S.F.			G reduced to 2 S.F.		
	$\gamma_1=\gamma_2$	$\bar{\varepsilon}$	Computed F	$\gamma_1=\gamma_2$	$\bar{\varepsilon}$	Computed F	$\gamma_1=\gamma_2$	$\bar{\varepsilon}$	Computed F	$\gamma_1=\gamma_2$	$\bar{\varepsilon}$	Computed F
	0.0		D	0.0		D	0.0		E	0.0		E
SM1	0.02	0.19	C	0.02	0.19	C	0.02	0.19	C	0.02	0.24	D
	0.02	0.21	B	0.03	0.21	B	0.03	0.22	B	0.04	0.28	C
	0.04	0.24	C	0.04	0.24	C	0.04	0.24	C	0.06	0.32	D
SM2	0.02	0.19	C	0.02	0.19	C	0.02	0.19	C	0.02	0.24	D
	0.03	0.21	B	0.03	0.21	B	0.03	0.22	C	0.04	0.29	C
	0.04	0.24	C	0.04	0.24	C	0.04	0.24	B	0.06	0.32	D
	Slightly better than SM1											
SM3	0.03	0.21	B	0.03	0.21	B	0.04	0.24	B	0.04	0.30	C
	0.04	0.24	A	0.04	0.24	A	0.06	0.28	A	0.06	0.33	C
	0.05	0.26	B	0.05	0.26	B	0.08	0.31	B	0.08	0.36	B
	Noticeably better than SM2											
SM4	0.04	0.27	A	0.04	0.27	A	0.04	0.28	A	0.06	0.36	C
	0.05	0.29	A	0.05	0.29	A	0.06	0.32	B	0.08	0.39	B
	0.06	0.31	B	0.06	0.31	B	0.08	0.35	B	0.10	0.42	C
	Slightly better than SM3											
SM5	0.04	0.27	B	0.04	0.27	A	0.04	0.28	A	0.06	0.36	C
	0.05	0.29	A	0.05	0.29	A	0.06	0.32	B	0.08	0.40	B
	0.06	0.31	B	0.06	0.31	B	0.08	0.35	B	0.10	0.43	C
	Hardly better than SM4											

* See footnotes to Tables 1 and 2. See also Table 2 for rating the computed solution F.

** The magnitude of each element of G is $(G)_{ij} \le 81$; ε_{ij} stands for the quadrature error.

and 2 S.F. We observe from Table 4* that, throughout the computations, the optimum results for the density matrix F were those corresponding to the choices of $\gamma_1 = \gamma_2$ for which the elements of AFB differ, on the average, from the corresponding elements of G by about 0.2 to 0.4, i.e., in the range of the expected error. Table 5 summarizes the computational and graphical results which correspond to the grid density M x N = 25 x 25. Here, the quadrature error is bounded by (0.0x), and the average quadrature

* A slight difference in the optimum choice of γ often still leads to reasonably accurate solutions.

TABLE 5. Evaluation of the computed density matrix F for the double peak distribution relative to its exact value; summary of numerical results for M x N = 25 x 25.*

	G : $G_{ij} \le xx$.** $\epsilon_{ij} \le 0.0x$ $\langle\epsilon_{ij}\rangle = 0.008 \pm 0.001$			G reduced to 4 S.F. error introduced $\le 0.00x$			G reduced to 3 S.F. error introduced $\le 0.0x$			G reduced to 2 S.F. error introduced $\le 0.x$		
	$\gamma_1=\gamma_2$	$\bar{\epsilon}$	Computed F	$\gamma_1=\gamma_2$	$\bar{\epsilon}$	Computed F	$\gamma_1=\gamma_2$	$\bar{\epsilon}$	Computed F	$\gamma_1=\gamma_2$	$\bar{\epsilon}$	Computed F
	0.0		D	0.0		E	0.0		E	0.0		E
SM1	0.002	8.2×10^{-3}	C	0.001	7.8×10^{-3}	C	0.04	0.025	C	0.3	0.13	D
	0.003	8.8×10^{-3}	C	0.002	8.4×10^{-3}	B	0.06	0.027	B	0.4	0.14	C
	0.004	9.4×10^{-3}	B	0.003	9.0×10^{-3}	C	0.08	0.029	C	0.5	0.15	D
SM2	0.002	7.7×10^{-3}	C	0.001	7.6×10^{-3}	C	0.04	0.021	C	0.3	0.13	D
	0.003	8.2×10^{-3}	B	0.002	8.0×10^{-3}	B	0.06	0.023	B	0.4	0.14	C
	0.004	8.5×10^{-3}	C	0.003	8.4×10^{-3}	C	0.08	0.026	C	0.5	0.15	D
	Slightly better than SM1											
SM3	0.001	7.3×10^{-3}	A	0.001	7.6×10^{-3}	B	0.02	0.018	B	0.1	0.12	C
	0.002	7.5×10^{-3}	B	0.002	7.7×10^{-3}	A	0.04	0.019	A	0.2	0.13	B
	0.003	7.7×10^{-3}	C	0.003	7.9×10^{-3}	B	0.06	0.022	B	0.4	0.15	C
	Noticeably better than SM2											
SM4	0.0005	7.5×10^{-3}	B	0.003	8.1×10^{-3}	B	0.02	0.020	A	0.1	0.11	C
	0.001	7.6×10^{-3}	A	0.004	8.2×10^{-3}	A	0.04	0.024	B	0.2	0.12	B
	0.00	7.7×10^{-3}	B	0.005	8.2×10^{-3}	B	0.06	0.027	B	0.4	0.13	C
	Slightly better than SM3											
SM5	0.0005	7.5×10^{-3}	A	0.002	8.1×10^{-2}	B	0.02	0.021	A	0.1	0.12	C
	0.001	7.6×10^{-3}	B	0.003	8.2×10^{-2}	A	0.04	0.024	B	0.2	0.12	B
	0.00	7.7×10^{-3}	B	0.004	8.3×10^{-2}	B	0.06	0.027	B	0.4		C
	Hardly better than SM4											

* See footnotes to Tables 1 and 2. See also Table 2 for rating the computed solution F.

** The magnitude of each element of G is $(G)_{ij} \le 81$; ϵ_{ij} is the quadrature error and $\langle\epsilon_{ij}\rangle$ is the average quadrature error.

error is 0.008 ± 0.001. We observe from Table 5 that the best choices of γ corresponding to G = AFB and G = AFB reduced to 4 S.F., are those for which $\bar{\epsilon}_{ij}$ is in the range 0.008 ± 0.001 of the average quadrature error. For G = (AFB reduced to 3 S.F.) and (AFB reduced to 2 S.F.), Table 5 indicates that the best choices of $\gamma_1 = \gamma_2$ are those which lead to $\bar{\epsilon}_{ij}$ in the range of the error introduced in G.

The symbols SM1 to SM5 in Tables 4 and 5 correspond to smoothing with the following types of boundary conditions (see Figure 7 for the exact density matrix F):

SM1. No boundary conditions imposed on the solution matrix F.

SM2. The first and last columns and rows of F are required to be relatively small.

SM3. The first and last columns and rows of F are required to vanish. This restriction corresponds to the fact that the actual distribution (see Figure 7) vanishes at the extreme boundaries.

SM4. The solution is required to vanish outside the actual non-negative part of the distribution (outside the range of the two peaks, see Figure 7).

SM5. The same conditions as for SM4 plus the requirement that values of the solution corresponding to the dividing line between the two peaks (see Figure 7) should vanish.

A sample of the results summarized in Tables 4 and 5 is presented in Figures 8-11. Figure 8 shows contours of the spectrum G corresponding to the mesh sizes M x N = 13 x 13 and 25 x 25. Figures 9a and b show the solution, Eq. (12) for M x N = 13 x 13, in the absence of smoothing. These figures complement each other in the sense that while Figure 9a shows the contours corresponding to the solution, Figure 9b (which shows the cross sections of the solution corresponding to one of the two peaks of the density function) indicates the relative magnitudes of the solution and the known exact value of the density function. In particular, Figure 9b indicates that the third and fourth contours circumscribing each part of this figure correspond to values of density higher than both the innermost and outermost contours. While the solution given in 9a is unacceptable, the smoothed

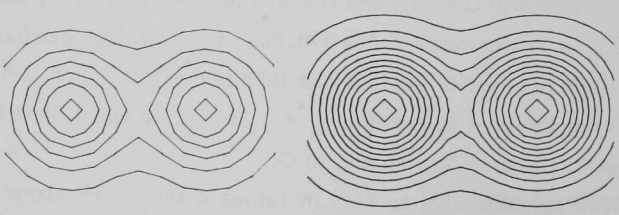

a) M x N = 13 x 13 b) M x N = 25 x 25

Fig. 8. Spectrum G

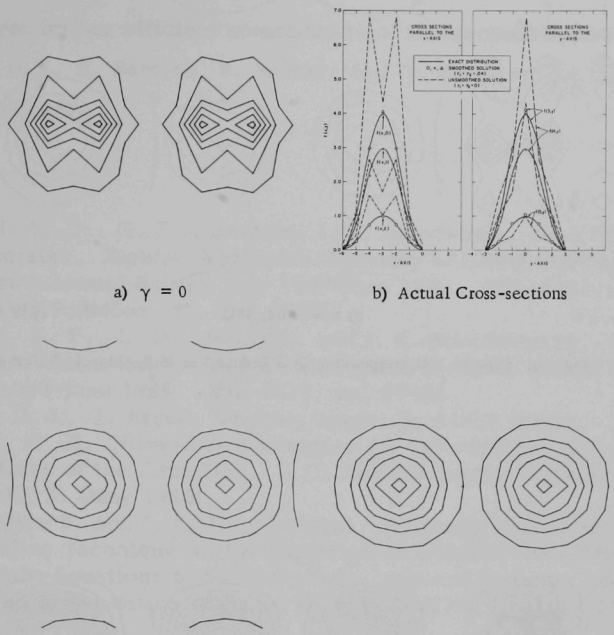

a) $\gamma = 0$

b) Actual Cross-sections

c) $\gamma = 0.004$, SM1

d) $\gamma = 0.04$, SM3

Fig. 9. Solution F Corresponding to G in Fig. 8a

solutions given in Figures 9b, c, and d are very close to the exact density function. Figure 9c corresponds to SM1 and shows that a slight error is introduced when the boundary conditions are not known. Figure 9d corresponds to SM3 with known boundary conditions (see above). Thus, as we would expect, the computational and graphical results show clearly that advance knowledge of useful information about a distribution may be utilized to improve the regularization unfolding solution.

Figure 10a, b, and c corresponds respectively to Figure 9a, c, and d when G is reduced to 4 significant figures. Figure 10a indicates the wide error introduced in the unsmoothed solution when an error of less than 0.1% is introduced in the spectrum. Finally Figure 11a, b, and c corresponds to Figure 10a, b and c when the mesh size is 25 x 25 instead of

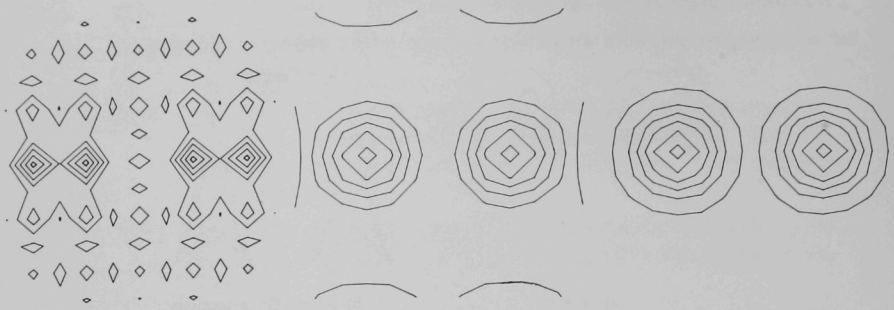

a) $\gamma = 0$ b) $\gamma = 0.04$, SM1 c) $\gamma = 0.04$, SM3

Fig. 10. Solution F Corresponding to G Reduced to 4S.F., M x N = 13 x 13

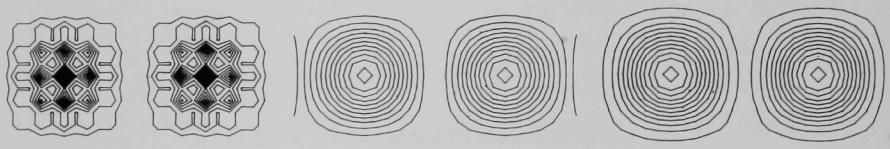

a) $\gamma = 0$ b) $\gamma = 0.004$, SM1 c) $\gamma = 0.001$, SM3

Fig. 11. Solution F Corresponding to G in Fig. 8b

13 x 13. Here again the unsmooth solution, though its contours are very appealing to the eye, is an unacceptable representation of the actual density; the smoothed solutions Figure 11b and c demonstrate the effectiveness of regularization unfolding technique for unfolding measured spectra.

The authors wish to express their gratitude to D. Phillips for his critical comments on the manuscript, to R. Wessel for his assistance and especially for supplying us with "contour plot" subroutines, and to Mrs.

Alice B. Meyer for her efficient programming of the computations. Thanks are also due to E. H. Bareiss, R. Buchal, and G. Zgrablich for their help and encouragement.

References

1. Marinelli, L. D., G. F. Clemente, I. K. Abu-Shumays, and O. J. Steingraber. Argonne National Laboratory Radiological Physics Division Annual Report, July 1967-June 1968. ANL-7489, pp. 1-12; see also Radiology 92, 167 (1969).
2. Clemente, G. F., L. D. Marinelli, and I. K. Abu-Shumays. Argonne National Laboratory Radiological Physics Division Annual Report, July 1968-June 1969. ANL-7615, pp. 87-95.
3. Phillips, D. L. J. Assoc. Comput. Mach. 9, 84-97 (1962).
4. Marshall, N. H. Numerical Techniques for Solving Fredholm's Integral Equations of the First Kind. U. S. Atomic Energy Commission Report IDO-17175 (May 1966).
5. Meyer, Alice B. and I. K. Abu-Shumays. A Special Regularization-Unfolding Technique for the Numerical Solution of Two-Dimensional Fredholm Equations of the First Kind. Argonne National Laboratory Applied Mathematics Division Program A1T8286 (IBM360/50/75), 1969.

A COMPARISON OF RECOVERY FROM α- and γ-RAY-INDUCED MITOTIC DELAY IN FERTILIZED SEA URCHIN EGGS

Patricia M. Failla

Recovery from the mitotic delay caused by fertilizing sea urchin eggs with γ-irradiated sperm has been previously studied and described. Experiments to test for similar recovery when the division delay is caused by α irradiation of the sperm were negative. This result is consistent with observations in other systems that there is little or no recovery from damage induced by densely ionizing radiation.

Postfertilization recovery from mitotic delay induced by exposure of sea urchin sperm to x or γ radiation has been studied for a number of years and described in previous publications.[1-4] In essence, the technique involves prolongation of the normal division cycle, which permits recovery during the prolongation period from mitotic delay caused by previous sperm irradiation. The system, however, has not been tested after exposure of the sperm to densely ionizing radiation. Since recovery in other biological systems is typically reduced or negligible when the damage is caused by high- as opposed to low-LET radiation, it was decided to examine the sea urchin postfertilization recovery system after treatment of the sperm with α rays.

Materials and Methods

Sea urchins of the species Arbacia punctulata* were maintained in two 25-gal refrigerated aquaria which recirculate artificial sea water continuously through a calcareous filtrant spread over the bottoms of the tanks.

Gametes were procured by electrical stimulation of the animals with an alternating potential of about 12 V.[5] In each experiment, all the eggs were taken from one female and all the sperm from one male. The eggs were rinsed three times with artificial sea water and fertilized with appropriate dilutions of control or irradiated sperm. Beginning 5 min after fertilization,

---

* Supplied by Glendle Noble, Panama City, Florida.

egg suspensions were bubbled for 30 min with nitrogen to interrupt progression through the cell cycle.

The sperm were exposed either to γ radiation from ^{137}Cs or α radiation from ^{244}Cm. The exposure arrangement for the α irradiation is shown in Figure 1. A drop of concentrated sperm was deposited in the center of a glass coverslip and covered with a small piece of 1/4-mil (6 μ) thick Mylar film. This thin film served both to flatten the drop to "negligible" thickness and prevent the sperm from drying out during the 20-min exposure period. The diameter of the spread sample was of the order of 5 mm.

The curium was electroplated from solution onto a platinum disc (~ 1" diameter). An autoradiograph of the source shown in Figure 2 shows that the activity is fairly uniformly deposited. The film (Kodak NTA) was placed at the same distance (3 mm) from the source as the sperm sample. It appears that the sperm should have received a relatively uniform α-radiation dose under these conditions.

The percentage of eggs that had divided in each sample at various times after fertilization was estimated visually using a dissecting microscope. Curves were then plotted of percent division against time, and the time at which 50% of the eggs had divided was ascertained. In general, this time is felt to be good to ± 1 min. When the eggs in all samples are dividing very synchronously, only the time of 50% division is determined.

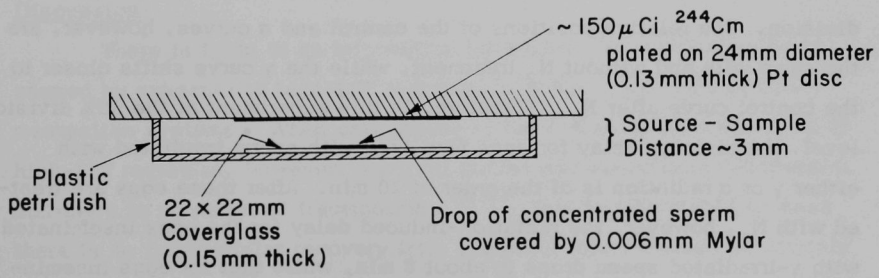

FIG. 1.--Experimental arrangement for irradiation of sperm samples with 5.8-MeV α particles of ^{244}Cm.

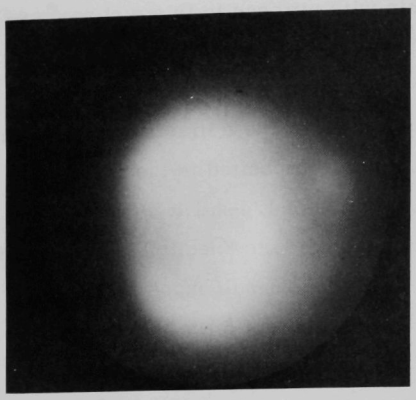

FIG. 2.--Autoradiograph (on Kodak NTA film) of ^{244}Cm source. Film placed in same geometry as sperm sample in Figure 1.

Results

The results of an experiment in which the sperm were exposed only to γ radiation (2500R) are shown in Figure 3. Without N_2 treatment the radiation-induced delay was about 35 min. After N_2 treatment, which in this case blocked the cell division process for about 45 min, the radiation-induced delay was reduced to 9 min. The delays are measured at the 50% division points, but since the curves are generally parallel, the magnitudes are approximately the same for other percentage division levels.

The results of an experiment in which some of the sperm were γ irradiated and some exposed to α radiation are shown in Figure 4. While the curves for eggs fertilized with control (C and CN_2) and γ-irradiated (γ and γN_2) sperm are all reasonably parallel, those for the eggs fertilized with α-irradiated (α and αN_2) sperm are much flatter. Therefore, the magnitude of the delay from α irradiation of the sperm varies with the degree of division. The relative positions of the control and α curves, however, are the same with and without N_2 treatment, while the γ curve shifts closer to the control curve after N_2. Therefore, in this experiment at the 50% division level, the division delay for eggs fertilized with sperm irradiated with either γ or α radiation is of the order of 20 min. After these eggs are treated with N_2, however, the radiation-induced delay for the eggs inseminated with γ-irradiated sperm drops to about 8 min, while that for eggs inseminated with α-irradiated sperm remains unchanged. Results of a similar nature were obtained in a series of about ten experiments; in some instances the delay due to α irradiation was even slightly larger after N_2 treatment.

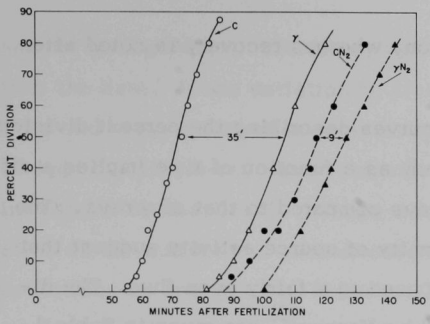

FIG. 3.--Percent Division of fertilized Arbacia eggs as a function of time after fertilization. Curves C and CN_2 describe the behavior of eggs fertilized with control sperm without and with 30-min N_2 treatment, respectively. Curves γ and γN_2 describe the behavior of eggs fertilized with γ-irradiated sperm (~ 2500 R) without and with 30-min N_2 treatment, respectively.

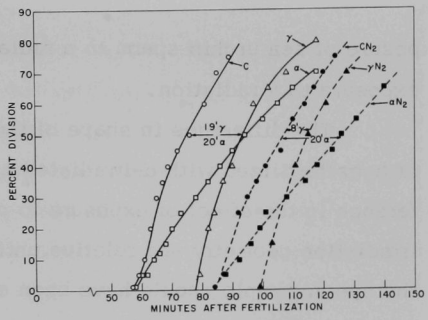

FIG. 4.--Percent division of fertilized Arbacia eggs as a function of time after fertilization. Designations of C, CN_2 γ and γN_2 are as described in legend of Figure 3. Curves α and αN_2 describe the behavior of eggs fertilized with sperm exposed to ^{244}Cm α particles without and with 30-min N_2 treatment, respectively.

It is apparent, therefore, that recovery can be demonstrated in this system from division delay resulting from exposure to γ radiation but not from that induced by α irradiation.

Discussion

There is little or no information on recovery from division delay caused by exposure to high-LET radiation in either mammalian or non-mammalian systems. When cell killing is the end point after exposure to high-LET radiation, however, survival curves are essentially exponential and there is no effect of fractionation.[6,7] This is interpreted to mean there is no intracellular recovery from sublethal injury caused by densely ionizing radiation.[8] There can, of course, be recovery at the tissue level as a result of repopulation by uninjured cells. It is not surprising, therefore, that no recovery was found from the division delay produced by ex-

posure of sea urchin sperm to a radiation, whereas recovery is noted after exposure to γ radiation.

The difference in shape of the curves describing the percent division of eggs fertilized with α-irradiated sperm as a function of time implies a difference in the effect of exposure to α rays compared to that of γ rays. The irradiation geometry and relative uniformity of source activity suggest that the sperm sample should have been exposed to a fairly even flux. The dimensions of Arbacia sperm as measured by Harvey[9] are given in Table 1.

TABLE 1. Spermatozoon of Arbacia punctulata[9]

	Head	Middle Piece	Tail
Height or length, μ	3.25	0.75	45.0
Diameter (maximum), μ	2.0	2.0	0.2
Volume (calculated), μ^3	3.4	2.4	1.4
Total volume 7.2 μ^3			

The sperm sample, thus, could be a number of "sperm layers" in thickness and still be well within the 45-μ tissue range calculated to remain after passage of the 5.8-MeV α particles through the 3-mm air gap and 6-μ Mylar cover. Although the depth of the sperm sample was not measured, the compression of the drop by the Mylar film, which was statically attracted to the coverslip and plastic petri dish, appeared to yield a sample of insignificant self-absorption.

If the assumption is made, therefore, that all the sperm in any sample were exposed to a uniform flux of α particles, the spread in biological effect can be attributed to statistical variation in the dose received by one or more small target areas. James and Kember[10] in a recent publication discuss the concept of dose variation in very small volumes as a function of variation in α-particle incidence. As yet no serious attempt has been made to calibrate accurately the curium source or study quantitatively the source and

sample homogeneity. Therefore, no meaningful value of RBE can be derived from the data. If the variation in slope between the curves describing controls and γ-ray damaged eggs as compared to those describing the behavior of eggs carrying α-ray damage can be attributed to variation in dose at the intrasperm nuclear level, perhaps further analysis would yield some information on the number and size of sensitive target areas. Also, under these conditions no one value of RBE would be applicable since the magnitude would vary with the degree of division of the eggs.

Nevertheless, since the curves for the eggs carrying α-irradiated sperm were parallel to each other with and without N_2 treatment, comparison could be made with appropriate curves for control eggs, and the conclusion reached that there is no recovery in this system after sperm exposure to α radiation.

References

1. Failla, P. Recovery from Radiation-Induced Division Delay of Cleavage of Gametes of Arbacia punctulata. Science 138, 1341-1342 (1962).
2. Failla, P. Recovery from Division Delay in Irradiated Gametes of Arbacia punctulata. Radiat. Res. 25, 331-340 (1965).
3. Failla, P. Recovery and Modification of Radiation-Induced Division Delay in Developing Sea Urchin Eggs. Radiology 93, 643-648 (1969).
4. Failla, P. and R. C. Rustad. Protein Synthesis and Recovery from γ-ray Induced Mitotic Delay in Fertilized Sea Urchin Eggs. Int. J. Radiat. Biol. 17, 385-388 (1970).
5. Harvey, E. B. A Simplified Electrical Method of Determining the Sex of Sea Urchins and Other Marine Animals. Biol. Bull. 105, 365 (1965).
6. Barendsen, G. W. Dose-Survival Curves of Human Cells in Tissue Culture Irradiated with Alpha-, Beta-, 20-kV X and 200-kV X radiation. Nature 193, 1153-1155 (1962).
7. Barendsen, G. W., H. M. D. Walter, J. F. Fowler, and D. K. Bewley. Effects of Different Ionizing Radiations on Human Cells in Tissue Culture. III. Experiments with Cyclotron-Accelerated Alpha Particles and Deuterons. Radiat. Res. 18, 106-119 (1963).
8. Fowler, J. F. Kinetics of Injury and Repair to Mammalian Tissue by High-LET Radiation. Radiat. Res. (Suppl.) 7, 276-287 (1967).
9. Harvey, E. B. The American Arbacia and Other Sea Urchins. Princeton University Press. Princeton, New Jersey, 1956.
10. James, A. C. and N. F. Kember. Alpha-Particle Incidence in Small Targets. Phys. Med. Biol. 15, 39-46 (1970).

APPLICATION OF CELLULOSE NITRATE FILMS FOR ALPHA AUTORADIOGRAPHY OF BONE. II. RESOLUTION AND SENSITIVITY OF CELLULOSE NITRATE FILMS

D. J. Simmons and K. T. Fitzgerald*

High resolution autoradiographs of thin line ^{239}Pu sources were prepared with several nuclear emulsions and cellulose nitrate (CN) films. The CN detector films made by the dipping method afforded better resolution of alpha tracks (after chemical etching) than Kodak Type A plates or AR-10 stripping film. Resolution could be improved by using thicker (30 μ) rather than thinner (15 μ) detector films. Tentative correction factors for alpha track counting in the CN films are presented.

Introduction

It is now well known that highly ionizing particles disrupt the atomic and molecular structure of electrically nonconducting solids and that the damaged areas can be revealed as tracks by chemical etching. It is significant that these solids (dielectric track detectors) are insensitive to beta or gamma rays, and that they have a high detection efficiency for low energy alpha particles. Several laboratories have explored the utility of certain dielectric track detectors for autoradiography of bone contaminated with ^{239}Pu.[1-3] In these studies, bone sections were sandwiched between polycarbonate films and exposed to thermal neutrons. The films were detached following irradiation and then etched to reveal the fission fragment tracks. Bleaney[1] employed 200-μ thick foils and established values for the distribution and dose rates delivered to microscopic regions in bone by visual track counting. Becker[2] used 6- to 10-μ thick cellulose acetate foils and quantitated the average total activity of $^{239}Pu/cm^2$ of bone surface by local evaporation of a thin layer of superimposed metal (aluminized Mylar) by sparking through the per-

*CSUI Honor Student. Present address: Stonehill College, North Easton, Massachusetts.

forations in the etched foils. These methods produce high resolution autoradiographs in a far shorter time than is possible using conventional nuclear emulsions, and they avoided the attendant problems of fogging and fading which plague the latter.

The images recorded by the "sandwich" technique are technically contact autoradiographs, for the foils are detached before etching. Bleaney[1] remarked that it may be difficult in some situations to know whether, by superposition of foil and section, alpha tracks (from plutonium) arise from activity on a bone surface or from bone and marrow cells near bone surfaces. It was for this reason that we initiated some experiments to determine if it was possible to coat bone sections with solutions of cellulose nitrate. Could we obtain a high resolution autoradiograph of a section prepared with cellulose nitrate by a dipping method akin to that devised for liquid nuclear emulsions by Messier and Leblond?[4] This method proved feasible with cellulose nitrate films which were only 3 μ thick[3] and appeared unexpectedly to give superb resolution (Figure 1). But some difficulties could be forseen. The fission track method which produces contact autoradiographs probably detects 100% of the alpha particles since the foils are etched from both sides. With the dipping technique, however, we could only etch tracks which penetrated to the

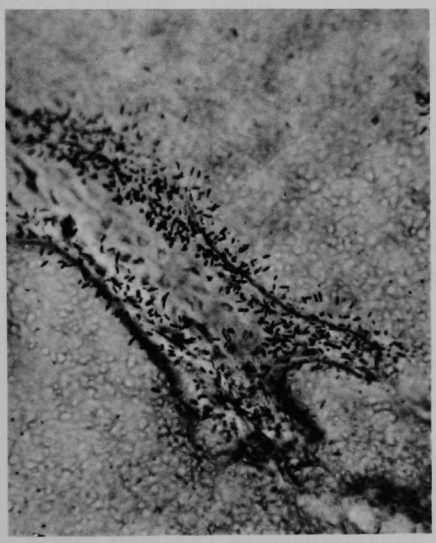

FIG. 1.--An autoradiograph showing alpha tracks etched in cellulose nitrate film over the surfaces of a bony trabeculum from a mouse injected with ionic ^{239}Pu. 100 X.

top surface of the film (away from bone), thus reducing the apparent detection efficiency of the film. On the other hand, we might well sacrifice efficiency at the expense of increasing resolution. By using thick films of cellulose nitrate, and taking advantage of the slow rate at which the bulk material is worn away by the NaOH etchant, we might see only those alpha tracks which penetrate perpendicular to the plane of the film. This scheme is illustrated in Figure 2.

The results of experiments described in this preliminary report suggest that resolution provided by cellulose nitrate alpha autoradiography does increase with the thickness of the detector film. Further, we have compared the resolution and detector efficiency of alpha autoradiographs prepared by the cellulose nitrate method and several nuclear emulsion

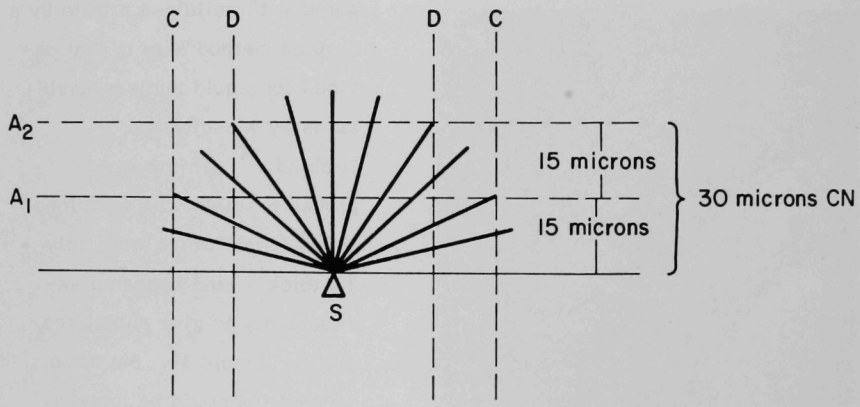

FIG. 2.--Schematic representation of the resolving power of thick and thin cellulose nitrate (CN) films. Monoenergetic alpha particles radiating from a point source (S) are penetrating two superimposed 15-μ thick layers of CN. The two upper surfaces of the films are labeled A_1 and A_2. Surface A_1 will reveal 9 alpha tracks after chemical etching in an area on the 15-μ film delineated by vertical lines C-C. While the etchable alpha tracks on Surface A_2 will be concentrated over a much narrower area of the film (D-D) when it is 30 μ thick, there is loss of efficiency and only 5 tracks penetrate A_2.

techniques, and have derived some tentative correction factors for track counts in CN detector films.

Method

Cellulose nitrate is known to have a certain threshold of specific ionization for the creation of tracks (0.6 to 5.5 MeV), and alpha particles with energies greater than 5.5 MeV do not expend energy at a rate sufficient to leave etchable tracks. In this study we employed a ^{239}Pu (5.1 MeV) source which was prepared by Dr. Arnold Friedman (Chemistry Division, ANL).

^{239}Source Preparation

We used thin line ^{239}Pu sources to intercompare the resolving power of cellulose nitrate detector films and conventional nuclear emulsions (Type A, AR-10). Figure 3 shows the manner in which the sources were constructed. Plutonium-239 (0.2 to 0.3 g) was sputtered onto the surface

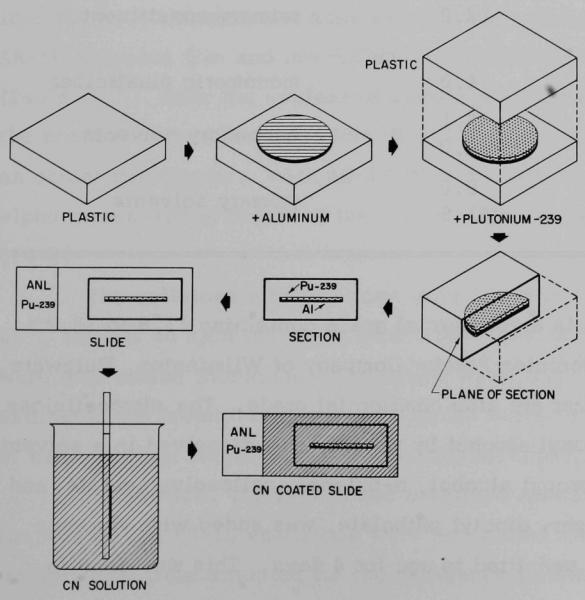

FIG. 3.--Scheme showing the preparation of ^{239}Pu line sources. A thin film of ^{239}Pu is deposited on aluminized plastic blocks. After plastic embedding, thin sections were cut perpendicularly to the ^{239}Pu film, and they were mounted on microscope slides for autoradiographic processing.

of an aluminized square of Lucite (methyl methacrylate); the radioactive surface (<1 μ thick) was covered with methyl methacrylate and permitted to polymerize. This plastic plutonium sandwich was then thin-sectioned in a plane perpendicular to the active spot by a high speed rotary saw. We attempted to mimick a bone section, and all the sections were infinitely thick with respect to the penetrability of alpha particles in Lucite. The sections were attached to microscope slides by a thin film of cellulose nitrate (2 μ thick when dry), and the preparations were dried horizontally overnight under cover.

Cellulose Nitrate Detector Film Preparation

The stock solution of cellulose nitrate was prepared according to the formula developed by Benton[5] (Table 1).

TABLE 1. Composition of the Nitrocellulose Stock Solution

Constituent	Quantity, % by weight	
5- to 6-sec viscosity RS nitrocellulose	17.0	primary constituent
Dioctyl phthalate	4.0	monomeric plasticizer
Isopropyl alcohol	5.1	secondary solvents
Butyl alcohol	4.0	
Cellosolve acetate	8.0	primary solvents
Ethyl acetate	61.9	

The nitrocellulose is a commercial grade containing 11.8 to 12.2% N_2 manufactured by the Hercules Powder Company of Wilmington, Delaware. The solvents and plasticizer are also commercial grade. The nitrocellulose, which contains 30% isopropyl alcohol by weight, was dissolved in a solvent solution composed of isopropyl alcohol, n-butanol, cellosolve acetate, and ethyl acetate. A plasticizer, dioctyl phthalate, was added with vigorous stirring, and the mix was permitted to age for 4 days. This was done to

allow the solution to achieve chemical equilibrium and to allow trapped air bubbles to dissipate. At the end of this time, the solution was ready for the preparation of detector films.

We prepared a number of dilutions of this stock solution to vary the film thicknesses (Table 2). These films (15 and 30μ) were used to intercompare the resolution possible within the cellulose nitrate technique and with the resolution of general nuclear autoradiographic emulsions.

TABLE 2. Dilution of Stock Nitrocellulose with Ethyl Acetate to Produce Various Film Thicknesses[3]

Amount of Stock Nitrocellulose, ml	Amount of Excess Ethyl Acetate, ml	Film Thickness, μ
25	8.75	30
25	16.2	15

Autoradiographic Technique

Kodak Type A contact autoradiographs were prepared from each thin line source. Alternate sections were then autoradiographed with Kodak AR-10 stripping film and the different solutions of cellulose nitrate (Table 2).[3] After the nuclear emulsions were developed, we measured the breadth of the blackened line of silver grains at regular intervals with an ocular micrometer. With AR-10 film, we also counted the number of alpha tracks/100-μ length of the source under an oil immersion lens at 970 X.

The cellulose nitrate slides were "developed" in 6.5 N NaOH at 25°C for 2 hr to etch the alpha tracks produced in the detector film. They were then rinsed thoroughly in distilled water and dried under cover. We estimated the breadth of the line of tracks etched in the film and the number of tracks/100-μ length of the source microscopically (vide supra).

In practice, the Type A and cellulose nitrate exposures were made for 6 days; the AR-10 emulsions were terminated after 3 days, and their track counts were adjusted for the difference in exposure time.

Results

The results of this preliminary study are tabulated in Table 3, and illustrated in Figure 4. The autoradiographs of the line source made with AR-10 stripping film were much better resolved than the contact autoradiographs produced on Type A plates. The breadth of the developed line of silver grains was 92 μ in AR-10 emulsion compared to 99.4 μ on the Type A plates. A marked improvement in resolution was afforded by the cellulose nitrate films, and this improved as the film thickness was increased. The 15-μ films registered alpha track lines that were 45.2 μ

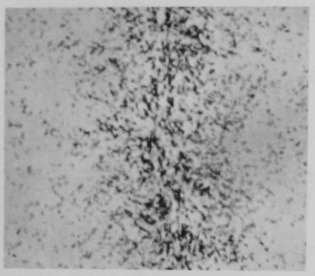

Type A

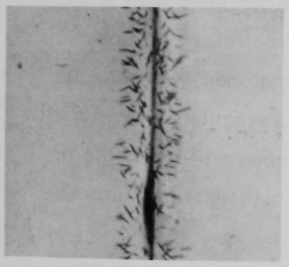

CN 15 μ

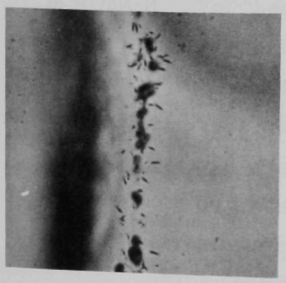

CN 30 μ

FIG. 4.--Photomicrographs comparing the resolving power of conventional nuclear emulsions (Kodak Type A plates) with cellulose nitrate (CN) films after exposure to ^{239}Pu line sources. AR-10 film provided better resolution than contact Type A plates, but the tracks could not be demonstrated successfully at these magnifications (100 X). The tracks recorded in the CN film were the more tightly grouped about the line source. Note the reduction of track counts as the thickness of the CN film was increased.

TABLE 3. Comparison of Autoradiographic Resolution and Efficiency between Cellulose Nitrate Detector Films and Nuclear Emulsions

Autoradiograph Preparation	Resolution, μ (mean ± S.E.)	No. of Tracks/100-μ length (mean ± S.E.)
Type A	99.44 ± 1.11 (10)[a]	-----
AR-10	92.0 ± 0.8 (20)[b]	522 ± 13 (10)[a]
Cellulose nitrate (15-μ film)	45.2 ± 0.2 (20)	237 ± 3 (20)
Cellulose nitrate (30-μ film)	24.1 ± 0.85 (20)	53 ± 2 (20)

[a] number of fields counted.

[b] $P < 0.02$ compared to Type A plates.

wide; the 30-μ cellulose nitrate films registered lines of tracks which were 24.1 μ wide. Compared to the AR-10 film, the cellulose nitrate films increased the resolution of the plutonium source by factors of 2 and 4, respectively.

As expected, the track counts in the AR-10 emulsion were always greater than those in cellulose nitrate films--by a factor of 2 compared to the 15-μ films and by a factor of 10 compared to the 30-μ films.

Discussion

These preliminary results strongly suggest that the cellulose nitrate detector films are capable of providing better resolution of alpha tracks (from line sources and tissue sections) than nuclear emulsions. Moreover, the resolution could be improved by using thicker rather than thinner films. The probable manner in which these differences were achieved is illustrated in Figure 2. The Figure shows monoenergetic alpha particles emanating from a point source. The horizontal dotted lines represent the upper surfaces of two 15-μ layers of cellulose nitrate film

applied over the point source. The vertical dotted lines (C-C, D-D) demarcate those alpha tracks which penetrate the full thickness of the film, and only their tracks will be revealed by chemical etching. The distance each particle travels in the cellulose nitrate is the same, but it is the angle at which the particle radiates from the point source and enters the detector film that determines whether it will penetrate the upper surface of the film. Thus, as the detector films become thicker, only particles passing perpendicularly to the film surface will be detected. The data on track counts demonstrate that loss of efficiency is unavoidable with cellulose nitrate films. The rate of bulk etching is slight, making visible only those tracks which penetrate through the film or to a point within 1 or 2 μ of its surface. But at a first approximation--assuming that AR-10 emulsions are 100% efficient--the track counts in 15- and 30-μ cellulose nitrate films can be corrected by factors of 2 and 10, respectively.

References

1. Bleaney, B. Plutonium Deposition on Bone Surfaces and in Bone Marrow Following Intravenous and Intramuscular Injections. Delayed Effects of Bone Seeking Radionuclides, Ed. C. W. Mays, W. S. S. Jee, R. D. Lloyd, B. J. Stover, J. N. Dougherty, and G. N. Taylor. University of Utah Press, Salt Lake City, 1969, pp. 125-135.
2. Becker, K. and D. R. Johnson. Nonphotographic Alpha Autoradiography and Neutron-Induced Autoradiography. Science 167, 1370-1372 (1970).
3. Cole, A., D. J. Simmons, H. Cummins, F. J. Congel, and J. Kastner. Application of Cellulose Nitrate Films for Alpha Autoradiography of Bone. Health Phys. 19, 55-56 (1970).
4. Messier, B. and C. P. Leblond. Preparation of Coated Autoradiographs by Dipping Sections in Fluid Emulsion. Proc. Soc. Exp. Biol. Med. 96, 7 (1957).
5. Benton, E. F. A Study of Charged Particle Tracks in Cellulose Nitrate. U. S. Govt. Report USNRDL-TR-68-14 (1968).

CHONDROCLASTIC RESORPTION IN THE LONG BONES OF NEWTS TREATED WITH PARATHYROID EXTRACT

D. J. Simmons, D. J. McWhinnie,* and H. T. Cummins

Histologic and autoradiographic studies of the hind limb bones of PTE-treated Triturus newts were undertaken to explain the peculiar staining characteristics of the different elements in cleared whole mount preparations. That certain epiphyses frequently show two bands of methylene blue stainable matrix after PTE treatment was found to be due to chondroclastic resorption, but the pattern and time of onset was variable in different bones. In the tibiofibula, the entire epiphyses was "shelled-out." Resorption in the metatarsals and phalanges was restricted to a totally intracartilaginous area. Labeling with ^{3}HTdR failed to delineate the origin and fate of the resorptive cells.

Introduction

Gross morphological studies of skeletal elements in Rana pipiens and Triturus viridescens treated with parathyroid extract have shown that there is an increase in the amount of matrix in the long bones which can be stained with methylene blue.[1] Widened and more densely staining matrix was observed at the ends of the tibiofibula, and the phalanges exhibited double bands of matrix between the articular cartilaginous cap and the ossified diaphyseal bone in the majority of animals after hormone treatment. When new bands of matrix appeared beneath the epiphyseal cap, they lay in a region topographically comparable to the zone of provisional calcification in mammalian long bones (metaphysis). The types of cells which may be responsible for these changes in the bone matrix of hormone-treated amphibians are undetermined. Although Schlumberger and Burk[2] were unable to elicit a hormone-mediated increase of osteoclasts in bone of R. pipiens, Irving and Solms[3] and Bélanger and Drouin[4] later reported that osteoclast numbers were elevated in several amphibian species as a consequence

* Department of Biological Sciences, DePaul University, Chicago, Illinois.

of Parathormone action. Moreover, Yoshida and Talmage[5] obtained an osteoclastic response in R. catesbeiana following calcium-free lavage, and this was due presumably to parathyroid stimulation.

While data are available concerning Parathormone-induced biochemical and gross morphological alterations in the epiphyseal terminals of amphibians,[1] the nature of the "metaphyseal" band of stainable matrix formed after hormone treatment is unknown. The present study was, therefore, undertaken to investigate the origin of this tissue in the newt, T. viridescens, employing high resolution autoradiographic and histochemical techniques.

Materials and Methods

Two varieties of the newt, Triturus viridescens, endemic to the southeastern United States, were used in these studies. The majority of animals were T. viridescens viridescens,* but in a few cases the closely related T. viridescens dorsalis were employed. All experiments were done with summer animals which were warm-acclimated in the laboratory at 18 to 20°C for 1 week before use in order to eliminate seasonal and temperature modifications of the response to Parathormone. Newts were maintained in individual containers and environmental water was changed daily; calf liver was force fed once weekly. To avoid unfavorable changes due to conditions of captivity, no animals were used beyond 1 month after arrival in the laboratory. The 104 T. viridescens v. used in this study weighed 1.0 to 4.5 g. Newts from these populations were randomly placed into control and parathyroid extract-treated groups. Both groups were given a single intraperitoneal injection of 0.5 μCi tritiated thymidine ^{3}HTdR/g body weight. The presence of minute quantities of ethanol in the isotope solution caused a transient vasodilation which disappeared 15 min post-injection.

The experimental animals were injected intraperitoneally with para-

---

*T. viridescens v. were kindly supplied by Dr. J. Dent, Department of Biology, University of Virginia, Charlottesville, Virginia.

thyroid extract (PTE)* once daily for 7 days. Newts weighing over 3.0 g received 15 units. Within 2 min after injection, jerking movements were observed in limbs, tail, and jaws. These uncoordinated responses, which subsided within 2 hr, may relate to the injected protein load rather than representing a physiological response to volume pressure; control newts injected with an equal volume of amphibian Ringer's solution failed to show such movements.

Groups of 2 to 6 newts from both the control and PTE-treated series were sacrificed at 1, 2, 4, 8, 12, 18, 24, and 36 hr, 2 to 8, 14 and 21 days following ^{3}HTdR administration. Cumulative doses of PTE administered to each newt, then, ranged from 15-20 to 105-140 units.

Newts were sacrificed by ether anaesthesia, and at autopsy, the hindlimbs were removed and fixed in 10% neutral formalin. The tissues were decalcified in 10% ethylenediaminetetraacetic acid (EDTA, pH 7.4), embedded in paraffin, and sectioned at 5μ along the long axis of the metatarsals and phalanges. Some sections were stained with hematoxylin and eosin or with methylene blue (pH 1.2, 3.7, 4.8, 6.0, 8.5), PAS + Alcian blue, or Mallory's aniline blue for mucopolysaccharides and connective tissue elements.

Autoradiographic Method.

High resolution autoradiographs were prepared by dipping alternate sections prestained with periodic acid Schiff (PAS) reagent in Kodak liquid emulsion (NTB-2), according to the method of Messier and Leblond,[3] to visualize cellular patterns of ^{3}HTdR incorporation. They were exposed in a freezer for 4 weeks, fixed, washed, and stained through the emulsion with hematoxylin. The autoradiographs were intentionally over-exposed to insure identification of labeled cells.

---

*We are indebted to Dr. J. McGuire of Eli Lilly Company, Indianapolis, for the bovine parathyroid extract used in these studies.

Results

Control Newts

In the foot bones from control newts, the diaphyseal surfaces of the epiphyses were quite smooth (Figure 1). In some instances they were partially overlain with a thin veneer of bone. Few cells lined the endosteal surfaces of bone, and these could not be identified as either osteoblasts or osteoclasts. The cartilage tissues were strongly metachromatic at pH 3.5.

PTE-Treated Newts

After PTE treatment, the surfaces of the bone trabeculae under the cartilages were rather less regular, presumably due to resorptive changes. Yet, the pattern and timing of resorption in the different bones was variable. Serial sections through the carpels revealed numerous foci of resorption 24 to 48 hr after the first injection of PTE, but histotypical multinucleated osteoclasts were not invariably present within the spaces in every section. Much later (14 days) resorptive cells shelled out the cartilages capping the tibiofibula, leaving a narrow zone of tissue adhering to the endosteum (Figure 2). In the metatarsals and phalanges, however, chondroclasts dissected the calcified zones of the cartilages and the spaces were filled with loose connective tissue (Figure 3). Fibrotic changes in the marrow were never observed during PTE treatment and they were rare even after 14 to 21 days. At no time did PTE induce cortical bone remodelling; but

FIG. 1.--Photomicrograph of the epiphysis of the metatarsal from a normal untreated newt. PAS and Alcian blue. 125 X.

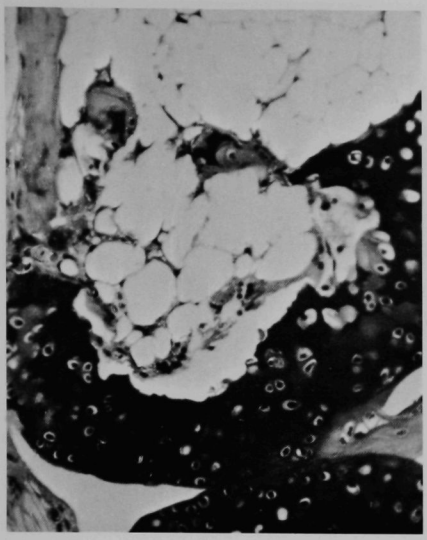

FIG. 2.--Photomicrograph of the distal end of a tibiofibula from a newt sacrificed 14 days after PTE treatment (7 injections at 24-hr intervals). Note the large number of multinucleated chondroclasts resorbing the cartilage. PAS and Alcian blue. 125 X.

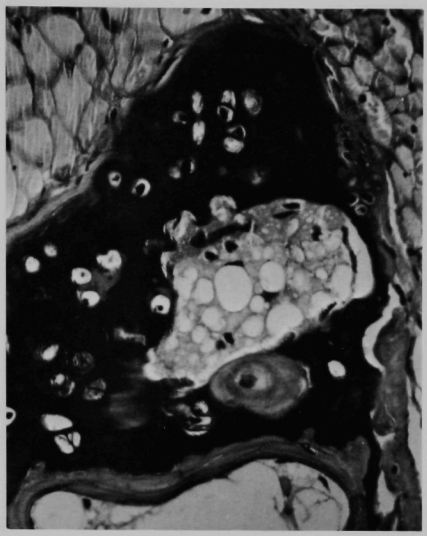

FIG. 3.--Photomicrograph of the proximal cartilage in the metatarsal of a newt sacrificed 14 days after PTE treatment (7 injections at 24-hr intervals). Note the presence of a resorptive cavity within the cartilage showing a large multinucleated chondroclast. PAS and Alcian blue. 125 X.

the epiphyseal caps stained irregularly with methylene blue or Mallory's aniline blue (Figure 4), suggesting that the hormone had depolymerized components of the cartilage matrix.

Autoradiography

The observations on ^{3}HTdR uptake by cartilage cells were common to both control and PTE-treated newts. First, none of the cartilage cells in the epiphyses of any bone showed evidence of tracer incorporation. Second, the only cells which regularly registered silver grains in the emulsions were those in the skin, and, occasionally, in the joint spaces. It was unusual to find labeled marrow cells at times shorter than 96 hr after

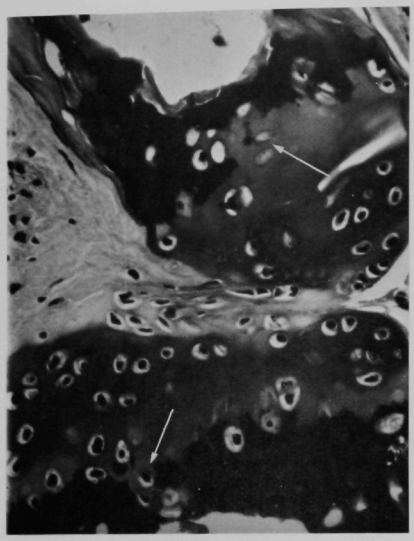

FIG. 4.--Photomicrograph of the epiphysis at the joint between the distal metatarsal (above) and first phalange (below) from a newt sacrificed 36 hr after 2 injections of PTE. Note the irregular staining in the calcified zones of the cartilages (arrows). Methylene blue. 125 X.

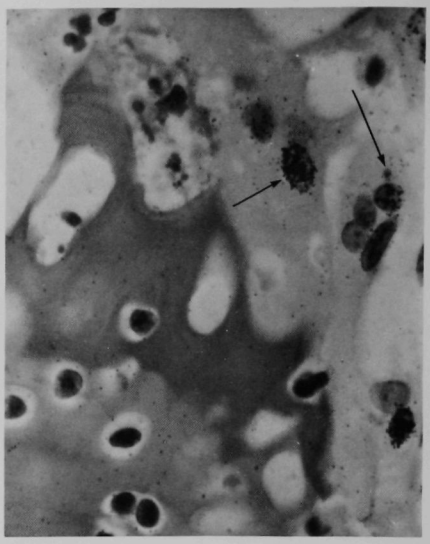

FIG. 5.--Autoradiograph showing chondroclasts with ^{3}HTdR-labeled nuclei (arrows) in the proximal cartilage from a newt sacrificed 7 days after PTE treatment (6 injections at 24-hr intervals). PAS and hematoxylin. 800 X.

tracer administration. In bone, labeled multinucleated osteoclasts were never observed earlier than 7 days after thymidine administration (Figure 5) and then only infrequently in the PTE-treated group.

Discussion

Certain features of the histology suggest that some of these newts may have been stunted, although it was difficult to ascribe such a failure of growth to poor nutrition,[7] since the animals had not been starved and they were used during their season of active growth. A growth disturbance was signaled by the presence of subchondral bony lamellae, suggestive of the condition described by Dawson[8] as lapsed union in the long bones of

older rats. The absence of tritiated thymidine incorporation in the cartilage cells of both the control and hormone-treated animals, in contrast to its strong uptake in epithelia, also suggests that the linear growth of these bones was arrested.[7]

The results of this study do explain the curious staining properties with methylene blue observed in cleared whole mounts of bone from PTE-treated anurans and urodeles described by one of us (McWhinnie). They are all consequences of hormone-induced resorptive activity. While this process in the tibiofibula primarily thins the cartilages, it leaves a shell of matrix laterally at the epiphyseal-diaphyseal junction, and under conditions of optimum cartilage growth, gross specimens stained for cartilage would appear to have thicker epiphyses than normal. The peculiar mode of intracartilaginous matrix resorption mediated by chondroclasts and subsequent connective tissue formation in the epiphyses of the metatarsals and phalanges could produce double bands of stainable matrix. All of these findings are consistent with the observation of increased numbers of resorptive cells in amphibian bone following the administration of parathyroid extract.[3,4]

Since Schenk and Spiro[9] have reported that chondroclasts and osteoclasts are indistinguishable in their fine structure, the cells appearing in newt bone subsequent to PTE treatment may also be interpreted to be osteoclasts. Resorptive osteoclasts were apparent within 48 hr after initiating PTE treatment, but the relative acellularity of the marrow cavities and the observation that labeling of marrow elements did not occur until the third day after ^{3}HTdR injection leaves the origin and fate of these osteoclasts in question.

The irregular staining properties of cartilage matrices in the hormone-treated animals is probably due to depolymerization of matrix, an interpretation consistent with the observations of Bélanger and Drouin[4] in R. catesbeiana and Engel[10] in rats.

References

1. McWhinnie, D. J. and J. R. Cortelyou. Am. Zool. 7, 857 (1967).
2. Schlumberger, H. G. and D. H. Burk. Arch. Pathol 56, 103 (1958).
3. Irving, J. T. and C. M. Solms. African J. Med. Sci. 20, 32 (1955).
4. Bélanger, L. F. and P. Drouin. Can. J. Physiol. Pharmacol. 44, 919 (1966).
5. Yoshida, K. and R. V. Talmage. Gen. Comp. Endocrinol. 2, 551 (1962).
6. Messier, B. and C. P. Leblond. Proc. Soc. Exp. Biol. Med. 96, 7 (1957).
7. Simmons, D. J. and A. S. Kunin. Clin. Orthopaed. 68, 261 (1970
8. Dawson, A. B. Anat. Rec. 43, 109 (1929).
9. Schenk, R. and D. J. Spiro. Cell Biol. 31, 99A (1966).
10. Engel, M. B. J. Exp. Med. 53, 339 (1952).

DEVELOPMENT AND HEALING OF RICKETS IN RATS. III. STUDIES WITH ^{3}H-URDINE

D. J. Simmons and A. S. Kunin*

Quantitative aspects of RNA (^{3}H-uridine) and mucopolysaccharide (^{35}S-sulfate) metabolism have been studied in cartilage and bone of rats by autoradiography during the development and healing of low-phosphate rickets. In normal cartilage, RNA and MPS synthesis occurs in most of the cells with an activity gradient which increases toward the metaphysis. But in rachitic cartilage the viable hypertrophic cells are performing less actively, and RNA turnover is impaired. Since the normal patterns of RNA metabolism are maintained in rachitic endosteal and metaphyseal osteoblasts, it may be concluded that the competent osteogenic cells in these sites in rachitic bone are producing bone matrix at a normal pace.

Introduction

As a result of experiments conducted in this laboratory and elsewhere, the mechanism by which young, growing rats develop rickets is becoming better understood. Our information is as yet incomplete, but we may summarize the state of the art insofar as growth cartilage is concerned:

1. In rats, rickets develops only when animals are fed an inadequate phosphate ration.[1-4] Grossly, the long bones are stunted, and histologically the epiphyseal cartilages are thickened owing to an accumulation of hypertrophic cells. This is due in part to the failure of the cartilage matrix to calcify normally and, as a consequence, the rate of endochondral bone formation is depressed. Moreover, Howell[5] and his colleagues suggest that the Ca x P ion activity product in the rachitic cartilage tissue fluid at the zone of primary calcification is very different from that in the blood.

2. The rate of DNA synthesis by individual cells in the proliferative zone of rachitic cartilage is probably normal,[3,6,7] but the number of

*Departments of Medicine and Orthopedic Surgery, University of Vermont, College of Medicine, Burlington, Vermont 05401.

cells which undergo division gradually diminishes during the development of the nutritional deficiency. This is in essence a "no-go" situation, and thus the chronological lifetime of these cells may be much extended.[8]

3. In rachitic cartilage, the cells and matrix appear normal to the electron microscope.[9] Autoradiographic studies[4,6,10] (^{3}H-cytidine, -glycine, -proline, ^{35}S), however, suggest that the ability of the oldest hypertrophic cells to undergo RNA, mucopolysaccharide (MPS) and collagen synthesis is impaired. Moreover, Matthews'[11] microincineration method reveals that most rachitic chondrocytes lack mitochondrial granules (intracellular calcium). Abnormal phospholipid patterns and increased lipid synthesis have also been detected in rachitic cartilage.[12,13]

4. Glycolysis as well as the activity of each of the major glycolytic enzymes is increased coordinately in rachitic cartilage.[14-17] Moreover, there seem to be more than adequate concentrations of ATP in rachitic cartilage for phosphorylation of the collagenous matrix requisite for mineralization.[1]

Recovery from the entire suite of rachitic changes can occur if the rats are fed adequate nutritional supplies of phosphate.[3,16-19] Vitamin D in large doses is also effective, but may act by a pharmacological mechanism in mobilizing phosphate from bones.[2,3,17] To explain the inability of the seemingly normal matrices of cartilage and bone to calcify in rachitic rats, Parson and Hampton[18] consider that the collagen fibrils may be poorly phosphorylated at sites specific for apatite nucleation.

The effect of phosphorus and Vitamin D on RNA synthesis in cartilage is less certain. In their studies with ^{3}H-cytidine, Mankin and Lippiello[6] did not attempt to heal rickets. Parsons and his coworkers[18-20], suggest that phosphate will increase RNA synthesis and collagen formation in rachitic rat bone as seen by urinary hydroxyproline excretion assays. However, our studies[4] with ^{3}H-proline indicated that the rates of appositional bone growth in different sites in rat tibiae were not especially abnormal in unhealed or phosphate-healed rickets. With respect to bone

matrix production, the differences between Parson's findings and ours may be more apparent than real. There may be, for example, a situation somewhat akin to the estrogen-treated mouse--namely that more bone is present or formed simply because there are more cells to perform this function.[21] Each individual cell is working at a normal pace. This may explain the increased excretion of hydroxyproline in rachitic rats healed by phosphorus[18,20] for Rohr[22] noted that rachitic metaphyses contained more osteoblasts than normal metaphyses. Our attempts to quantify bone matrix formation with radioproline by grain counting suggested that RNA synthesis (and turnover) should be essentially normal in rickets. Actinomycin D, for instance, which blocks DNA-directed RNA synthesis, appears to diminish urinary hydroxyproline excretion (bone formation rates?).[23]

We have attempted to clarify this problem by autoradiographic studies utilizing ^{3}H-uridine. In this manner, we hoped to measure the synthesis and turnover of RNA in chondrocytes and osteoblasts. Could we account for the mechanism underlying the increased concentration of glycolytic enzymes in rachitic cartilage? Would RNA turnover be more rapid in osteogenic cells on metaphyseal bone surfaces than at other sites (such as the endosteum)? A positive response would support Rohr's[22] contention that bone matrix deposition was increased in rickets. A negative response would tend to confirm our previous findings that osteoblasts and most chondrocytes perform adequately in the face of phosphate and Vitamin D deprivation, and support the hypothesis that the increased urinary hydroxyproline excretion observed in phosphate-healed rickets is due to a larger complement of cells competent to synthesize collagen. The results of this study compel us to advance this latter explanation.

Methods

Weanling rats (Sprague-Dawley Strain) were made rachitic by feeding on a semisynthetic, low phosphorus, Vitamin D-free diet for 2 weeks. During the third week, the rats were reassigned to groups which were either

maintained on the basal rachitogenic ration or fed the basal diet enriched with phosphorus and/or Vitamin D_2. Three groups of control rats were employed. The first was permitted free access to Purina Laboratory Chow; the second, also given Purina Chow, was pair-fed with the rats maintained on the basal rachitogenic diet, while the third group was fed a fully supplemented (phosphate plus Vitamin D) basal ration ad libitum. For purposes of comparison, this protocol was identical to that employed in our previous studies.[3,4]

At the end of the third week, the rats in each group were injected intraperitoneally with ^{3}H-uridine (5 μCi/g body weight).* Some were sacrificed by cervical dislocation after 1, 4, or 72 hr. The tibiae were recovered at autopsy, fixed in 10% neutral formalin, decalcified in 10% EDTA (pH 7.2-7.4) embedded in paraffin, and sectioned along the long axis at 5μ on a rotary microtome. The sections were then autoradiographed by the dipping technique with liquid Kodak NTB-2 emulsion. The slides were exposed for 3 months in a freezer. They were then developed in Kodak D-19, fixed, and washed at 20°C, and the sections stained through the emulsion with hematoxylin and eosin.

The rates of synthesis and intracellular turnover of ^{3}H-uridine were followed in the proximal epiphyseal growth cartilages, and in the osteoblasts lining the metaphyseal trabeculae and endosteum by grain counting methods. In the tissues from rats sacrificed after 1 and 72 hr, we estimated the grain counts over the nucleus and cytoplasm of 100 chondrocytes from the upper-middle layers (proliferative zone), 50 cells from the lower layer (hypertrophic zone), 50 osteoblasts from the metaphysis, and 50 osteoblasts along the endosteum. These counts were performed under an oil immersion lens (970 X). In the tissues from other groups of rats sacrificed 4 hr and 3 days after tracer injection, the total number of grains over the

---

* Uridine-5-^{3}H, New England Nuclear Corp., Lot No. 510-123, specific activity 24.4 Ci/mM.

cells and matrix were calculated in 5 adjacent oil immersion fields. While uridine labeled in the 5 position is a specific tracer for RNA metabolism,[24] Owen[25] noted that there were always some grains associated with bone matrix, suggesting that there had been some degradation of the pyrimidine (but probably not by any major pathway) to form amino acids which could be incorporated into newly-formed collagen. In this study other data are also included from parallel experiments using ^{35}S to measure the ability of the chondrocytes to form sulfated mucopolysaccharides of cartilage matrix.

Results

Epiphyseal Cartilage Plate

1-Hr Uptake of ^{3}H-Uridine (Table 1).--Controls.--Most of the cells throughout the epiphyseal cartilages from control rats were actively synthesizing RNA at the time of injection (Figures 1 and 2). The increased number of grains counted over the hypertrophic cells showed these to be the more active, i.e., 3 to 4 times more grains than over the young cells in the upper proliferative layer (Figure 2). In the proliferative cells, the grain counts over the cytoplasm were 2 to 2.5 times greater than those over the nucleus.

Rachitic Rats.--At 1 hr the uptake of tritiated uridine by the cells in the upper and middle layers of the rachitic cartilages was essentially normal (*ad lib.*- and pair-fed controls). However, uptake of the tracer into cells in the lower hypertrophic cell layer was diminished. Only the youngest cells were heavily labeled, yet their grain counts were 40% lower than normal (Figure 3A,B). In contrast, the oldest chondrocytes were lightly labeled (Figure 3B,C).

The literature concerning defective protein-polysaccharide synthesis in rachitic cartilage generally refers to the inability of the most mature hypertrophic cells to incorporate radioactive precursors. We measured the cytoplasmic incorporation of radiosulfur (^{35}S) in the upper and middle layers of control and rachitic cartilages 3 hr after tracer administration. The

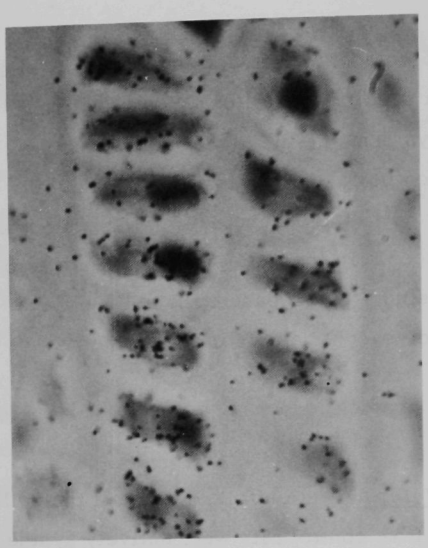

FIG. 1.--Autoradiograph showing nuclear and cytoplasmic uptake of ^{3}H-uridine by chondrocytes in the upper layer (proliferative cells) of a tibial cartilage plate 1 hr after injection. Hematoxylin and eosin. Original magnification 970 X.

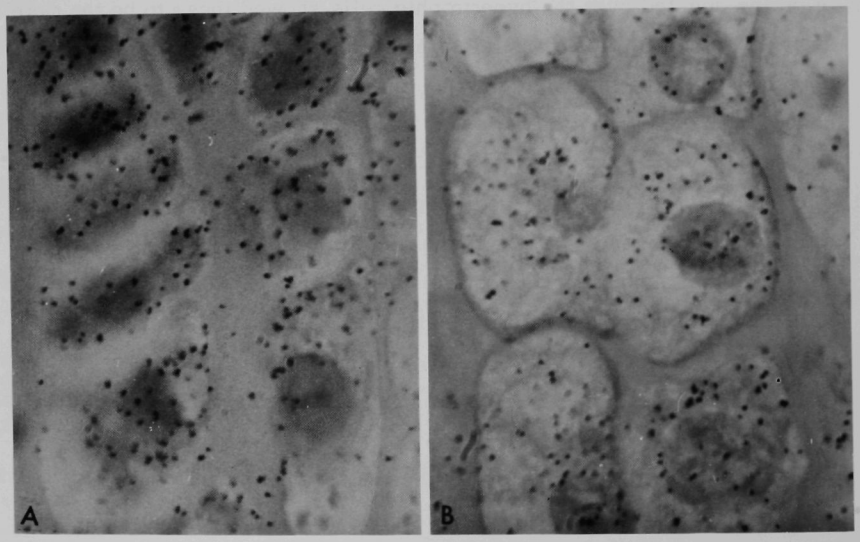

FIG. 2.--Autoradiograph showing the uptake of ^{3}H-uridine by hypertrophic cells (lower layer) in a control rat 1 hr after injection. (A) youngest cells; (B) oldest cells. Hematoxylin and eosin. Original magnification 970 X.

TABLE 1. Chondrocyte Grain Counts.

	Upper-Middle Layers				Lower Layers					
	1 Hr		3 Days			1 Hr		3 Days		
Group	Nucl.	Cytopl.	Nucl.	Cytpol.	U.Z.[a]	N.[b]	L.Z.[c]	U.Z..	N.	.L.Z.
Ad lib.	5.0	9.66				46.8				
	6.66	12.58				61.9				
Avg/m	5.83	11.12	1.10	4.10		54.3			32.0	
S.E.			±0.62	±0.47					±6.2	
n	2	2	3	3		2			3	
Rachitic										
M	4.75	12.20	2.58	6.59	36.00		9.60	35.21		19.76
S.E.	±0.41	±0.27	±0.14	±0.39	±2.34		±0.27	±2.66		±5.87
n	3	3	3	3	3		3	3		3
Pair-fed	5.34	14.72	0.69	3.08		66.74			19.64	
	3.64	10.71	0.18	2.46		59.74			12.31	
M/avg	4.49	12.71	0.43	2.77		63.24			15.97	
S.E.										
n	2	2	2	2		2			2	
Rachitic + Vit. D.							11.12			
							22.33			
M	4.93	11.50	1.44	4.53	33.50		16.76		29.84	
S.E.	±0.84	±0.87	±0.19	±0.43	±2.4				±3.9	
n	3	3	3	3	3		2		3	
Rachitic + P			1.07	3.25					36.57	
			2.38	4.80					43.98	
M/avg	6.45	14.83	1.73	4.03	36.49		12.87		40.27	
S.E.	±0.92	±2.31			±4.97		±4.5			
n	3	3	2	2	3		3		2	

(a) U.Z. = Upper zone of young hypertrophic cartilage cells.
(b) N = Normal layer of hypertrophic cartilage cells.
(c) L.Z. = Lower zone of old hypertrophic cartilage cells.

results suggested that these cells were also normal in terms of their ability to synthesize chondroitin sulfate:

^{35}S-Cytoplasmic Grain Counts (100 Cells, Mean ± S.E.)

Control	Rachitic
5.49 ± 0.60 (3)	5.10
	4.20

Healing Rickets.--Unlike our previous experience, the cartilages from the rachitic rats fed supplements of phosphorus or Vitamin D were not healed completely histologically. Moreover, the cellular pattern of labeling

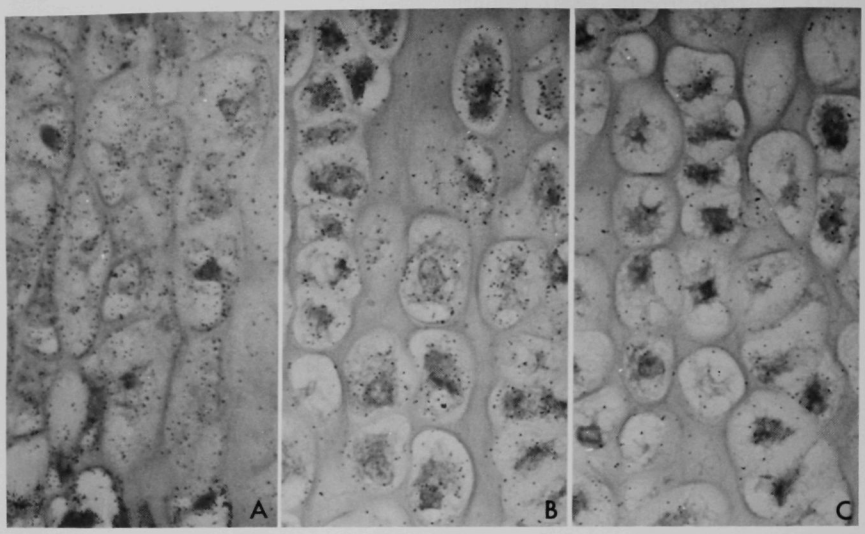

FIG. 3.--Autoradiographs comparing the uptake of ^{3}H-uridine by hypertrophic cells in control and rachitic rats 1 hr after injection. (A) control; (B) youngest cells in the rachitic cartilage; (C) oldest cells in the rachitic cartilage. Hematoxylin and eosin. Original magnification 400 X.

and the amount of label built into structural RNA was similar to that observed in the rachitic group.

3 Days after Labeling (Table 1).--If linear bone growth in young rats is on the order of 150 μ/day[26,27] then the chondrocytes which were at the "top" of a column of cells at the time of injection would come to lie in the hypertrophic zone after 3 days. Under normal circumstances we ought not to expect to find very many labeled cells in the upper and middle layers of the tissue. But where linear growth is retarded, such as in florid and healing rickets,[3] there should be a great many cells labeled with ^{3}H-uridine in the upper layers. In view of these expectations, it was somewhat anomalous to find labeled cells in the upper-middle layers of the cartilages from control rats.

Rickets.--The nuclear and cytoplasmic grain counts over rachitic cells were greater than normal, doubtless due to poor linear bone growth. On this basis, the overall retention of tracer by rachitic cells was 54%. This is a very high value, suggesting that protein-polysaccharide formation is impaired in rickets. One must assume that reutilization of uridine is slight in view of Owen's[25] studies on bone cells. Even though there is normally a transfer of activity within cells from nuclear to cytoplasmic compartments within the first 24 hr after injection and a parallel loss of activity from these compartments with time thereafter, our experimental design did not permit an estimate of rates of intracellular transfer.

Healing Rickets.--The nuclear and cytoplasmic grain counts in the cartilage from rachitic + phosphate- or rachitic + Vitamin D-treated rats were essentially normal. In these groups and in the controls, the average activity retained by the nucleus and cytoplasm was 21% and 31% respectively. Therefore, our data do not suggest that RNA turnover is more rapid in the cartilages from rachitic rats that are being healed. From these data, coupled with our previous findings with ^{3}H-thymidine[7] (that phosphate and Vitamin D deprivation do not affect the rate of DNA synthesis by individual chondrocytes), it would appear that the intracellular machinery in rickets is fully operative in those cells which continue to undergo replication.

These experiments were repeated and confirmed with rats whose rickets had been more completely healed by dietary phosphorus and Vitamin D supplements. The first group was sacrificed at 4 hr to provide an intermediate time check on RNA metabolism; the second group was again sacrificed at 3 days. When we counted the total number of silver grains over both matrix and cells, the data reinforced our initial impression (Table 2) that RNA synthesis and turnover is normal in rachitic cartilage. The significantly higher total grain counts recorded at 3 days in the upper and middle layers of the cartilages from the phosphorus- and Vitamin D-supplemented rats can be interpreted in light of our studies with ^{3}H-thymidine[3]--that there was less cartilage renewal due to stunting. The rates of linear

TABLE 2. Chondrocyte/Matrix Grain Counts

	Upper-Middle Layers		Lower Layer					
	4 hr	3 Days	4 hr			3 Days		
Group			U.Z.[c]	N[d]	L.Z.[e]	U.Z.	N.	L.Z.
Ad lib.								
M	393.7	113.0		132.1			95.6	
S.E.	±98.7	±26.1		±18.6			±24.2	
n	3	3		3			3	
Rachitic								
M	300.7	101.3	121.2		25.4[a]	103.9		110.9
S.E.	±48.6	±10.7	±48.1		±7.2	±11.8		±25.8
n	3	3	3		3	3		3
Pair-fed								
M	349.3	64.7		171.6			50.9[b]	
S.E.	±45.0	±27.0		±41.3			±12.4	
n	3	3		3			3	
Rachitic + Vit. D								
M	328.3	157.3[a][b]		108.2			144.3[b]	
S.E.	±44.9	±8.5		±18.0			±8.8	
n	3	3		3			3	
Rachitic + P								
M	296.4	126.9		152.1			142.0	
S.E.		±56.9					±51.9	
n	1	3		1			3	
Rachitic + P + Vit. D								
M	354.8	190.4[a][b]		195.8			154.5[b]	
S.E.		±20.9					±16.1	
n	1	3		1			3	

(a) $P < 0.01$ vs. pair-fed controls.
(b) $P < 0.01$ vs. rachitic rats.
(c) U.Z. = Upper zone of young hypertrophic cartilage cells.
(d) N = Normal layer of hypertrophic cartilage cells.
(e) L.Z. = Lower zone of old hypertrophic cartilage cells.

bone growth were low in these groups owing to voluntary starvation and poor utilization of food.

These data are significant because they provide a ready explanation for the increase in glycolytic enzyme activity and increased histochemical enzyme localization in rachitic cartilage reported by Kunin and others.[1,14-17] Although the enzymes localized histochemically were increased in every layer of the rachitic cartilage, this probably does not

represent an increased RNA-dependent synthesis.[14] We suggest that enzyme turnover is reduced, and that the enzymes simply accumulate because they are not destroyed. Further studies on a biochemical level are being conducted to explore this possibility.

Bone

The 1-hr uptake of ^{3}H-uridine into the nucleus and cytoplasm of metaphyseal and endosteal osteoblasts was normal during the development and healing of rickets (Table 3, Figure 4). But unlike the situation in cartilage, the turnover (3-day grain counts) of RNA in these compartments appeared to occur at a uniform rate independent of diet (~ 37%). These data also indicate that the rates of RNA synthesis and turnover by endosteal and

TABLE 3. Osteoblast Grain Counts

	Metaphyseal Grains				Endosteal Grains			
	1 Hr		3 Days		1 Hr		3 Days	
Group	Nucl.	Cytopl.	Nucl.	Cytopl.	Nucl.	Cytopl.	Nucl.	Cytopl.
Ad lib.	8.60	13.00			3.00	11.54		
	4.87	11.61			6.39	15.17		
Avg/M	6.74	12.31	1.94	3.16	4.70	13.34	2.50	4.90
S.E.			±0.32	±0.40			±0.58	±0.28
n	2	2	3	3	2	2	3	3
Rachitic								
M	5.33	12.10	2.44	4.64	5.42	13.67	2.44	4.64
S.E.	±0.55	±0.88	±0.24	±0.26	±0.34	±2.72	±0.24	±0.26
n	3	3	3	3	3	3	3	3
Pair-fed	6.26	13.68	1.51	3.21	3.80	15.36	0.95	3.99
	4.89	12.43	0.96	2.38	5.25	14.01		
Avg	5.58	13.06	1.24	2.79	4.52	14.69	0.95	3.99
n	2	2	2	2	2	2	1	1
Rachitic + Vit. D								
M	6.27	13.07	2.27	4.67	6.31	13.33	1.67	4.01
S.E.	±0.58	±0.35	±0.10	±0.34	±0.86	±1.28		
n	3	3	3	3	3	3	1	1
Rachitic + P			2.69	4.61	6.14	14.18	3.71	6.22
			2.74	5.36	4.55	11.86		
Avg/M	5.98	12.96	2.72	4.99	5.35	13.02	3.71	6.22
S.E.	±0.52	±1.69						
n	3	3	2	2	2	2	1	1

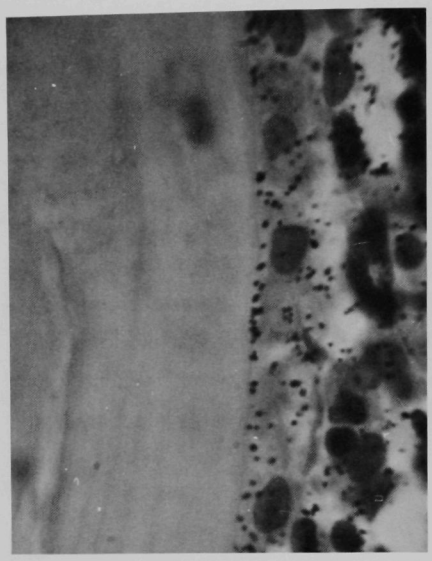

FIG. 4.--Autoradiograph showing nuclear and cytoplasmic uptake of ^{3}H-uridine by metaphyseal osteoblasts in a pair-fed control rat 1 hr after injection. Hematoxylin and eosin. Original magnification 970 X.

and metaphyseal osteoblasts are similar. This is important in terms of Rohr's[22] suggestion that the rate of appositional bone growth is increased in the rachitic metaphysis. We believe that the uniformity of RNA metabolism in osteoblasts revealed in this study makes it likely that our data on appositional bone growth (^{3}H-proline)[4] for the endosteum is a good approximation for the metaphysis. The absence of any great variation in labeling intensity of bone matrix at the endosteum attributable to diet is illustrated in Figure 5. These results also provide evidence that the changes in urinary hydroxyproline recorded during the development and healing of rickets are a direct consequence of the number of competent osteogenic cells, not of their individual level of activity.

Summary

RNA synthesis and turnover were studied autoradiographically in the proximal tibiae of rats made rachitic by feeding them a phosphate deficient, Vitamin D-free diet, and in rachitic rats healed by dietary supplements of phosphate and Vitamin D. The animals were sacrificed at 1, 4, and 72 hr after a single intraperitoneal injection of ^{3}H-uridine. The autoradiographs were quantitated by grain counting.

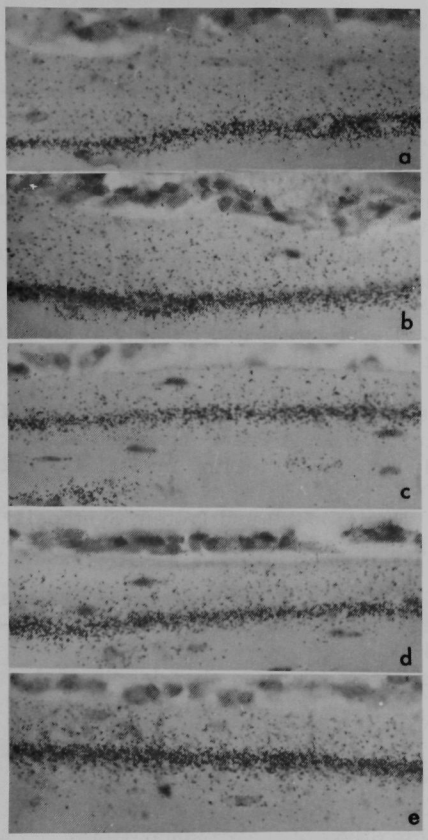

FIG. 5.--Autoradiographs showing bands of silver grains over labeled bone endosteal matrix in rats 3 days after an intraperitoneal injection of ^{3}H-proline. (a) control fed ad lib.; (b) pair-fed control; (c) rachitogenic diet; (d) rachitogenic diet + phosphorus; (e) rachitogenic diet + Vitamin D. Note that the grain densities do not differ markedly in any group. Hematoxylin and eosin. Original magnification 970 X.

In rachitic epiphyseal cartilage, the synthesis of RNA by the cells in the upper and middle layers was normal, but was impaired in the hypertropic cells. The nuclear and cytoplasmic grain counts after 3 days were greater than normal, indicating that the intracellular turnover of RNA was reduced. The pattern of cartilage matrix synthesis measured 4 hr after an injection of ^{35}S-sulfate paralleled the uridine data.

RNA metabolism in the osteoblasts lining the metaphyseal trabeculae and endosteal surfaces was essentially normal during the development and healing of rickets. Moreover, the nuclear and cytoplasmic grain counts were identical at these two sites. From this information we can infer that appositional bone formation rates are probably unchanged in nutritional rickets.

The authors wish to acknowledge the excellent technical assistance of Helen Cummins and Michael Giancola.

References

1. Krane, S. M., V. Parsons, and M. J. Glimcher. Biochemical Processes in the Mineralization of Organic Matrices. L'Osteomalacie, Ed. D. J. Hioco. Masson et Cie, Paris, 1967, pp. 159-170.
2. Rasmussen, P. The Action of Vitamin D Deficiency on Bone Tissue and the Epiphyseal Plate in Rats Given Adequate Amounts of Calcium and Phosphorus in the Diet. Arch. Oral Biol. 14, 1293 (1969).
3. Simmons, D. J. and A. S. Kunin. Development and Healing of Rickets in Rats. I. Nutritional Considerations and Studies with Tritiated Thymidine. Clin. Orthopaed. No. 68, 251 (1970).
4. Simmons, D. J. and A. S. Kunin. Development and Healing of Rickets in Rats. II. Studies with Tritiated Proline. Clin. Orthopaed. No. 68, 261 (1970).
5. Howell, D. S., J. Pita, J. F. Marquez, and J. Madruga. Partition of Calcium Phosphate and Protein in the Fluid Phase Aspirated at Calcifying Sites in Epiphyseal Cartilage. J. Clin. Invest. 47, 1121 (1968).
6. Mankin, H. J. and L. Lippiello. Nucleic Acid and Protein Synthesis in Epiphyseal Plates of Rachitic Rats. J. Bone Joint Surg. 51A, 862 (1969).
7. Simmons, D. J. Rickets in Rats, A Progress Report. Argonne National Laboratory Radiological Physics Division Annual Report, July 1966-June 1967. ANL-7360, p. 124.
8. Rohr, H. P. Autoradiographische Untersuchungen über das Knorpel-Knocken-Langenwachstum bei der Experimentellen Rattenrachitis. Z. Ges. Exp. Med. 137, 248 (1963).
9. Sheldon, H. and R. A. Robinson. Studies on Rickets. I. The Fine Structure of Uncalcified Bone Matrix in Experimental Rickets. Z. Zellforsch. 53, 671 (1961).
10. Hjertquist, S. O. Autoradiographic Study of the Proximal Tibial Growth Zone in Normal and Rachitic Rats after Administration of Radiosulphate. Acta Path. Microbiol. Scand. (Suppl.) 154, 99 (1962).
11. Matthews, J. L., J. H. Martin, H. W. Sampson, A. S. Kunin, and J. H. Roan. Mitochondral Granules in the Normal and Rachitic Rat Epiphysis. Calc. Tiss. Res. 5, 91 (1970).
12. Havivi, E. and B. S. Bernstein. Lipid Metabolism in Normal and Rachitic Rat Epiphyseal Cartilage. Proc. Soc. Exp. Biol. Med. 131, 1300 (1969).
13. Howell, D. S., J. F. Marquez, and J. C. Pita. The Nature of Phospholipids in Normal and Rachitic Costochondral Plates. Arthritis and Rheumatism 8, 1039 (1965).
14. Balogh, K., Jr. and A. S. Kunin. The Effects of Vitamin D_2 and Dietary Phosphorus on Oxidative Enzymes in the Epiphyseal Cartilage of Rachitic Rats: A Histochemical Study. Lab. Invest. 18, 782 (1968).

15. Dixit, P. K. Quantitative Histochemistry of Rachitic Rat Cartilage Enzyme Activity during Healing Induced by Vitamin D and Starvation. J. Histochem. Cytochem. 17, 411 (1969).
16. Kunin, A. S. and S. M. Krane. The Effect of Dietary Phosphorus on the Intermediary Metabolism of Epiphyseal Cartilage from Rachitic Rats. Biochim. Biophys. Acta 107, 203 (1965).
17. Meyer, W. L. and A. S. Kunin. Inductive Effect of Rickets on Glycolytic Enzymes of Rat Epiphyseal Cartilage and its Reversal by Vitamin D and Phosphate. Arch. Biochem. Biophys. 129, 438 (1969).
18. Parsons, V. and C. Hampton. Phosphate Deficiency and Collagen Metabolism. Nutritional Aspects of the Development of Bone and Connective Tissue, Ed. J. C. Somogyi and E. Kodicek. S. Karger, Basel, 1969, pp. 46-57.
19. Parsons, V., G. Stirling, and C. Davies. Autoradiographic Studies of Healing Phosphate Deficiency Rickets in Rats. Cal. Tiss. Res. 4 (Suppl.), 157 (1970).
20. Parsons V. and M. Self. Urinary Hydroxyproline Excretion in Phosphate Depleted Rachitic Rats. Nature 217, 551 (1968).
21. Simmons, J. D. Collagen Formation and Endochondral Ossification in Estrogen Treated Mice. Proc. Soc. Exp. Biol. Med. 121, 1165 (1966).
22. Rohr, H. P. Autoradiographische Untersuchungen über den Kollagenstoffwechsel bei der Experimentallen Rattenrachitis. Z. Ges. Exp. Med. 139, 621 (1965).
23. Parsons, V., C. Davies, and M. Jenkins. The Effects of Actinomycin D on the Increased Total Hydroxyprolinuria in Healing Rats. Biochim. Biophys. Acta 192, 252 (1969).
24. Hayhoe, A. J. and D. Quaglino. Autoradiographic Investigations of RNA and DNA Metabolism of Human Leucocytes Cultured with Phytohaemagglutin; Uridine-5^{3}H as a Specific Precursor of RNA. Nature 205, 151 (1965).
25. Owen, M. Uptake of [^{3}H] Uridine into Precursor Pools and RNA in Osteogenic Cells. J. Cell. Sci. 2, 39 (1967).
26. Kember, N. F. Cell Division in Endochondral Ossification. J. Bone Joint Surg. 42B, 824 (1960).
27. Tapp, E. Tetracycline Labeling Methods of Measuring the Growth of Bones in the Rat. J. Bone Joint Surg. 48B, 517 (1966).

MINERAL METABOLISM IN THE SKELETONS OF TELEOSTS--A REVIEW*

D. J. Simmons

The calcium and phosphorus requirements of the higher bony fish (teleosts) are met in large part by their ability to absorb these ions directly from the environment. The major regulation of ion influx and efflux occurs at the levels of the gills, fins, and oral epithelia. These structures all operate to good effect in marine fish, but the gills have greater capacity in fresh water forms. Moreover, on a comparative basis, calcium ion transport across the gills appears to be more efficient in fresh water--a factor of probable adaptive value for animals living in a calcium-poor medium. While only marine fish drink water in large amounts, absorption of calcium across the intestinal mucosa from water and food sources is a small part of total mineral homeostasis. Calcium excretion is performed principally by the gills and kidneys; the small endogenous fecal component has not as yet been quantified. With respect to calcium, then, the blood of fish can be considered co-extensive with the external environment (the "bone-body fluid continuum"), but it is not clear to what extent other factors influence this process. Do, for instance, the relatively lower concentrations of vitamin D in the livers of fresh water fish imply its greater participation in calcium absorption via the gills or gut?

Bone and skin are the major repositories for absorbed calcium in fish, but there is little evidence that the mineralization of structures such as the scales is accomplished by an extravascular mechanism which involves topical absorption of calcium from the water. The rate of uptake, the depositional pattern, the blood disappearance curves, and the retention of alkaline earth tracers (Sr and Ca) by the hard parts appear generally similar in freshwater and marine species and independent bone types, i.e., osteocytic or acellular bone. Detailed autoradiographic observations, even at long times after administration, reveal only surface labeling and the absence of a diffuse component (long-term exchange). With respect to calcium, no major discrimination against strontium absorption appears at the level of the gills, but such a mechanism is operative in the assimilation of these ions from dietary sources.

The endocrine control of calcium metabolism is understood only imperfectly, in part because of significant species differences. Hypophysectomized fish may become either hyper- or hypocalcemic. Seasonal

---

*Abstract of paper accepted for publication in Clinical Orthopaedics and Related Research.

hypercalcemia--an estrogen effect--is observed regularly in female fish during the breeding season, and estrogen treatment can antagonize the hypocalcemic response to ACTH during nonreproductive periods in both sexes. The amorphous fraction of bone mineral may be an important labile reservoir for calcium which can be metabolized upon demand in cellular boned species. An evanescent but severe hypercalcemia can be produced in teleosts by ablation of the corpuscles of Stannius. The level of blood calcium is unaffected largely by cortical and parathyroid extract. It is difficult to separate the morphogenetic and growth promoting roles of the thyroid. The skeletons of thyroidectomized fish may be poorly calcified, while postoperative blood calcium levels remain normal. The normo- or hypocalcemia found in fish treated with thyroid hormones may be a calcitonin effect. Teleosts which have developed hyperplastic thyroids (pinealectomy, thyroid stimulating hormone, migration) may also have enlarged ultimobranchial bodies; yet only certain species become hypocalcemic when treated with porcine thyrocalcitonin, and the response may include an atypical hypophosphaturic component. Because resorptive bone changes have only rarely been described following injections of parathyroid extract and estrogen, the major effect of the endocrine system may be on electrolyte balance regulating ion absorption at the level of the gills and other membranes.

ELECTRON MICROSCOPE MEASUREMENTS OF ALKALINE EARTH TRANSPORT

Elizabeth Lloyd

Introduction

Many processes have been suggested for the mechanism of calcification, but none have received complete acceptance.

As part of a wider study on calcium transport in growing bone, electron microscope and electron microscope autoradiography were used to examine an area of rapidly forming bone on the periosteal surface of the proximal end of the tibia of a 15-day-old mouse. This area of bone was chosen as a site where osteoblasts are known to be laying down bone and where the process of calcification is uncomplicated by other changes which are taking place in the more commonly studied site in the cartilage plate area.

Calcified cartilage differs from bone in that the collagen fibrils do not show the 640-Å banding and are much thinner than those found in bone.[1] There may be reason to suppose, therefore, that the mechanism of calcification at this site may not necessarily be the same as that which takes place in bone formation at other sites.

In view of the recent work of Martin and Matthews,[2,3] suggesting that mitochondrial granules seen in chondrocytes may be involved with the onset of matrix calcification in the cartilage plate area, it was decided to see whether the same process could be implicated in bone formation at periosteal bone surfaces. Barium-133 was used instead of ^{45}Ca to study alkaline earth transport in an effort to improve the autoradiographic resolution.

Experimental Methods

Two 15-day-old mice were injected, one with saline to act as a control and the other with 1 mCi of ^{133}Ba. The latter was scarificed 10 min after injection. The tibias and femurs were dissected out rapidly (within

1 min) and placed in 2% glutaraldehyde in caccodylate buffer for further dissection into 0.5-mm lengths until the whole bones were sectioned. The bones were allowed to stand in glutaraldehyde with buffer for 3 hr to obtain good penetration. They were then washed and transferred to the osmium postfixing solution (2 parts 2% osmium tetraoxide:1 part S-collidine buffer). The tissues were fixed for a further 1 hr in this solution. The bones were imbedded in epon or a low viscosity medium.[4] One-micron sections were cut, stained with 1% toluidine blue in 1% Na_2CO_3 solution, and examined under the light microscope to determine the site on the periosteal surface where osteoblasts were most numerous. Thin sections were cut with the ultramicrotome onto water to which NaOH was added to maintain a pH of 8, using thymol blue as an indicator. This was necessary to prevent loss of calcium from the sections which tends to leach out at neutral or acid pH's. The sections were stained with 0.2% lead citrate in water with NaOH added to give a pH of 12.

Other sections were prepared for autoradiography. Those sections for examination with the light microscope were cut about 1μ to 2μ thick, placed on a glass slide and covered with Ilford L4 emulsion (1 part L4: 1 part water). These were stored in light-tight boxes to which some Drierite had been added. The exposure times were of the order of a few weeks. These sections were developed in D19 for 2 min at 20°C, dipped in 0.05% acetic acid, fixed in Edwal fixer for 3 min, and washed in running water for 30 min. The sections were then dipped in distilled water and stained with 1% toluidine blue. The correct exposure for the electron microscope autoradiographic studies was determined from the autoradiographs of these sections examined under the light microscope. An exposure time of a factor of three longer was allowed for the thinner electron microscope sections.

For the EM autoradiographs, the sections were floated onto parlodion-coated copper grids which were attached to a glass slide using fine strips of double-sided scotch tape. The glass slides were dipped in

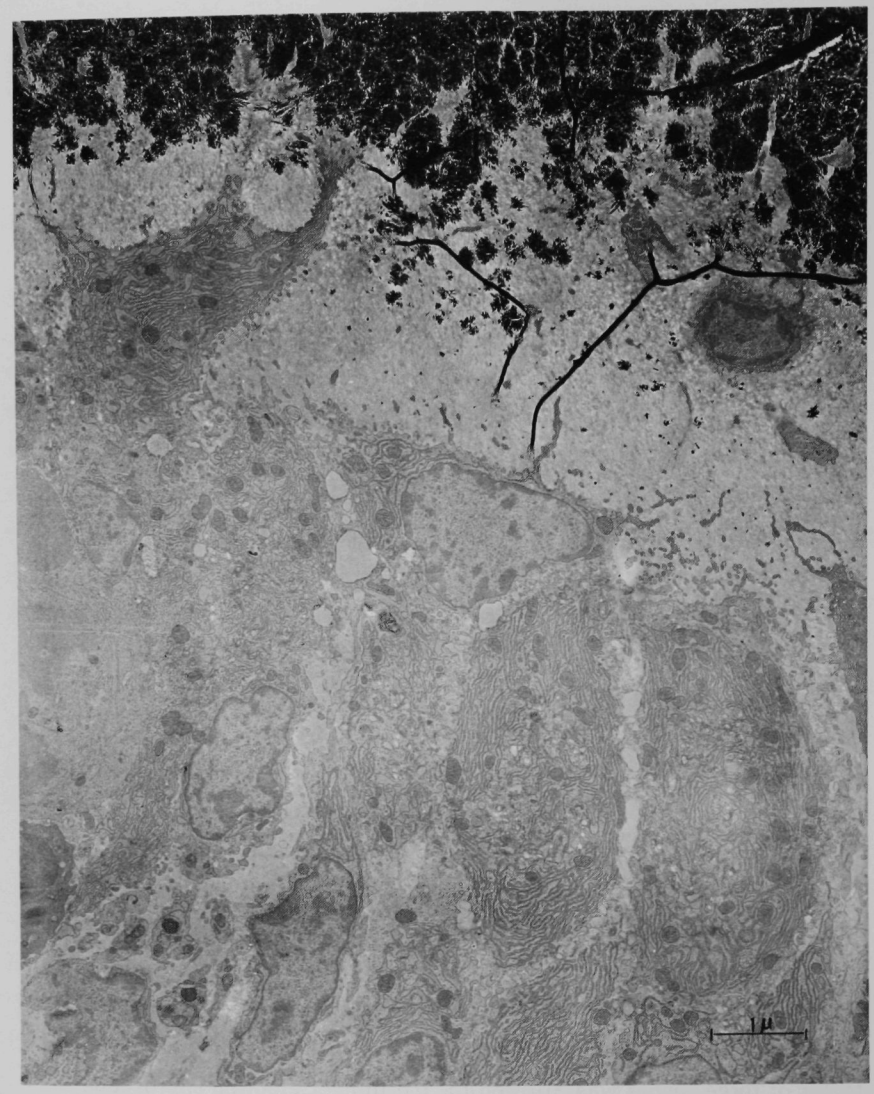

FIG. 1.--Electron microscope picture showing the periosteal surface of bone taken from the proximal tibia of a 15-day-old mouse. The section was fixed in glutaraldehyde followed by osmium and stained with lead citrate.

Ilford L4 emulsion (1 part emulsion:1 part water) and allowed to dry in a dust-free atmosphere before being stored in the same way as for the light microscope.

After exposure (about 3 months) the slides were removed, developed in D19 for 4 min, dipped in 0.5% acetic acid, fixed in 20% sodium thiosulfate for 4 min, and washed very gently for 10 min in each of 3 changes of distilled water. The grids were then stained with 0.3% Pb citrate[5] and viewed with the Siemens model 1A electron microscope.

Results

Figure 1 is typical of many sites of calcification in the periosteal region of the proximal end of the mouse tibia. Here we see a number of osteoblasts and many small centers of ossification in the collagen matrix.

The following observations, characteristic of our findings, appear to be pertinent:

1. The small centers of calcification are found close to the mass of calcified bone which has already been laid down. There is a decreasing concentration of these calcification centers as we move away from the surface of calcified bone.

2. The osteoblasts are in general separated from the surface of calcified bone by a considerable thickness (about 5 μ) of uncalcified material (osteoid). Only the extremities of a few cell processes are visible in the areas of active calcification.

3. There is no preponderance of mitochondria in the sites adjacent to bone calcification.

4. Most of these mitochondria appear to contain no granules of the types found by Matthews in the cartilage plate area.

The latter observation was made from pictures such as Figures 2, 3, and 4 showing portions of the osteoblasts at much higher magnifications than Figure 1.

FIG. 2.--Electron microscope picture, same as Figure 1, at a slightly higher magnification. Portions of the osteoblasts outlined are shown at a higher magnification in Figures 3 and 4.

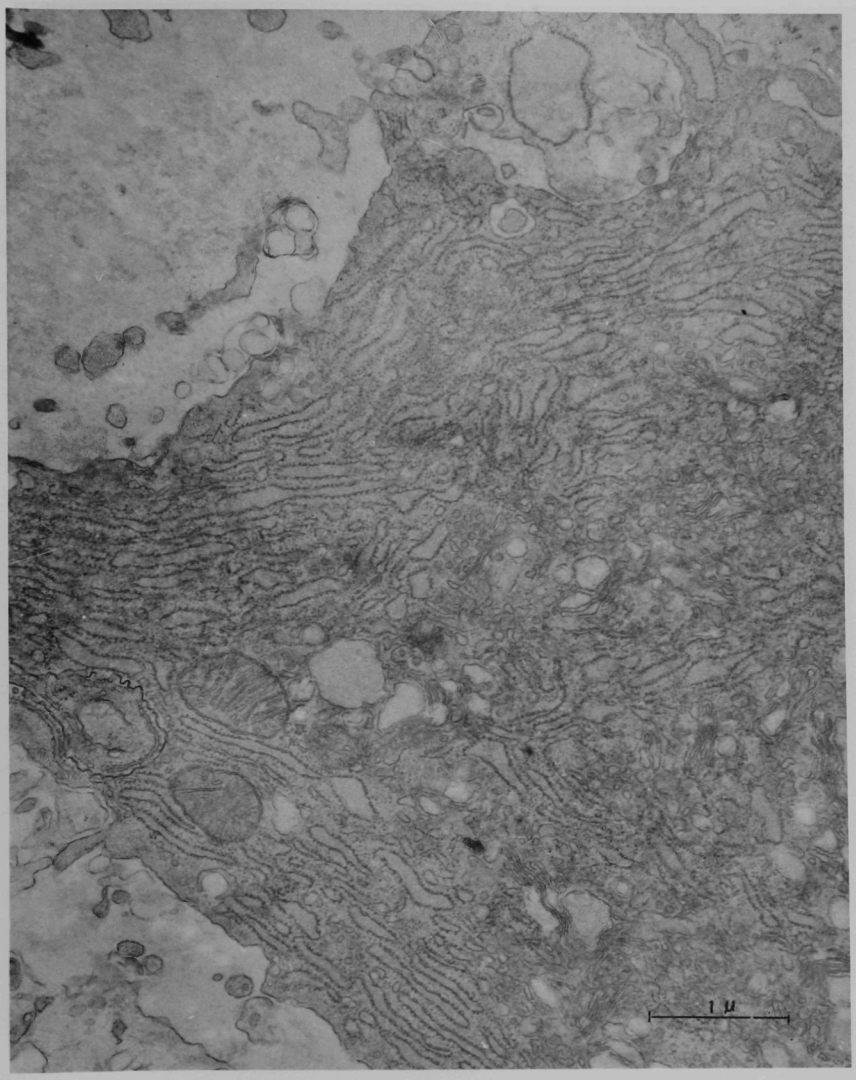

FIG. 3.--Higher magnification of the portion of the osteoblast outlined and numbered 3 on Figure 2.

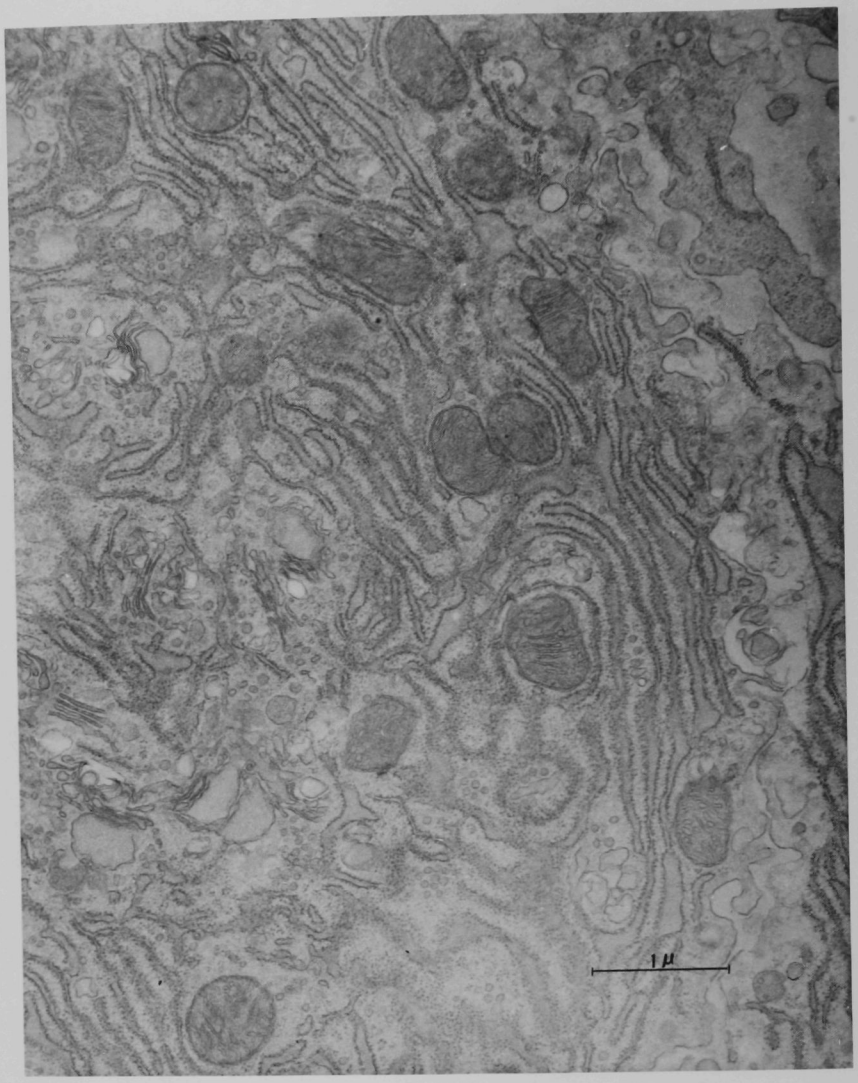

FIG. 4.--Higher magnification of the portion of the osteoblast outlined and numbered 4 in Figure 2.

EM Autoradiographic Studies

Our autoradiographic studies are incomplete but preliminary results suggest that ^{133}Ba was localized mainly in regions of solid bone close to osteocyte processes; however, many grains were also seen over the collagen matrix on the periosteal surface. By comparison, only occasional grains were found over either osteoblasts or any of the other cells. This suggests either that the cells did not accumulate the label or that it passed through the cells so quickly that even after 10 min little or no tracer was left in the cells.

Discussion

Although no granules were observed in the osteoblasts illustrated in Figures 1-4, occasional granules were seen in other cells, as seen in Figure 5. However, it would appear that this number was probably less than is observed under normal conditions in liver cells, a tissue not specifically concerned with the calcification process. Figure 6 shows a picture of liver cells in a mouse with an average number of granules for that tissue. Other tissues unconnected with the calcification process where mitochondrial granules are normally found are the kidney and the heart. Peachey[6] has also observed mitochondrial granules in epithelial and smooth muscle cells of the toad urinary bladder. In his in vitro studies he showed how the density of the mitochondrial granules could be increased by altering the medium--in particular by adding calcium. Parathyroid hormone[7-9] and Vitamin D[10,11] have also been shown to affect the mitochondrial granules in cells in vivo.

From the present study it appears unlikely that mitochondrial granules are important in the calcification process in bone formation at the site studied. The mechanism of calcification at this site is more likely to be extracellular, although the possibility of a very rapid transport of calcium ions through the cell cannot be ruled out.

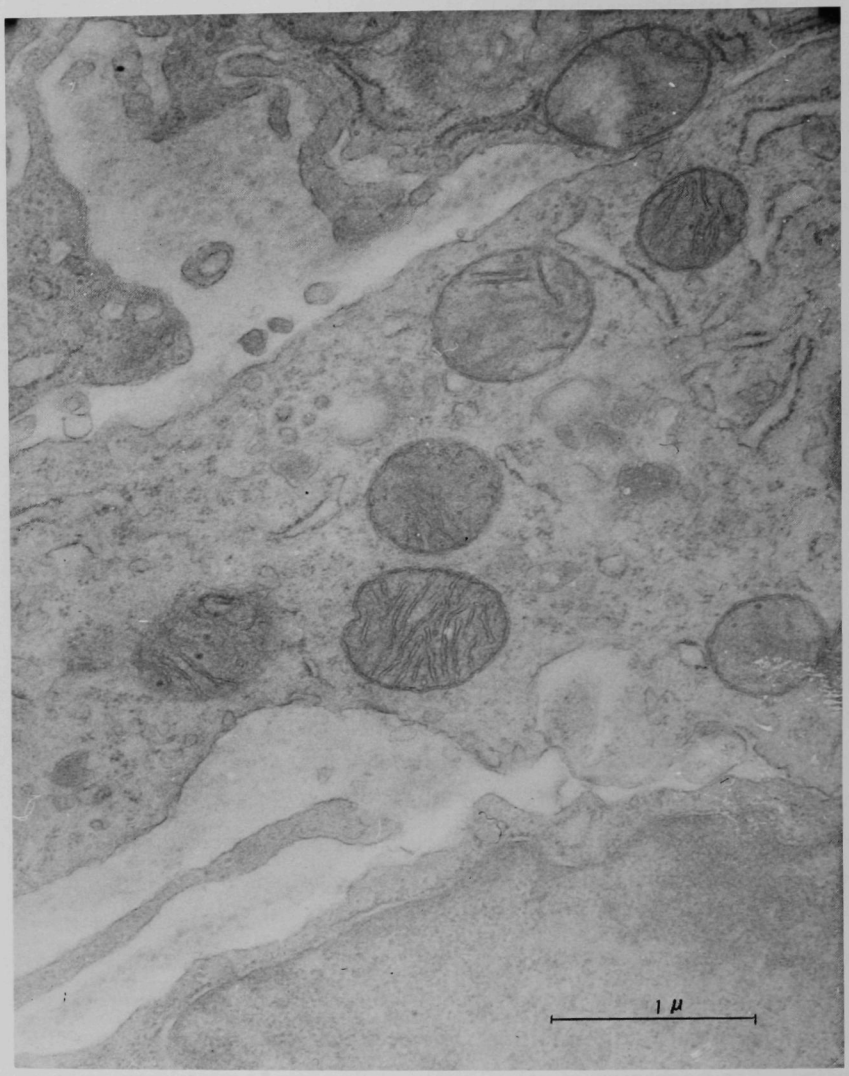

FIG. 5.--Picture of part of a cell showing granules in the mitochondria.

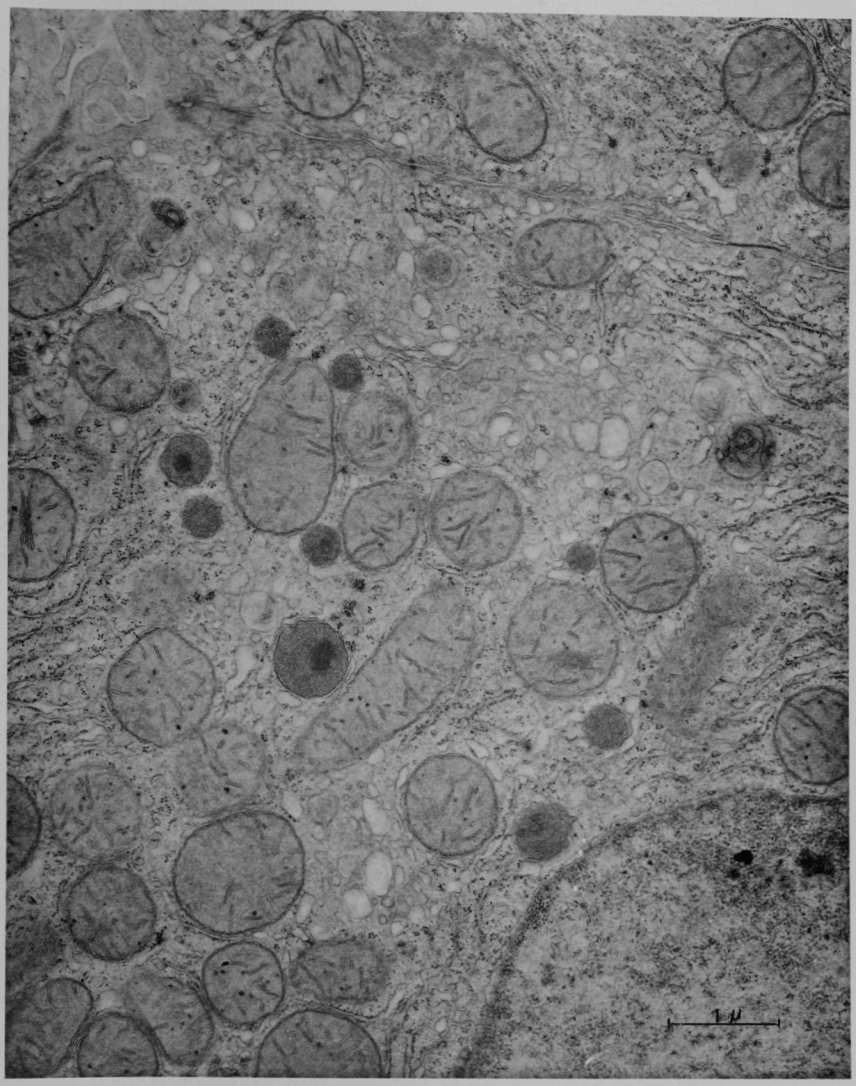

FIG. 6.--Picture of a cell taken from mouse liver showing mitochondrial granules.

Summary

The transport of calcium in the calcification process has been studied at the periosteal surface of the proximal end of the tibia in a rapidly growing mouse using electron microscopy and electron microscope autoradiography with ^{133}Ba as a tracer. These studies showed that the site of calcification is close to the extremities of cell processes, but that mitochondrial granules are probably not involved in the process.

I wish to thank F. Mackevicius for her excellent technical assistance.

References

1. Eastoe, J .E. The Place of Cartilage and Bone among Vertebrate Mineralized Tissues, Calc. Tiss. Res. 4 (Suppl.); 24 (1970).
2. Martin, J. H., and J. L. Matthews. Mitochondrial Granules in Chondrocytes. Calc. Tiss. Res. 3, 184 (1969).
3. Martin, J. H. and J. L. Matthews. Mitochondrial Granules in Chondrocytes, Osteoblasts and Osteocytes. Clin. Orthopaed. 68, 273 (1970).
4. Spurr, A. R. A Low-Viscosity Epoxy Resin Embedding Medium for Electron Microscopy. J. Ultrastructure Res. 26, 31 (1969).
5. Venable, J. H. and R. Coggeshall. A Simplified Lead Citrate Stain for Use in Electron Microscopy. J. Cell. Biol. 25, 407 (1965).
6. Peachey, L. D. Electron Microscopic Observations on the Accumulation of Divalent Cations in Intramitochondrial Granules. J. Cell. Biol. 20, 95 (1964).
7. Cameron, D. A., H. A. Paschall, and R. A. Robinson. Changes in the Fine Structure of Bone Cells after the Administration of Parathyroid Extract. J. Cell. Biol. 33, 1 (1967).
8. Cohn, D. V., R. Bawdon, and G. Eller. The Effect of Parathyroid Hormone In Vivo on the Accumulation of Calcium and Phosphate by Kidney and on Kidney Mitochondrial Function. J. Biol. Chem. 242, 1253 (1967).
9. DeLuca, H. F., G. W. Engstrom, and H. Rasmussen. The Action of Vitamin D and Parathyroid Hormone In Vitro on Calcium Uptake and Release by Kidney Mitochondria. Proc. Natl. Acad. Sci. 38, 1604 (1962).
10. Engstrom, G. W. and H. F. DeLuca. The Action of Vitamin D In Vivo and In Vitro on the Release of Calcium from Kidney Mitochondria. J. Biol. Chem. 237, PC 974 (1962).
11. Matthews, J. L., J. H. Martin, N. W. Sampson, A. S. Kunin, and J. H. Roan. Mitochondrial Granules in the Normal and Rachitic Rat Epiphysis. Calc. Tiss. Res. 5, 91-99 (1970).

PUBLICATIONS

Clemente, G. F., L. D. Marinelli, and I. K. Abu-Shumays. Regularization Unfolding in Low γ-Activity Measurements: I. Evaluation of One-Dimensional Scanning. Int. J. Appl. Radiat. Isotopes 6, 307-318 (June 1970).

Cole, A., D. J. Simmons, H. Cummins, F. J. Congel, and J. Kastner Application of Cellulose Nitrate Films for Alpha Autoradiography of Bone. Health Phys. 19, 55-56 (July 1970).

Dedolph, R., Gary Ter Haar, R. B. Holtzman and Henry F. Lucas, Jr. Sources of Lead in Perennial Ryegrass and Radishes. Environ Sci. Technol. 4, 217-223 (March 1970).

Ellsasser, J. C., J. E. Farnham, and J. H. Marshall. Comparative Kinetics and Autoradiography of ^{45}Ca and ^{133}Ba in Ten-Year-Old Beagle Dogs. The Diffuse Component Distribution Throughout the Skeleton. J. Bone Joint Surg. 51-A (7), 1397-1412 (October 1969).

Failla, Patricia. Recovery and Modification of Radiation-Induced Division Delay in Developing Sea Urchin Eggs. Radiology 93, 643-648 (September 1969).

Failla, P. M. and R. C. Rustad. Protein Synthesis and Recovery from Gamma-Ray Induced Mitotic Delay in Fertilized Sea Urchin Eggs. Int. J. Radiat. Biol. 17 (4), 385-388 (February 1970).

Holtzman, R. B. Sources of ^{210}Pb in Uranium Miners. Health Phys. 18, 105-112 (February 1970).

Holtzman, R. B. Isotopic Composition as Natural Tracer of Lead in Man's Environment. Environ. Sci. Technol. 4, 314-318 (1970).

Lucas, H. F., Jr., J. H. Marshall and L. A. Barrer. The Level of Radium in Human Blood Forty Years after Ingestion. Radiat. Res. 41, 637-645 (March 1970).

Marshall, J. H., J. Rundo, and G. E. Harrison. Retention of Radium in Man. Radiat. Res. 39, 445-451 (August 1969).

Rowland, R. E. and J. E. Farhman. The Deposition of Uranium in Bone. Health Phys. 17, 139-144 (1969).